Photophysics of Thermally-Activated Delayed Fluorescence Emitters and its Impact on the Performance of Organic Light-Emitting Diodes

DANIEL ALFREDO DE SA PEREIRA

Photophysics of Thermally-Activated Delayed Fluorescence Emitters and its Impact on the Performance of Organic Light-Emitting Diodes

Daniel de Sá Pereira

A Thesis Presented for the Degree of Doctor of Philosophy

Organic Electroactive Materials Research Group

Department of Physics

University of Durham

2019

Abstract

Research in thermally-activated delayed fluorescence (TADF) emitters is gathering momentum and rapidly progressing towards commercial application in display industry. Successful TADF combines design strategies that result in thermal up-conversion of non-emissive triplets into emissive singlet excitons, increasing the maximum internal efficiency from 25 to 100 % in purely organic systems. Its performance can therefore compete with current leading emitters used in industry, however it is not without its hurdles and a full understanding of how to produce efficient TADF systems and stable organic light-emitting diodes (OLEDs) is still elusive.

This thesis aims at illuminating strategies to achieve highly efficient and stable TADF. By examining the photophysical aspects of different donor-acceptor systems (D-A, D_2-A, D_3-A, D_4-A and D-A-D) and, more importantly, establishing comparisons between different subsets of molecules, subtle but important aspects of the performance of these emitters are isolated to allow understanding of future design rules for better combinations. These comparisons are then correlated with the emitters' performance in devices.

In a multi-donor platform, the inherent TADF mechanism and in host are both considered by comparing the effect of number and position of donors as well as rigidity and polarity of the host environment to the D-A angles. A separate comparative study elucidates the real heavy atom effect in an emitter with dual emission from two different conformations. Furthermore, the application of a well-established spectroscopy technique novel to TADF tests its physical mechanism by probing character and mixing of the excited states involved. Finally, in a more application-driven approach, a combination of three different TADF molecules for the production of white light is studied in simple device structures. In this sense, guidelines of how to produce optimised TADF systems emerge, moving the technology ever close to its industrial application.

Table of Contents

Acronyms

A	Electron-accepting Unit/Acceptor
CCD	Charge Coupled Device
CCT	Correlated Colour Temperature
CIE	Commission Internationale de l'Eclairage
CRI	Colour Rendering Index
CT	Charge-Transfer
CTGDoS	Charge Transfer Density of States
D	Electron-donating Unit/Donor
DCM	Dichloromethane
DF	Delayed Fluorescence
EA	Electroabsorption
EBL	Electron Blocking Layer
EIL	Electron Injection Layer
EML	Electroluminescence Layer
ET	Electron Transfer
ETL	Electron Transport Layer
FWHM	Full Width at Half Maximum
HFC	Hyperfine Coupling
HBL	Hole Blocking Layer
HIL	Hole Injection Layer
HOMO	Highest Occupied Molecular Orbital
HTL	Hole Transport Layer
IT	Integration Time
ITO	Indium Tin Oxide
LE	Local Excited State
LiF	Lithium Fluoride
LUMO	Lowest Unoccupied Molecular Orbital

MCH	Methyl Cyclohexane
Nd:YAG	Neodymium doped Yttrium Aluminium Garnet
nr	Non-radiative Transition
OD	Optical Density
PF	Prompt Fluorescence
PH	Phosphorescence
PL	Photoluminescence
(r)IC	(reverse) Internal Conversion
(r)ISC	(reverse) Intersystem Crossing
RGB	Red Green Blue
RTP	Room Temperature Phosphorescence
SOC	Spin-Orbit Coupling
SSL	Solid-State Lighting
TADF	Thermally-Activated Delayed Fluorescence
TF	Tooling Factor
TD	Time Delay
TDDFT-TDA	Time-Dependent Density Functional Theory – Tamm-Dancoff Approximation
TTA	Triplet-Triplet Annihilation
VTE	Vacuum Thermal Evaporation
(W-)OLED	(White) Organic Light-Emitting Diode

List of Publications

(Under Review)

(1) **Daniel de Sa Pereira**, Chan Seok Oh, Paloma L. dos Santos, Ha Lim Lee, Jun Yeob Lee and Andrew P. Monkman, "Multiple Vibronically Coupled rISC Channels Independently Dictate Maximum Device Efficiency and Roll-off in Multi-donor TADF OLED Emitters", under review.

(2) Paloma L. dos Santos, **Daniel de Sa Pereira**, Jonathan S. Ward, Martin R. Bryce, Andrew P. Monkman, "Fine Tuning Isomerization of Thermally-Activated Delayed Fluorescence Emitters to Avoid Conformational Traps", under preparation.

(3) Ana I. Rodrigues, Cláudia A. Figueira, Clara S. B. Gomes, D. Suresh, Bruno Ferreira, Roberto E. Di Paolo, **Daniel de Sa Pereira**, Fernando B. Dias, Maria José Calhorda, Jorge Morgado, António L. Maçanita, Pedro T. Gomes, "Boron complexes of aromatic 5-substituted iminopyrrolyl ligands: synthesis, structure, and luminescent properties", under review.

(Published)

2019

(4) **Daniel de Sa Pereira**, Christopher Menelaou, Andrew Danos, Christel Marian and Andrew P. Monkman, "Electroabsorption as a Tool to Probe Charge Transfer and State Mixing in Thermally-Activated Delayed Fluorescence Emitters", *J. Phys. Chem. Lett.* 2019, 10, 3205−3211.

(5) **Daniel de Sa Pereira**, Dong Ryun Lee, Nadzeya A. Kukhta, Kyung Hyung Lee, Cho Lung Kim, Andrei S. Botsanov, Jun Yeob Lee, Andrew P. Monkman, "The Effect of a Heavy Atom on the Radiative Pathways of an Emitter with Dual Conformation, Thermally-Activated Delayed Fluorescence and Room Temperature Phosphorescence", J.Mater.Chem.C, DOI: 10.1039/C9TC02477H.

(6) Konstantin M. Morozov, Konstantin A. Ivanov, **Daniel de Sa Pereira**, Christopher Menelaou, Andrew P. Monkman, Galia Pozina and Mikhail A. Kaliteevski, "Revising of the Purcell effect in periodic metal-dielectric structures: the role of absorption", *Sci. Rep.*, 2019, 9, 9604.

2018

(7) Chan Seok Oh, **Daniel de Sa Pereira**, Si Hyun Han, Hee-Jun Park, Heather F. Higginbotham, Andrew P. Monkman, and Jun Yeob Lee, "Dihedral Angle Control of Blue Thermally Activated Delayed Fluorescent Emitters through Donor Substitution Position for Efficient Reverse Intersystem Crossing", *ACS Appl. Mater. Interfaces* 2018, 10, 41, 35420-35429.

(8) Marco Colella, Piotr Pander, **Daniel de Sa Pereira**, Andrew P. Monkman, "Interfacial TADF Exciplex as a Tool to Localise Excitons, Improve Efficiency and Increase OLED Lifetime", *ACS Appl. Mater. Interfaces*, 2018, 10, 46, 40001-40007.

(9) **Daniel de Sa Pereira**, Andrew P. Monkman, Przemyslaw Data, "Production and Characterization of Vacuum Deposited Organic Light Emitting Diodes", *Journal of Visualized Experiments*, 2018, 141, e56593.

2017

(10) **Daniel de Sa Pereira**, Przemyslaw Data, Andrew P. Monkman, "Methods of Analysis of Organic Light Emitting Diodes", *Display and Imaging*, 2017, 2, 323-337.

(11) **Daniel de Sa Pereira**, Paloma L. dos Santos, Jonathan S. Ward, Przemyslaw Data, Masato Okazaki, Youhei Takeda, Satoshi Minakata, Martin R. Bryce and Andrew P. Monkman, "An Optical and Electrical study of full TADF White OLEDs", *Sci. Rep.*, 2017, 7, 6234.

Declaration

All material contained in this thesis is original and is the result of my own work except where explicit reference is made to the work of others. This thesis has not been submitted in whole or part for the award of a degree at this or any other university.

Photophysics of Thermally-Activated Delayed Fluorescence Emitters and its Impact on the Performance of Organic Light-Emitting Diodes

Daniel de Sa Pereira

Acknowledgements

I would like to firstly thank my supervisor, Professor Andy Monkman for his guidance, support and to constant challenging of my own abilities, helping me become a better scientist. If anything prevailed during these last 4 years was his enthusiasm for this area, something that was definitely passed along.

To all the members of the OEM group, past, present and future and all the ESRs in the Excilight project whose different personal and academic backgrounds were extremely stimulating and encouraging. To all the collaborators that were a prominent part of my studies from the research groups of Prof Martin Bryce, Prof Jun Yeob Lee and Prof Christel Marian.

To Paloma for being someone I can count on, no matter what, thank you for such an amazing friendship. To Chris and Heather whose perseverance in making me question my own knowledge still prevails and to Roberto for his friendship and for giving me the most thorough introduction to the iCCD system. To all others that have been part of my PhD studies, either in or out of the lab, a big thank you: Rongjuan, Erhan, Vasco, Marco, Patrycja, Fernando, Fernanda, Rita, Inês, Paula, Nadzeya, Dan, Aneta, Piotr, Andrew, Marc and Przemek.

Aos meus amigos da Trofa pela compreensão, paciência e apoio.

A Farah, Emanuel e Catarina, um muito obrigado por quase uma década de amizade. Ao André, muito obrigado por três anos de selfies diárias.

Por fim, o mais importante, aos meus pais Rui e Esmeralda, aos meus irmãos, Vera e Ricardo e ao meu cunhado Ariel, obrigado pela maravilhosa família que são, pelo investimento constante na minha educação e por me ensinarem a fazer aquilo que mais gosto acima de tudo.

To the EXCILIGHT project funded by the European Union's Horizon 2020 Research and Innovation Programme under grant agreement No 674990.

Chapter 1: Introduction

1.1 Motivation

Consumer electronics are applications designed specifically for the general public. It is a fact that the technological evolution made them a big part of our lives since its inception with the radio in the early 20th century. Fast forward 100 years, these consumer electronics now travel with us everywhere, while also connecting us to the World Wide Web from a multitude of sources. Of course, this rise has been a result of not only more efficient, faster and bigger electronical applications, but also in consumer demand.

Displays are no exception of said evolution with more and better being commercialised every day. The recent interest in more advanced displays for smartphones, smartwatches, computers, tablets, augmented video-reality (VR) and curved TVs is a good example of that. The world has gone a long way from the early days of the bulky cathode ray tubes (CRT), TVs that paved the way to liquid crystal displays (LCDs) and, more recently, organic light-emitting diodes, or OLEDs. Although still considered a luxury application, OLED displays are gathering momentum. They are built on top of a thin-film transistor array and so, they are extremely thin and about 40% lighter than LCDs. As each pixel is self-emitting, OLED displays do not require any backlight (which is one of the greatest demerits of LCDs), improving colour quality, contrast ratio and energy consumption. Organic materials also emit uniformly and with a general small display thickness, they are mostly Lambertian, emitting equally in all directions.[1]

2019 has already been the year that LG announced the first-ever commercially-available rollable OLED TV (Figure 1.1a) and expanded their transparent OLED signage, promising to release transparent OLEDs to the public by the end of the year.[2,3] Samsung, the other big leader in the field, having dominated the industry of OLED displays for smartphones, has recently released its Galaxy Fold product, the first foldable smartphone using a foldable OLED display (Figure 1.1b).[4] All of this links back to the increase in consumer electronic demands and so, one can start wondering, what will the next big thing be in terms of display technology?

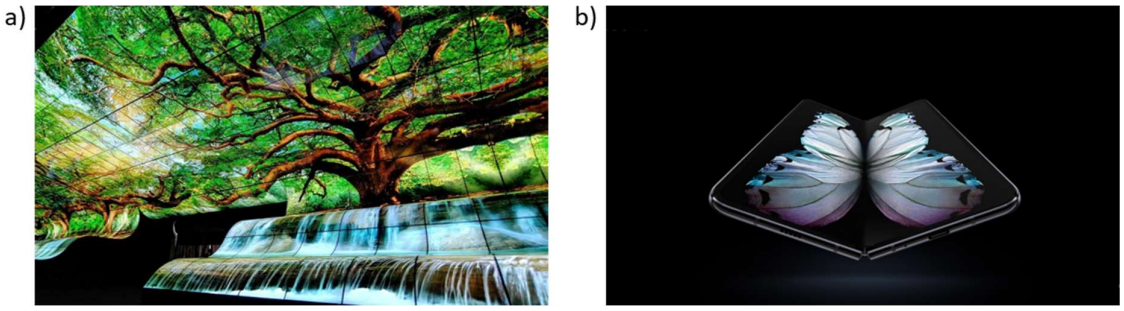

Figure 1.1 – a) LG announced its first commercially available rollable OLED display in 2019 (figure from LG website). b) Also announced in 2019 was Samsung's first-ever foldable smartphone (figure from Samsung website).

Though OLEDs have shown true great promise, they are not without their faults. Focusing only on the emitting pixels, three main generations of organic emitters have been reported successfully in devices (Figure 1.2a), all having something in common: the spin-statistic character of their excited states that, under electrical excitation, results in a 25/75 % ratio of emissive singlet/non-emissive triplet excitons formed. Gen I, also known as fluorescence and first reported 30 years ago by Tang and VanSlyke,[5] was limited to the harvesting of only the 25 % singlets; Gen II, or phosphorescence, uses heavy metal atoms like iridium or platinum to generate and harvest emissive triplet excitons. These materials however, are scarce and not environmentally friendly, while iridium and platinum extraction is very expensive; Finally, Gen III is based on design strategies to obtain purely organic emitters with small singlet-triplet energy gaps for the up-conversion of non-emissive triplets into singlets. Gen III is also known as thermally-activated delayed fluorescence (TADF). Gens II and III can therefore harvest both types of excitons, increasing the maximum internal efficiency (when all other parameters are considered) to 100 % and the external quantum efficiency to between 20 and 30 %. But why is this relevant? Going back to displays, nowadays OLED-applications all use only Gen I blues (as Gen II blues are too unstable) and Gen II green and reds, resulting in pixels that are 1) not efficient or 2) using harmful materials. The TADF mechanism promises to tackle both these aspects, where stable blue-emitting TADF emitters are a promise and efficient blue, green and red emitters have already been reported. They also promise to show stabilities similar to those of Gen II.

Having been reported in OLEDs with high efficiencies for the first time in 2012 by Adachi and his group,[6] research in TADF has evolved extensively (Figure 1.2b) resulting in the creation of different strategies that have been put in place to improve, not only the efficiency and colour purity of the devices, but also their stability, particularly at useful brightness for displays. This development brought together leaders from different areas of expertise like

chemistry, computational chemistry, electrochemistry, physics and engineering to understand their inherent phenomena, interactions with the environment they are dispersed into and their behaviour in both optical and electrically-driven environments. This allowed to filter through a series of design principles, both molecular and in device, and to move forward with the technology. In this sense, display-suitable TADF emitters are becoming a reality.

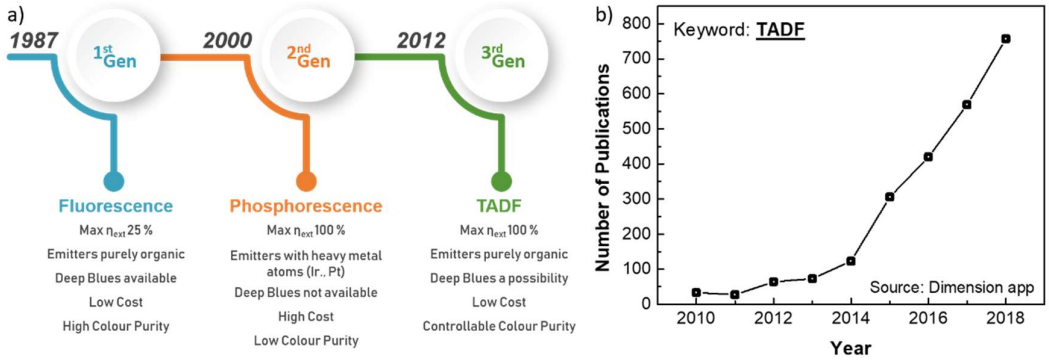

Figure 1.2 – a) Main generations and corresponding properties of organic emitters for OLED applications; b) number of publications over the years with keyword "TADF".

This reality serves as starting point for this thesis. The work presented here uses this great advantage of multidisciplinary to connect different areas of TADF research and gain deeper insight into the mechanisms and applications. It is divided into groups that focus on three main aspects: design principles (Chapter 4-6), physics (Chapter 7) and device engineering (Chapter 8). Therefore, by challenging current models that inform design strategies for efficient molecules, this thesis shows that the path to efficient OLEDs is more complicated than first assumed.

1.2 Thesis Organization

Chapter 2 introduces the reader to the topic of OLEDs, more particularly the field of TADF with all the background theory necessary to understand the context and motivation for the results chapters.

Chapter 3 is divided in three main parts, firstly with all the organic materials used in the course of this thesis, followed by the different sample preparation methods and finally by the measurements that are featured in this thesis. More particularly, a how-to guide on electroabsorption spectroscopy is given, where all the details that were part in the setting of the spectroscopy technique are shown.

Chapter 4 is the first of a two-part photophysical characterisation of a donor-acceptor (D-A) family containing carbazole and triazine as D and A, respectively. Six D_2-A constitutional isomers were studied with this change in position affecting heavily the torsion conformation of the A as well as the dihedral angle of the D-A linkages. This has a direct effect on the HOMO/LUMO separation and therefore in the energy gap of the different molecules, and consequently on the device performance.

Chapter 5 continues the study of this family by comparing the photophysical characteristics of the emitters that showed the strongest TADF emission across D_2-A, D_3-A and D_4-A subcategories. The same trend of controlling energy gaps by controlling molecular conformation is seen, however this chapter expands and deepens this understanding. Firstly, it is proven that these conformational effects are host-dependant and that the local triplet state (^{3}LE) is not as stationary as the current model for TADF assumes. Secondly, increasing the number of Ds can induce parasitic traps to the delayed fluorescence (DF). These findings have led to the introduction of the idea of a charge-transfer gaussian density of states (CTGDoS), with different coupling mechanisms in different hosts. Bridging with device performance, the CTGDoS model helps with the understanding of how these molecules can show similar maximum efficiencies but highly divergent resistances to roll-off.

Chapter 6 provides a detailed photophysical characterisation of emitters that show dual conformation and complex triplet dynamics, arising from both TADF and room temperature phosphorescence (RTP). This is done by comparing an emitter with known conformational dependence (PTZ-Trz) with a newly synthesised molecule (PSeZ-Trz) differing only by a heavier selenium heteroatom in the donor unit. It is shown that both the direct heavy-atom effect and associated conformational changes have minimal effect on the TADF but greatly enhances the RTP.

Chapter 7 describes a more advanced spectroscopy approach to study TADF, specifically using electroabsorption spectroscopy to compare two structurally-similar TADF emitters that show different photophysical and device performances. This technique allows to not only probe the charge-transfer character of both materials but also the state-mixing unique to the better performing emitter, a mechanism that has been proved to efficiently enhance the performance of TADF molecules.

Chapter 8 focuses on an application of TADF-based OLEDs by combining blue (DDMA-TXO2), green (DPO-TXO2) and orange (POZ-DBPHZ) emitters into a multi-emitting device

structure for white-light emission. By focusing on different parts of the device dynamics, this chapter therefore provides a template for device engineering strategies to obtain white emitting devices with high efficiency and controllable colour properties.

Chapter 9 concludes by summarising the findings and key achievements of this thesis while outlining further work that may build on these.

1.3 References Chapter 1

1. Yuen, C. OLED vs LED LCD: What's the best display technology? *Trusted Reviews* (2019). Available at: https://www.trustedreviews.com/opinion/oled-vs-led-lcd-2924602?jwsource=cl. (Accessed: 11th February 2019)
2. Mertens, R. LG to finally launch its transparent OLED signage displays. *OLED-info* (2019). Available at: https://www.oled-info.com/lg-launch-its-transparent-oled-signage-displays. (Accessed: 11th February 2019)
3. Keller, V. CES 2019: Rollable TV gives OLED new life. *LG Magazine* (2019). Available at: https://www.lg.com/uk/lg-magazine/tech-story/rollable-tv-ces-2019. (Accessed: 11th February 2019)
4. Maring, J. & Martonik, A. Samsung Galaxy Fold: Everything you need to know! *Android Central* (2019). Available at: https://www.androidcentral.com/samsung-galaxy-fold. (Accessed: 2nd March 2019)
5. Tang, C. W. & VanSlyke, S. A. Organic electroluminescent diodes. *Appl. Phys. Lett.* **51,** 913–915 (1987).
6. Uoyama, H., Goushi, K., Shizu, K., Nomura, H. & Adachi, C. Highly efficient organic light-emitting diodes from delayed fluorescence. *Nature* **492,** 234–238 (2012).

Chapter 2: Background Theory

This chapter introduces all the background theory necessary for the understanding of the results sections that follow. Starting from a fundamental introduction of different types of excitons (singlets vs. triplets, Frenkel vs. charge-transfer), the different transitions between the excited states are then examined. The thermally-activated delayed fluorescence (TADF) mechanism, the main focus of this thesis, follows next including the physics, design considerations and strategies for model optimisation. A more advanced technique, electroabsorption spectroscopy, is then presented as a method to identify the origin of different states, deeply connected to the main focus of the thesis. Lastly, operating principles and design considerations of organic light-emitting diodes (OLEDs) are considered, with fabrication methods for the production of state-of-art white-light emission in devices concluding the chapter.

2.1 Fundamental Theory

2.1.1 Excitons in Organic Materials

a) Singlet and Triplet States

An exciton is a coupled state between an electron and a hole, bound by Coulomb attraction. It can be generated directly by absorption of light or by recombination of free electrons and holes after electrical pumping. Upon optical excitation, organic molecules most commonly undergo electronic reconfiguration as electrons transition from a π-orbital (highest occupied molecular orbital HOMO) to a π*-orbital (lowest unoccupied molecular orbital LUMO). This process requires the energy of the absorbed photon to be equal or higher to the HOMO/LUMO energy gap (Figure 2.1a) and a non-zero transition dipole moment. Investigation of this transition is the basis for the photophysical characterization of any given organic system.

Although HOMO/LUMO bands are a good model for device science (facilitating in particular the understanding of carrier transport and carrier injection in devices), it ignores electron-electron interactions and the relative spin of the electrons involved. In using a molecular orbital and energy level model however, these aspects can be included, making it easier to understand the origin and differences between singlet and triplet states, explained later on.

Starting with the Bohr model, it sees electrons orbiting around the dense nucleus of an atom in defined energy levels. The probability of finding an electron at a particular point in space relative to the fixed position of the nuclei (spatial coordinates) combined with the electron spin (spin wavefunction) provides a full description of the atomic state. Therefore, a set of quantum numbers are used to describe the size (principal quantum number - n), shape (angular quantum number - l), orientation (magnetic quantum number – m_l) and spin (spin quantum number - m_s) of an atomic orbital, the latter in particular giving either spin-up (↑, +) or spin-down (↓, -) and so $m_s = \pm ½$. According to Pauli's exclusion principle, no two electrons possess the same set of quantum numbers.

The total spin angular momentum S is used in spectroscopy and quantum chemistry as a means to quantify the spin of a state related to its energy and is defined by the total sum of the spin vectors of all the electrons. Paired electrons with anti-parallel spins do not contribute to the total spin of the system. From S, the spin multiplicity can be determined, M = 2S+1. The total spin magnetic quantum number M_S is the sum total of the z-components of the electrons'

inherent spin. For a two-electron system ($1s^2 2s^2 2p^2$): S=0,1, M=1,3 and M_S=1,0,-1. Therefore, four spin eigenstates are possible, and these differentiate the singlet from triplet states, Figure 2.1b). A singlet (triplet) state occurs when the spin of an electron in the π* orbital and that of the remaining electron in the π-orbital are antiparallel (parallel) and so add up to a total S of zero (one). Therefore, because a singlet exciton has a M of 0 (M_S = 0) and the triplet exciton 1 (M_S = -1, 0 and 1), on average 75% of the excitons are triplet states, with the remaining 25% being singlets. Consequently, the orbital picture of the singlet and the triplet states differ on this basis as well, Figure 2.1c) and without any excitation, the ground state of a molecule will have paired electrons, typical of a singlet state (S_0) and for simplicity, its energy taken as 0 eV. More details on these fundamental aspects can be found in either Köhler and Bässler's book on electronic processes in organic semiconductors or Turro, Ramamurthy and Scaiano's book on the principles of molecular photochemistry.[1,2]

Symmetry representations derived from group theory for each individual state allow quick understanding of allowed and forbidden transitions between states. Many transitions are possible but not all are allowed for symmetry reasons. Moreover, symmetry is also intrinsically connected to radiative and non-radiative transitions. In this representation, symmetry with respect to the principal axis is defined with a capital letter "A" (symmetric) or "B" (antisymmetric) and symmetry with respect to an inversion centre is represented with a subscripted *g* (*gerade* or even) or *u* (*ungerade* or uneven). Any electronic transition is allowed if a change in parity occurs (Laporte rule: $g \rightarrow u$ or $u \rightarrow g$). In turn, radiative transitions (one photon allowed) can only occur between states of opposite symmetry (A → B). In a single notation, it is therefore possible to define different transitions with different radiative and spin characters. For example, for a fluorescent system with radiative emission from the first excited singlet state; S_0, S_1, T_1 and S_2 can be represented by 1^1A_g, 1^1B_u, 1^3B_u and 2^1A_g, respectively.

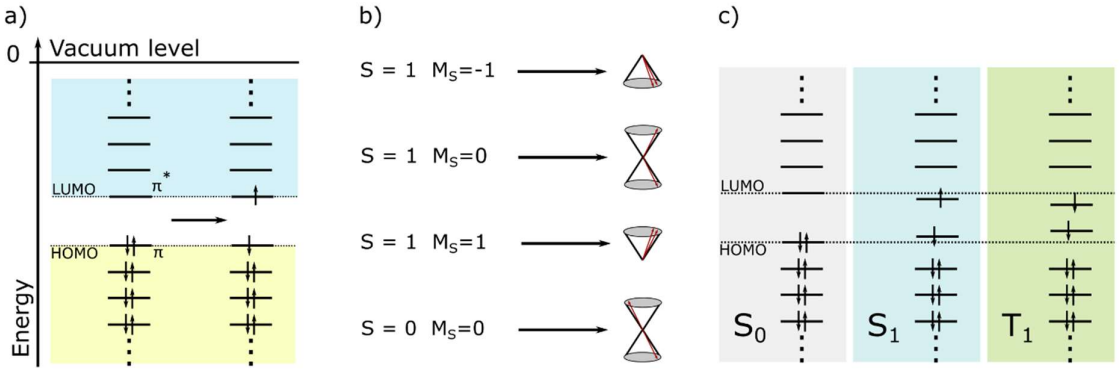

Figure 2.1 – States involved in an organic molecule: a) transition of an electron from the HOMO to the LUMO levels after excitation; b) spin wavefunctions and vector diagram of the two spins for the singlet and triplet states; c) orbital picture of the singlet and triplet states. Figures adapted from Köhler 2015.[1]

The total energy of the first singlet (E_{S_1}) and triplet (E_{T_1}) states considers firstly the orbital energy (E_{orb}), the energy associated with the one-electron orbital for a fixed nuclear framework in the excited state. To this is added the Coulomb integration integral (K) and the exchange energy (J), i.e. the first-order correction involving electron-electron repulsion due to the Pauli's principle:

$$E_{S_1} = E_{orb} + K + J \quad (2.1)$$

$$E_{T_1} = E_{orb} + K - J \quad (2.2)$$

The first excited singlet state will therefore have higher energy than the first triplet state due to the sign difference of J. The singlet-triplet energy gap (ΔE_{ST}) is dependent on their exchange energy, calculated using the HOMO and LUMO wavefunctions, (Φ_H and Ψ_L) integrated over the possible two electron positions (r_1 and r_2):

$$\Delta E_{ST} = E_{S1} - E_{T1} = 2J = 2 \iint \Phi_H(r_1)\Psi_L(r_2)\left(\frac{e^2}{r_1 - r_2}\right)\Phi_H(r_2)\Psi_L(r_1)dr_1 dr_2 \quad (2.3)$$

A key requirement in thermally-activated delayed fluorescence (TADF) emitters discussed below is a small ΔE_{ST} which, from equation 2.3, comes from increasing the spatial separation of the HOMO and LUMO orbitals ($r_1 - r_2$).

b) Frenkel and Charge-Transfer excitons

Adapting the crystalline lattice formalism originally developed for inorganic materials, the most common types of excitons in organic semiconductors are Frenkel and Charge-Transfer (CT). The main difference between these is the exciton radius. A Frenkel exciton has a tightly bound electron-hole pair located on the same atom or molecule with a binding energy in the order of 0.1 to 1 eV, and so the Frenkel exciton is frequently regarded as a strongly coupled, small-radius exciton. This binding energy means that the electron will be freely orbiting its respective hole, while having the ability to move through the lattice as a pair without a permanent dipole. Frenkel excitons dominate the optical absorption and emission spectra of organic materials. Conversely Wannier-Mott excitons have electron and hole separation more than an order magnitude than the site separation. Wannier-Mott excitons are more common in inorganic systems, and therefore do not feature in this thesis.

If Frenkel and Wannier-Mott are two extremes with respect to e-h separation, CT excitons appear in the middle. CT excitons occur between two molecules, or different chromophores on the same molecule that are not strongly conjugated with the electron-hole pair located on separate chromophores. In molecules with electron-donating (**D**) and electron-accepting (**A**) units, electron transfer (ET) from the **D** to the **A** forms the CT excited state.

Direct excitation to the low energy absorption bands that appear in the **D-A** conjugate is also possible, but much less likely. In the case of ET, the electron no longer orbits the hole resulting in different charge density across the **D-A** complex and therefore a permanent dipole is formed. Detailed description of these electronic states can be found in "Thin Films and Nanostructures" by Knoester and Agranovich.[3]

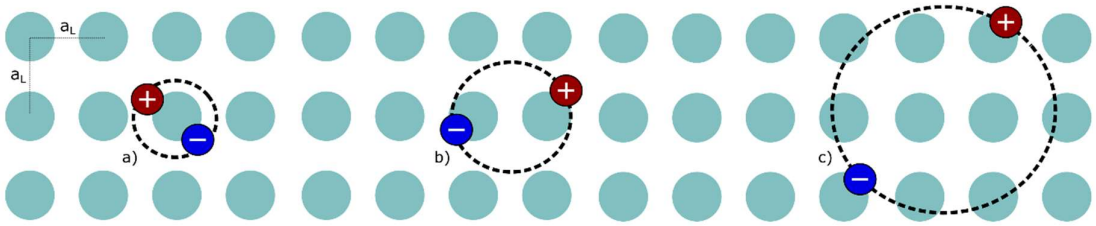

Figure 2.2 – Schematic diagram showing the types of excitons that are formed in a crystal with a lattice spacing of a_L: a) Frenkel (or local) exciton; b) CT exciton; c) Wannier-Mott exciton.

A lattice-based description of these three types of excitons can be seen in Figure 2.2 for a) Frenkel, b) CT and c) Wannier-Mott. Organic TADF molecules are commonly comprised of D-type and A-type units. Combining this with the different concepts of excitons introduced this far, an energy diagram of the states involved in organic molecules can be built. This will consider both Frenkel (either **D** or **A**), also commonly known as local excitons (LE), and CT (between **D** and **A**) excitons, with singlet and triplet versions of each.

2.1.2 Jablonski Diagram

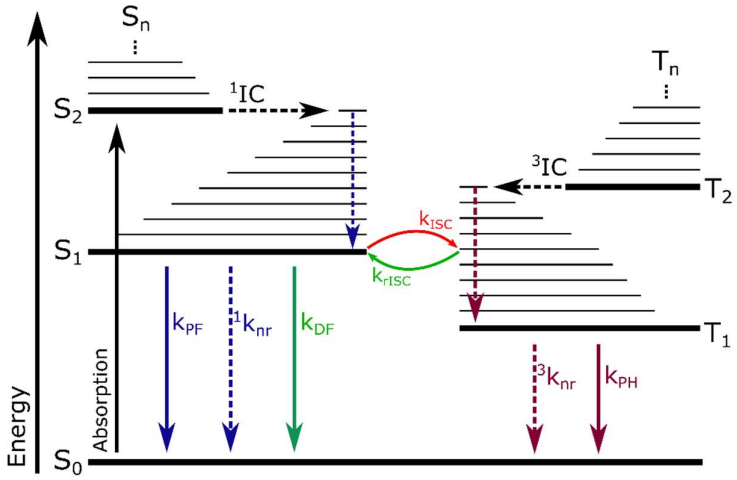

Figure 2.3 –Jablonski diagram for transitions between relevant vibronic states in an organic molecule. Upon excitation, transition from the ground state (S_0) to an excited state with the same multiplicity (S_n) can occur if the energy of the incoming photon is bigger than the S_n-S_0 gap. Vibrational relaxation and IC (as non-radiative, nr, transitions) relax the electron to the lowest possible excited singlet state (S_1). From here, three pathways are possible: radiative (PF) or nr transitions to the ground state and intersystem crossing (ISC) to the triplet state (T_1). Although formally forbidden, T_1 can also relax to the ground state through radiative (in the form of phosphorescence - PH) or nr transitions. Alternatively, reverse ISC (rISC) from T_1 back to S_1 can occur and gives rise to a fourth pathway, delayed fluorescence (DF) with a decay rate which is orders of magnitude slower than the rate of PF but with the same spectrum.

Figure 2.3 shows all the relevant transitions between states in a typical Jablonski diagram with the states organised vertically by energy. For every electronic state (thick line) there is a series of vibrational states and within each vibrational there is a set of rotational states. For simplicity reasons only the electronic and vibrational states are considered.

a) Radiative Transitions: Absorption, Fluorescence and Phosphorescence

A radiative transition between two states of a molecule (absorption or emission) occurs when the energy of that transition is in the form of a photon. The probability of radiative transitions depends on three main factors: electronic, vibrational and spin wavefunctions of the initial and final states and control the transition probability, shape and type, respectively. Transitions between orbitals of the same type within the same molecule (ππ*) are more likely (due to improved overlap between initial and final states) than those between orbitals in different parts (nπ*, CT), therefore more intense.* The strength of a transition is also known as *oscillator strength*, *f*. The weakest transitions are those which are forbidden by symmetry and/or involve a change of spin, i.e. transitions between singlet and triplet states. Radiative decay between S_1-S_0 is known as fluorescence (also known as prompt fluorescence PF: $S_1 \rightarrow S_0 + h\nu$) with a fast decay lifetime (PF: τ_{PF}, pico to nanosecond range) and large rates calculated using $k_{PF} = \frac{1}{\tau_{PF}}$. The T_1-S_0 radiative transition is known as phosphorescence (PH: $T_1 \rightarrow S_0 + h\nu$) with a rate of $k_{PH} = \frac{1}{\tau_{PH}}$ and a long decay lifetime (PH, τ_{PH}, late micro to seconds). PH is normally spin-forbidden but becomes partly allowed through spin-orbit coupling (SOC) although the intensity remains orders of magnitude lower than fluorescence in most cases. Finally, another type of radiative transition is known as delayed fluorescence (DF) and comes from electrons that were previously in triplet states and up-converted back to singlets through spin-flip mechanisms, explained further ahead. The DF rate is defined as $k_{DF} = \frac{1}{\tau_{DF}}$ and the decay component's lifetime is between late nano to late microseconds regions. Mechanistically the DF is identical to PF, with a longer lifetime due to the repopulation mechanism of the S_1 state. When an overlap between DF and PH rates is present, great care must be taken not to confuse the two as there can be only subtle differences in emission spectral band shape and energy onset. Given that both DF and PH are dependent on the lifetime of the

In molecules with sp^2 hybridization, bonding π orbitals (or antibonding π orbitals) are formed from the constructive (destructive) overlap of two atomic p_z orbitals. Using the carbonyl functional group as an example, if an atom does not hybridise (providing electron lone pairs that do not interact with the other atoms) the highest-energy occupied orbital comes from this unhybridized atom. This so-called n-orbital will have an energy in-between the ππ* gap and neither stabilises or destabilises the bond between the atoms under consideration. The **D-A** molecules studied here are separated by a N atom with highest energy electrons in nonbonding lone pairs.

electrons in the triplet state, measuring these contributions involves using high vacuum in order to avoid oxygen quenching (oxygen has a ground state triplet and therefore quickly quenches any available excited triplet states).[1] Moreover, non-radiative transitions compete heavily with PH which means low temperatures are necessary to obtain clear PH spectra.

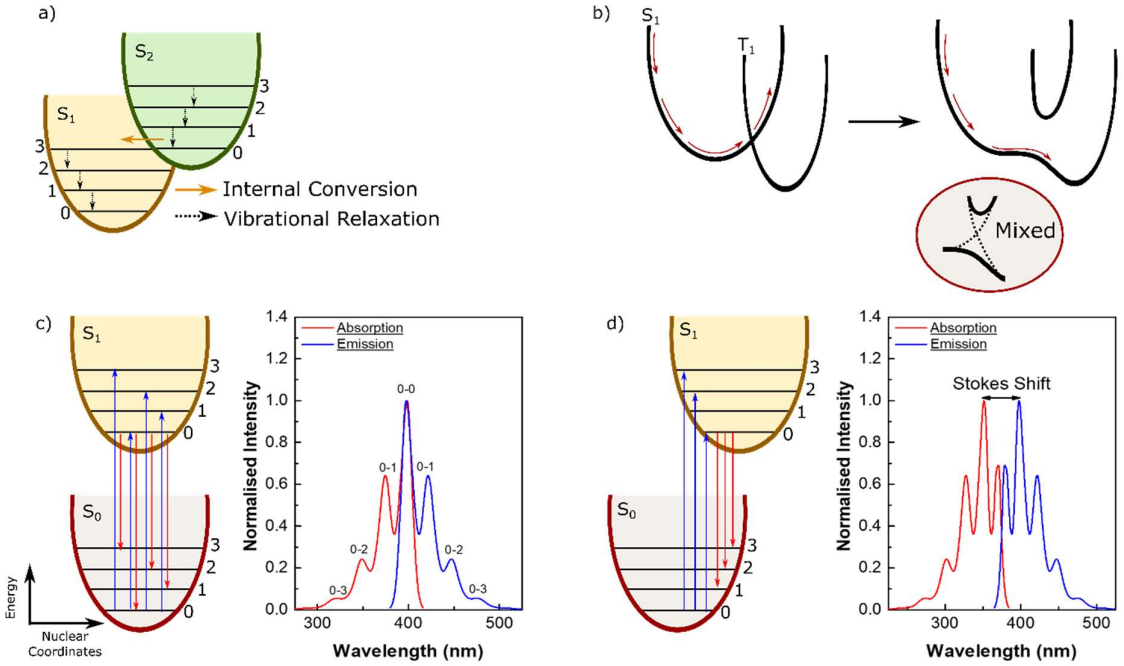

Figure 2.4 – a) Internal conversion and vibration relaxation between states of the same multiplicity; b) schematic diagram of the S_1-T_1 state mixing due to spin orbit coupling (SOC); c) the Franck-Condon principle assuming no reorientation of the nucleus giving rise to a strong 0-0 transition overlapping in both absorption and emission or d) significant reorientation of the nucleus in the excited state redshifting the 0-0 transition and giving rise to a Stokes shift. Transition λs and relative strengths are indicative only.

b) Radiationless transitions: internal conversion and vibrational relaxation

Kasha's rule states that radiative emission occurs from the lowest possible energy state of a given multiplicity as almost radiative rates are much slower than IC and vibrational relaxation.[4] Transitions between excited states of the same multiplicity or between vibrational levels of the same excited state occur through these non-radiative transitions. Internal conversion (IC: $S_2{}^{0\text{th}} \rightarrow S_1{}^{k\text{th}}$) is an isoenergetic transition between the *0*th vibrational level of an upper state to the *k*th vibrational level of a lower state of the same multiplicity. It is usually followed by vibrational relaxation ($S_1{}^{k\text{th}} \rightarrow S_1{}^{0\text{th}}$ + heat) in the form of thermal relaxation, Figure 2.4a). Though between excited states these processes are fast (between 10^{-14} to 10^{-11}), IC and vibrational relaxation from S_1-S_0 transition are slower, due to it often having the largest energy gap and lack of isoenergetic S_0 vibronic states that S_1 can couple to, being outcompeted by radiative transitions.

c) (reverse) Intersystem Crossing

Transitions between states of different spins are normally forbidden by the rules of quantum mechanics set out above, and therefore to a zero-order approximation if the molecule is in the singlet state, it will remain in the singlet state, as shown on the left side of Figure 2.4b). However, a change in spin angular momentum, can be compensated by an opposite change in orbital angular momentum thus conserving the total angular momentum and making a spin forbidden process overall allowed: spin-orbit coupling (SOC). Therefore, if the spin-orbit interactions are strong, the triplet state will acquire a singlet character and vice-versa. Thus, a spin mixing at the crossing point between S_1 and T_1 of the energy surfaces, righthand side of Figure 2.4b), results in a non-radiative adiabatic transition from the singlet to the triplet ($S_1{}^{n\text{th}} \rightarrow T_1{}^{k\text{th}}$) states. This is known as intersystem crossing (ISC). From quantum mechanics, the magnitude of the SOC is proportional to the size of the atom ($SOC \propto Z^4$), as bigger nuclei accelerate the electrons more and therefore increase the orbital motion. Incorporating a heavy atom in a chromophore can make the interaction between orbitals strong enough to increase the rate of SOC which is one aspect of the "heavy atom effect".[5,6] The ISC process however, will only occur if one of the states involved in the transition is localised between, for example, the $p_x \rightarrow p_y$ orbitals and so, a set of selection rules emerges for SOC: a S($\pi\pi^*$) state couples strongly with a T($n\pi^*$) state and vice-versa while S($\pi\pi^*$) $\rightarrow$ T($\pi\pi^*$) and S($n\pi^*$) $\rightarrow$ T($n\pi^*$) are only weakly coupled. These are the El-Sayed rules.[7] A more in-depth description of these selection rules can be found in "Principles of Molecular Photochemistry".[2]

ISC can occur in both directions if the energy gap between the singlet and the triplet states is small. Although ISC most commonly refers to S $\rightarrow$ T transitions, excitons on the triplet manifold can flip-back to the singlet state ($T_1{}^{n\text{th}} \rightarrow S_1{}^{k\text{th}}$) by the same mechanism, although termed reverse ISC (rISC).[8]

d) Frank-Condon and Stokes shift

The Franck-Condon principle controls the absorption and emission transitions in a molecular system, the intensity of each transition governed by the wavefunction overlap of the initial and final states. Absorption occurs in 10^{-15} s and is regarded as an instantaneous event due to the differences in mass between the nuclei and the electron, a timeframe too short for any significant displacement of the nuclei. Therefore, in a potential energy diagram, these transitions are drawn vertically (with the change of nuclei displacement defined horizontally). Rearrangement of the electrons changes the electric potential felt by the nuclei which brings them into motion and thus, after absorption, relaxation to the lowest vibrational level of the

excited state is most commonly proceeded by emission. This results in an emission that is redshifted from the absorption. In some instances, electronic excitation does not greatly alter the nuclear geometry and the spacing of the vibrational energy levels of the excited states is similar to that of the ground state. The vibrational structures seen in the resulting absorption and emission spectra are similar. In a case where the excited state equilibrium geometries are similar and there is no reorientation of the excited state conformation of the nuclei, the absorption and emission are a mirror of each other, with overlapped 0-0 transitions (Figure 2.4c). In contrast, if the molecule reorients itself to the new excited state conformation, and the potential wells of ground state and excited states are displaced from each other, this results in a difference in wavefunction overlap between ground and excited states and a noticeably redshifted emission, particularly between the 0-0 absorption and emission transitions (Figure 2.4d). The difference between the peak of emission and absorption is defined as the Stokes shift. In the case of TADF molecules commonly formed of **D** and **A** units, absorption of either unit individually gives rise to a low energy CT state after subsequent ET between **D** and **A** and so, the emission will be redshifted further.

2.2 Thermally-Activated Delayed Fluorescence (TADF)

The concept of exciton harvesting has been fundamental in organic light-emitting diode (OLED) research, with successful design strategies reported pursuing for the increased SOC strength or engineering of molecules with small energy gaps to enhance rISC. In this thesis, the latter approach is investigated using TADF materials. Prior to the recent interest in OLEDs, DF was considered as a scientific curiosity, with reports dating all the way back to 1929.[9] The years that followed saw some interesting developments, particularly the discovery of the temperature dependence of the DF (TADF), but this was mostly for research purposes with no industrial application forthcoming.[10–15] However, thermally-activated or E(osin)-type[10] DF found renewed interest in 2009 when Adachi and co-workers reported a small energy splitting between singlet and triplet states in Sn^{4+}–porphyrin devices giving rise to DF in OLEDs rebranded as TADF.[16] Three years later, they reported a series of carbazolyl dicyanobenzene (CDCB) **D**-**A** structures, showed high HOMO/LUMO separation and a small ΔE_{ST} gap. Fluorescence with dual kinetics (PF and DF) was recorded and different colour-emitting OLED devices with efficiencies of 19 % obtained, directly competitive with state-of-the-art OLEDs based on phosphorescent materials.[8] With the increased interest in this field, the last 7 years of research have taught us how to control the mechanisms and design strategies for high-

performing TADF emitters with varied stabilities, emitting colours, charge transport properties, etc. allowing the production of high efficiency devices.[17–20]

2.2.1 Design Considerations of TADF Emitters

As stated previously, TADF relies on the small energy gap between singlet and triplet states to promote rISC and fluorescence with PF and DF components. From equation 2.3, minimising the ΔE_{ST} follows from decreasing the overlap between wavefunction frontier orbitals, i.e. separated HOMO and LUMO. Short lived DF emission is sought as it strongly correlates to faster rISC rates, decreasing the likelihood of non-radiative transitions in the triplet state, and allowing excitons to more rapidly recombine in devices resulting in good stabilities. Another important factor for the general use of an emitter in OLEDs is the high luminescent efficiency, something that is achieved with overlapped HOMO and LUMO orbitals. These two factors seemingly contradict each other which is why regulating the extent of HOMO/LUMO overlap must be considered in order to find the best compromise between the two:

i. The basic strategy for separation of HOMO/LUMO orbitals uses **D** and **A** moieties, connected by a N-C bond, electronically decoupling **D** and **A**. With this, CT states between them are formed. Both singlet and triplet CT and LE (**D** and **A**) coexist in a TADF molecule. The low spatial overlap between **D** and **A** is also typically associated with low *f* for the CT transition;[20]
ii. The strength of each unit will dictate the emission wavelength of the CT state. For example, to obtain blue-emitting CT species, weak **D**s and **A**s are preferred. In contrast, red emission can be obtained with strong units. Recent reviews provide an extensive list of different TADF emitters with different colours;[21,22]
iii. Though nearly orthogonal **D**-**A** units are believed to have lower energy gaps, as they completely separate HOMO and LUMO orbitals (equation 2.3), recent studies have shown that rigidity enforces orthogonality but inhibits TADF, meaning a certain degree of vibrational freedom is required for its efficiency.[18] Therefore, though steric hindrance inducing structures such as twisty, bulky or spiro junctions are good strategies, a compromise between the orthogonality of the system and its efficiency must be met;
iv. When combining **D** and **A** units, these combinations may form more than one stable conformation, resulting in different orientations of the **D**-**A** angle[23] or within one of the units.[24] Thus, different CT states will be formed which can either be beneficial [25] or harmful to the TADF performance;[26]

2.2.2 Current Model of TADF

Based on recent experimental works from the Monkman group[18,27] and works by Lim[28], Gibson[29], Marian[30], Chen[31] and Ogiwara,[32] in Figure 2.5 the current model of the TADF mechanism is presented. Contrary to what was first assumed, transitions between ^{1}CT and ^{3}CT are formally forbidden as SOC between states of the same spatial orbital is zero.[28] For TADF, a nonzero SOC that promotes significant mixing between singlet and triplet manifolds must occur and thus, states of different character must be involved. A state with a ππ* character such as a local triplet (^{3}LE) could interact with the nπ* or mixed nπ*/ππ* ^{1}CT state to produce rISC ($^3\text{LE} \xrightarrow{SOC} {}^1\text{CT}$).[30] However, the SOC pathway alone has been calculated to have rISC rates about 5 times smaller than the ones experimentally reported.[31] Through electron paramagnetic resonance (EPR), it was proposed that efficient rISC could arise, not only from the SOC-induced between ^{3}LE and ^{1}CT, but also from the hyperfine coupling (HFC) between the CT states ($^3\text{CT} \xrightarrow{HFC} {}^1\text{CT}$).[32] As the HFC rates are small, this contribution still did not satisfactorily explain the large k_{rISC} observed. Point iii) of the previous subsection pointed out that a degree of steric freedom is required for efficient TADF.[18] This revealed a dynamical aspect to the TADF mechanism that is promoted by molecular vibrations on the triplet manifold. Spin-vibronic mixing between the multiple excited states was therefore proposed as the cause of efficient rISC. Quantum dynamics taking into account the SOC, the HFC (to a lesser degree) and the vibronic coupling contributions have since confirmed to be fundamental in obtaining rISC rates as high as the ones reported experimentally.[29] The rate of rISC is calculated with a second-order perturbation theory and defined by equations 2.4 and 2.5:

$$K_{rIC} = \frac{2\pi}{\hbar}\left|\left\langle \Psi_{^3CT}\middle|H_{vib}\middle|\Psi_{^3LE}\right\rangle\right|^2 \delta(E_{^3CT} - E_{^3LE}) \tag{2.4}$$

$$K_{rISC} = \frac{2\pi}{\hbar}\left|\frac{\left\langle \Psi_{^1CT}\middle|H_{SOC}\middle|\Psi_{^3LE}\right\rangle\left\langle \Psi_{^3LE}\middle|H_{vib}\middle|\Psi_{^3CT}\right\rangle}{E_{^3CT} - E_{^3LE}}\right|^2 \delta(E_{^1CT} - E_{^3LE}) \tag{2.5}$$

In this sense, a two-step process is required: i) vibronic coupling between ^{3}LE and ^{3}CT results in an equilibrium between the two states (reverse IC, rIC); ii) once in this coupled state, rapid SOC between ^{1}CT and ^{3}CT using ^{3}LE as an intermediate can occur. In Figure 2.5a), following excitation to the ππ* local excited state (^{1}LE, **D** or **A**), ET forms the CT states. Excitation to the weak ^{1}CT can also occur however, ET is the more probable situation (see 2.1.1a). Since ET is a relatively slow process (10^8 s^{-1} due to **D-A** orthogonality and competing with the ^{1}LE-S_0) ^{1}LE emission is common at early times after UV photoexcitation.[27] The

majority of excitations however, form the ^{1}CT state, with several pathways then possible. Radiative and non-radiative transitions may occur to S_0, or ISC to ^{3}LE through SOC. The spin-vibronic model mixes the vibrational levels of both the ^{3}CT and ^{3}LE, and vibrational motion allows the molecule to reach an isoenergetic crossing point to the ^{1}CT manifold (Figure 2.4b). An adiabatic spin-flip (rISC) then repopulates ^{1}CT and gives rise to DF. As the population of ^{3}CT is very small, the most likely processes to outcompete rISC are the radiative(k_{PH}) and non-radiative ($^3k_{nr}$) transitions from ^{3}LE to the ground state. Aiming at optimising the TADF performance, design strategies are required to i) minimise the energy gap between singlets and triplets and ii) obtain a better coupled ^{1}CT-S_0 which in turn secure maximised rISC rates and a higher *f* of the ^{1}CT relaxation, respectively.[25] The mechanism described is for optically-driven systems where formation of triplets upon excitation is strictly forbidden by spin-statistics (2.1.1). However, in an electrically driven scenario, such as the one in OLEDs, formation of singlets and triplets follows the 25/75 % ratio where exciton formation is not dependent on spin allowed transitions. Details on rate constants and quantum yields involved in both optically and electrically driven systems can be found in works by Berberan-Santos.[33]

In Figure 2.5b) three types of TADF systems are described, one where the ^{3}LE state goes from being above (Type I) to almost isoenergetic (Type II) and below (Type III) the CT manifold. Strategies to minimise the energy gaps of the system (^{1}CT-^{3}LE and ^{3}CT-^{3}LE) are sought, trying to achieve Type II systems. The next sub-section will look into those strategies.

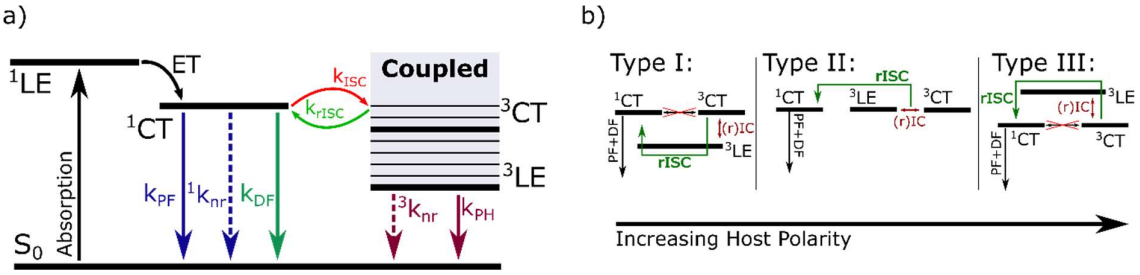

Figure 2.5 – a) The TADF model considering the spin-vibronic coupling for the rISC mechanism following D or A photoexcitation. For simplicity, ^{1}LE → S_0 radiative and nonradiative decays, ISC between ^{1}LE → ^{3}LE, and direct excitation to the ^{1}CT state were omitted from this diagram; b) energy-level diagrams on the environmental effects to the ^{1}CT-^{3}LE energy gap and the TADF mechanism (adapted from Etherington *et al.*[34]).

2.2.3 Host:Guest Interactions

As a general rule, most organic emitters suffer from concentration-induced decrease of the radiative decay efficiency, requiring the use of supporting host matrices.[35,36] Although design strategies to reduce the concentration quenching effect and bypass the need for a host environment have seen increased research interest (due to the simplification of device architecture), progress in this specific topic remains slow.[37] Effects of chromophore orientation

(often induced by host interactions) is another topic of interest that has been growing attention.[38] Despite recent developments, the most common approach is to randomly embed the emissive material in an inert host. In devices, at low concentrations of guest molecules the host will have the function of promoting charge transport and exciton formation in the emissive guest. Host materials should therefore possess good HOMO/LUMO alignment with the guest and the neighbouring charge injection layers, as well as having triplet energy higher than the guest molecule to avoid triplet quenching mechanisms, good film forming properties and (ideally) ambipolar characteristics. For TADF materials, the host has significant effects in the inherent mechanism, and details on these effects are described next.

a) Solvatochromism

One of the most common strategies for the minimisation of the energy gaps comes from the control of the CT energy onset (Figure 2.5b). This can be initially done by embedding the TADF emitter guest into a host with the appropriate polarity. CT states possess a large dipole moment (2.1.1) and therefore interact strongly with local solvent molecules, which reorient to form favourable dipolar interactions with the solute. Those interactions are different between ground and excited state geometries and shield the molecular dipole of the TADF molecules, by rearrangement of the solvent shell around the molecule and lowering the total energy of the system. This translates into changes in the emission spectrum of the TADF emitter in terms of position, intensity, and shape of the spectroscopic bands. In other words, the most obvious effect is a change in colour of the solution. These are known as solvatochromic effects, or solvatochromism. A negative (positive) solvatochromism, also known as a hypsochromic (bathochromic) shift refers to a shift to higher (lower) energies, i.e. blue (red) shift. As LE states do not possess a dipole moment (2.1.1), it is not expected that changes in the polarity of the environment will change the emission profile. Therefore, to minimize the ΔE_{ST} gap, one needs to choose an environment with the proper polarity to shift the CT down from its vacuum energy towards the ^{3}LE. Similar effects are also observed in the solid-state when a molecule exhibiting a low-lying CT state is doped into host of relatively high polarity, though to a lesser degree. More details on both spectroscopy and quantum simulation aspects of solvatochromic effects can be found in works by dos Santos *et al.* ,[39] Dias *et al.*[27] or Northey *et al.*[40]

b) Packing effects

It has been widely assumed that the main effect of choosing different hosts will be in terms of polarity-induced shift of the CT ensemble. This is generally true for mostly rigid molecules.[25] However, in the case of more flexible emitters, how the guest packs around the

host may change depending on the rigidity of both species and on the voids between molecules (polymers vs. small molecules). Packing effects can also affect the geometry of the emitter molecule, effectively changing the **D-A** angle and thus the HOMO/LUMO separation and conjugation across the emitter, both affecting the character of the CT state. Changes in conjugation also affect the triplet (i.e. more conjugated molecules tend to have redshifted triplets) all of which have further effect on the ISC efficiency and emission. This thesis – particularly Chapter 5 – will look in more detail at this effect. It will be shown that in multiple **D-A** systems, the heterogeneity of the **D-A** angles induces different CT and LE characteristics which, in turn will have small important effects in the TADF performance.

2.2.4 Other Mechanisms and Variations of DF

With the emergence of TADF and a better understanding on how to control it, other mechanisms that generate DF and surpass the 25 % internal quantum efficiency (η_{int}) limit in fluorescent OLEDs are worth being revisited. These are shown in Figure 2.6.

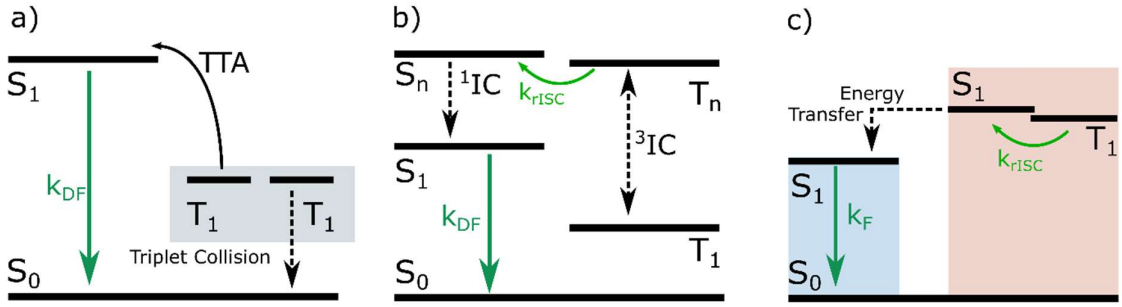

Figure 2.6 – Alternative mechanisms for the generation of DF: a) triplet-triplet annihilation (TTA), b) upper state crossing and c) hyperfluorescence. For simplicity reasons, only the transitions involved in the main mechanisms are shown. In c), two different materials interact with each other, giving rise to energy transfer processes. The blue (left) area refers to a fluorescence-emitting guest and the red (right) to a TADF sensitizer.

a) Triplet-Triplet Annihilation (TTA)

TTA (Figure 2.6a), or P(yrene)-type[41] DF, is a bimolecular process that occurs from the collision of two triplets, where one gets promoted to an upper excited state, while the other relaxes back to the S_0 state. From the spin conservation rule and depending on the spin of both triplets, the collision potentially leads to the formation of different excitons, singlets (total spin S = 0), triplets (S = +1) or quintets (S = +2), the latter possible from spin-conservation rules but not experimentally observed.[1] For the first case, the equation that governs the singlet formation is: $T_1 + T_1 \xrightarrow{k_{TTA}} S_n + S_0 +$ heat and DF emission then proceeds from the S_1 state. TTA can achieve a theoretical maximum of 62.5 % η_{int}, a result of the 25 % initial singlets plus ½ of the 75 % of triplets formed yielding singlets via triplet fusion, a smaller efficiency than in TADF but with longer device lifetime and operational stability.[42,43] Though not the focus of

this thesis, a strategy to identify TTA is by measuring the DF intensity as a function of the excitation dose. This is a result of the quadratic dependence of singlet production through TTA on excitations, at lower triplet concentrations.[44]

b) Upper State Crossing

Also known as "hot exciton", upper state crossing involves rISC between upper excited singlet and triplet states, $T_n \xrightarrow{k_{rISC}} S_n$ which is followed by relaxation to the S_1 state and finally emission (Figure 2.6b), giving rise to the DF character of the emission. Though this technique does allow η_{int} to reach 100 %, as increased competition of non-radiative decays in the triplet manifold (^{3}IC) limits their performance and thus, the number of reports using this strategy in OLEDs is still limited.[45] However, a specific kind of upper state crossing with transition between the T_2 and the S_1 states ($T_2 \xrightarrow{k_{rISC}} S_1$) has been reported to produce high efficiency and even sharp emissions though it remains to be seen the connection between the two.[46]

c) Hyperfluorescence

Also considered by some research groups as a new generation in OLED research, hyperfluorescence is based on the use of a TADF emitter to pump the radiative decay of a fluorescent dye. The TADF acts as a sensitizer (St), harvesting triplets for subsequent emission by the fluorescent emitter following energy transfer (En. T.). This process, greatly increasing the performance of the emitting guest (G) – which would otherwise be unable to utilise triplet excitons – $(T_2)^{St} \xrightarrow{k_{rISC}} (S_1)^{St} \xrightarrow{En.T.} (S_1)^{G}$.[47] It also helps breaking the conflicting demands of high rISC and unitary photoluminescence quantum yield (PLQY) of TADF emitters and thus, by avoiding direct injection to the guest, the η_{ext} of typical fluorescent OLEDs can be greatly improved.[48,49] Adding a fluorescence emitter to the system can also improve the device stability due to reduced excited state lifetime. However, to properly understand how to optimise hyperfluorescence, systematic research in this topic is still necessary. In particular the complex photophysics and device structures to benefit only energy transfer between singlet states while preventing triplet energy transfer processes and ensure the low triplet guest does not quench the TADF assistant before rISC can occur. Moreover, as most TADF emitters require a host of their own for high performance, production of the emitting layer becomes challenging, particularly for blue fluorescent dyes.[49] Nonetheless, this system (theoretically) offers the great advantage of increasing the efficiency of these typical fluorescence materials while keeping their colour purity.

2.3 Electroabsorption Spectroscopy

In 1913, Johannes Stark observed the splitting of the absorption lines of the hydrogen atom induced by an electric field.[50] This pioneer work was the basis for what today is called Stark spectroscopy and includes electroabsorption (EA). As shown in the first section of this introductory chapter, there are different types of states involved in an organic molecule, either from a spin statistics (singlet and triplets) or from an electron-hole pair binding distance (Frenkel, CT or Mott-Wannier) perspectives. Connecting this to TADF, through developing a better understanding of the precise nature of the electronic excited states and their mutual interactions, inherent phenomena can be revealed that may not be otherwise immediately evident. Most spectroscopic characterisation techniques are limited to investigating direct optically-allowed transitions, while the elucidation of forbidden transitions and excited state interactions relies almost exclusively on sophisticated theoretical modelling and calculations. EA spectroscopy however provides direct information on the character of essential excited states and their interactions in a simple and relatively inexpensive manner.[51–53] Based on the Stark effect†, EA measures changes in absorption of the transition energy caused by a perturbing external electric field, equation 2.6, in particular peak shifts and line shape changes.

$$\Delta A = A^F(E) - A(E) \tag{2.6}$$

The Stark spectra can be fitted using the Liptay model[54,55] expressing the change in absorption, ΔA, as a Taylor series expansion truncated at second order. As such, the electroabsorption spectra are treated as a combination of zeroth, first and second differential of A with respect to energy (E) according to the equation 2.7:

$$\Delta A = (k-1)A(E) + k\Delta E\frac{dA}{dE} + \frac{k\Delta E^2}{2}\frac{d^2(A)}{dE^2} \tag{2.7}$$

This change in energy is itself comprised of linear and non-linear Stark effect terms according to equation 28 as derived by Sebastien and Weiser for solid-state tetracene and pentacene.[55] The effective field differs from the applied electric field (F_{app}) since it considers the dielectric constant of the medium (ε). For non-polar environments,[56] $F = (2\varepsilon + 1)F_{app}/3$. In this thesis, both corrected and uncorrected (where $F = F_{app}$) fields are considered.

$$\Delta E = -\frac{1}{2}\Delta\alpha F^2 - \Delta\mu F \tag{2.8}$$

† The Stark effect is based on the alteration of the absorption lines and selection rules of optical transition upon the application of a high external field.

From equation 2.8, these changes allow determination of parameters such as the change in electric dipole moment ($\Delta\mu$) and polarizability ($\Delta\alpha$) on excitation caused by the perturbing field, as well as the character of the excited states associated with a specific optical transition. Since Frenkel and CT excitons are characterized by differences in terms of permanent dipole moments (2.1.1), EA becomes particularly interesting for determining the origin of these different types of states.[57,58] An explanation of how this can be understood is as follows: in a rigid environment with a uniform spread of molecules, the two cases are thus considered:

i. The main contributor to the Stark effect is the change in dipole moment, Δμ, (Figure 2.7a) – CT excitons: the molecules will have random orientations of $\Delta\mu$ that vary through parallel, antiparallel and perpendicular to the electric field. The shift in energy with the applied field is given by $\Delta E = -\Delta\vec{\mu}.\vec{F}_{ext}$ and will shift the transition energy to a range that is dependent on the direction of both vectors. Their transition energies are instead shifted to higher or lower energies i.e. a field induced broadening of the absorption line $A^F(E)$. The field-on minus field-off will thus be governed by the second term of equation 2.8 and the associated change in line shape will follow the second derivative of the ground state absorption spectrum. Combining equations 2.7 and 2.8, with C_L a constant, experimentally determined to be 1/3,[55] one obtains the linear Stark effect:

$$\Delta A = \frac{1}{2} C_L \Delta\mu^2 F^2 \frac{d^2(A)}{dE^2} \tag{2.9}$$

ii. The main contributor to the Stark effect is the change in polarizability, $\Delta\vec{\alpha}$, (Figure 2.7b) – Frenkel excitons: the electric field induces a dipole in the direction of the applied field that mimics a dipole in an oriented sample. This is known as the quadratic Stark effect as equation 2.8 simplifies to its first term and the observed effect is a band shift that follows the line shape of the first derivative of the absorption.

$$\Delta A = -\frac{1}{2} \Delta\alpha F^2 \frac{dA}{dE} \tag{2.10}$$

From equations 2.9 and 2.10, both the linear and quadratic Stark effects that make the EA spectrum have a quadratic dependence with the applied field. Analysing an EA spectrum requires the measurement of a noise free absorption spectra to properly differentiate and fit to the EA – equation 2.7. To avoid noise from numerical differentiation of the absorption measurement, a reconstruction of the absorption spectrum with a set of Gaussians that sum to faithfully reproduce the absorption line and will give rise to smooth derivatives. A least square fitting model is then used to fit the EA spectrum to the derivatives of the absorption and

determine the constants of interest. In Chapter 3, a how-to guide of electroabsorption containing sample production, system setup and data analysis is presented.

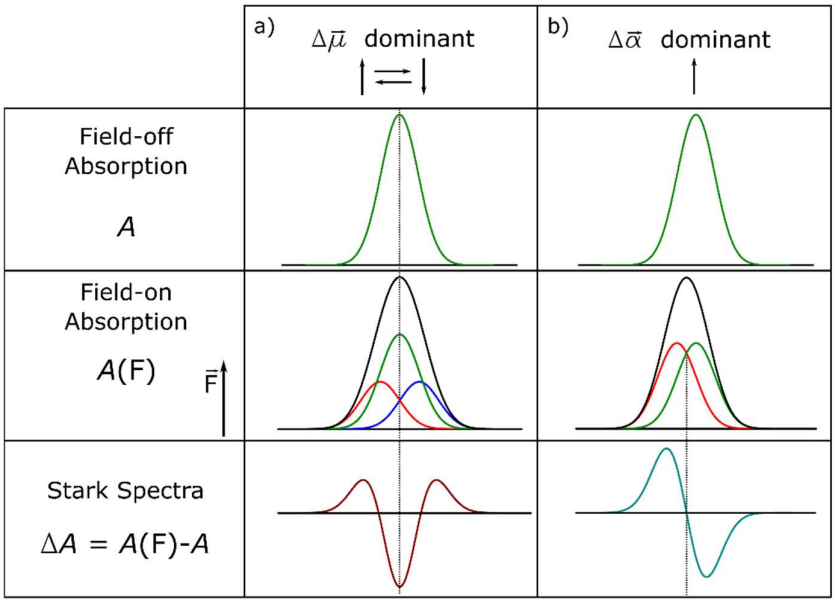

Figure 2.7 – Field induced changes to the absorption spectrum of an immobilized molecule. Two different types of materials are considered: a) the change in dipole moment ($\Delta\boldsymbol{\mu}$) dominates shifting the change in energy to higher or lower values; b) a neutral molecule will have an induced dipole in the direction of the field – change in polarizability($\Delta\boldsymbol{\alpha}$). The Stark (Field-on minus Field-off) spectra can probe these different domains as the EA line follows either the second or the first differentials of the main absorption, respectively (adapted from Boxer[51]). In *A(F)* the left red curve represents a shift to lower energies, the right blue curve a shift to higher energies, the green curve the field-off absorption (*A*) and the black the sum of these three.

2.4 Organic Light-Emitting Diodes (OLEDs)

In 1983, Tang and VanSlyke filed a patent for the first organic electroluminescence device, reporting it 4 years later as a letter in 1987 and revolutionising the landscape of organic electronics for display applications.[59,60] 30 years since this first report, research in the field has culminated in the described three main OLED generations and in different OLED-driven applications. An OLED is a stack of organic molecules, all sandwiched between two electrodes, with at least one of them transparent for light output (Figure 2.8). Under an applied bias, charge injection to opposite sides of the device – the cathode injects electrons while the anode injects holes, (Figure 2.8a) – initiates the device operation. The electric field transports charges across the different organic layers (Figure 2.8b) until they meet and recombine to form an exciton (Figure 2.8c) that then decays radiatively (Figure 2.8d), with emission characteristic to the layer in which recombination occurs.

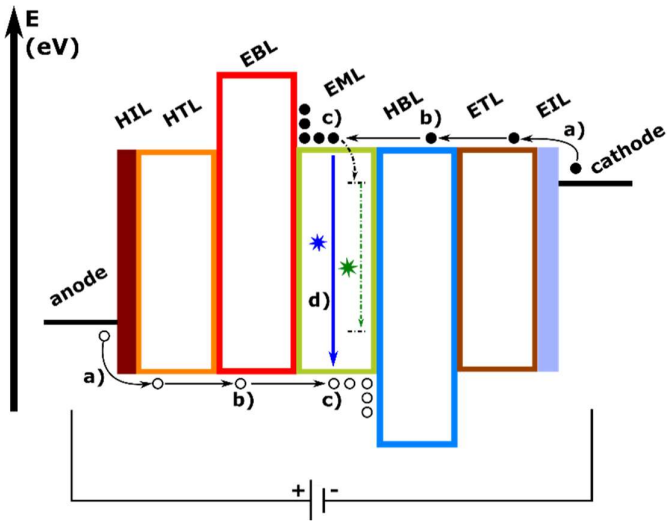

Figure 2.8 – The ideal OLED structure according to HOMO and LUMO alignment of each layer and physical mechanism of each layer: a) carrier injection, b) carrier transport, c) carrier blockage, d) exciton recombination. The blue straight arrow represents the emission from the host while the green dashed arrow, the emission from the guest. From left to right: HIL – hole injection layer; HTL – hole transport layer; EBL – electron blocking layer; EML – electroluminescence layer; HBL – hole blocking layer; ETL – electron transport layer; EIL – electron injection layer.

To build an organic stack, one has to consider the energy levels of each material, mainly defined by their HOMO and LUMO levels, along with the charge mobility and film forming properties. It is thus possible to denote different layers according to the dominant charge carrier and to its basic function in the device as hole (H) or electron (E) injection (HIL and EIL), transport (HTL and ETL) and blocking (HBL and EBL) layers. Recombination and light emission occur in the electroluminescence layer (EML). A more detailed description of each layer for a top-emitting device[61] follows. Details on the molecular structures and chemical names of the materials used in this thesis can be found in Chapter 3.

Anode: ideally an electrode with a high work function, high transparency, low roughness and good conductivity, as these are all important parameters for hole injection (Figure 2.8), film uniformity and light extraction. Indium Tin Oxide (ITO), a ternary composition of various amounts of Indium, Tin and Oxygen is the most commonly used electrode, with a work function that varies with the content in oxygen, typically around 4.5 eV;

HIL: a material with a high hole mobility that has the sole purpose of lowering the energy barrier between the anode and the HTL. In this thesis, PEDOT:PSS was used as HIL;

HTL(ETL): a hole (electron) conducting material with an important role of transporting holes (electrons) to the EML. NPB, TAPC were used as HTL whereas TPBi was used as ETL;

EBL(HBL): hole (electron) transporting materials with shallow LUMO (deep HOMO) that block carriers, confining them in the EML. TSPO1 was used as HBL;

EML: As shown in section 2.2.3, the EML is composed of a host:guest blend, with a host material doped (10-30 %) with an emitting guest. The host materials featured in this thesis were DPEPO, CBP and mCBP;

EIL: lithium fluoride (LiF) is the most commonly used EIL for electron injecting. Though a dielectric in nature, small amounts of LiF form tunnels that facilitate injection to the ETL;

Cathode: typically a low work function metal (with a small energy barrier with the LUMO of the ETL) that should be stable under an oxygen environment. Though not the best candidate, aluminium (Al) offers the best of both worlds in terms of work function (~4.1 eV) and stability.

2.4.1 Strategies for White-OLEDs

Apart from the display industry, OLEDs are also being considered as good candidates for solid-state lighting (SSL) applications producing high white colour quality, homogeneous illumination, high quality colour rendering and stability.[62] The development of white OLEDs (W-OLEDs) for lighting has not seen the same increase in popularity and product demand as it has for displays, mostly because the production costs of these systems are still too high, a result of rather complex architectures. However, W-OLEDs have found their niche market in more artistic and luxury high-end lighting applications and it remains to be seen if they will ever be able to compete with other sources for general lighting purposes. Strategies to produce different white emitting structures are summarised in (Figure 2.9), producing architectures with various complexities and colour stabilities under different electrical stress. Efficient and colour stable devices may be obtained using tandem (Figure 2.9a) or pixelated (Figure 2.9b) device structures though problems arising from mask alignment and evaporation precision may arise, increasing their production costs. Simpler structures can be used such as the use of white emitting materials (Figure 2.9c) or of a blue emitter with green and red down-converting layers (Figure 2.9d), however efficiency will be limited to the performance of the main molecule. Finally, either RGB emitting sublayers (Figure 2.9e) or the use of a host with RGB guest emitters are also an option (Figure 2.9f). These seem good candidates for simplicity, but colour stability may be an issue, a result of the increased energy barriers in the emitting layer(s). Multiple hybrid W-OLEDs implementing fluorescent[63] or phosphorescent[64] emitters, was well as with multiple other structures,[65–67] have been developed using the below strategies. In this

thesis, sublayers of emitting orange, green and blue are used following a structure similar to the one presented in Figure 2.9e).

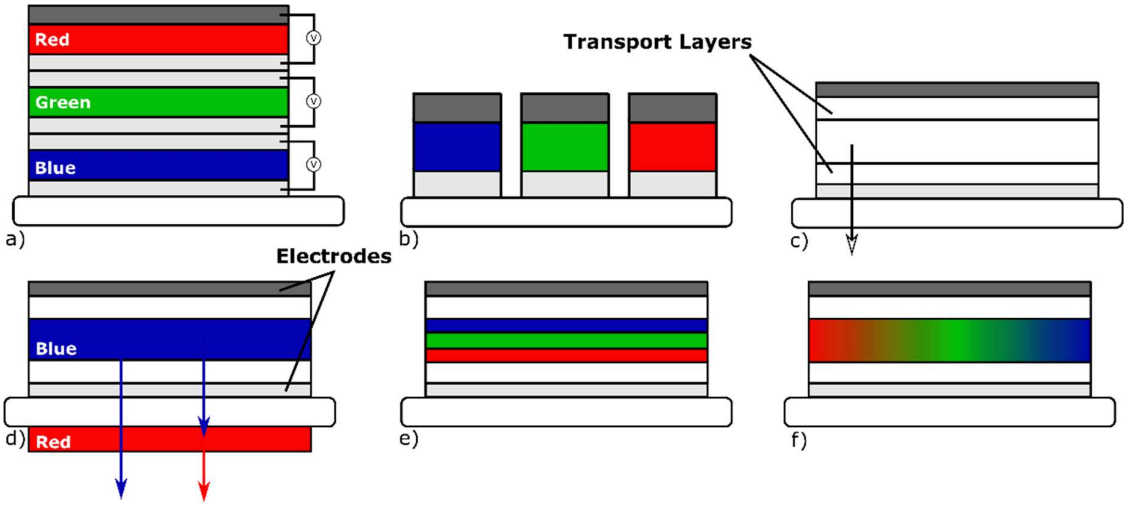

Figure 2.9 – State of the art of applied structures used for white light emission on bottom emitting W-OLEDs. a) Tandem b) pixelated monochrome, c) single-emitter-based, d) blue OLEDs with down-conversion layers, e) single OLEDs with a sublayer EML design and f) single emitting layer OLEDs with RGB emitting guests (adapted from [62]).

a) TADF based W-OLEDs

TADF-based W-OLEDs in particular have also attracted considerable attention as a possible SSL alternative. One of the disadvantages of TADF emitters for the smartphone industry is in their broad emission profile, a result of their CT transitions. In SSL, this can be an advantage, as it offers full visible-spectrum emission which translates into good colour rendering properties. The high energy character of blue emitters tends to be harmful for the human eye, affecting heavily each person's circadian rhythm, so white sources with lower contributions of blue (without affecting the colour rendering) should be pursued.[68] Reports have already shown white emission from either phosphorescent/TADF hybrid[69,70] or full TADF [71–73] stacks. As of February 2019, the maximum efficiency for a full, two-colour TADF-based W-OLED is 19.8 %,[74] taking advantage of these materials' high efficiencies and broad emission. Still, the performance of this device drops abruptly and at 1,000 cd/m^2, it shows only about 35 % of the maximum efficiency, translating to a poor roll-off. Therefore, the challenge remains to find suitable TADF emitters and host materials that combine relatively high resistance to roll-off and high efficiency with stable optical and electrical properties, particularly for blue TADF materials, all of it in a simple device structure.[22] It is crucial to design devices that promote high carrier balance inside each emitter, avoid quenching mechanisms[69] and have low enough contribution of blue emitters without affecting the white colour quality.

2.5 References Chapter 2

1. Köhler, A. & Bässler, H. *Electronic Processes in Organic Semiconductors*. (2015).
2. Turro, N. J., Ramamurthy, V. & Scaiano, J. C. *Principles of Molecular Photochemistry: An Introduction*. (2009).
3. Knoester, J. & Agranovich, V. M. in *Thin Films and Nanostructures* 1–34 (2003).
4. Lewis, G. N. & Kasha, M. Phosphorescence and the Triplet State. *J. Am. Chem. Soc.* **66,** 2100–2116 (1944).
5. Yook, K. S. & Lee, J. Y. Organic Materials for Deep Blue Phosphorescent Organic Light-Emitting Diodes. *Adv. Mater.* **24,** 3169–3190 (2012).
6. Baldo, M. A. *et al.* Highly efficient phosphorescent emission from organic electroluminescent devices. *Nature* **395,** 151–154 (1998).
7. El-Sayed, M. A. The Triplet State: Its Radiative and Nonradiative Properties. *Acc. Chem. Res.* **1,** 8–16 (1968).
8. Uoyama, H., Goushi, K., Shizu, K., Nomura, H. & Adachi, C. Highly efficient organic light-emitting diodes from delayed fluorescence. *Nature* **492,** 234–238 (2012).
9. Perrin, Francis. La fluorescence des solutions - Induction moléculaire. - Polarisation et durée d'émission. - Photochimie. *Ann. Phys.* **10,** 169–275 (1929).
10. Wilkinson, F. & Horrocks, A. R. Phosphorescence and delayed fluorescence of organic substances. *Lumin. Chem.* 116–153 (1968).
11. Lewis, G. N., Lipkin, D. & Magel, T. T. Reversible Photochemical Processes in Rigid Media. A Study of the Phosphorescent State. *J. Am. Chem. Soc.* **63,** 3005–3018 (1941).
12. Parker, C. A. & Hatchard, C. G. Triplet-singlet emission in fluid solutions. Phosphorescence of eosin. *Trans. Faraday Soc.* **57,** 1894 (1961).
13. Berberan-Santos, M. N. & Garcia, J. M. M. Unusually Strong Delayed Fluorescence of C70. *J. Am. Chem. Soc.* **118,** 9391–9394 (1996).
14. Horrocks, A. R. & Wilkinson, F. Triplet state formation efficiencies of aromatic hydrocarbons in solution. *Proc. R. Soc. London. Ser. A. Math. Phys. Sci.* **306,** 257–273 (1968).
15. Baleizão, C. & Berberan-Santos, M. N. Thermally Activated Delayed Fluorescence in Fullerenes. *Ann. N. Y. Acad. Sci.* **1130,** 224–234 (2008).
16. Endo, A. *et al.* Thermally Activated Delayed Fluorescence from Sn4+-Porphyrin Complexes and Their Application to Organic Light Emitting Diodes - A Novel Mechanism for Electroluminescence. *Adv. Mater.* **21,** 4802–4806 (2009).
17. Bergmann, L., Zink, D. M., Bräse, S., Baumann, T. & Volz, D. Metal–Organic and Organic TADF-Materials: Status, Challenges and Characterization. *Top. Curr. Chem.* **374,** 22 (2016).
18. Ward, J. S. *et al.* The interplay of thermally activated delayed fluorescence (TADF) and room temperature organic phosphorescence in sterically-constrained donor–acceptor charge-transfer molecules. *Chem. Commun.* **52,** 2612–2615 (2016).
19. Dias, F. B., Penfold, T. J. & Monkman, A. P. Photophysics of thermally activated delayed fluorescence molecules. *Methods Appl. Fluoresc.* **5,** 012001 (2017).
20. dos Santos, P. L., Etherington, M. K. & Monkman, A. P. Chemical and conformational control

of the energy gaps involved in the thermally activated delayed fluorescence mechanism. *J. Mater. Chem. C* **6,** 4842–4853 (2018).

21. Kim, J. H., Yun, J. H. & Lee, J. Y. Recent Progress of Highly Efficient Red and Near-Infrared Thermally Activated Delayed Fluorescent Emitters. *Adv. Opt. Mater.* **6,** 1800255 (2018).

22. Bui, T.-T., Goubard, F., Ibrahim-Ouali, M., Gigmes, D. & Dumur, F. Recent advances on organic blue thermally activated delayed fluorescence (TADF) emitters for organic light-emitting diodes (OLEDs). *Beilstein J. Org. Chem.* **14,** 282–308 (2018).

23. Etherington, M. K. *et al.* Regio- and conformational isomerization critical to design of efficient thermally-activated delayed fluorescence emitters. *Nat. Commun.* **8,** 14987 (2017).

24. Tanaka, H., Shizu, K., Nakanotani, H. & Adachi, C. Dual intramolecular charge-transfer fluorescence derived from a phenothiazine-triphenyltriazine derivative. *J. Phys. Chem. C* **118,** 15985–15994 (2014).

25. dos Santos, P. L. *et al.* Triazatruxene: A Rigid Central Donor Unit for a D-A 3 Thermally Activated Delayed Fluorescence Material Exhibiting Sub-Microsecond Reverse Intersystem Crossing and Unity Quantum Yield via Multiple Singlet-Triplet State Pairs. *Adv. Sci.* **5,** 1700989 (2018).

26. dos Santos, P. L., Ward, J. S., Batsanov, A. S., Bryce, M. R. & Monkman, A. P. Optical and Polarity Control of Donor-Acceptor Conformation and Their Charge-Transfer States in Thermally Activated Delayed-Fluorescence Molecules. *J. Phys. Chem. C* **121,** 16462–16469 (2017).

27. Dias, F. B. *et al.* The role of local triplet excited states and D-A relative orientation in thermally activated delayed fluorescence: Photophysics and devices. *Adv. Sci.* **3,** 1600080 (2016).

28. Lim, B. T., Okajima, S., Chandra, A. K. & Lim, E. C. Radiationless transitions in electron donor-acceptor complexes: selection rules for S1 → T intersystem crossing and efficiency of S1 → S0 internal conversion. *Chem. Phys. Lett.* **79,** 22–27 (1981).

29. Gibson, J., Monkman, A. P., Penfold, T. J. & Jamie Gibson, Andrew Monkman, T. P. The Importance of Vibronic Coupling for Efficient Reverse Intersystem Crossing in Thermally Activated Delayed Fluorescence Molecules. *ChemPhysChem* **17,** 2956–2961 (2016).

30. Marian, C. M. Mechanism of the Triplet-to-Singlet Upconversion in the Assistant Dopant ACRXTN. *J. Phys. Chem. C* **120,** 3715–3721 (2016).

31. Chen, X.-K., Zhang, S.-F., Fan, J.-X. & Ren, A.-M. Nature of Highly Efficient Thermally Activated Delayed Fluorescence in Organic Light-Emitting Diode Emitters: Nonadiabatic Effect between Excited States. *J. Phys. Chem. C* **119,** 9728–9733 (2015).

32. Ogiwara, T., Wakikawa, Y. & Ikoma, T. Mechanism of Intersystem Crossing of Thermally Activated Delayed Fluorescence Molecules. *J. Phys. Chem. A* **119,** 3415–3418 (2015).

33. Palmeira, T. & Berberan-Santos, M. N. Kinetic Criteria for Optimal Thermally Activated Delayed Fluorescence in Photoluminescence and in Electroluminescence. *J. Phys. Chem. C* **121,** 701–708 (2017).

34. Etherington, M. K., Gibson, J., Higginbotham, H. F., Penfold, T. J. & Monkman, A. P. Revealing the spin–vibronic coupling mechanism of thermally activated delayed fluorescence. *Nat. Commun.* **7,** 13680 (2016).

35. dos Santos, P. L., Ward, J. S., Bryce, M. R. & Monkman, A. P. Using Guest–Host Interactions To Optimize the Efficiency of TADF OLEDs. *J. Phys. Chem. Lett.* **7,** 3341–3346 (2016).

36. Data, P. *et al.* Dibenzo[a,j]phenazine-Cored Donor-Acceptor-Donor Compounds as Green-to-Red/NIR Thermally Activated Delayed Fluorescence Organic Light Emitters. *Angew. Chem.,*

Int. Ed. **55,** 5739–5744 (2016).

37. Zhang, X. *et al.* Host-free Yellow-Green Organic Light-Emitting Diodes with External Quantum Efficiency over 20% based on a Compound Exhibiting Thermally Activated Delayed Fluorescence. *ACS Appl. Mater. Interfaces* acsami.8b18798 (2019). doi:10.1021/acsami.8b18798

38. Watanabe, Y., Sasabe, H. & Kido, J. Review of Molecular Engineering for Horizontal Molecular Orientation in Organic Light-Emitting Devices. *Bull. Chem. Soc. Jpn.* **92,** 716–728 (2019).

39. Santos, P. L. *et al.* Engineering the singlet–triplet energy splitting in a TADF molecule. *J. Mater. Chem. C* **4,** 3815–3824 (2016).

40. Northey, T., Stacey, J. & Penfold, T. J. The role of solid state solvation on the charge transfer state of a thermally activated delayed fluorescence emitter. *J. Mater. Chem. C* **5,** 11001–11009 (2017).

41. Parker, C. A. Sensitized P -type delayed fluorescence. *Proc. R. Soc. London. Ser. A. Math. Phys. Sci.* **276,** 125–135 (1963).

42. Monkman, A. P. Singlet Generation from Triplet Excitons in Fluorescent Organic Light-Emitting Diodes. *ISRN Mater. Sci.* **2013,** (2013).

43. Kondakov, D. Y. Triplet-triplet annihilation in highly efficient fluorescent organic light-emitting diodes: current state and future outlook. *Philos. Trans. R. Soc. A Math. Phys. Eng. Sci.* **373,** 20140321–20140321 (2015).

44. Kukhta, N. A. *et al.* Deep-Blue High-Efficiency TTA OLED Using Para - and Meta -Conjugated Cyanotriphenylbenzene and Carbazole Derivatives as Emitter and Host. *J. Phys. Chem. Lett.* **8,** 6199–6205 (2017).

45. Hu, D., Yao, L., Yang, B. & Ma, Y. Reverse intersystem crossing from upper triplet levels to excited singlet: a 'hot excition' path for organic light-emitting diodes. *Philos. Trans. R. Soc. A Math. Phys. Eng. Sci.* **373,** (2015).

46. Northey, T. & Penfold, T. J. The intersystem crossing mechanism of an ultrapure blue organoboron emitter. *Org. Electron.* **59,** 45–48 (2018).

47. Kim, K.-H., Yoo, S.-J. & Kim, J.-J. Boosting Triplet Harvest by Reducing Nonradiative Transition of Exciplex toward Fluorescent Organic Light-Emitting Diodes with 100% Internal Quantum Efficiency. *Chem. Mater.* **28,** 1936–1941 (2016).

48. D'Andrade, B. W. *et al.* High-efficiency yellow double-doped organic light-emitting devices based on phosphor-sensitized fluorescence. *Appl. Phys. Lett.* **79,** 1045–1047 (2001).

49. Jeon, S. K., Park, H. & Lee, J. Y. Highly Efficient Soluble Blue Delayed Fluorescent and Hyperfluorescent Organic Light-Emitting Diodes by Host Engineering. *ACS Appl. Mater. Interfaces* **10,** 5700–5705 (2018).

50. Stark, J. Observation of the Separation of Spectral Lines by an Electric Field. *Nature* **92,** (1913).

51. Boxer, S. G. Stark Realities. *J. Phys. Chem. B* **113,** 2972–2983 (2009).

52. Iimori, T., Ito, R., Ohta, N. & Nakano, H. Stark Spectroscopy of Rubrene. I. Electroabsorption Spectroscopy and Molecular Parameters. *J. Phys. Chem. A* **120,** 4307–4313 (2016).

53. Yanagi, K., Gardiner, A. T., Cogdell, R. J. & Hashimoto, H. Electroabsorption spectroscopy of β -carotene homologs: Anomalous enhancement of Δμ. *Phys. Rev. B - Condens. Matter Mater. Phys.* **71,** 195118 (2005).

54. Liptay, W. in *Excited States* **1,** 129–229 (Elsevier, 1974).

55. Sebastian, L., Weiser, G. & Bässler, H. Charge transfer transitions in solid tetracene and pentacene studied by electroabsorption. *Chem. Phys.* **61,** 125–135 (1981).

56. Long, W. & Caoc, H. The local field correction factor for spontaneous emission. **232,** 15–24 (1997).

57. Feller, F. & Monkman, A. Optical spectroscopy of oriented films of poly(2,5-pyridinediyl). *Phys. Rev. B* **61,** 13560–13564 (2000).

58. Legaspi, C. M. *et al.* Rigidity and Polarity Effects on the Electronic Properties of Two Deep Blue Delayed Fluorescence Emitters. *J. Phys. Chem. C* **122,** 11961–11972 (2018).

59. Tang, C. W. & VanSlyke, S. A. Organic electroluminescent diodes. *Appl. Phys. Lett.* **51,** 913–915 (1987).

60. VanSlyke, S. A. & Tang, C. W. Organic Electroluminescent Devices having Improved Power Conversion Efficiencies. *United States patent No US4539507A* (1985).

61. de Sa Pereira, D., Data, P. & Monkman, A. P. Methods of Analysis of Organic Light Emitting Diodes. *Disp. Imaging* **2,** 323–337 (2017).

62. Reineke, S., Thomschke, M., Lüssem, B. & Leo, K. White organic light-emitting diodes: Status and perspective. *Rev. Mod. Phys.* **85,** 1245–1293 (2013).

63. Pereira, D., Pinto, A., California, A., Gomes, J. & Pereira, L. Control of a White Organic Light Emitting Diode's emission parameters using a single doped RGB active layer. *Mater. Sci. Eng. B* **211,** 156–165 (2016).

64. Xue, M. M. *et al.* De Novo Design of Boron-Based Host Materials for Highly Efficient Blue and White Phosphorescent OLEDs with Low Efficiency Roll-Off. *ACS Appl. Mater. Interfaces* **8,** 20230–20236 (2016).

65. Hung, W.-Y. *et al.* The First Tandem, All-exciplex-based WOLED. *Sci. Rep.* **4,** 4–9 (2014).

66. Kim, S. H., Park, S., Kwon, J. E. & Park, S. Y. Organic light-emitting diodes with a white-emitting molecule: Emission mechanism and device characteristics. *Adv. Funct. Mater.* **21,** 644–651 (2011).

67. Song, W., Lee, I. & Lee, J. Y. Host Engineering for High Quantum Efficiency Blue and White Fluorescent Organic Light-Emitting Diodes. *Adv. Mater.* **27,** 4358–4363 (2015).

68. Boyce, P. R. in *Human factors in lighting - 3rd Edition* 6–10 (CRC Press, 2014).

69. Wu, Z. *et al.* Management of Singlet and Triplet Excitons: A Universal Approach to High-Efficiency All Fluorescent WOLEDs with Reduced Efficiency Roll-Off Using a Conventional Fluorescent Emitter. *Adv. Opt. Mater.* **4,** 1067–1074 (2016).

70. Gao, K. *et al.* An ideal universal host for highly efficient full-color, white phosphorescent and TADF OLEDs with a simple and unified structure. *J. Mater. Chem. C* **5,** 10406–10416 (2017).

71. Nishide, J., Nakanotani, H., Hiraga, Y. & Adachi, C. High-efficiency white organic light-emitting diodes using thermally activated delayed fluorescence. *Appl. Phys. Lett.* **104,** 233304 (2014).

72. Duan, C. *et al.* Multi-dipolar Chromophores Featuring Phosphine Oxide as Joint Acceptor: A New Strategy toward High-Efficiency Blue Thermally Activated Delayed Fluorescence Dyes. *Chem. Mater.* **28,** 5667–5679 (2016).

73. Chen, Y. *et al.* Highly efficient white light-emitting diodes with a bi-component emitting layer based on blue and yellow thermally activated delayed fluorescence emitters. *J. Mater. Chem. C* **6,** 2951–2956 (2018).

74. Zhao, J. *et al.* Highly-efficient fully non-doped white organic light-emitting diodes consisting entirely of thermally activated delayed fluorescence emitters. *J. Mater. Chem. C* **6,** 3226–3232 (2018).

Chapter 3: Materials and Experimental Methods

In this chapter, experimental details for data collection common to all the results chapters is given. The first part covers all the materials studied, either newly synthesized, previously published or commercially available (for calibration or OLED production). The second part details sample preparation methods for solution and solid-state samples. This is then followed by the three main steady-state and time-resolved optical techniques used in the course of this thesis. A detailed guide on electroabsorption spectroscopy follows and includes sample structure, system setup and sample measurement. Finally, vacuum thermal evaporation to produce evaporated films or OLEDs is discussed, with details on electrical and optical characterization methods appropriate for such samples.

The work presented in this chapter can partly be found in the following publications:

- Daniel de Sa Pereira, Andrew P. Monkman, **Production and Characterization of Vacuum Deposited Organic Light Emitting Diodes,** Journal of Visualized Experiments, 2018, 141, e56593.
- Daniel de Sa Pereira, Przemyslaw Data, Andrew P. Monkman, **Methods of Analysis of Organic Light Emitting Diodes**, Display and Imaging, 2017, 2, 323-337.
- Daniel de Sa Pereira, Christopher Menelaou, Andrew Danos, Christel Marian and Andrew P. Monkman, **Electroabsorption as a Tool to Probe Charge Transfer and State Mixing in Thermally-Activated Delayed Fluorescence Emitters**, Journal of Physical Chemistry Letters, 2019, 10, 3205−3211.

3.1. Organic Semiconductors Studied

This thesis focuses on the characterization and application of different organic emitters, aiming towards a deeper understanding of mechanisms associated with thermally-activated delayed fluorescence (TADF). Much of the work conducted throughout this project (particularly chapters 4, 5 and 6) was done on newly synthesized materials produced in cooperation between the Organic Electroactive Materials (OEM) group at the Physics Department of Durham University and the Department of Chemical Engineering of Sungkyunkwan University, South Korea. Chapters 7 and 8 were conducted on previously published emitters, synthesized in the Chemistry department of Durham University or the department of Applied Chemistry of Osaka University, Japan. Chapter 7 also uses profilometer measurements performed at the Engineering Department of Durham University and state-of-the-art DFT/MRCI calculations, performed by Prof Christel Marian from the Institute for Theoretical Chemistry and Computer Chemistry at the University of Düsseldorf, Germany. When necessary, commercially available materials were used, often for calibration of experimental techniques or as host and transport materials to produce organic light-emitting diodes (OLEDs). In this last group, materials were purchased from Sigma Aldrich or Lumtec.

Table 3.1-3.3 summarise the chemical structures and lists acronyms of all materials involved in this study: 3.1. separate donor (**D**) and acceptor (**A**) units; 3.2. new materials synthesised with 2,4,6-triphenyl-1,3,5-triazine (TRZ) as accepting unit; 3.3. previously published **D-A-D** materials and host and transport materials used in OLED production.

Table 3.1 – Molecular structures of the units (donor – D or acceptor – A) used for this thesis, chemical names, acronyms and chapters where they are featured.

Chemical Structure	Chemical Name	Acronym	Type	Chapter
Donor (D) and Acceptor (A) units				
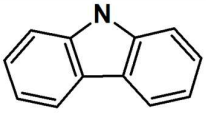	Carbazole	Cz	D	4,5
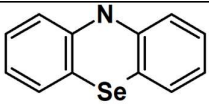	Phenoselenazine	PSeZ	D	6
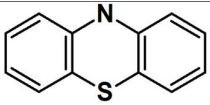	Phenothiazine	PTZ	D	6

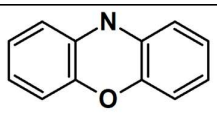	Phenoxanize	POZ	D	6
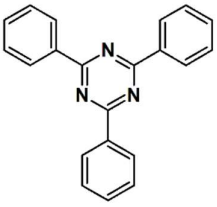	2,4,6-triphenyl-1,3,5-triazine	TRZ	A	4,5,6
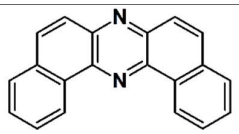	dibenzo[a,j]phenazine	DBPHZ	A	7

Table 3.2 – Molecular structures, acronyms and featured chapters of all 2,4,6-triphenyl-1,3,5-triazine (TRZ) based emitters.

TRZ-based emitters

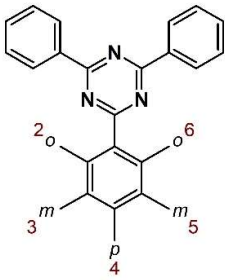

o - ortho; m - meta; p - para;

Acronym	Type	2	3	4	5	6	Chapter
23CT	**D_2-A**	Cz	Cz	H	H	H	4, 5
24CT	**D_2-A**	Cz	H	Cz	H	H	4
25CT	**D_2-A**	Cz	H	H	Cz	H	4
26CT	**D_2-A**	Cz	H	H	H	Cz	4
34CT	**D_2-A**	H	Cz	Cz	H	H	4
35CT	**D_2-A**	H	Cz	H	Cz	H	4
234CT	**D_3-A**	Cz	Cz	Cz	H	H	5
345CT	**D_3-A**	H	Cz	Cz	Cz	H	5
2345CT	**D_4-A**	Cz	Cz	Cz	Cz	H	5
PSeZ-TRZ	**D-A**	H	H	PSeZ	H	H	6
PTZ-TRZ[1]	**D-A**	H	H	PTZ	H	H	6

Table 3.3 – Molecular structures, chemical names, acronyms and featured chapters of all previously published emitters, host and transport materials used in characterization and device chapters.

Chemical Structure	Name	Acronym	Type	Chapter
D-A-D emitters				
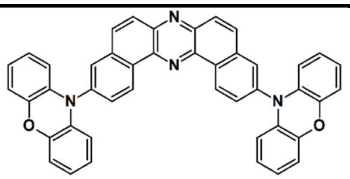	3,11-di(10H-phenoxazin-10-yl)dibenzo[a,j] phenazine	POZ-DBPHZ[2]	D-A-D	7,8
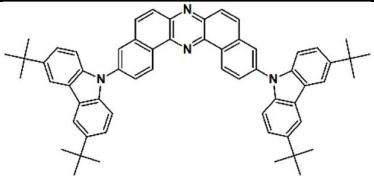	3,11-di-*tert*-butyl-carbazole dibenzo[*a,j*]phenazine	*t*-BuCz-DBPHZ[2]	D-A-D	7
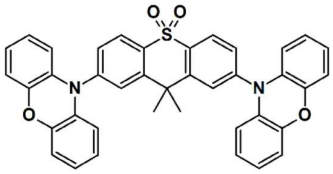	2,7-bis(phenoxazin-10-yl)-9,9-dimethylthioxanthene-S,S-dioxide	DPO-TXO2[3]	D-A-D	8
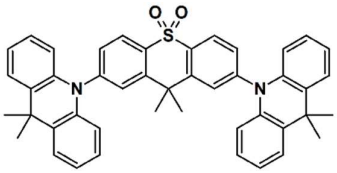	2,7-bis(9, 9-dimethyl-acridin-10-yl)-9,9-dimethylthioxanthene-S,S-dioxide	DDMA-TXO2[4]	D-A-D	8
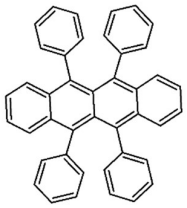	5,6,11,12-tetraphenyltetracene	Rubrene[5]	Emitter	3
Host (H) and transport (T) layers for photophysics and OLEDs				
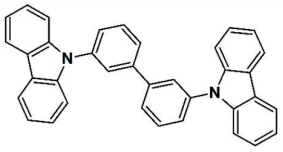	3,3-Di(9H-carbazol-9-yl)biphenyl	mCBP	H	6
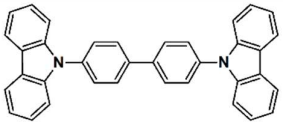	4,4′-bis(N-carbazolyl)-1,1′-biphenyl	CBP	H	8

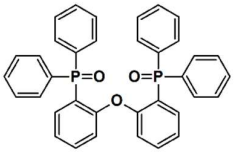	bis[2-(diphenylphosphino)phenyl] ether oxide	DPEPO	H	4,5,8
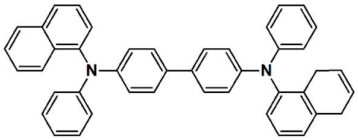	N,N′-di(1-naphthyl)-N, N′-diphenyl-(1,1′-biphenyl)-4,4′-diamine	NPB	T	8
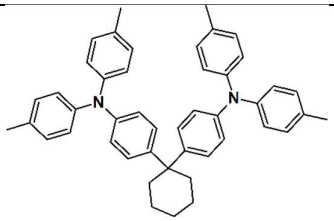	1,1-Bis[(di-4-tolylamino)phenyl] cyclohexane	TAPC	T	4,5,6
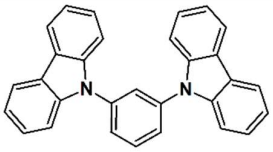	1,3-Bis(N-carbazolyl)benzene	mCP	T	4,5,6
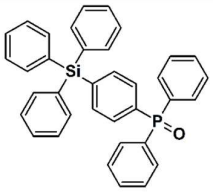	Diphenyl[4-(triphenylsilyl)phenyl]phosphine oxide	TSPO1	T	4,5,6
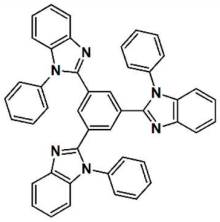	2,2′,2″-(1,3,5-benzinetriyl)-tris(1-phenyl-1H-benzimidazole)	TPBi	T	4,5,6,8
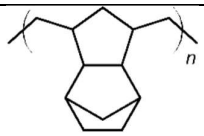	Cyclo Olefin Polymer	Zeonex	H	4,5,6,7

3.2. Sample Preparation

3.2.1. Solution-state Samples

Photophysical characterisation of each new emitter was conducted in both solution and solid-state. For solution-state measurements, the solvents used were (in order of increasing

polarity) methylcyclohexane (MCH), toluene, and dichloromethane (DCM), with dielectric constants (ε) of 2.02, 2.4 and 9.0 respectively. When necessary, for complete dissolution, the solutions were additionally stirred, placed on a hotplate (30 to 80˚C) and sealed to prevent solvent loss. Any changes in solvent volume were later compensated. Final concentrations were 10^{-3}-10^{-6} M. Measurements were performed using quartz cuvettes with a path length of 1 cm.

3.2.2. Solid-state Samples

For solid-state measurements, solutions of emitter in toluene (1 mg/mL) and commercial zeonex in toluene (130 to 150 mg/mL) were first prepared. The solutions were then mixed to prepare a small volume of emitter-in-zeonex at 1% w:w ratio. Then, between 70 to 90 µL were drop-cast (Figure 3.1) onto a quartz or sapphire substrate and placed in vacuum for a few hours to slowly evaporate any residual solvent. Alternatively, the solution was drop-cast onto the substrate on a hotplate at 30 degrees and left until dry. Both methods allowed the production of highly uniform films of well dispersed emitter using the zeonex host.

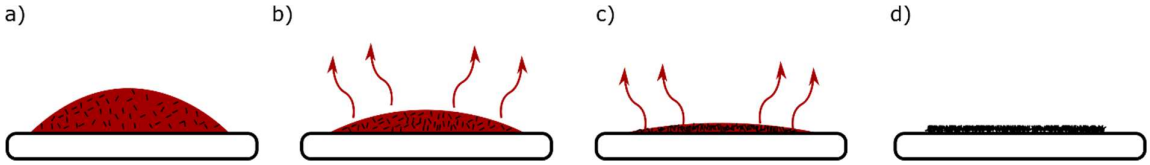

Figure 3.1 – Schematic diagram of the drop-cast method. After dropping a certain amount of solution onto the substrate (a), the solvent starts evaporating (b) and further evaporation solidifies the material (or blend of materials) in study (c) eventually forming the final film (d). This method can be done on a hotplate or in vacuum, allowing control over the speed at which the films are formed and affecting their final quality.

For films where the host is also a small molecule, the drop-cast method formed extremely rough films. While this is acceptable for time-resolved measurements, low roughness and known thickness are fundamental factors for the electroabsorption (EA) measurements. Therefore, the spin-coating technique (Figure 3.2) was the preferred method for the production of emitter-in-host and EA samples using zeonex host.

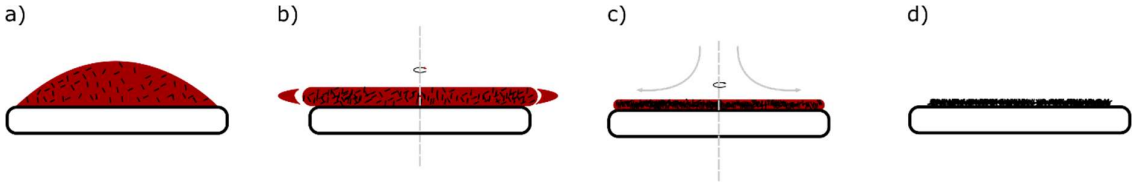

Figure 3.2 – Schematic diagram of the spin-coating method. After dropping a certain amount of solution onto a substrate (a) on rotation at a certain speed (b) so that most of the solvent is flung off the side (c). The film is left drying under ambient air or under temperature (depending on the solvent) going from a liquid to a plasticised state and finally a solid film (d).

For the photophysics of emitters in emitter-in-host blends, solutions of each material were prepared in chloroform with concentrations of 1 mg/mL and 10 mg/mL for emitter and

host, respectively. In each blend, the resulting solutions were mixed in a 1:1 ratio. For the EA measurements, samples of ~7 mg of emitter dispersed into 1 mL of toluene with ~143 mg zeonex (1:20 ratio w:w) were used. In both cases, around 70 μL of the solution was spun for 30 s at 2000 rpm using a Laurell Technologies spin-coater.

A third technique to produce thin films based on vacuum thermal evaporation (VTE) is detailed in section 3.5.

3.3. Steady-State and Time-resolved Measurements

3.3.1. Optical Absorption

Absorption spectra are related to the likelihood of a photon of a certain wavelength to be absorbed by a molecule, i.e. the probability of a transition from the ground state to different excited states (Chapter 2). In this thesis, absorption spectra were collected using a Shimadzu model UV3600 double beam Ultraviolet-Visible (UV-Vis) spectrometer. This technique generally uses a broadband light source (such as a deuterium lamp for the UV or a halogen lamp for the Vis-to-near-IR range) and a monochromator that selects one specific wavelength at a time. With a beam splitter, this monochromatic light is then divided into two separate beams. One beam passes through a cuvette containing the sample in study; the other through a reference (blank) cuvette containing just the solvent in use. The intensities of the transmitted rays are measured by a detector (photomultiplier tube, PMT, for the UV-Vis region; InGaAs detector for the Vis-to-near-IR range). The intensity of the transmitted light (I_x) follows the Beer-Lambert law, $I_x = I_S 10^{-\varepsilon x c}$, where I_S represents the intensity of the incident light, ε the molar absorption coefficient and x the optical path of the photon across the cuvette. The absorption spectrum is recorded in units of optical density (OD) as a function of wavelength and is defined by the equation $OD = \log_{10}(\frac{I_{Ref}}{I_\lambda})$, with I_{Ref} and $I_\lambda$being the intensity of the transmitted light through the reference and the sample, respectively. Absorption spectra were collected at room temperature in aerated environments, in solution-state or solid-state samples.

3.3.2. Photoluminescence

The photoluminescence (PL) spectrum of a molecule is measured following photoexcitation, with emission arising from the transition of excited states back to the ground state (Chapter 2). It is a complement to the absorption data provided by the UV-VIS absorption spectrometer and reveals the intensity and wavelength distribution of emission intensity after

excitation. In this thesis, PL spectra were collected using either a Jobin Yvon Horiba Fluoromax 3 or Fluorolog spectrometers. These instruments consist of a light source (Xe arc-lamp), an excitation monochromator, a reference detector (photodiode - PD), a sample holder, an emission monochromator and a signal detector (PMT).

Light is emitted from the source and the desired excitation wavelength selected by the first monochromator (with slits to control the resolution). The monochromatic beam then excites the sample, where emission occurs. Emission is collected perpendicularly to the incident excitation beam, and the intensity measured with the PMT at different wavelengths by scanning emission monochromator. The reference detector monitors the excitation beam, in order to correct for the different wavelength- and time-dependent fluctuations in the lamp output. Furthermore, to account for the spectral response of the emission monochromator and PD a correction must be applied to ensure that the spectra give true comparisons of intensity across different wavelengths. Therefore, for each instrument, a correction must be applied – although this is usually performed automatically before the spectrum is displayed to the user.

3.3.3. Time-Gated Acquisition – CCD

The time-resolved measurements of the PL spectrum provide understanding of the decay profiles of which states are involved in the emission to determine contributions from prompt fluorescence (PF) delayed fluorescence (DF) and phosphorescence (PH) (Chapter 2). The time-resolved emission spectra were collected using a home-built setup, Figure 3.3. Two different pulsed-laser systems were available for excitation: a Nd:YAG EKSPLA PS5052 with readily accessible, 355 and 532 nm, 3rd and 2nd harmonic outputs (FWHM of 150 ps) and a N_2 laser with a 337 nm (FWHM of 3 ns) emission. The laser is directed to the sample mounted in a cryostat at an angle of around 45^{o} to the excitation beam. Emission is collected by lenses at right angles to excitation and then passes through a multi-grating spectrograph coupled to a 4Picos intensified charge-coupled device (CCD) camera from Stanford Computer Optics with a 200 ps temporal resolution. The CCD detector is composed of an array of pixels that map the intensity at a given interval‡ by charge generated at the surface of each pixel. An image intensifier converts the photons into electrons that are accelerated by a high electric field and amplified by a microchannel plate (MCP). These amplified electrons are then converted back

‡ As an example, a 400 nm range dispersed onto a detector array with 1240 columns of pixels, each pixel records intensity with an interval of around 0.32 nm. However, while the interval of each pixel might correspond to 0.32 nm for this example, a different grating and a different focal length of the spectrograph gives different measurable windows. It is also important to note that CCDs usually have different pixel sizes which vary between manufacturers and models.

into photons resulting in an intensified emission, greatly increasing the sensitivity of the CCD pixel array. Pixel columns are summed to give a total intensity measured as a function of pixel position and an emission spectrum is obtained.

The CCD camera and the laser are temporarily synchronized by two triggers: for the N_2 laser, the excitation beam is split and sampled by a PD that is connected to the CCD with the remaining beam exciting the sample (Figure 3.3); for the Nd:YAG laser, an electrical pulse is sent from the laser to the CCD. In both cases, this serves as a trigger and the response of the camera is to open its shutter after a controllable delay time (TD) and for a software-controllable duration, or integration time (IT). Each TD-IT interval is repeated a certain number of times to improve signal-to-noise and account for any possible fluctuations of the laser intensity.

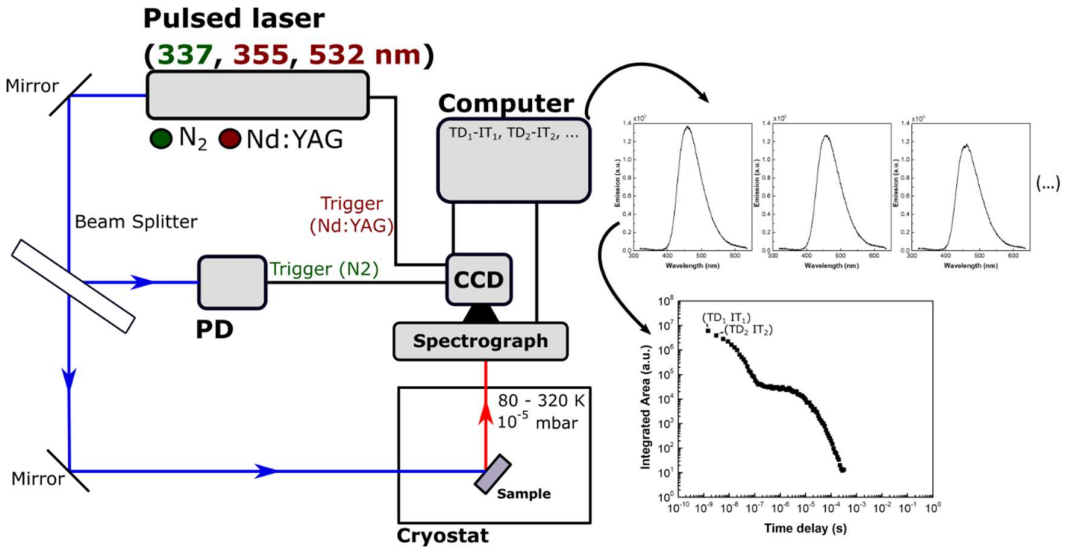

Figure 3.3 – Time-gated acquisition setup. The output from a pulsed layer is split into two beams: one of which is detected by a fast photodiode that emits electrical pulses and are used to trigger the electronic gating process in the intensified charge-coupled device (CCD camera); the second pulse is used to photoexcite a sample held in a liquid nitrogen cooled cryostat in which there is direct flow of gas through the sample chamber. Emitted fluorescence is passed through a monochromator and focussed onto the detector array of the CCD. By doubling the frequency of the 532 nm laser, a 266 nm excitation could be obtained allowing excitation of each individual unit that forms the emitters (Table 3.1).

The TD and IT for single acquisitions are controlled using the CCD camera software (4Picos). Each emission decay measurement is comprised of a set of emission spectra obtained using a script to acquire multiple spectra over specific TD and IT, increasing logarithmically without overlap and allowing comparison between different decays. The area of each emission spectrum is normalised by IT (integrated area) and plotted against the TD. For this thesis, all measurements were collected with samples held under vacuum at room temperature of under a stream of dry nitrogen for temperatures between 80 and 320 K (~10 min equilibrium time). All

lasers were operated at a repetition rate of 10 Hz (TD + IT < 0.1 s) although, when necessary this was reduced to collect emission from longer-lived species.

One important aspect when performing this measurement, particularly using the Nd:YAG laser, is the time-correction mostly due to the flashlamp-laser lifetime timing delay which needed to be considered. To determine true zero time of the system, a series of spectra were collected with short IT and varying TDs, allowing the determination of the laser maximum – the zero time when the pulse departs from the sample and the emission begins to decay. This maximum is shown in Figure 3.4, where each point represents the integrated area at the different TD. To exclude the interference between the emission rise time and the decay, the first point in plotted decay series is was after this maximum (975.5 ns) and defined by the script in use. Moreover, throughout this thesis, the zero TD used varied slightly, this difference coming from the periodic change of components within the system. In this matter, in later photophysics chapters, the next available point shifted to 980.1 ns. However, this value is measured independently in every decay as well by collecting frames before, during and after the laser pulse.

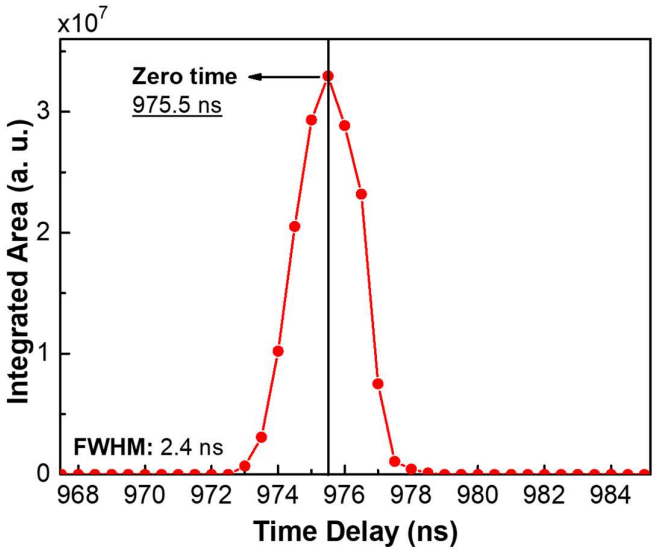

Figure 3.4 – Sequence of emission intensities identifying the zero-time of the Nd:YAG laser; Integrated time-resolve spectra collected using 0.5 ns integration time.

3.4. Electroabsorption Spectroscopy

One of the main projects demonstrated in this thesis was assembling an electroabsorption (EA) spectroscopy system in order to reveal the states and transitions involved in the TADF mechanism that are not optically measurable. In EA, a large electric

field perturbs the optical absorption of a monochromated white light source. Depending on the origin of the states, the electric field will induce changes in the orbitals, making potentially forbidden states accessible with the white light (Chapter 2). In the following sections, a detailed guide contains all the details that were part of the setting-up and use of the EA rig.

3.4.1. Sample Details

For the EA sample preparation, several experiments allowed to take conclusions to the best possible type of samples and materials to use:

- **i.** the TADF emitters in question are small molecules and must be photostable under strong photoexcitation for the long duration of the experiment;
- **ii.** ideally, the TADF emitter should possess a well-defined charge-transfer (CT) absorption band (Chapters 2, 4-6) within the detection-limit of the measurement (governed by the optical excitation source) and above 300 nm (<4.15 eV);
- **iii.** the *OD* of the sample should be high enough to allow rapid and well-resolved detection of the absorption bands, particularly the CT (*OD* ~ 0.3, 0.4);
- **iv.** to properly measure the EA spectrum of a TADF emitter, it must be dispersed into an insulating environment without any EA within the spectral range of the emitter's response – zeonex;
- **v.** the obtained samples should have a low roughness to avoid shorting of electrodes and uniformize the electric field across the two electrodes;

The first step in obtaining the best sample was the reproducing the sample type used 20 years prior to this work in Durham. At the time, a polymeric film was spun onto a quartz substrate, followed by the evaporation of 100 nm of interdigitated gold electrodes, separated by 160 μm.[6] Assuming an applied voltage of 100 V, the maximum electric field would be in the range of 60 kV/cm. Because this was done in neat polymer films with intense and well-resolved absorption bands (in contrast to the weak CT band of a TADF molecule), this electric field was enough to provide good EA signal. For TADF molecules, a much higher electric field was required.

a) Electrode configuration

The idea of using interdigitated electrodes was therefore quickly abandoned in favour of a sandwich structure with a film in between two electrodes. However, though this solves the limitation imposed by the electric field (allowing much higher fields at much lower voltages), several new issues became evident in particular the necessity of semi-transparent electrodes. Additionally, sapphire was used as a substrate instead of quartz due to its high thermal

conductivity combined with high transparency, particularly in the UV. The sapphire substrates used were also significantly smoother (with no variation between individual substrates) due to their hardness, whereas the quartz substrates accumulate unique damage patterns over time. Secondly, aluminium (Al) was chosen over gold due to a better adhesion to the sapphire (Al_2O_3) substrates. Thin films of Al however suffer heavily from oxidation, losing their conductivity in just a matter of hours in air. Between 9 and 12 nm-thick layers presented a good trade-off between electrode transmission and conductivity. In between measurements all samples were kept under a controlled environment (glovebox) with low oxygen and humidity, increasing the lifespan of the Al films for a few days (or even weeks). Thirdly, to decrease the roughness of the films (v), the spin-coated method was chosen over the drop-cast method (Figure 3.2). This ensured a good spread of material around the substrate. Lastly, the evaporation of the top Al layer should be done while avoiding contact with the bottom layer.[§]

b) TADF emitters studied

To secure a high intensity signal, particularly within the CT absorption band, concentrations higher than the typical emitter-in-zeonex samples used elsewhere in this thesis were needed. A 5 % w:w concentration was found to provide good signal and workable solubility. Also, each emitter should be preferably soluble in toluene, as other solvents (particularly the chlorinated ones) are difficult to handle in spin-coating, especially when aiming for low film-roughness. These limitations amplify each other though, as most TADF emitters are not soluble at such high concentrations in toluene. Therefore for the first study, **POZ-DBPHZ** and ***t*-BuCz-DBPHZ**, two TADF emitters with diverging photophysical characteristics,[2] were chosen in part due to their good solubility in toluene, particularly at high concentrations.

c) Sample preparation

The full sample production procedure is shown in Figure 3.5a) with a cross section version in Figure 3.5b). After substrate cleaning with toluene, the sapphire substrates were loaded into the Kurt J. Lesker Spectrus II deposition system (Section 3.5) where the evaporation of a 9 nm-thick layer of Al was performed at a rate of 1 Å/s. For good film uniformity and conductivity, it is recommended to achieve high rate stabilisation prior to material evaporation. The films were then removed from the vacuum chamber and a layer of

[§] Interestingly, it was soon discovered that one should not leave a zeonex film under a high vacuum for an extended period before or after the top Al evaporation. While not affecting the properties of the emitter, this forcibly removes remaining oxygen that is stuck inside, severely affecting the roughness of the film. The result is a non-conductive top Al, and a batch of non-working samples.

emitter-in-zeonex blend was spun on top. A DekTac 3ST profilometer was used to determine the thickness of a sample layer of 5% w:w emitter-in-zeonex to be around 2.3 µm, deposited with one round of spinning (Section 3.1.2). Samples were then reloaded into the vacuum chamber for the evaporation of a 12 nm-thick top layer of Al.[**] A mask was used to keep part of the blend layer uncovered so it would be possible to later remove the zeonex and contact the bottom layer. Toluene was used for the patterning step as it allows gentle removal of the blend without affecting the Al layer on the bottom (that has a good adhesion to sapphire). A schematic of the full sample stack is shown in Figure 3.5c) and a picture of a sample in Figure 3.5d). The final step is the use of silver paste to contact two wires to the two layers (Figure 3.5e).[††]

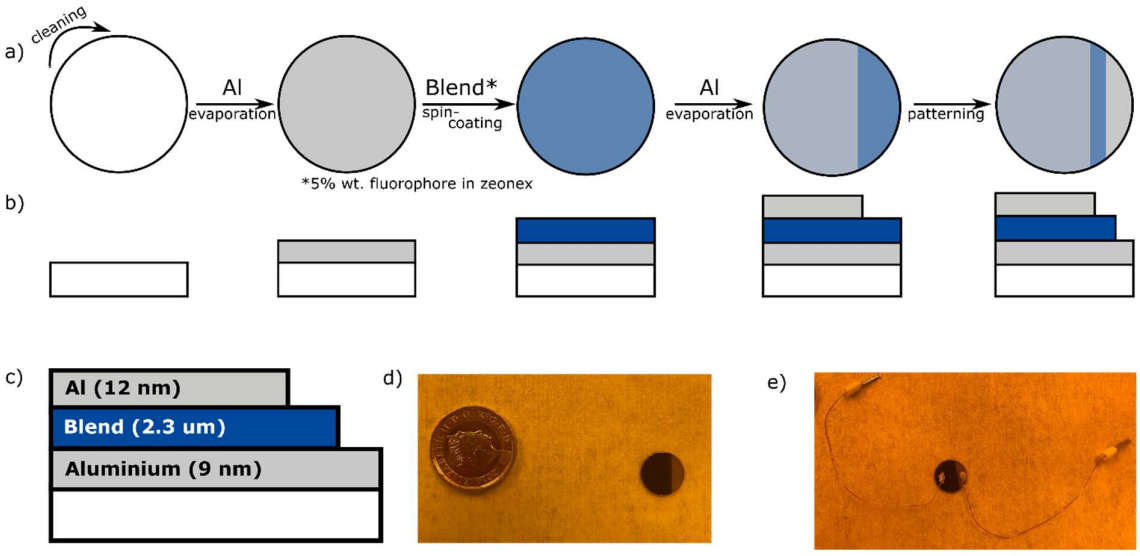

Figure 3.5 – Electroabsorption sample preparation. a) firstly, a sapphire substrate is cleaned with toluene. Then two layers of aluminium are evaporated with an appropriate pattern between a spin-coated film of the fluorophore in zeonex (1:20 w:w). In b) and c), the cross-section and the full stack are shown. d) and e) show a picture of a sample before and after the electrical connections were made, respectively.

3.4.2. Experimental Set-up

With a newly prepared sample, the next step was conducting the experiments. EA measurements were performed in a home-built setup (Figure 3.6) comprising a vacuum cryostat with optical windows and a high voltage feedthrough, a laser driven white-light source (Energetiq EQ-99X) which was focused off the sample to appropriately limit power density and avoid photodamage. The transmitted beam was passed through a monochromator (Bentham TMc300) and measured with a silicon PD. The voltage to supply the electric field

[**] A thicker top layer was chosen due to minimal changes in transparency (between 9 and 12 nm) but higher film lifespan as this is more exposed to oxygen during sample mounting and transport.
[††] A high viscosity silver paste is preferred so the solvent in the paste does not penetrate through the zeonex blend and shorten the Al layers.

was supplied by a Trek 10/10 voltage amplifier, capable of amplifying the sinusoidal internal oscillator output (f=173 Hz) of a Signal recovery DSP 7225 lock-in amplifier by a factor of 1000. The field induced change in transmission (ΔT) and the nominal transmission (T) were detected by the PD connected to the lock-in amplifier at specific monochromator wavelengths with the lock-in measuring both average signal voltage (V) and the oscillating component with the same 173 Hz frequency of the perturbation (ΔV). This ΔV/V at different wavelengths is equivalent to the spectrum of ΔT/T. All measurements were conducted at room temperature under vacuum (<10^{-5} mbar). All cables were shielded, and earth loops were prevented by making the optical table grounded, thus preventing additional noise in the measurements. The combination of the high fields, the type of samples used, and the setup, allowed for signal to be detected down to the order of 10^{-6}.

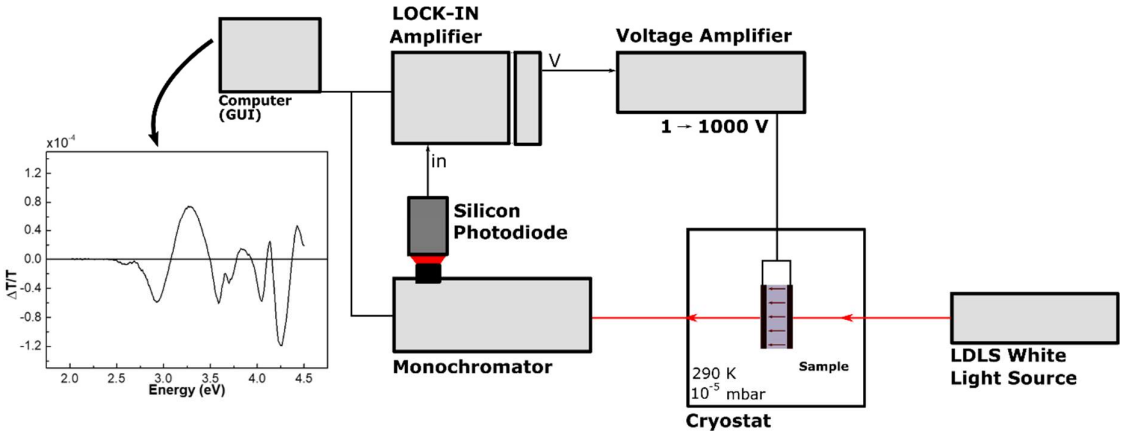

Figure 3.6 – Experimental setup used for the measurement of the Electroabsorption spectra. The experiment is based on electrical perturbation at transmission from a LDLS white light source. The sample is put under a high electric field and then excited by the white light. The field induced change in transmission (ΔT) and the nominal transmission (T) were detected by the photodiode connected to the lock-in amplifier at specific monochromator wavelengths. This in turn provided the energy dispersion of ΔT/T.

Multiple measurements (with different parameters) on the same system were conducted to understand the EA behaviours of each molecule, as degradation products also form EA bands. Therefore, care was taken to avoid measurement of these products, done by comparing EA signal coming from shorter (with less averages and/or bigger time steps) and longer (more averages and/or smaller time steps) duration scans which then translated into the final set of measurements.

a) Graphical user interface

To conduct the EA measurements with different controllable parameters, a graphical user interface (GUI) was created to combine control of the lock-in, the monochromator and the detection in the PD. The GUI is shown in Figure 3.7. In a) scan settings are defined: the energy range (E_i:E_{step}:E_f, E_i,< E_f), the amplitude of the sinusoidal voltage output of the lock-in

(increased 1000x by the amplifier) and the number of averages. b) refers to all the sample information; c) to the lock-in control where the options to reinitialise and autophase were possible; and d) to the monochromator control, as a tool for signal optimisation. e) gives the output from the X and Y channels of the lock-in corresponding to ΔV signal in and out of phase with the oscillator, respectively, f) the analogue-to-digital converter channel (ADC) to measure V and g) allows for signal alignment by opening a separate plot of V against time to allow optimisation of the optics, arc check (the voltage for measurement is tested for a short period of time to check sample durability and sparking inside the cryostat) and finally the start and stop buttons for the measurement run.

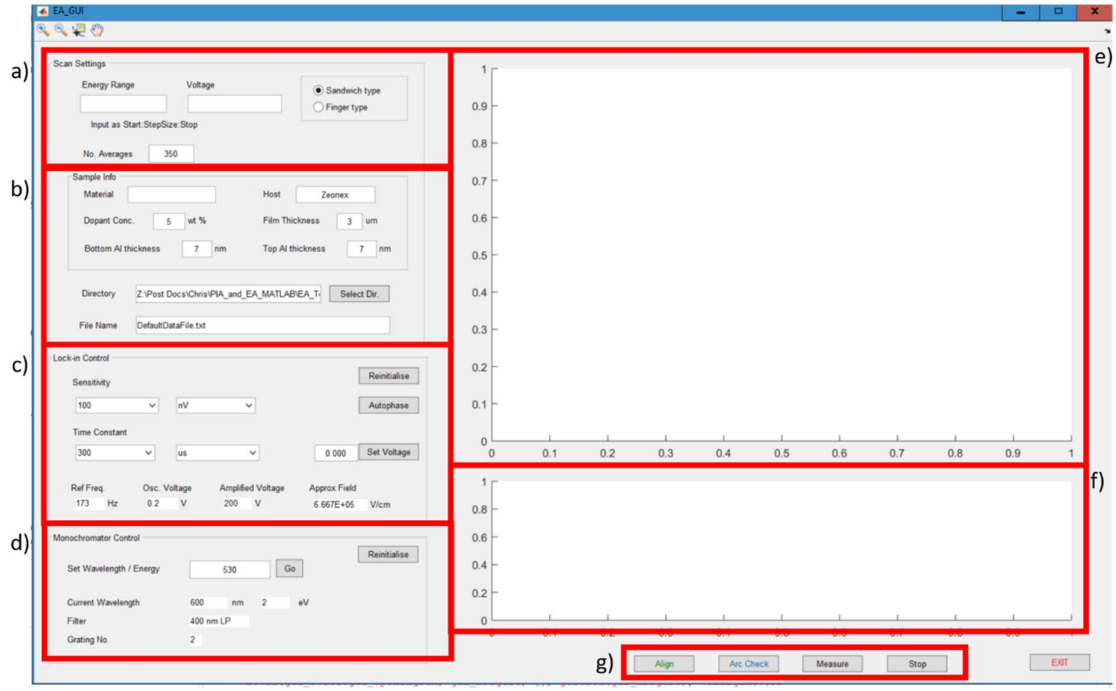

Figure 3.7 – Graphical user interface (GUI) used for the measurements of the Electroabsorption spectra. a) scan settings; b) sample information; c) Lock-in control settings; d) Monochromator control settings; e) Lock-in x and y channels, f) ADC channel and g) system alignment and measurement;‡‡

b) Fitting routine

For the analysis of the EA spectra, a MATLAB routine was developed. This used the absorption spectrum from the independent UV/Vis measurements to reproduce the obtained EA spectra. As the analysis involves fitting a sum of the absorption spectrum and its first and second derivatives to the EA spectrum (Chapter 2), a suitably high resolution and smooth absorption line is necessary to obtain noise-free differentials. Therefore, two methods were considered for this: i. very slow scans when measuring the absorption spectra or ii.

‡‡ GUI created by Dr Christopher Menelaou from the Physics Department at Durham University.

approximating the absorption spectra with several analytic gaussians where the sum of those faithfully reproduce the absorption line due to the inherent noise produced by numerical differentiation. Option ii. was the preferred method for the fitting routine. The absorption spectra are thus firstly fitted with the minimum necessary number of gaussian curves. Though some works have tried to establish a physical meaning to the number of gaussians,[7] here no such meaning was attributed and these were purely used as an analytical approximation to the measured absorption spectrum. Following the Liptay model,[8] the zeroth (absorption), first and second differentials were fitted to the EA spectrum using a least squares fitting model. From the theoretical considerations introduced in Chapter 2, the change in dipole moment, $\Delta\mu$, and change in polarizability, $\Delta\alpha$, with applied field were extrapolated.

c) System reproducibility – Rubrene

Having optimised sample preparation and EA measurements, the last part of setting-up the EA spectroscopy system was the comparison with previously published results. This was done for rubrene following works by Iimori *et al.*[5] Figure 3.8 shows the absorption spectrum (a), gaussian approximation (b) and the measured and fitted EA spectra (c) showing a good fit.

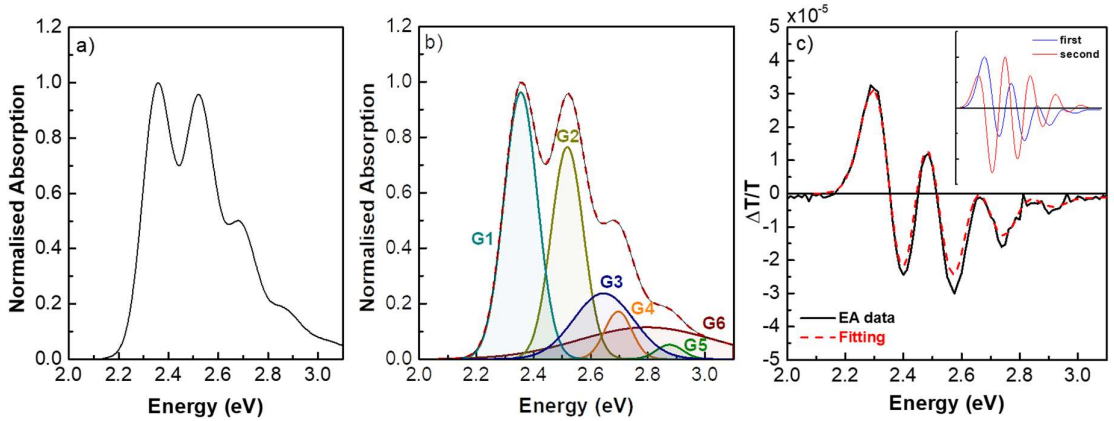

Figure 3.8 – Electroabsorption system reproducibility. Using rubrene with a known absorption (a) and a minimal number of gaussians (b) that allows the reproduction of the absorption line, the Liptay model was used to fit the zeroth, first and second differentials to the EA spectrum (c) resulting in a good fit, also in agreement to the results that are published for rubrene. The electric field used in this calibration study was 457 kV/cm (using applied field and sample thickness).

d) Extinction Coefficient Determination

From earlier discussions of the analysis of EA data, Chapter 2, the absorption coefficient is necessary to compare the EA fitting and the measured absorption. Extinction coefficient for the zeonex films were determined by producing five samples with increasing thickness, obtained with the same spinning routine over the course of multiple scans (1 to 5 layers). Good reproducibility was found between samples from different scans, thus ensuring

the quality of the measurement. Physical thicknesses of the series were then measured with the Dektac profilometer and *OD* measured with both the UV-Vis spectrometer and in a custom single-beam mode using a white light-emitting diode (LED) and fibre spectrometer OceanOptics QEpro. Single beam measurements were made against a substrate containing one larger film to account for the reflection of the films. Then, from the *OD* at a peak (for example 460 nm – CT maximum of POZ-DBPHZ, Chapter 7), the change in absorption was plotted against the change in thickness. The slope gives the extinction coefficient of the material times the concentration which was 5 % throughout. The full absorption spectrum could then be scaled at the same wavelength to give an extinction spectrum.

3.5. Organic Light-Emitting Diodes (OLEDs)

3.5.1. Fabrication

Devices produced in chapters 4, 5 and 6 of this thesis were produced in co-operation with Sungkyunkwan University, South Korea. The samples used in Chapter 7 and the devices in Chapter 8, however, were produced using a vacuum thermal evaporation (VTE) system that allows the evaporation of both organic and inorganic layers. VTE is based on the use of a high current in a crucible containing the material to be evaporated. Through Joule heating, the material starts evaporating and sprays towards a substrate under rotation. With the high vacuum, the mean free path of the molecules gets increased and the result is a highly uniform film. As described in Chapter 2 of the thesis, an OLED is composed of multiple evaporated layers of organic materials, sandwiched between two electrodes. The OLEDs in Chapter 8 of this thesis were built in a Kurt J Lesker Spectrus II deposition system composed of six organic and three inorganic sources, with a vacuum system composed of a roughing pump (SCROLLVAC, Leybol Ltd) and a turbomolecular pump (TMU521P, Pfeiffer Ltd) that evacuate the chamber to 10^{-6} mbar, Figure 3.9. The system is also equipped with a software designed by the Kurt J. Lesker company, controlling the vacuum system and the evaporation (SQS-242 from Sigma Instruments). To control the thickness of the films produced, a quartz crystal microbalance system (QCM) was used, controlled with precision below the nm by the SQS software. The working principle of a QCM sensor uses the change in frequency of a quartz crystal resonator as material deposits onto it. The true film thickness as measured by the QCM is not only material-dependent but also needs to be corrected due to differences in height between the sensor and the substrate by a parameter called the tooling factor (TF). To measure the TF, the real thickness (tk_r) of an evaporated material on a SiO_2 coated substrate (itself with

known thickness) needs to be measured and compared with the thickness measured by the QCM sensor (tk_{QCM}) using an initial guess at the tooling factor (TF'). The properly calibrated TF is then given by $TF = tk_r(\frac{TF'}{tk_{QCM}})$. Measurement of tk_r was obtained with a J Woollam JAW5964 Ellipsometer. The VTE system available in house contains one QCM sensor per two organic sources. This allows for co-evaporation of two materials, as long as they do not share the same sensor.

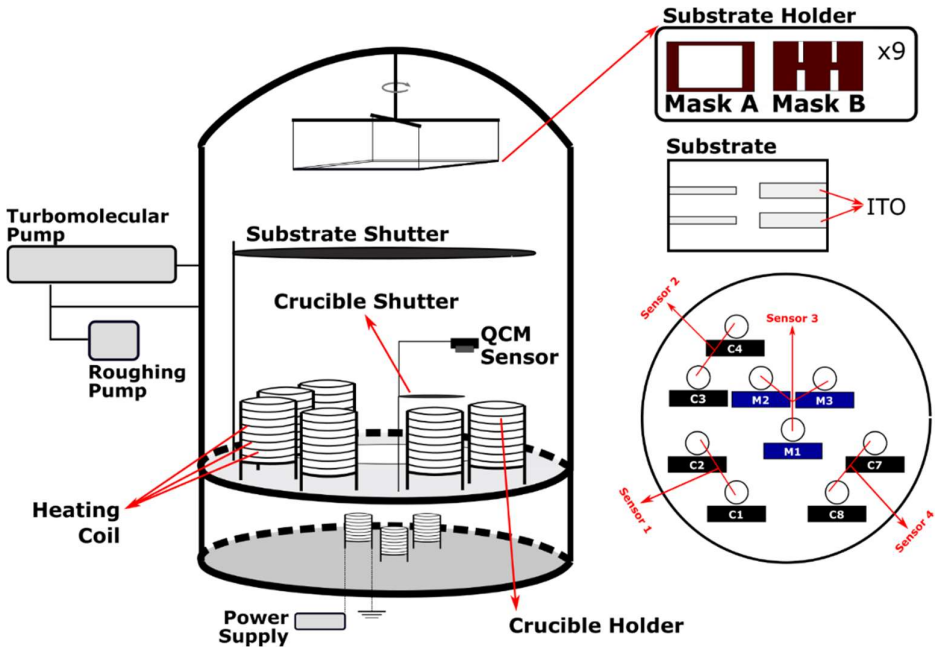

Figure 3.9 – Schematic diagram of the Kurt J. Lesker Spectros II vacuum thermal evaporation system. Six organic and three inorganic sources are available and controlled by quartz crystal microbalance (QCM) sensors as shown on the right. Each crucible also has a small shutter attached while a shutter for the substrate holder is also available. To produce OLEDs, two masks are used: Mask A for the evaporation of all organics and lithium fluoride and Mask B for the evaporation of aluminium in the specific pattern. An example of a substrate and patterned Indium Tin Oxide (ITO) pads is also shown.

The devices produced here were built on pre-patterned indium tin oxide (ITO)-coated glass substrates (Ossila with a sheet resistance of 20 Ω/sq and ITO thickness of 100 nm). All materials were pre-purified using a Creaphys sublimator. Prior to material evaporation, the substrates were cleaned using an ultrasonic bath, first in acetone for 15 min and then in isopropyl-alcohol for another 15 min. After drying with a pressurised air-gun, the substrates were loaded into a Diener Electronics Femto UV Ozone cleaner for six minutes (100 W, 40 kHz) to remove all leftover contaminants, improve the wettability of the substrates and lower the work function of the ITO films by oxygen penetration.[§§] The substrates were then loaded

[§§] This excess oxygen typically desorbs from the treated ITO within a few hours, therefore the organic layers must be deposited promptly on the ITO after treatment.

into the vacuum chamber and all organic layers and lithium fluoride (LiF) evaporated using Mask A (Figure 3.9), and finally 100 nm of Aluminium using Mask B. A maximum of nine substrates were possible to use per round of production, each substrate composed of four different pixels with different sizes, one 4x4, two 4x2 and one 2x2 mm^2. After device production, the final step before measurement is encapsulation of the devices, in a controlled environment (glovebox) to protect them from atmospheric oxygen and moisture during measurement. This is done by dispensing a UV-curable resin on the substrate and sealing with an encapsulation glass. After curing the resin, the substrates were removed from the glovebox for characterization.[9]

3.5.2. Testing

To evaluate the performance characteristics of an OLED and its potential to use in more complex applications, a set of characterizations, both electrical and optical, were used. These give important parameters such as power consumption, efficiency, colour figures of merit, etc. These parameters are obtained through the measurement of the total light output (averaged in all directions) from the device and compared to the total electrical input injected to it. This optical directional averaging is achieved using an integrated sphere (Labsphere) coated with a highly reflective material (Spectralon) allowing collection of light from a source into 4π radians solid angle and sampled behind to give an intensity proportional to the direction of the averaged output. Information on how to set-up and calibrate an integrating sphere can be found in the literature.[10] Table 3.4 shows the parameters used in this thesis to characterise each OLED.

Table 3.4 – Parameters used to characterise the OLEDs of this thesis.

V (voltage)	**I** (Current)	**J** (Current Density)	**L** (Brightness)	**EL** (Electroluminescence)	
V	A	mA/cm^2	Cd/m^2	Arbitrary	
$\boldsymbol{\eta_C}$ (Current efficiency)	$\boldsymbol{\eta_P}$ (power efficiency)	$\boldsymbol{\eta_{ext}}$ (external quantum efficiency)	**CIE(x,y)** (Colour Coordinates)	**CCT**[a] (Correlated Colour Temperature)	**CRI**[a] (Colour Rendering Index)
cd/A	lw/W	%		K	

[a] only calculated for the white OLEDs chapter

e) Electrical and Efficiency

The characterization of a light system is based on a set of standardized measurements that allow possible comparison to other sources measured elsewhere. Firstly, the luminous flux (given in lumen, lm) is defined as the amount of light capable of sensitizing the human eye per unit of time, or the total photometric power emitted in all directions from a light source. It is standardized to the (ideal) eye's nominal minimum sensitivity, defined at a wavelength of 555

nm which is the wavelength to which the human eye is most sensitive. At this wavelength, 1 lumen corresponds to 1/680 W. Secondly, the luminous intensity (measured in candela, cd) takes the colour of the light and its propagation direction into account and is defined as the luminous flux emitted in a specific solid angle. Lastly, the brightness, L, is the luminous intensity per unit of area.[10] For display applications, such as smartphones and TVs, typical brightness levels are between 100-400 cd/m^2 whereas general lighting has these values at around 5000 cd/m^2. The current efficiency, η_C, can be calculated using current density flowing through the device, J, with an emissive area (Ar) necessary to produce a certain L, expressed by the equation 3.1 in cd/A:

$$\eta_C = \frac{LAr}{I} = \frac{L}{J} \tag{3.1}$$

The power efficiency, η_P, is the ratio of the optical flux to the electrical input. Giving the current efficiency at an applied voltage, V_i equation 3.2 expresses η_P in units of lm/W:

$$\eta_P = \eta_C \frac{f_D \pi}{V_i} \tag{3.2}$$

Where f_D(equation 3.3) is the angular distribution of the emitted light in the forward hemisphere considering two angles (θ, φ) and the light intensity in the forward direction:

$$f_D = \frac{1}{\pi I_0} \int_0^{\pi/2} \int_{-\pi}^{+\pi} I(\theta, \varphi) \sin(\theta)\ d\varphi\ d\theta \tag{3.3}$$

The external quantum efficiency, η_{ext} or EQE, is given by the ratio between the number of photons emitted from the surface of the device and the number of injected electrons. It can also be expressed as the product between the internal quantum efficiency, η_{int}, and the outcoupling efficiency, η_{out} – equation 3.4. η_{int} (or IQE) is defined as the product between the charge balance factor, γ, or fraction of injected carriers that form excitons, the fraction of spin-allowed excitons, η_{ST}, and the photoluminescence quantum yield (Φ_{PL} or PLQY) defined as the ratio of emitted to absorbed photons and is a property of the emitting molecule:[10]

$$\eta_{ext} = \eta_{int} . \eta_{out} = (\gamma . \eta_{ST} . \Phi_{PL}) \eta_{out} \tag{3.4}$$

In a well-optimized device with perfectly matched electron and hole currents, γ can reach unity, the PLQY can also be close to one, depending on molecular design. η_{ST} varies according to the triplet harvesting of the emitter in question governed by quantum spin statistics as explained in the theory section of this thesis. The values of η_{out} vary but are usually between 0.2 and 0.3.

The evolution of η_{ext} with brightness is a typical plot used to compare different structures and new emitters in devices. This is known as roll-off and provides information about

device stability, charge balance and potential optimisation strategies. As standards, maximum efficiencies together with efficiencies at 100 cd/m^2 and at 1.000 cd/m^2 are used to quantify roll-off. Its origin can be inherent to the emitting molecule or from the device structure itself. However this, at times, is difficult to probe.[11]

f) Optical

For illumination purposes, the quality of a light source is characterized by empirical figures of merit that enables to qualitatively define their colour quality: the commission internationale d'Eclairage (CIE) chromaticity coordinates (x,y), the correlated colour temperature (CCT) and the colour rendering index (CRI). All of these are calculated from the electroluminescence (EL) spectrum of the source.

Every colour in the visible range maps onto a two coordinate space – the CIE 1931 (x,y), a horseshoe-shaped diagram where each boundary represents a monochromatic light – Figure 3.10a). The CIE 1931 maps each colour according to the human eye's perception of light intensity and colour, composed of three independent retinal compounds, stimuli sensitive to three main groups of wavelengths in the visible spectrum – Red, Green and Blue (RGB) with large overlap. All colours can be expressed as a combination of the three primary colours which thus serves as a comparison for different sources, be they lab produced or industry available.[12]

The CRI is the measure of how well a light source can reproduce environmental colours. It quantifies how different a set of test colours appear when illuminated by different sources – Figure 3.10b). Monochromatic light, such as an orange lamp for example, will only ever properly render orange colours resulting in a poor CRI. Polychromatic light with balanced RGB components is able to reproduce all different colours from different objects and thus has a high CRI. It therefore defines the quality of a light source (from a lighting perspective) quantified on a 0-100 scales, where 100 represents true colour representation.

True 'colour temperature' is the colour of radiation emitted from a perfect blackbody radiator at a particular temperature in Kelvin (K). The light of an incandescent bulb comes from thermal radiation approximating closely to a blackbody, so the colour temperature associated with the temperature of the filament and the emitted spectrum are well defined. Other sources are described in terms of the CCT. The CCT is the temperature of a blackbody radiator that has a colour that closely matches the emission from the non-blackbody radiator. Figure 3.10c) shows a range of sources and corresponding CCT.

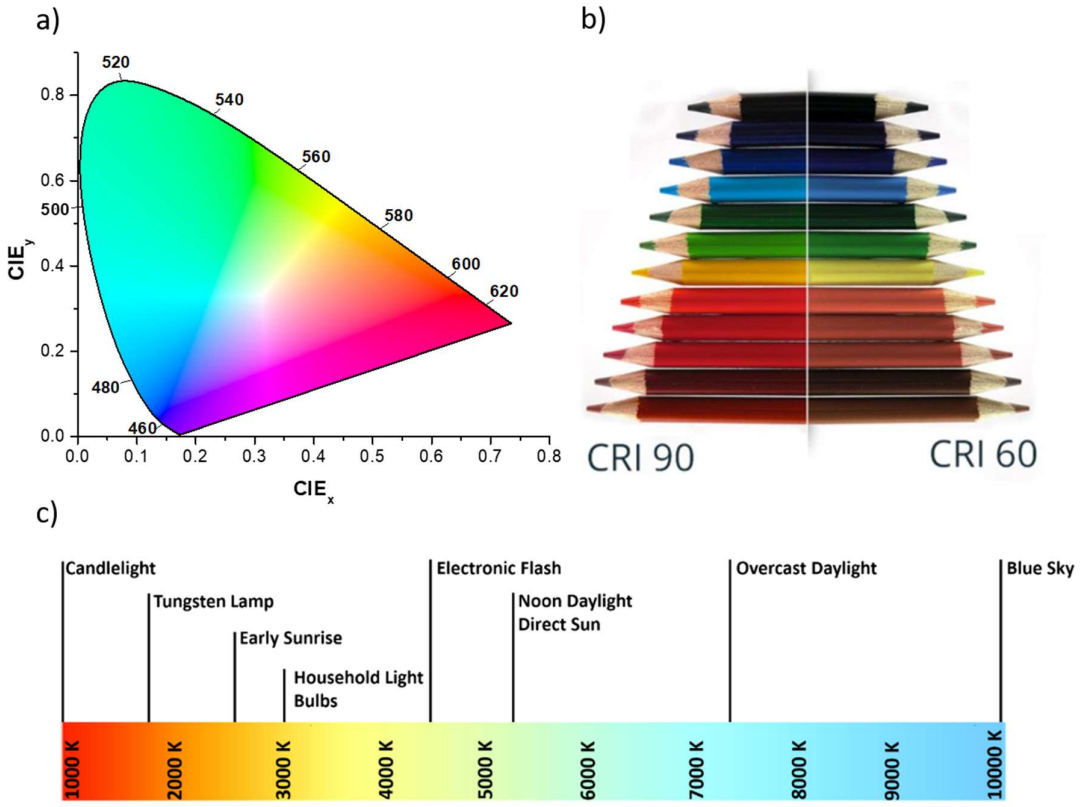

Figure 3.10 – Light figures of merit used to define light sources: a) the commission internationale d'Eclairage (CIE) colour coordinates (x,y), b) example of the colour rendering of an object illuminated by a light with different colour rendering index (CRI) and c) correlated colour temperature (CCT) of different sources.

3.6. Data Analysis

3.6.1. Decay Interpretation

In section 3.3.3, a detailed explanation on the operating mechanism of a time-resolved spectroscopy technique was described. As explained, PL spectra are obtained for each individual TD and IT, and thus it is possible to map out a decay of a specific molecule - Figure 3.11. This provides information on the states involved in the emission of light for a given fluorophore as PF, DF and PH have distinct time scales (early ns, late ns to early ms and late ms-onwards, respectively). These regions are easier to identify when the temperature of the sample is decreased to 80 K, as probability for vibrational relaxation is decreased and therefore, the phosphorescence becomes stronger (Chapter 2). Figure 3.11a) shows the decay of an emitter at 80 K with each individual region identified. From such decay, the fluorescence and PH spectra can be obtained, by measuring their high energy onsets, the energy of the states involved can be determined (Figure 3.11b). For comparison of the excited-state energies, the

wavelength of the onset was directly converted into energy ($E = hv/\lambda$) without any scaling of the intensity. This does not take into account the Jacobian corrected spectral shapes or areas.[13]

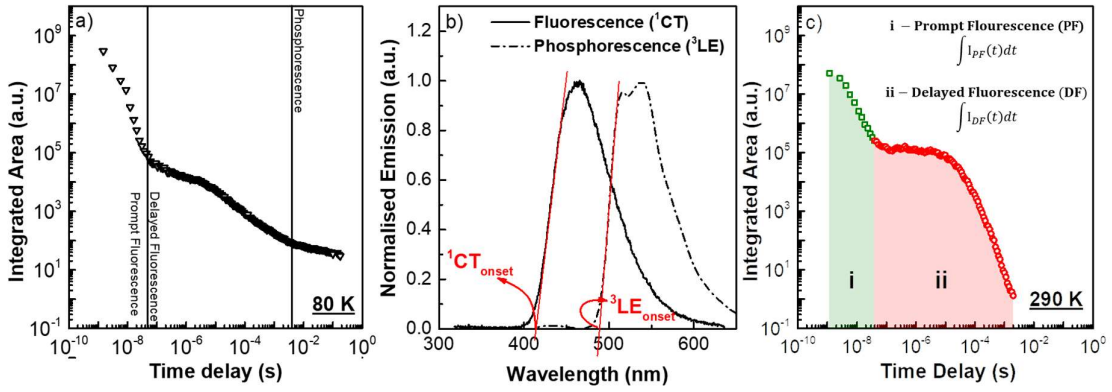

Figure 3.11 – Data analysis of a time-resolved spectroscopy measurement. In a) for a TADF molecule, three regions of emission can be identified, Prompt Fluorescence (DF), Delayed Fluorescence (DF) and Phosphorescence (PH), depending on states (and interaction between states) that are involved in the emission. b) shows how to determine the onset of the excited-states involved in emission in the prompt and the PH regions. In c) at room temperature, the integrated area beneath the prompt and delay regions is the basis for determination of the DF/PF ratio, which was used to determine the intersystem crossing rates.

3.6.2. Time Constants and Decay Rate Calculations

Calculations of the rate constants for intersystem crossing (k_{ISC}) and reverse intersystem crossing (k_{ISC}) processes were performed following the TADF method presented by Dias *et al.*[14] The fluorescence yield of TADF emitters (Φ_F) is the result of the fluorescent decay of the singlet in the prompt, Φ_{PF}, and delayed, Φ_{DF}, intervals as a multistep triplet harvesting as shown in equation 3.5.

$$\Phi_F = \Phi_{PF} + \Phi_{DF} = \sum_{i=0}^{n} \Phi_{PF}(\Phi_{ISC}\Phi_{rISC})^i = \Phi_{PF}\left(\frac{1}{1-\Phi_{ISC}\Phi_{rISC}}\right) \quad (3.5)$$

where Φ_{ISC} and Φ_{rISC} are the intersystem crossing (ISC) and reverse ISC (rISC) yields, respectively. The ratio between Φ_{DF} and Φ_{PF} is experimentally determined to calculate $\Phi_{ISC}\Phi_{rISC}$. This ratio can be determined according to the equation 3.6 considering the integrated area in the DF ($\int I_{DF}(t)dt$) and PF ($\int I_{PF}(t)dt$) regions, Figure 3.11c).

$$\Phi_{DF}/\Phi_{PF} = \frac{\int I_{DF}(t)dt}{\int I_{PF}(t)dt} \quad (3.6)$$

In good TADF systems, where the Φ_{DF}/Φ_{PF} is above 4,[1] the product $\Phi_{ISC}\Phi_{rISC}$ is above 0.8, so Φ_{rISC} can be assumed to be 1. Therefore, equation 3.5 can be simplified to:

$$\Phi_{ISC} = \frac{\Phi_{DF}/\Phi_{PF}}{1+\Phi_{DF}/\Phi_{PF}} \quad (3.7)$$

In terms of decays, using the OriginPro 9.0 software, the PF and DF regions were fit individually using single ($A_1 \neq 0$; $A_2 = A_3 = 0$), double ($A_1, A_2 \neq 0$; $A_3 = 0$), or triple (A_1, A_2, $A_3 \neq 0$) exponential decay terms:

$$y = A_1 \exp\left(\frac{-(\mathrm{t} - t_0)}{\tau_1}\right) + A_2 \exp\left(\frac{-(\mathrm{t} - t_0)}{\tau_2}\right) + A_3 \exp\left(\frac{-(\mathrm{t} - t_0)}{\tau_3}\right) \quad (3.8)$$

where t_0 is the first time considered for the decay, τ_n the lifetime of each species (determined from the decay) and A_n the fit parameters. Thus, from the decay curves, all the rate constants can be calculated with equations 3.9 and 3.10:

$$k_{ISC} = \frac{\Phi_{ISC}}{\tau_{PF}} = \frac{1}{\tau_{PF}} \frac{\Phi_{DF}/\Phi_{PF}}{1 + \Phi_{DF}/\Phi_{PF}} \quad (3.9)$$

$$k_{rISC} = \frac{1}{\tau_{DF}} \frac{1}{(1 - \Phi_{ISC})} = \frac{1}{\tau_{DF}} (1 + \Phi_{DF}/\Phi_{PF}) \quad (3.10)$$

3.7. References Chapter 3

1. Tanaka, H., Shizu, K., Nakanotani, H. & Adachi, C. Dual intramolecular charge-transfer fluorescence derived from a phenothiazine-triphenyltriazine derivative. *J. Phys. Chem. C* **118,** 15985–15994 (2014).

2. Data, P. *et al.* Dibenzo[a,j]phenazine-Cored Donor-Acceptor-Donor Compounds as Green-to-Red/NIR Thermally Activated Delayed Fluorescence Organic Light Emitters. *Angew. Chem., Int. Ed.* **55,** 5739–5744 (2016).

3. Santos, P. L. *et al.* Engineering the singlet–triplet energy splitting in a TADF molecule. *J. Mater. Chem. C* **4,** 3815–3824 (2016).

4. dos Santos, P. L., Ward, J. S., Bryce, M. R. & Monkman, A. P. Using Guest–Host Interactions To Optimize the Efficiency of TADF OLEDs. *J. Phys. Chem. Lett.* **7,** 3341–3346 (2016).

5. Iimori, T., Ito, R., Ohta, N. & Nakano, H. Stark Spectroscopy of Rubrene. I. Electroabsorption Spectroscopy and Molecular Parameters. *J. Phys. Chem. A* **120,** 4307–4313 (2016).

6. Feller, F. & Monkman, A. Optical spectroscopy of oriented films of poly(2,5-pyridinediyl). *Phys. Rev. B* **61,** 13560–13564 (2000).

7. Legaspi, C. M. *et al.* Rigidity and Polarity Effects on the Electronic Properties of Two Deep Blue Delayed Fluorescence Emitters. *J. Phys. Chem. C* **122,** 11961–11972 (2018).

8. Liptay, W. in *Excited States* **1,** 129–229 (Elsevier, 1974).

9. de Sa Pereira, D., Monkman, A. P. & Data, P. Production and Characterization of Vacuum Deposited Organic Light Emitting Diodes. *J. Vis. Exp.* **141,** (2018).

10. de Sa Pereira, D., Data, P. & Monkman, A. P. Methods of Analysis of Organic Light Emitting Diodes. *Disp. Imaging* **2,** 323–337 (2017).

11. Murawski, C., Leo, K. & Gather, M. C. Efficiency Roll-Off in Organic Light-Emitting Diodes. *Adv. Mater.* **25,** 6801–6827 (2013).

12. CIE - Commission Internationale d'Eclairage. Available at: http://div2.cie.co.at/?i_ca_id=985.

13. Mooney, J. & Patanjali, K. Get the Basics Right: Jacobian Conversion of Wavelength and Energy Scales for Quantitative Analysis of Emission Spectra. *J. Phys. Chem. Lett.* **4,** 3316–3318 (2013).

14. Dias, F. B., Penfold, T. J. & Monkman, A. P. Photophysics of thermally activated delayed fluorescence molecules. *Methods Appl. Fluoresc.* **5,** 012001 (2017).

Chapter 4: Dihedral and Torsional Angle Control of Blue TADF Emitters I: Effect of Donor Substitution Position for Efficient rISC

This chapter focuses on a photophysical study to validate a molecular design strategy for controlling the dihedral and torsional angles in a series of donor-acceptor constitutional isomers, each composed of two carbazole donors linked to a 2,4,6-triphenyl-1,3,5-triazine acceptor by a phenyl unit (D_2-A). Using this approach, six thermally-activated delayed fluorescence emitters were synthesised with the donors placed in various positions around the central phenyl core of the acceptor. The effect of the donor position to the donor-acceptor dihedral and triazine torsional angles was consequently investigated. These angles affect both the strength of the charge-transfer state and the conjugation across the entire molecule, effectively tuning the singlet-triplet energy gap of the system. Materials containing two substituted -*ortho* donors or one -*ortho* and an adjacent -*meta* have the smallest energy gaps and the shortest delayed fluorescence lifetimes. On the other hand, emitters with no -*ortho* substitution have larger energy gaps and slow-to-negligible delayed fluorescence. These results give important insights into the molecular requirements for efficient and stable TADF systems.

The work presented in this chapter was published in ACS Applied Materials and Interfaces, Chan Seok Oh, Daniel de Sa Pereira, Si Hyun Han, Hee-Jun Park, Heather F. Higginbotham, Andrew P. Monkman, and Jun Yeob Lee, **Dihedral Angle Control of Blue Thermally Activated Delayed Fluorescent Emitters through Donor Substitution Position for Efficient Reverse Intersystem Crossing,** ACS Appl. Mater. Interfaces 2018, 10, 41, 35420-35429. Chan Seok and Daniel De Sa Pereira contributed equally to this work. Chan Seok designed and synthesized the isomers; Hee Jun Park analysed the single crystal structure of the materials and Si Hyun Han fabricated the devices; Photophysical characterization was carried out by Daniel De Sa Pereira together with Heather F. Higginbotham and Andrew P. Monkman.

4.1 Introduction

From the introductory chapter, it is evident that one key aspect required for high-efficiency organic light-emitting diodes (OLEDs) is the optimisation of molecular design strategies for thermally-activated delayed fluorescence (TADF) emitters. This alone has been a great challenge and is only magnified when combined with similar requirements on device colour, stability and brightness.[1] This becomes particularly evident when blue TADF-based devices are sought, where both the molecular performance and the effects of emitter-host combination are fundamental.[2]

This chapter focuses on one particular design aspect of TADF: how the substitution position of donor (**D)** units placed in different positions of an acceptor (**A**) in a **D_2-A** system affects the photophysical properties of the final TADF emitter obtained. The main objective is to systematically establish correlations between constitutional isomerism (materials with the same molecular formula but different bonding between atoms) and in particular how this impacts photophysical and device performances through dihedral (β) and torsional (α) angles. As a starting point, carbazole and 2,4,6-triphenyl-1,3,5-triazine (TRZ) were chosen as electron-donating, **D**, and electron-accepting, **A**, units respectively (Figure 4.1a), as this is a system that has been widely studied due to its exceptional performance in devices.[3–6] A simple way to understand these two angles in this system is to imagine three planes: one with the TRZ core and the outer phenyl rings, one at the central phenyl ring and finally at the carbazole unit. β describes the angle between the carbazole plane and the central phenyl ring and α the twist angle between the TRZ and the central linker planes. Therefore, for this system, two β angles are described, one for each carbazole unit. Moreover, TRZ in particular is a well-known electron-accepting unit widely exploited in the design of OLED emitters,[7–10] with outstanding acceptor characteristics.[6,11–14] All six possible molecules with the two donor carbazoles positioned around the acceptor in different combinations were studied (Figure 4.1b). The synthetic procedure of these emitters can be found in Seok *et al.*[15] For nomenclature purposes, the isomers are numbered anticlockwise around the ring where the carbazoles could potentially be attached.

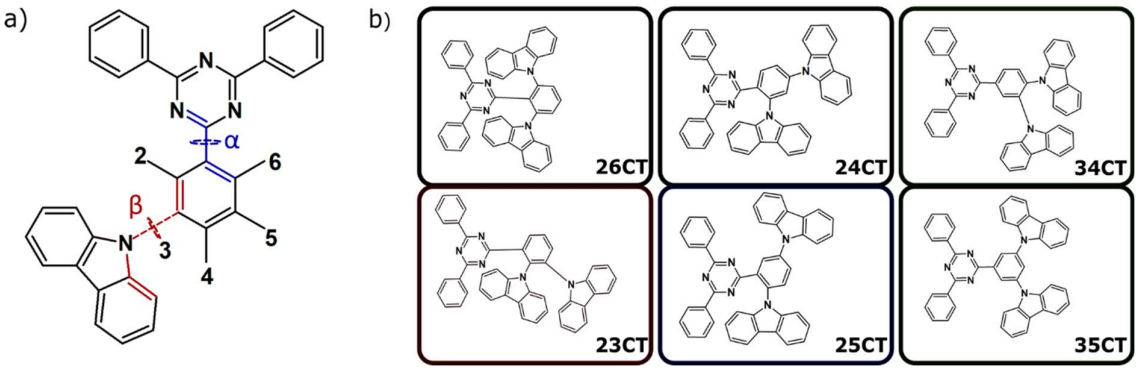

Figure 4.1 – Chapter 4 project diagram. a) Structural subunits used in this study based on a triphenyl-triazine acceptor (A) linked to two carbazole donors (D). The study revolves around the dihedral (β) and the torsional angle (α) effects on the optical properties of the emitters. b) Set of six D_2-A molecules studied. For reference, as an example, 23CT is the emitter with carbazoles in the -2 and -3 substitution positions of the acceptor.

4.2 Molecular Structure Analysis

Prior to emitter characterisation, frontier orbital analysis was carried out on each emitter to estimate their highest occupied molecular orbital (HOMO), lowest unoccupied molecular orbital (LUMO) and geometry. The latter provides both the torsion of the **A** between the triazine core and the phenyl ring where the **D**s are placed and the dihedral angles of each carbazole to the **A**. Figure 4.2 summarises the frontier orbital analysis results calculated using density functional theory (DFT) at B3LYP (Becke, three-parameter, Lee-Yang-Parr) level of theory and 6-31G* basis set using Gaussian G09w. The HOMO/LUMO distribution of each emitter is mostly placed on the carbazole **D**s and **A**, respectively, however the degree of overlap at the phenyl bridge varies between emitters, from **26CT** where they are completely separated to **35CT** showing big overlap.

In **26CT**, the HOMO is evenly distributed across both carbazoles with the LUMO placed on the triazine core and its two outer rings, i.e. they are completely decoupled. **23CT** and **25CT** also show distribution of HOMO on both **D**s however, there is some overlap over the phenyl bridge, mostly due to the LUMO being more dispersed across it. **23CT**, however, has its LUMO more densely distributed on the outer rings of the **A** than **25CT**. **24CT** shows HOMO distribution across the *-ortho* carbazole and LUMO largely distributed across the triazine core and the phenyl linker. The same trend is observed in the LUMO of **34CT** and **35CT**, though with even distribution of HOMO. This means that molecules with a donor in the -4 position display orbitals with more conjugation, while molecules with donors in the -2/-6 or -2/-3 positions display stricter electronic decoupling of the HOMO and LUMO. The torsion angle of the triazine (α) also varies between groups from highly twisted in **26CT** and **23CT**, to

less twisted in **24CT** and **25CT** and almost entirely planar in **34CT** and **35CT**. Therefore, the emitters with the largest HOMO/LUMO delocalization have the highest dihedral and torsional angles as is from other reports on **D-A-D** molecules.[16,17]

(1)(2)CT	26CT	23CT	24CT	25CT	34CT	35CT
β (α) angles	69.04, 69.04 (56.83)	70.68, 70.50 (40.97)	64.75, 52.01 (35.77)	64.96, 52.87 (35.81)	55.35, 62.75 (2.53)	54.48, 53.62 (4.47)
Molecular Structure	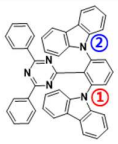	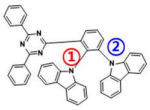	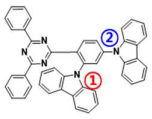	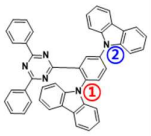	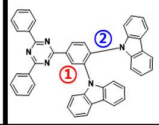	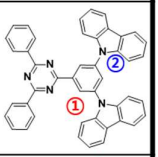
HOMO	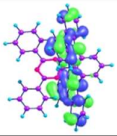	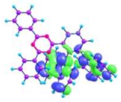	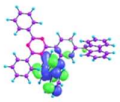	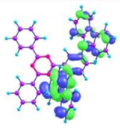	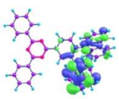	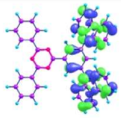
LUMO	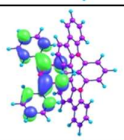	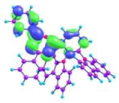	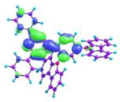	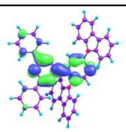	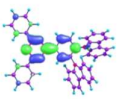	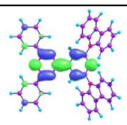

Figure 4.2 – HOMO and LUMO distribution of the six D_2-A isomers used in this study together with dihedral angles of each carbazole (numbered accordingly, 1 and 2 refer to the order of carbazole substitution) and torsional angle of the phenyl ring connected to the donors.*

In this sense, it is possible to group each isomer accordingly:

i) Emitters with closely packed **D**s and **A** (**23CT** and **26CT**) had both β angles at around 70° and the highest α angle of the acceptor;

ii) Emitters with only one **D** unit close to the **A** (**24CT** and **25CT**) have the *-ortho* carbazole twisted to about 65° while the other is slightly more planar (around 53°) and a α angle smaller than group i);

iii) Emitters with no *-ortho* **D**s, i.e. containing **D**s positioned away from the **A** (**34CT** and **35CT**) have both carbazoles with an angle between 54 to 62° and the highest level of planarity in the acceptor.

The geometry of each isomer was confirmed by single crystal X-ray diffraction. The crystal structures of the emitters are presented in Figure 4.3 with the dihedral β angle of each carbazole unit and the torsional angle of the acceptor identified with red arrows. The order of the emitters' β from largest to smallest is 23CT≈26CT>24CT≈25CT>34CT in line with the results from the DFT calculations. In the case of **26CT**, the two carbazole **D**s induce large steric hindrance and distort the acceptor from the phenyl plane. In **23CT**, the **D** at the *-meta* position induces a large β in the neighbouring carbazole, which consecutively induces the distortion of

*DFT calculations performed by Hee Jun Park and Jun Yeob Lee from the Sungkyunkwan University, South Korea.

the phenyl ring of the **A**. In group ii) the emitters show moderate distortion of the triazine because one of the carbazoles has a bigger effect on the geometry than the other. Finally, **34CT** from group iii) does not have any **D** unit next to the triazine core, resulting in its more planar orientation with the phenyl linker allowing the whole molecule to be more conjugated, reducing the energy of the ground state. The X-Ray diffraction of **35CT** was not measured though the geometry can be found in the work by Kim *et al.*,[18] where the planarity of the triazine is discussed.

(1)(2)CT	26CT	23CT	24CT	25CT	34CT
Cz (trz) angles	76.3, 81.0 (53.2)	75.8, 63.9 (67.1)	69.6, 45.6 (34.4)	67.9, 60.6 (33.8)	59.1, 64.7 (5.3)
Structure	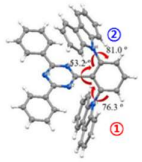	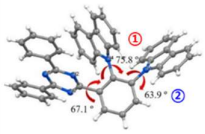	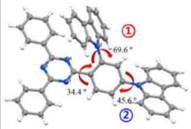	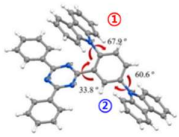	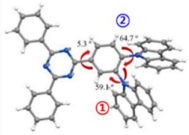

Figure 4.3 – Single crystal structures of D_2-A isomers obtained through X-Ray scattering. 1 and 2 refer to the order of carbazole substitution.†

The dihedral angles of the carbazole **D**s follow the same order as that of the triazine torsional angles, except for **34CT** which is similar to that of **24CT** and **25CT**. Large distortion of the **D** is observed in the **23CT** and **26CT** by means of steric hindrance between the two **D**s and the **A**. In particular, in both emitters, the dihedral angle of the **D** unit adjacent to the **A** was larger possibly due to **D-A** non-covalent interactions. A similar effect was detected in **24CT** and **25CT**. In summary, group i) showed large distortion in the acceptor (α) and moderate-to-large distortion in the donors (β), group ii) exhibited moderate distortion in all three angles, and **34CT** displayed moderate distortion in the donors but little distortion in the acceptor.

4.3 Photophysical Characterisation

In order to understand the effect of both dihedral and torsion angles on the optical properties of each isomer, the solution and solid-state photophysical behaviours were studied. This includes steady-state and time-resolved measurements which were then rationalised in terms of the molecular distortion observed in the DFT and X-Ray analysis.

4.3.1 Solution Properties

†X-Ray analysis performed by Hee Jun Park and Jun Yeob Lee from the Sungkyunkwan University.

Figure 4.4 shows the normalised absorption spectra of all six compounds in methylcyclohexane (MCH) solution. All isomers display three distinct features which can be assigned to each individual subunit. Peaking at approximately 275 nm is the ππ* transition of the TRZ **A** unit while transitions at ~320 and 335 nm are attributed to the ππ* absorption of the carbazole **D** unit. This superposition of the **D** and **A** moieties hints at the electronic decoupling required for charge-transfer (CT).

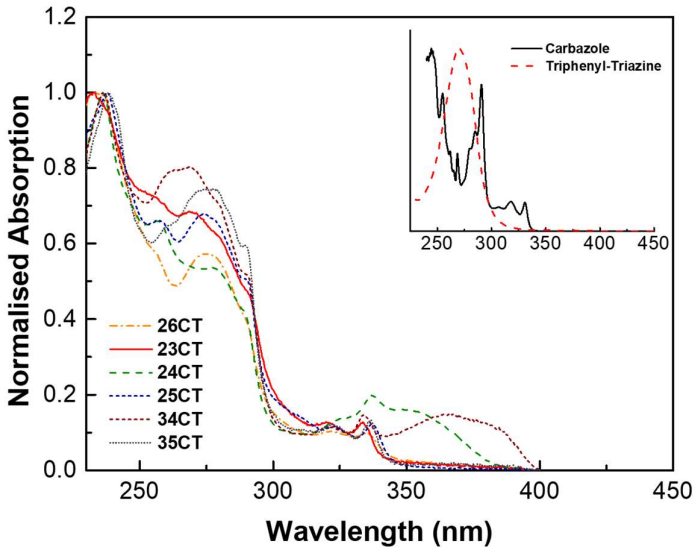

Figure 4.4 – Normalised absorption spectra of the D_2-A isomers in MCH solution. The inset shows the absorption spectra of the carbazole donor and the triphenyl-triazine acceptor in MCH solution.

An additional lower energy feature can be identified at wavelengths higher than 340 nm in all isomers. This band is more intense in **24CT** and **34CT** (where a **D** unit is placed in the *-para* position) observed at 350 and 360 nm, respectively. The origin of this band was investigated by looking at the absorption spectra in toluene and dichloromethane (DCM) – Figure 4.5. **24CT** (Figure 4.5a) shows a mixture of both nπ* and ππ* characters, a result of the overlapping of this new band with the ππ* absorption of pure carbazole (inset of Figure 4.4). **34CT**, shows a clear hypsochromic shift with increasing polarity, displaying negative solvatochromism that corresponds to the nπ* transition (Figure 4.5b). In both cases, and extending this analysis to all six isomers, this nπ* transition is assigned as the appearance of a CT absorption band, typical of some **D-A** systems.[16,17,19]

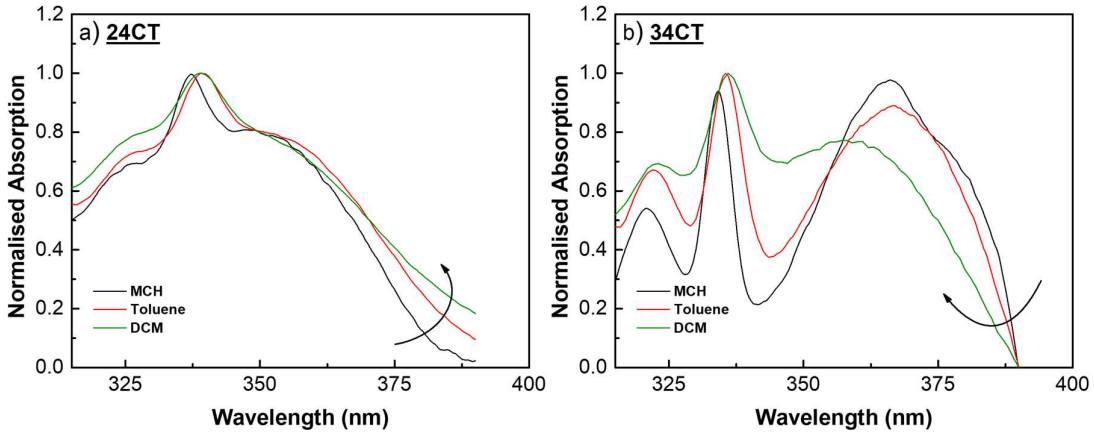

Figure 4.5 – Solvent effects on the low energy absorption bands of 24CT and 34CT in solvents with increasing polarity: MCH, toluene and DCM. a) 24CT shows a mixture of both nπ* and ππ* characters due to the band being overlapped with the carbazole ππ* transition while the hypsochromic shift in b) 34CT is typical of a nπ* transition. The arrows indicate the polarity effect to the absorption band at lowest energy.

Figure 4.6 shows the effect on the emission of each isomer in solvents with increasing polarity: a) MCH (ε = 2.02), b) toluene (ε = 2.4) and c) DCM (ε = 9.0). This gives insights on the dipole moment and the strength of the CT state of each individual molecule. The shift with polarity also shows which isomers hold a higher local character, seen by the resistance of each isomer to have its emission shifted. The emission of pure carbazole and pure triazine are shown in the inset of Figure 4.6a), while emission dependency with excitation wavelength is shown in the inset of Figure 4.6b) for **23CT**, and is a representative of all isomers in that emission does not change when exciting the donor all the way to the CT excitation band (Figure 4.4). In non-polar MCH, the isomers show vibronic-like features, some more structured (**24CT**, **25CT**, **26CT** and **35CT**) than others (**23CT** and **34CT**), related to a higher degree of local excited singlet (^{1}LE) character that mixes with the ^{1}CT. In more polar toluene (Figure 4.6b), all six molecules display an emission spectrum with a gaussian profile and shift to lower energies (further redshifted in DCM) both features typical of CT (Figure 4.6c). This behaviour is typical of strong positive solvatochromic effects.[20] Interestingly, in DCM all isomers have nearly converged to the same energy (around 2.80 ± 0.02 eV), indicating a saturation of the CT stabilisation that is somewhat independent of molecular geometry. Comparing emission between solvents, the largest redshift was for the isomers that do not possess a carbazole in the -*ortho* position, indicating that larger molecular dipole moments correlate with their respective dihedral angles (Figure 4.3). Further inspection of the onset energy of each emitter in the same solvent and in non-polar environments (Figure 4.6a) show that the most redshifted spectra, therefore with the highest CT strength, resides within the -*ortho* isomers. **23CT** shows the

smallest shift and is the most sterically hindered of all four -*ortho* substituted emitters, which takes as evidence of the higher restriction in the rotation of its torsional angles.

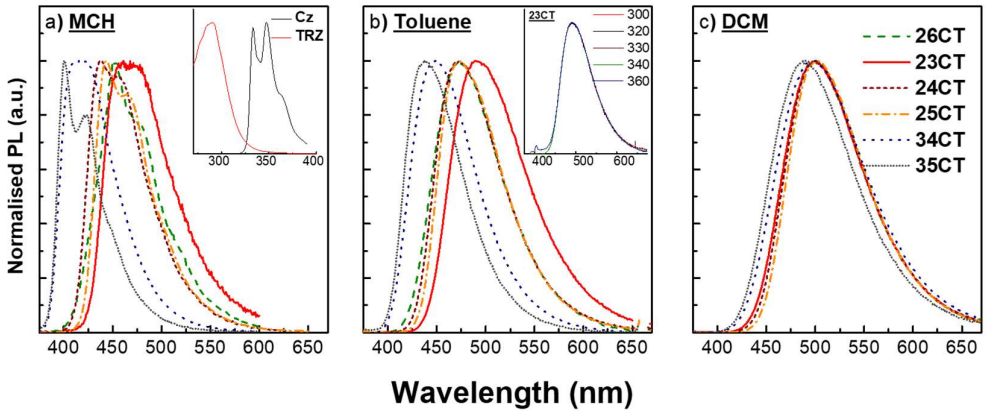

Figure 4.6 – Solvatochromic effect on the emission of the D_2-A family of emitters with increased polarity: a) MCH, b) Toluene and c) DCM. All solutions were excited with a wavelength of 337 nm. The emission of the carbazole and the triazine units are shown in the inset of a) with a 300 and a 260 nm excitation, respectively. The inset of b) shows the emission spectra of 23CT with excitation from 300 to 360 nm, representative of how the emission remains unchanged with the change in excitation.

4.3.2 Solid-state Properties

For solid-state analysis, each isomer was mixed (1 % w:w) into the non-polar solid-state host environment zeonex and the time-dependent emission was recorded at a range of temperatures. Figure 4.7 shows the normalised decays of all isomers at room temperature (RT). As expected from TADF materials with contribution from both singlet and triplet states (the latter in particular recycled to the singlet) the emission profiles have two distinct regions with different time decays: prompt (PF) and delayed (DF) fluorescence.

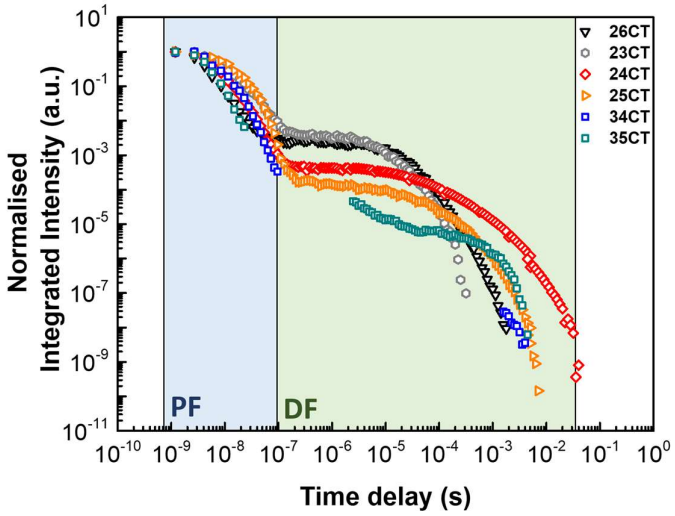

Figure 4.7 – Normalised time-resolved photoluminescence (PL) decay of the D_2-A isomers at room temperature with an excitation of 355 nm and time delays (TD) up to 0.03 s. Two main decay regimes are distinguished in all emitters, corresponding to prompt (PF) and delayed (DF) fluorescence.

The effect of temperature on the DF of each isomer was investigated next. Figure 4.8 shows the decay profiles at temperatures ranging from 80 to 290 K divided into the same three groups as described above. Firstly, the -*ortho* emitters show DF that increases with increasing temperature, a result of an increased rISC rate for the triplet excitons into the singlet excited states. Temperature may also influence the molecular vibrations in the molecule, increasing the rate of decay from non-radiative pathways (Chapter 2). Thus, isomers in the "Slow-to-negligible" DF group (**34CT** and **35CT**) have very long DF components that mostly appear after a TD of 0.1 ms and with a small dependence between temperature and DF rate. However, it will be established later-on that the emission still comes from a ^{1}CT state, seen by the relative spectral overlap with the emission in the PF region. This excludes any other phenomena like room temperature phosphorescence (RTP) for this radiative depopulation of the excited state.

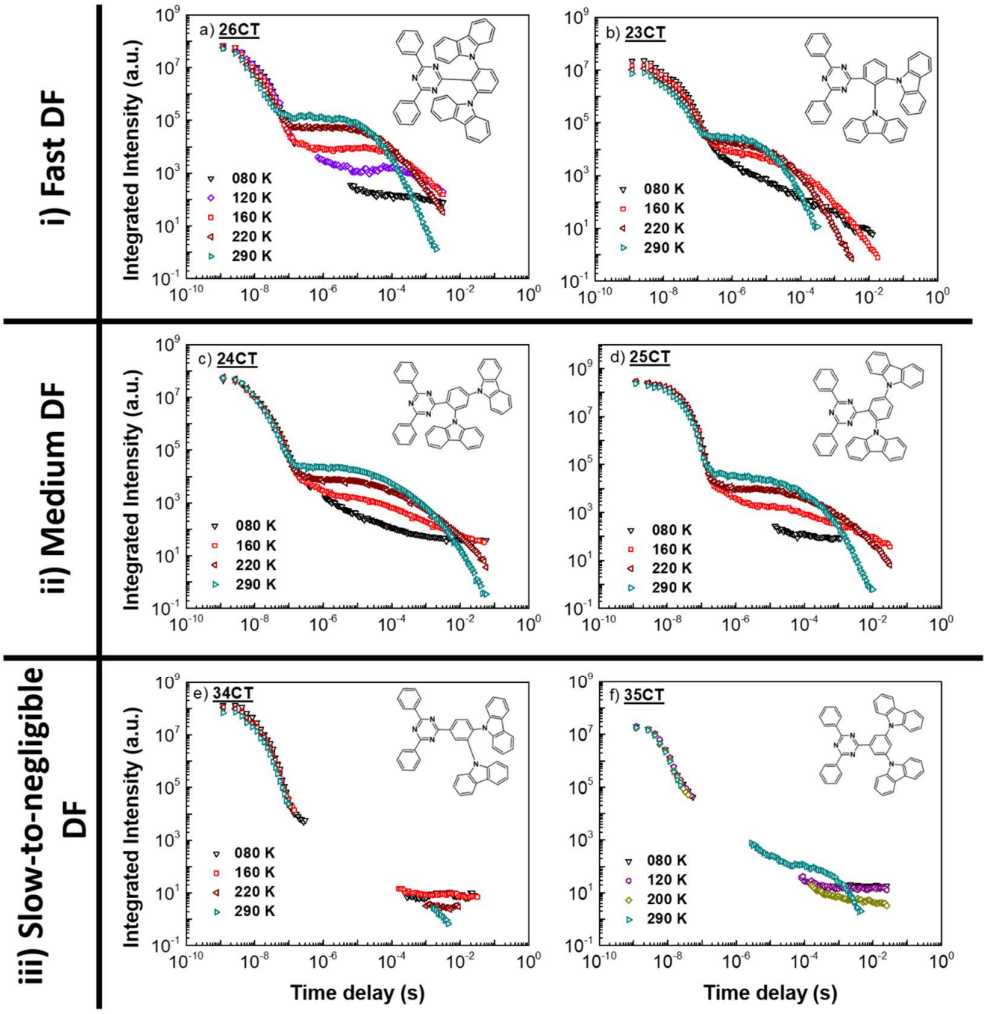

Figure 4.8 - Time-resolved fluorescence decay curves at different temperatures in different time regimes of the six isomers in zeonex: Fast DF - a) 26CT, b) 23CT; Medium DF – c) 24CT, d) 25CT; Slow-to-negligible DF – e) 34CT, f) 35CT. The molecular structure of each isomer is seen in the inset of each graph.

The differences in RT and low temperature decays of all six isomers indicate substantial differences in the energy gaps that in turn are dependent on molecular geometry. Given that each point of the graphs in Figure 4.8 corresponds to an emission spectrum, the evolution of the emission can be analysed, going from ^{1}CT to ^{3}LE, with the latter being the phosphorescence (PH) spectra of each isomer that mediates the DF. The ^{1}CT was determined using steady-state photoluminescence (PL) while emission at 80 K with TD above 25 ms was considered as PH (regardless of shape change to provide consistency for comparison throughout this study). The onset of the PL and PH emissions give the energy levels of ^{1}CT and ^{3}LE, with an error of ± 0.02 eV, Figure 4.9.

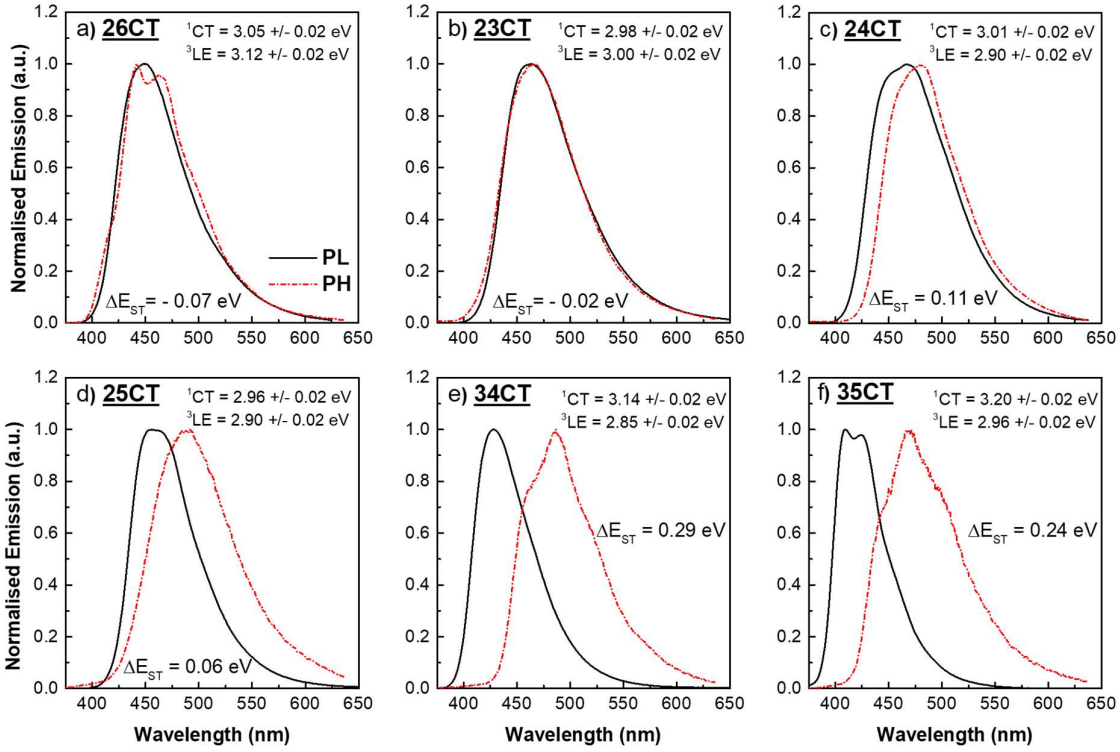

Figure 4.9 – Photoluminescence (PL – black straight line) and phosphorescence (PH – dashed red line) spectra of the six isomers in zeonex: a) 26CT, b) 23CT, c) 24CT, d) 25CT, e) 34CT and f) 35CT. The onset of each spectrum provided the energy of the corresponding state i.e. the PL corresponds to ^{1}CT emission and the PH to the ^{3}LE. The PL was taken at room temperature with an excitation of 337 nm and the PH was obtained with a time delay above 25 ms, at 80 K.‡

The excitation power dependence was measured for all six isomers in the delayed emission region to understand the origin of the DF, Figure 4.10. With slopes close to 1, it is confirmed that the main origin of the DF in compounds **23CT**, **24CT**, **26CT** and **34CT** is

‡ The isomers in this study showed substantial differences in terms of CT relaxation in the prompt region, making the comparison of the ^{1}CT onset difficult. Therefore, the steady state PL was used, and the onset of that emission considered as ^{1}CT, even though some emitters showed contributions from an LE state (the most obvious being **35CT**). The phenomena of the CT relaxation will be studied in more detail in Chapter 5.

thermally-activated (TADF). In context, **25CT** and **35CT**, with higher gradients, presented a small contribution from other mechanisms, particularly triplet-triplet-annihilation (TTA, Chapter 2) which is likely a consequence of the longer-lived triplet states and larger energy gaps, although with a small contribution.

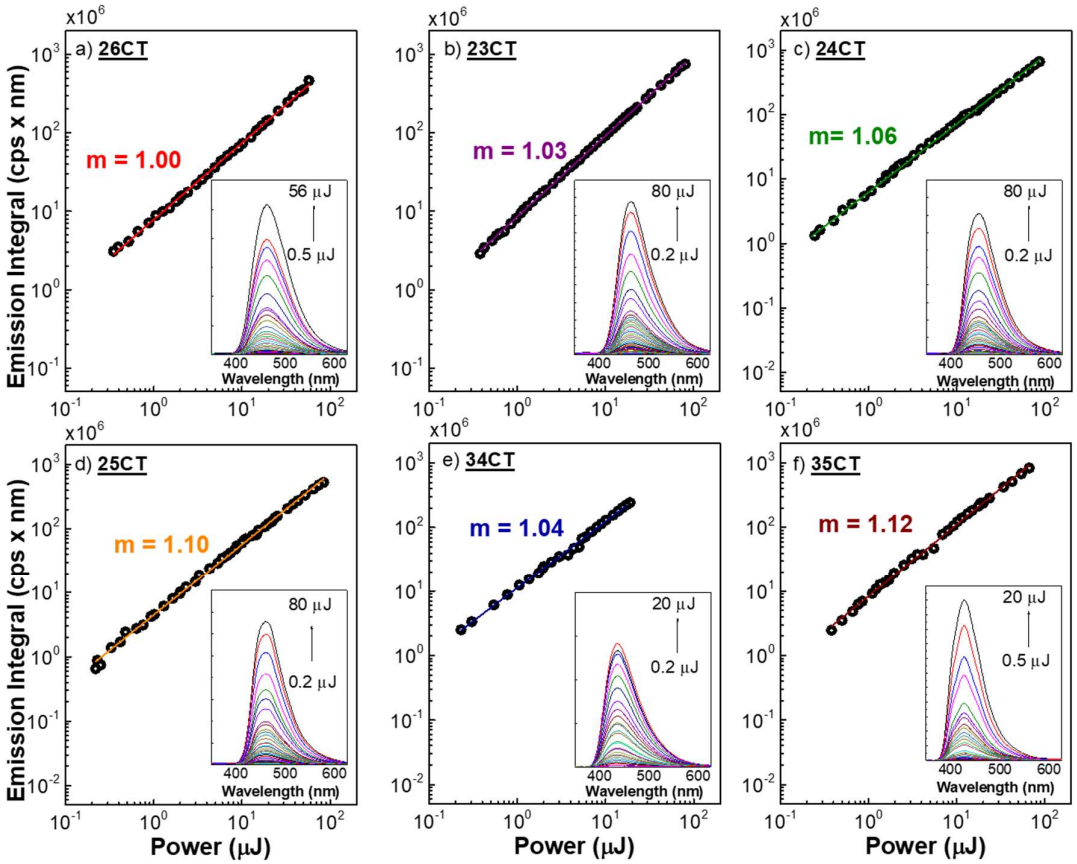

Figure 4.10 – Power dependence of each emitter in zeonex at room temperature and corresponding linear fit (with a slope of m). Emission was collected at each delayed fluorescence region as shown in the inset of each figure: a) 26CT (131 to 19889 ns), b) 23CT (141 to 9062.9 ns), c) 24CT (163 to 83942 ns), d) 25CT (215 to 50449.25 ns), e) 34CT (1.5 to 4.4 ms) and f) 35CT (0.0028 to 4.5 ms).

Figure 4.11 shows both PF and DF decay rates of all -*ortho* isomers at RT, fitted with single and/or double exponentials. In the prompt region, all four isomers were best fitted with single exponential decays. The fitting of the DF region however changed between groups, with the Fast and Medium DF fitting best with mono and bi-exponential curves, respectively. From the exponential expressions, the corresponding time constants can be determined (Chapter 2) and their relative weight to the fitting. Table 4.1 shows the rate constants of each emitter. As expected, for **26CT**, 94% of the emission comes after accessing a triplet state, and the small energy gap results in a high 1.0×10^6 s^{-1} rISC rate. **23CT** and **24CT** have similar rates (~5.5×10^5 s^{-1}) though their TADF behaviours are opposite: **23CT** has a low triplet yield (~80%) but the small ΔE_{ST} allows for a faster up-conversion, while **24CT** has a 92% triplet yield, but its dual

DF contribution from both carbazoles effectively decreases the emission efficiency (increased non-radiative pathways). This contribution becomes more evident in **25CT** as the -5 substitution delays the DF to a point that the non-radiative pathways become dominant, even though the ΔE_{ST} is small.

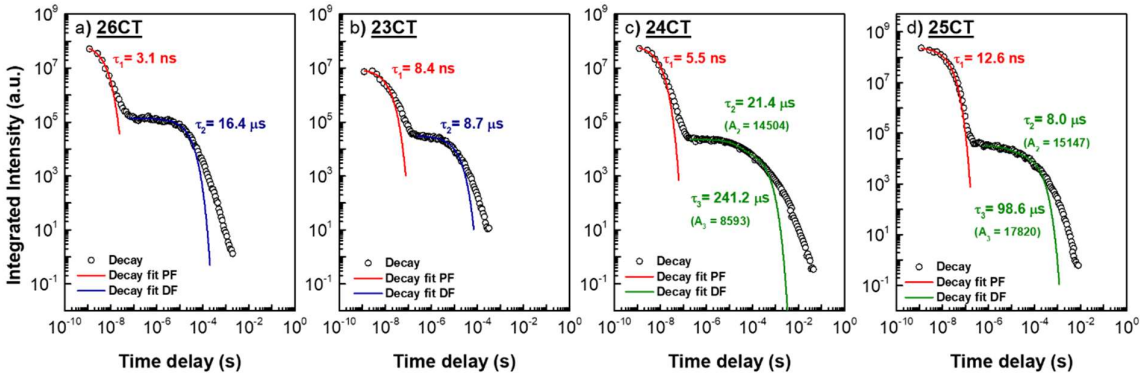

Figure 4.11 – Decay rates of the prompt (τ_1) and delayed ($\tau_{2,3}$) fluorescence of all -ortho based isomers: a) 26CT, b) 23CT, c) 24CT and d) 25CT. All isomers showed a mono-exponential within the prompt decay region (red). In the DF region, 26CT and 23CT emitters showed mono-exponential decays (blue) whereas 24CT and 25CT were fitted with bi-exponential decays (green). The fitting used in the single and bi-exponential decays followed the expressions in Chapter 3.

Table 4.1 - Time constants and decay rates of 26CT and 23CT from the fast DF group and 24CT and 25CT from the medium DF group in the prompt (PF) and delayed (DF) regions. In the case of the 24CT and 25CT, a bi-exponential decay was used and correlated with each carbazole ([1]-2/-6 and [2]-4/-5, respectively). Two exponentials were necessary to correctly fit the decay. More details on the calculation of these constants can be found in Chapter 3.

	τ_{PF} (ns)	$\tau_{DF}{}^1$ (µs)	$\tau_{DF}{}^2$ (µs)	$\frac{\Phi DF}{\Phi PF}$	Φ_{ISC} (%)	k_{ISC} (s^{-1})	$k_{rISC}{}^1$ (s^{-1})	$k_{rISC}{}^2$ (s^{-1})
26CT	3.1 ± 0.1	16.4 ± 0.9	-------	15.2	94	$3.0x10^8$	$1.0x10^6$	---------
23CT	8.4 ± 0.8	8.7 ± 0.3	-------	4.0	80	$9.5x10^7$	$5.8x10^5$	---------
24CT	5.5 ± 0.3	21.4 ± 1.9	241.2 ± 32.8	10.8	92	$1.7x10^8$	$5.5x10^5$	$4.9x10^4$
25CT	12.6 ± 0.5	8.0 ± 1.2	98.6 ± 10.6	0.9[a)]	46	$3.7x10^7$	$2.3x10^5$	$1.9x10^4$

[a] It is generally accepted that if ΦDF/ΦPF is above 4, the product $\Phi_{ISC}.\Phi_{rISC}$ will be above 0.8. 25CT does not fall in this category though the same assumption was applied for comparative purposes.

4.3.3 Relationship Between DF Depopulation Rates and Molecular Structure

Combining results from DFT calculations, steady-state and time-resolved spectroscopies, an understanding on how each carbazole contributes to the photophysical properties of the emitters can be drawn.

Fast DF (where the DF decays between 10^{-7} and 10^{-4} s) was observed with both carbazoles placed closely to the **A** unit resulting in mono-exponential decays for both PF (10^{-9}-10^{-8} s) and DF regions (Figure 4.11). **26CT** and **23CT** showed the smallest energy gaps of

the entire series (Figure 4.9). They also have the lowest wavefunction overlap and conjugation across the molecules induced by the larger distortion between **A** and **D** at the phenyl linker (Figure 4.2). Moreover, the large **D-A** dihedral angles and the twist of the phenyl ring around the triazine core electronically decouples the electron-rich and electron-poor units, meaning that it is expected that the ^{3}LE states are localised on their respective **D** or **A** unit with higher energies if they are more delocalised. Therefore, in **26CT**, a clear PH spectrum with an energy onset of 3.12 ± 0.02 eV is observed that resembles the PH spectrum of pure carbazole (Figure 4.12a). The onset energy measurement results (^{1}CT = 3.05 ± 0.02 eV and ^{3}LE = 3.12 ±0.02 eV) give a ΔE_{ST} of -0.07 ± 0.04 eV. **23CT** on the other hand did not show a clear and resolved PH spectrum even at TD above 25 ms (Figure 4.12b) and low temperatures (80 K), as the triplet emission continuously overlapped with the ^{1}CT state, with only a slight change in the band-shape observed. This observation can be indicative of a small ΔE_{ST} and efficient rISC rate.[21] Further investigations into the inherent mechanism of this particular emitter will be presented in Chapter 5 of this thesis. The onset energies of both the PL (^{1}CT = 2.98 ± 0.02 eV) and PH (^{3}LE = 3.00 ± 0.02 eV) of **23CT** are both lower than in **26CT** which correlates with a lower CT strength and increased conjugation, giving a ΔE_{ST} of around -0.02 ± 0.04 eV, well inside the error of the onset measurement.

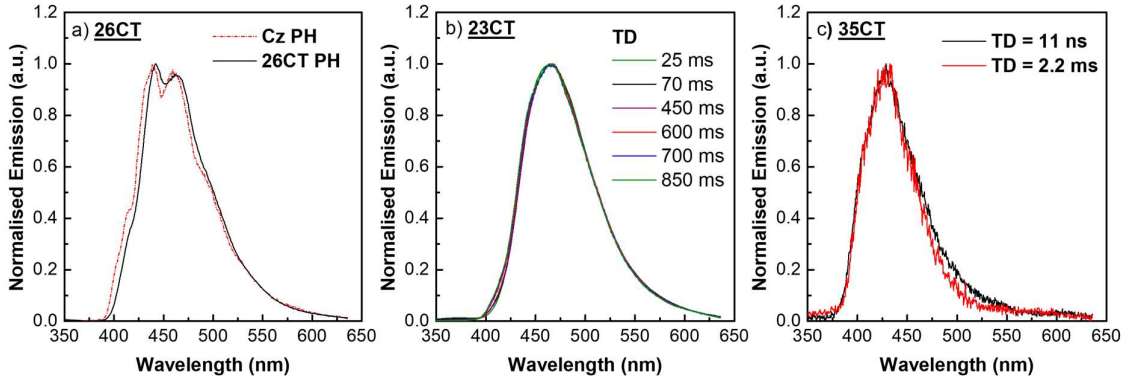

Figure 4.12 – a) Normalised phosphorescence (PH) spectra of carbazole (Cz) and 26CT in zeonex at 80 K showing a good overlap between the two. In this case, it is possible to conclude that the PH of 26CT comes from local excited triplet state (^{3}LE) of one of the Cz donors. b) Normalised PH of 23CT at different time delays (TD) at 80 K. c) Normalised emission of 35CT at TD of 11 ns and 2.2 ms at room temperature (RT). Their overlap and shape are evidence of emission from the same state, this case being ^{1}CT.

Medium DF (with a longer DF lifetime, between 10^{-7} and 10^{-3} s) was seen in isomers with one *-ortho* carbazole and the other in either the *-para* (**24CT** – Figure 4.9c) or *-meta* (**25CT** – Figure 4.9d) positions i.e. not directly adjacent to either the first **D** or the triazine core (Figure 4.1). In terms of molecular geometry, this design not only sees the -2 carbazole more twisted than the -4/-5, but also the triazine acceptor twists less than those of the Fast DF group.

Moreover, two slightly larger ΔE_{ST} (0.11 and 0.07 ± 0.04 eV, for **24CT** and **25CT** respectively) are obtained. Further comparisons can be established between the four -*ortho* isomers by analysis of their DF decays. **24CT** and **25CT** show a longer lived DF with a dual contribution: a fast component with a rate similar to the ones from the Fast DF group, assigned to the more orthogonal carbazole (in position -2) and a slow component assigned to an unrestrained rotation of the -*para* and -*meta2* carbazoles (Figure 4.11). Therefore, in distancing the second **D** from the acceptor and/or the -*ortho* **D**, the planarization induces longer-lived components to the DF. These longer-lived species are the main focus of part two of this series (Chapter 5). Moreover, while the -*ortho* **D** can still induce a strong enough CT, the second carbazole decreases the twisting of the units, resulting in an increased conjugation and redshifted ^{3}LE. It is understandable therefore that the PH does not resemble that of any of its units. From the pre-exponential factor of the bi-exponential fitting, **24CT** has a bigger contribution from the -*ortho* carbazole (~62% vs ~38% of the -*para*) than **25CT** (~46% -*ortho* vs. ~54% -*meta2)*. Therefore, in these conditions, **24CT** is a better emitter than **25CT** though both could potentially be optimised with host tuning, driving the ^{3}LE in resonance with the ^{1}CT (Section 4.4).[17]

Finally, Slow-to-negligible DF (with DF only observable beyond 10^{-3} s) was seen when neither carbazole units were -*ortho* to the triazine, core allowing for the highest level of planarization of all isomers (Figure 4.3), particularly between the phenyl linker and the triazine core. The HOMO-LUMO distribution of both **34CT** and **35CT** (Figure 4.2) shows the largest wavefunction overlap at the linker, which induces the highest conjugation of the six molecules investigated. This conjugation has a two-fold effect; Firstly, conjugation through **D** and **A** moieties serves to redshift the local excitons (^{1}LE and ^{3}LE). Secondly, such increased HOMO/LUMO overlap serves to weaken/destabilise the CT state and increases separation between the mediated ^{1}CT and ^{3}LE states – Figure 4.9e and f. Both these conditions result in larger ΔE_{ST} (0.29 and 0.24 ± 0.04 eV for **34CT** and **35CT**, respectively) than the -*ortho* isomers. The PH of both shows similar shapes to **D-A-D** based on the same units.[22] The decays of the DF regions of **34CT** and **35CT** were left out of this analysis due to poor DF performance at RT (Figure 4.7), however the emission spectra of **35CT** in the PF and DF regimes are shown in Figure 4.12c) to prove that there is no contribution from phenomena like RTP.[23]

4.4 Electroluminescence and OLED performance

Based on the analysis of the photophysical data, **23CT**, **24CT** and **34CT** were selected as being representative of the Fast, Medium and Slow-to-negligible DF groups and were used

for device fabrication and testing. Firstly, cyclic voltammetry (CV) was used to determine the energy levels of each emitter. The HOMO level of the emitters was found to be in the range of -6.11 ~ -6.16 eV and the LUMO level was between -3.47 ~ -3.55 eV as can be estimated from the oxidation and reduction potentials in cyclic voltammetry (CC).[15§] To boost the performance of all emitters in devices, Bis[2-(diphenylphosphino)phenyl] ether oxide (DPEPO) was chosen as host material due to its high polarity and triplet energy (2.98 eV).[24] The electrical and optical characterisation of the optimised devices with structure ITO (120 nm)/ PEDOT:PSS (60 nm)/ TAPC (20 nm)/ mCP (10 nm)/ DPEPO:TADF dopant (25 nm, 30 wt%)/ TSPO1 (5 nm)/ TPBi (20 nm)/ LiF (1.5 nm)/ Al (200 nm) is shown in Figure 4.13. Information on the molecular structures of all other layers can be found in Chapter 3. Figure 4.13a) shows the energy level diagram of the device produced. Figure 4.13b) shows the current density (J) dependence with voltage of the TADF-based devices. The turn-on voltage of all OLEDs was around 3.8 V, a promising result for blue devices[2] and the current density was also similar for all three confirming the differences in the performance of the molecules arise from their molecular geometry. The external quantum efficiency (η_{ext}) vs luminance (L) of Figure 4.13c) shows the maximum η_{ext} of devices based on **23CT**, **24CT** and **34CT** to be 21.8, 22.4, and 13.3 %, respectively, all of them above the theoretical limit of 5 % η_{ext} for purely fluorescent OLEDs hence confirming triplet harvesting. **23CT** has the highest maximum L of the three, close to 20,000 cd/m^2, followed by **24CT** (max. L of 6,000 cd/m^2) and **34CT** (max. L of 4,300 cd/m^2). **24CT** has a slightly higher maximum efficiency (though well inside the error of the measurement) than **23CT**, however its resistance to roll-off is smaller: at 1,000 cd/m^2, **23CT**, **24CT**, and **34CT** efficiencies dropped to 20.8, 14.5, and 5.6 %, respectively. **23CT**, from the Fast DF group maintained 95 % of its maximum η_{ext} at 1,000 cd/m^2, Medium DF emitter **24CT**, approximately 65 % and **34CT** from the Slow-to-negligible DF group exhibited only 42 % of its maximum η_{ext}.

Electroluminescence (EL) spectra in Figure 4.13d) shows that all TADF emitters emit in the blue region of the electromagnetic spectrum, with **34CT** being the deepest blue of the three. The Commission Internationale de l'Eclairage (CIE) colour coordinates of the **23CT**, **24CT**, and **34CT** are (0.17, 0.33), (0.15, 0.26) and (0.15, 0.17), respectively. This appears to follow the trend seen in the steady-state PL studies (Figure 4.6). Table 4.2 lists L, η_{ext}, current

§ Cyclic voltammetry analysis performed by Chan Seok Oh and Jun Yeob Lee from the Sungkyunkwan University.

efficiency, η_L, power efficacy, η_P, and CIE of the devices at different voltages corresponding to set brightness (maximum values, 100 cd/m^2 and 1,000 cd/m^2).

Table 4.2 – Electrical properties of devices based on 23CT, 24CT, and 34CT including external quantum efficiency (η_{ext}), luminance (L), current efficiency (ηL), luminous efficacy (ηP), and Commission Internationale de l'Eclairage (CIE) at the maximum values, at 100 and 1,000 cd/m^2.

	L^1 cd/m^2	$\eta_{ext}{}^1$ %	$\eta_L{}^1$ lm/W	$\eta_P{}^1$ cd/A	$\eta_{ext}{}^2$ %	$\eta_L{}^2$ lm/W	$\eta_P{}^2$ cd/A	$\eta_{ext}{}^3$ %	$\eta_L{}^3$ lm/W	$\eta_P{}^3$ cd/A	CIE^3 (x,y)
23CT	19288	21.8	45.9	30.9	21.8	45.8	35.5	20.8	43.8	27.5	(0.17,0.33)
24CT	5938	22.4	40.0	35.9	20.4	36.0	28.0	14.5	25.0	15.0	(0.15,0.26)
34CT	4367	13.3	21.5	19.3	9.4	13.6	9.5	5.6	7.3	3.5	(0.15,0.17)

[1]Measured maximum values. [2]Measured values at a luminance of 100 cd/m^2. [3]Measured values at a luminance of 1,000 cd/m^2.

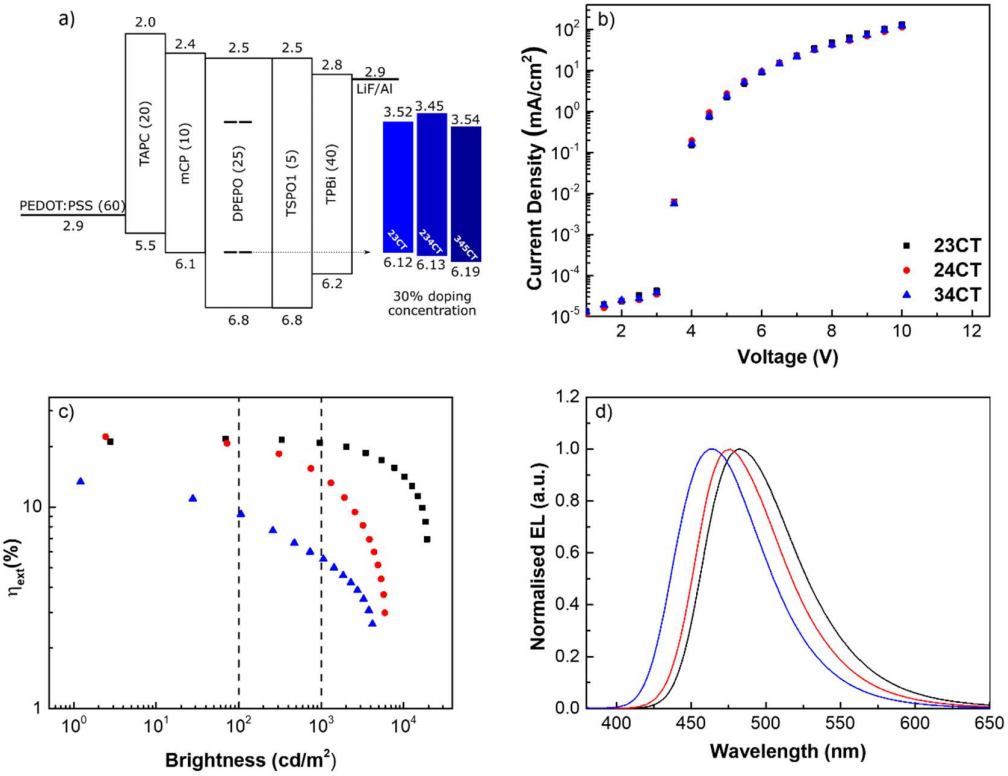

Figure 4.13 – Device performance of 23CT, 24CT and 34CT from the fast, medium and slow DF groups. a) Device structure used for each emitter, b) Current density vs Voltage, c) External quantum efficiency vs Brightness and d) Electroluminescence spectra (at 10 V).**

In this matter, **23CT** was the best performing isomer in devices. This result is in line with both the variation of the ΔE_{ST} and rISC rates meaning that **23CT** (with the smallest gap)

** Devices produced by Si Hyun Han and Jun Yeob Lee from the Sungkyunkwan University, South Korea. Device interpretation by Daniel de Sa Pereira and Andrew P. Monkman.

has the highest conversion rate of triplets while the increase in energy gaps of the other groups leads to reduction of the η_{ext} and electrical instability through quenching mechanisms at high current. By distancing one of the **D**s (**24CT**) from the acceptor, the energy gap is still small enough to provide good maximum efficiency. However, the added slower rISC components give poorer device roll-off. In distancing the second carbazole (**34CT**), both the maximum efficiency and the roll-off get severely affected. One question remains though: if **23CT** showed the smallest ^{1}CT-^{3}LE gap in zeonex and assuming the host tuning effect (where one chooses the host with the appropriate polarity to decrease the singlet-triplet gap) to boost the performance of OLEDs,[17] by placing the emitters in DPEPO, should it not be expected that **34CT** to perform best? To answer this question, the photophysics of **23CT** will be revisited in Chapter 5 of this thesis.

4.5 Conclusion

In conclusion, this chapter tests the consequences of a molecular design strategy based on the control of both the dihedral angles of two carbazole **D**s linked to a triazine-based **A** and the torsional angle of the **A** unit itself. By systematically categorising each of the six isomeric **D_2-A** TADF emitters by their photophysical properties, it was shown that these angles can affect the strength of the CT state, molecular conjugation and therefore singlet-triplet energy gap, their rISC rates and overall TADF performances. By doing so, this molecular design strategy therefore shows that positioning the donor and acceptor units in such a way that the dihedral angle between the subunit and bridging phenyl ring also maximises performance. When this is the case, the phenyl ring acts both as a bridge and a barrier to conjugation, effectively decoupling the donor and acceptor units. Therefore, closely packed **D**s and **A** facilitate the twisting of the entire molecule. **D**s at -2/-6 and -2/-3 positions on the bridged **A** present the smallest energy gaps and the shortest delayed fluorescence lifetimes. In contrast, -3/-4 and -3/-5 substitution showed large energy gaps and slow-to-negligible delayed fluorescence decay rates. Applying the materials into devices gave the same trend in OLEDs with various optoelectronic performances. From the group that showed the fastest DF, a high η_{ext} of 21.8% and suppressed efficiency roll-off was obtained by efficient, single channel rISC. However, the question remains regarding the real polarity effect on the device performance of these emitters when placed in a polar small molecular-weight host such as DPEPO. In the next chapter, a more detailed photophysical investigation of **23CT** will be further discussed in Chapter 5 aiming for deeper understand into this molecular design strategy. Nonetheless, the

approach of distorting the donor moiety from the acceptor can be used as an effective platform to synthesise future TADF emitters aiming for high efficiency and controlled roll-off.

4.6 References Chapter 4

1. dos Santos, P. L., Etherington, M. K. & Monkman, A. P. Chemical and conformational control of the energy gaps involved in the thermally activated delayed fluorescence mechanism. *J. Mater. Chem. C* **6,** 4842–4853 (2018).
2. Bui, T.-T., Goubard, F., Ibrahim-Ouali, M., Gigmes, D. & Dumur, F. Recent advances on organic blue thermally activated delayed fluorescence (TADF) emitters for organic light-emitting diodes (OLEDs). *Beilstein J. Org. Chem.* **14,** 282–308 (2018).
3. Hirata, S. *et al.* Highly efficient blue electroluminescence based on thermally activated delayed fluorescence. *Nat. Mater.* **14,** 330–336 (2015).
4. Cui, L.-S. *et al.* Blue OLEDs: Controlling Synergistic Oxidation Processes for Efficient and Stable Blue Thermally Activated Delayed Fluorescence Devices. *Adv. Mater.* **28,** 7620–7625 (2016).
5. Lee, D. R. *et al.* Design strategy for 25% external quantum efficiency in green and blue thermally activated delayed fluorescent devices. *Adv. Mater.* **27,** 5861–7 (2015).
6. Serevičius, T. *et al.* Enhanced electroluminescence based on thermally activated delayed fluorescence from a carbazole–triazine derivative. *Phys. Chem. Chem. Phys.* **15,** 15850 (2013).
7. Kukhta, N. A. *et al.* Effect of linking topology on the properties of star-shaped derivatives of triazine and fluorene. *Synth. Met.* **195,** 266–275 (2014).
8. Chen, H.-F. *et al.* 1,3,5-Triazine derivatives as new electron transport–type host materials for highly efficient green phosphorescent OLEDs. *J. Mater. Chem.* **19,** 8112–8118 (2009).
9. Jiang, Y. *et al.* Multibranched triarylamine end-capped triazines with aggregation-induced emission and large two-photon absorption cross-sections. *Chem. Commun.* **46,** 4689–4691 (2010).
10. An, Z.-F. *et al.* Conjugated Asymmetric Donor-Substituted 1,3,5-Triazines: New Host Materials for Blue Phosphorescent Organic Light-Emitting Diodes. *Chem. - A Eur. J.* **17,** 10871–10878 (2011).
11. Tanaka, H., Shizu, K., Miyazaki, H. & Adachi, C. Efficient green thermally activated delayed fluorescence (TADF) from a phenoxazine-triphenyltriazine (PXZ-TRZ) derivative. *Chem. Commun.* **48,** 11392–11394 (2012).
12. Matulaitis, T. *et al.* Impact of Donor Substitution Pattern on the TADF Properties in the Carbazolyl-Substituted Triazine Derivatives. *J. Phys. Chem. C* **121,** 23618–23625 (2017).
13. Sun, J. W. *et al.* Thermally Activated Delayed Fluorescence from Azasiline Based Intramolecular Charge-Transfer Emitter (DTPDDA) and a Highly Efficient Blue Light Emitting Diode. *Chem. Mater.* **27,** 6675–6681 (2015).
14. Lin, T.-A. *et al.* Sky-Blue Organic Light Emitting Diode with 37% External Quantum Efficiency Using Thermally Activated Delayed Fluorescence from Spiroacridine-Triazine Hybrid. *Adv. Mater.* **28,** 6976–83 (2016).
15. Oh, C. S. *et al.* Dihedral Angle Control of Blue Thermally Activated Delayed Fluorescent Emitters through Donor Substitution Position for Efficient Reverse Intersystem Crossing. *ACS*

Appl. Mater. Interfaces **10,** 35420–35429 (2018).

16. Dias, F. B. *et al.* The role of local triplet excited states and D-A relative orientation in thermally activated delayed fluorescence: Photophysics and devices. *Adv. Sci.* **3,** 1600080 (2016).

17. dos Santos, P. L., Ward, J. S., Bryce, M. R. & Monkman, A. P. Using Guest–Host Interactions To Optimize the Efficiency of TADF OLEDs. *J. Phys. Chem. Lett.* **7,** 3341–3346 (2016).

18. Kim, M., Jeon, S. K., Hwang, S.-H. & Lee, J. Y. Stable Blue Thermally Activated Delayed Fluorescent Organic Light-Emitting Diodes with Three Times Longer Lifetime than Phosphorescent Organic Light-Emitting Diodes. *Adv. Mater.* **27,** 2515–2520 (2015).

19. Higginbotham, H. F., Yi, C. L., Monkman, A. P. & Wong, K. T. Effects of Ortho-Phenyl Substitution on the rISC Rate of D-A Type TADF Molecules. *J. Phys. Chem. C* **122,** 7627–7634 (2018).

20. Santos, P. L. *et al.* Engineering the singlet–triplet energy splitting in a TADF molecule. *J. Mater. Chem. C* **4,** 3815–3824 (2016).

21. dos Santos, P. L. *et al.* Triazatruxene: A Rigid Central Donor Unit for a D-A 3 Thermally Activated Delayed Fluorescence Material Exhibiting Sub-Microsecond Reverse Intersystem Crossing and Unity Quantum Yield via Multiple Singlet-Triplet State Pairs. *Adv. Sci.* **5,** 1700989 (2018).

22. Kukhta, N. A. *et al.* Deep-Blue High-Efficiency TTA OLED Using Para - and Meta -Conjugated Cyanotriphenylbenzene and Carbazole Derivatives as Emitter and Host. *J. Phys. Chem. Lett.* **8,** 6199–6205 (2017).

23. Huang, R. *et al.* The contributions of molecular vibrations and higher triplet levels to the intersystem crossing mechanism in metal-free organic emitters. *J. Mater. Chem. C* **5,** 6269–6280 (2017).

24. Zhang, J., Ding, D., Wei, Y. & Xu, H. Extremely condensing triplet states of DPEPO-type hosts through constitutional isomerization for high-efficiency deep-blue thermally activated delayed fluorescence diodes. *Chem. Sci.* **7,** 2870–2882 (2016).

Chapter 5: Dihedral and Torsional Angle Control of Blue TADF Emitters II: Donor Interactions and Host Crowding Effects on Multiple Vibronically Coupled rISC Channels

This chapter focuses on the extended photophysical characterisation of a donor-acceptor (D-A) family of thermally-activated delayed fluorescent (TADF) emitters using carbazole and 2,4,6-triphenyl-1,3,5-triazine as D and A respectively. By increasing the number of closely packed interacting Ds around the linking phenyl ring of the A, the changes in dihedral angles of the Ds and the twist within the A are found to affect the HOMO/LUMO separation and the resulting energy gaps. Moreover, multiple unique D-A dihedral angles causes different donor conjugation and local triplet states with different energies in each D leading to the introduction of the concept of a charge-transfer gaussian density of states (CTGDoS). The multiple coupling between these triplet states and the CTGDoS leads to the appearance of multiple rISC channels with different rISC rates, a phenomenon that is also host-dependant due to different packing induced twisting of the dihedral angles. In devices, the fastest rISC channels lead to external quantum efficiencies above 20 %. However, the slower rISC rates act as parasitic traps severely affecting device roll-off. This explains why emitters in the same family can have excellent peak external quantum efficiencies but at the same time very poor roll-off. The chapter also introduces the concept of competing decay channels independently affecting aspects of molecular functionality.

At the time of submission, the work presented in this chapter was under review: Daniel de Sa Pereira, Chan Seok Oh, Paloma L. dos Santos, Ha Lim Lee, Jun Yeob Lee and Andrew P. Monkman, **Multiple Vibronically Coupled rISC Channels Independently Dictate Maximum Device Efficiency and Roll-off in Multi-donor TADF OLED Emitters,** Under review. Chan Seok Oh designed and synthesized 2345CT. Ha Lim Lee performed the chemical analysis of the materials. Daniel de Sa Pereira performed the photophysical characterisation of 23CT, 234CT, 345CT and 2345CT. Data interpretation was performed by Daniel de Sa Pereira together with Paloma dos Santos and Andrew P. Monkman.

5.1 Introduction

Various strategies combining different donor (**D)** and acceptor (**A)** units in different proportions (**D-A**, **D-A-D**, **D-A$_3$**, **D$_3$-A**) and their effect on the highest occupied/lowest unoccupied molecular orbital (HOMO/LUMO) distributions, energy levels, thermally-activated delayed fluorescence (TADF) efficiency and device performances have been thoroughly studied.[1–4] In Chapter 4, an effective design route to efficient TADF by the control of dihedral (β) and torsional (α) angle of the **D**s regarding the **A** was demonstrated in a family of **D$_2$-A** emitters. By placing two carbazole (Cz) donors in different positions of the phenyl ring of a 2,4,6-triphenyl-1,3,5-triazine (TRZ) acceptor, changes in the charge-transfer (CT) character and conjugation of a set of different **D$_2$-A** emitters were detected, effectively controlling the resulting energy gaps and rISC rates. The same study with three Cz **D** units showed a similar trend, the main conclusion being that closely packed **D**s and **A** also tend to have restricted dihedral angles and better TADF performances.[5] The dihedral angles of each emitter are therefore affected by the substitution position in a two-fold manner: i) the acceptor becomes distorted from the phenyl ring by close proximity to the Cz donors, particularly with an -*ortho* substitution and ii) closely packed Czs tend to have more twisted dihedral angles. Device results from these two studies showed high η_{ext} for most materials, however the resistance to roll-off varied greatly in some instances decaying very rapidly. Interestingly, the emitter with **D**s in the -*ortho/meta* position (**23CT**) showed the best DF performance, both in the low-polarity polymeric matrix zeonex and in the high-polarity small-molecular-weight host, Bis[2-(diphenylphosphino)phenyl] ether oxide (DPEPO), seemingly contradicting the host-tuning effect that has been described extensively in the literature.[1,3,6,7]

In this chapter, a more in-depth photophysical characterization of the same basic **D-A** system is presented. This is done by establishing comparisons between the emitters that showed the best TADF performances, with increasing number of Cz donor units and with one Cz at the -2 position (-*ortho*). These comparisons are extended by adding a novel **D$_4$-A** emitter with four Czs placed in neighbouring positions around the **A** (Figure 5.1), and also by comparing with a three Cz system without -*ortho* substitution. The main objective of this work is to further understand how the number and position of Cz substitutions affects the TADF mechanism of emitters that already have exceptionally good photophysics. The proximity effect of the **Ds** to the **A** is also investigated. By detecting the small differences in DF, it is possible to identify

the “best of the best” and improve the design rules that will translate into better devices, not only in terms of efficiency but also resistance to roll-off.

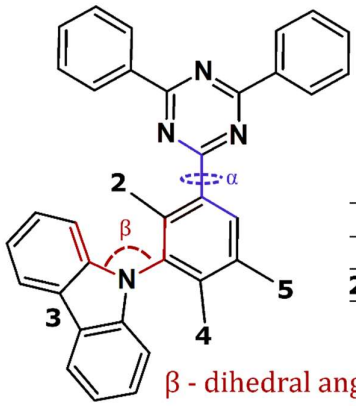

	2	4	5
23CT	Cz	H	H
234CT	Cz	Cz	H
2345CT	Cz	Cz	Cz
345CT	H	Cz	Cz

Figure 5.1 – Chapter 5 project diagram. Using a molecular design based on a 2,4,6-triphenyl-1,3,5-triazine (TRZ) acceptor (A) and a carbazole (Cz) donor (D), the effect of increasing the number of Ds on the photophysical properties of high-performing emitters is studied. The number of Ds will affect the dihedral angle (β) between the D and the phenyl ring of the A and the torsional angle (α) between that same phenyl ring and the TRZ core. Therefore, four emitters are studied: three of them with -*ortho* substituted Cz and with increasing number (n) of Ds (D_n-A, n=2,3 or 4) and the last with three non-*ortho*, closely packed Ds, 345CT.

5.2 Molecular Structure Analysis

The previous chapter showed that placing 2 **Ds** around one of the phenyl rings of the triazine affects the β angle of the **D**s. Similar phenomena is expected from a 3-carbazole system.[5] When these **D**s are adjacent to each other and the **A**, β tends to increase towards orthogonality with the **A** unit, lowering conjugation and increasing the CT character. That in turn results in decreased energy gaps and higher rISC rates (Chapter 4). One might wonder if, by adding more closely packed **D**s, will this behaviour be enhanced, i.e. even smaller energy gaps and faster rISC rates obtained? To answer this question and understand further this behaviour, a new **D_4-A** emitter was synthesized having four Czs placed near each other. The result is an emitter with **D**s in the -2/-3/-4/-5 substitution positions around one of the phenyl rings of the TRZ **A**, a molecule referred to as **2345CT** – Figure 5.1. To understand how the number of Czs affects the photophysics of this **D-A** system, **2345CT** is compared with three other emitters: **23CT**, **234CT** and **345CT**. The latter in particular was chosen[8] because the Czs are placed in close proximity with each other but away from the triazine and thus the effects of the TRZ folding (α) can also be understood.

Density functional theory (DFT) calculations, based on a B3LYP (Becke, three-parameter, Lee-Yang-Parr) level of theory and 6-31G* bases set using Gaussian G09w was carried out to obtain the geometry and HOMO/LUMO distributions of **2345CT** in comparison

to the other three molecules – Figure 5.2. Overall, the HOMO/LUMO distributions of **23CT**, **234CT** and **2345CT** are similar, with the LUMO being localized within the TRZ acceptor. The HOMO is highly localized within the -2/-3 carbazoles in all three however, increasing the number of **Ds** results in increased orbital distribution into the -*para* substituent. Interestingly, in **2345CT**, no distribution of HOMO is seen in the carbazole at the -5 position. **234CT** and **2345CT** have therefore almost identical orbital distributions. By contrast, **345CT** shows even HOMO distribution across all **Ds** and LUMO mostly localised at the triazine core and phenyl linker.

Name	**23CT**	**234CT**	**2345CT**	**345CT**
Cz angle (β)	2) 70.68; 3) 70.50;	2) 70.93; 3) 66.00; 4) 67.45;	2) 72.05; 3) 65.97; 4) 66.88; 5) 42.27;	3) 66.02; 4) 61.11; 5) 66.02;
TRZ angle (α)	40.97	41.04	42.27	3.91
HOMO	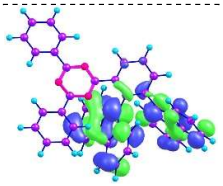	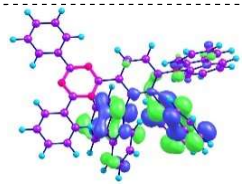	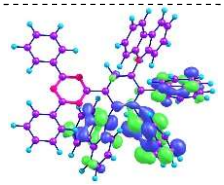	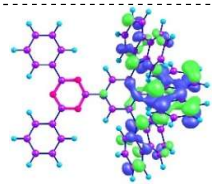
LUMO	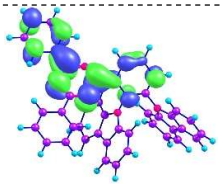	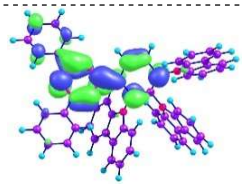	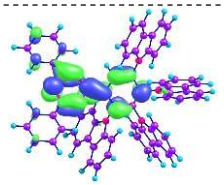	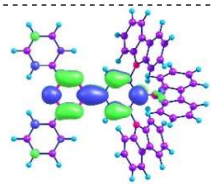

Figure 5.2 – Density functional theory (DFT) calculations of the highest occupied/lowest unoccupied molecular orbitals (HOMO/LUMO) distributions of 23CT, 234CT, 2345CT and 345CT. From the DFT, the dihedral angles (β) of the carbazole donors to the phenyl ring of the triazine acceptor and the torsion (α) within the acceptor are also determined. DFT calculated at B3LYP level of theory and 6-31G* basis set using Gaussian G09w.[*]

In terms of the DFT-calculated angles, **23CT** has both carbazoles equivalent with β angles of ca. 70.5°. In **234CT**, the -2 position remains at ca 70.9° whereas -3 and -4 position carbazole relax to a new dihedral of around 66°-67°, i.e. non-equivalently to the -*ortho* **D** β. **2345CT** carries this trend, except the fourth carbazole stabilizes at 42°, much more planar

[*] DFT calculations performed by Chan Seok Oh and Jun Yeob Lee from Sungkyunkwan University, South Korea.

resulting in three non-equivalent dihedral angles. This seemingly increases the HOMO distribution on the -*para* carbazole, creating increased conjugation throughout the molecule. In **345CT** the outer **D**s (positions -3 and -5) stabilize at 66º whereas the central one is more planar at 61º. From the DFT calculations, α is similar in all emitters containing -*ortho* donor substituents (between 41 and 42º) but much more planar in **345CT** (around 4º).† Closely packed **Ds** placed in proximity to the **A** forces it to distort, pushing the LUMO away from the benzene ring. These small changes and non-equivalent β angles are very important as electron exchange energy and therefore rISC rates depend exponentially on the magnitudes of the energy gaps between the coupled singlet and triplet states.[4]

5.3 Photophysical characterisation

5.3.1 Solution Properties

Figure 5.3a) shows the normalised absorption of the four molecules in a dichloromethane (DCM) solution. By comparison with the absorption of individual **D** and **A** units (inset of Figure 5.3a), the peak at approximately 275 nm is assigned as the ππ* transition of the TRZ **A** unit. The transitions between ~300 and 340 nm are attributed to the ππ* absorption of the carbazole **D** unit. At low energies, a third band appears peaking at 375 nm assigned as "direct" CT absorption with a nπ* (or mixed ππ*/nπ*)[1,6,9] character, in line with Chapter 4.

CT excited states are characterized by large dipole moments, making them very sensitive to the polarity of their environment.[10] As shown in the previous chapter, a typical study to identify and evaluate the strength of CT states is to measure the solvatochromic shift of their emission spectra. Figure 5.3b) shows the emission spectra of **23CT**, **234CT**, **2345CT** and **345CT** in solvents with increasing polarity. In MCH, the emitters show vibronic-like features, which is associated with a higher local excited singlet (^{1}LE) character or the mixing of both ^{1}LE and ^{1}CT. In toluene and DCM, the emission spectra become gaussian-like and start to redshift. All the molecules containing **D**s in the -*ortho* position showed similar shifts from MCH to toluene but **234CT** and **2345CT** have a bigger redshift in DCM. **345CT**, with no -*ortho* substitution, was the emitter with the largest bathochromic shift and therefore the least sterically hindered of the group. In line with the previous chapter, all -*ortho* emitters showed

† On a side note, these angles are also similar to the ones for 34CT and 35CT of the previous chapter.

strong CT character, **23CT** remains the strongest, with smallest solvatochromic redshift as the **D-A** dihedrals are already the largest.

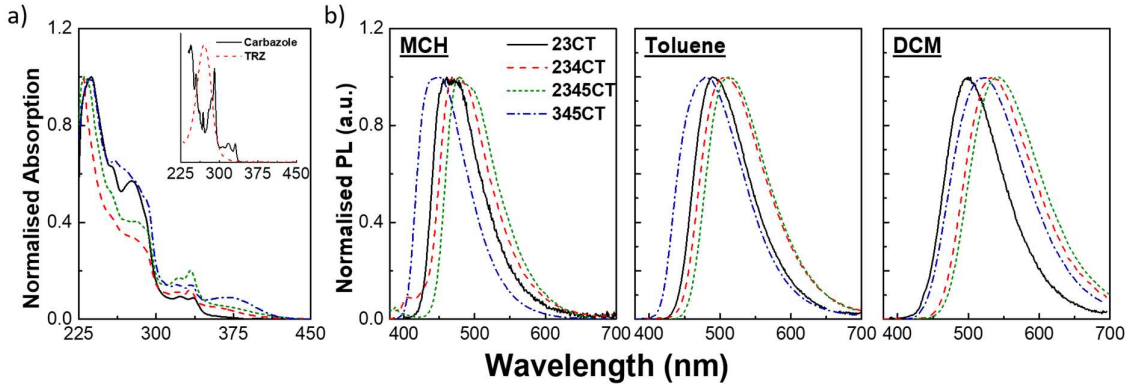

Figure 5.3 – a) Normalised absorption of 23CT, 234CT, 2345CT and 345CT in a dichloromethane (DCM) solution. Inset shows the absorption of the carbazole and TRZ donor and acceptor, respectively. b) Solvatochromic effect on the emission of 23CT, 234CT, 2345CT and 345CT in solvents with increased polarity: MCH, Toluene and DCM. All solutions were excited with 355 nm.

5.3.2 Solid-state Properties

Figure 5.4 shows the time-dependent emission profiles of a) **23CT**, b) **234CT**, c) **2345CT** and d) **345CT** in the non-polar zeonex matrix where emission from early (time delay – TD of 1.6 ns) to late times (TD up to 0.1 s), collected from 80 K to 320 K. In Figure 5.4e) the normalised room temperature (RT) decays of all four are displayed together allowing better comparison of each in terms of prompt (PF) and delayed (DF) fluorescence intensities.

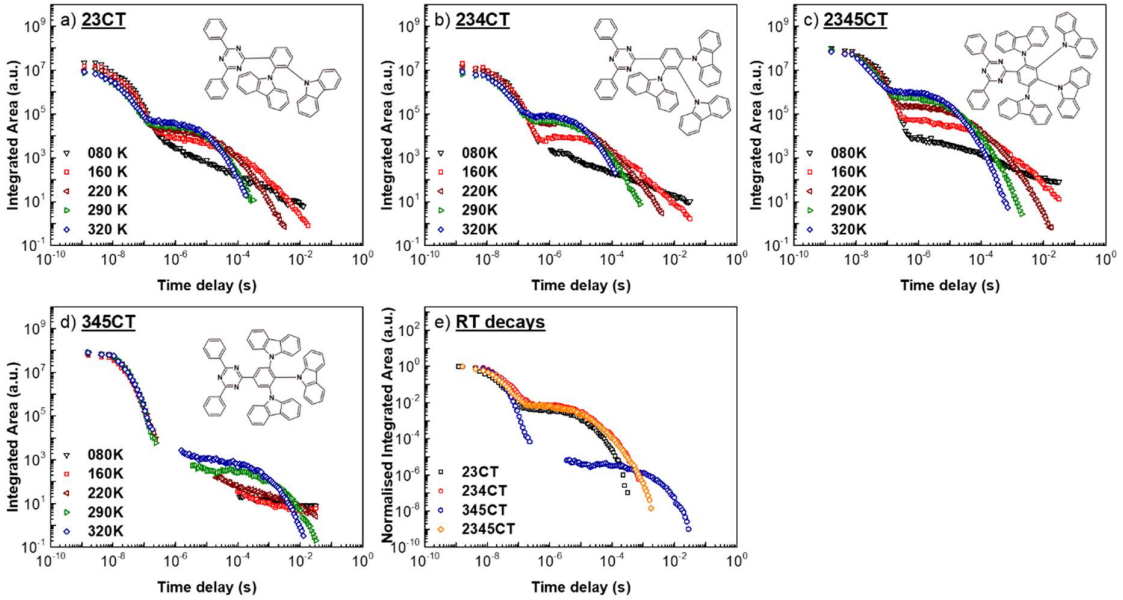

Figure 5.4 – Time-resolved emission decay curves at different temperatures with an excitation of 355 nm and time delays up to 0.03 s of the four emitters in zeonex: a) 23CT, b) 234CT, c) 2345CT, d) 345CT. In e) the normalised decays of each at room temperature are overlaid. The molecular structure of each isomer is shown in the inset of each graph.

All four emitters show two individual regions, PF (fast emission) and DF (long lived emission). The intensity of the DF component increases about two orders of magnitude from 80 K to RT. With the -*ortho* containing emitters, the DF decays are very similar (Figure 5.4e) although the thermal saturation of the DF occurs later with increasing number of **D**s: **23CT** shows little increase of DF from 160 to 320K, **234CT** starts to saturate at 220 K whereas **2345CT** only shows saturation at 290 K, indicative of decreasing ^{3}CT-^{3}LE coupling strength.[11] With a rough comparison of the DF profile, there is also a slight difference in DF when comparing the molecules with 2 to 4 **D** substituents, i.e. **23CT** to **2345CT**. **234CT** and **2345CT** both have longer lifetime DF tails, indicative of a slower rISC rate contribution. In contrast **345CT** shows much slower and weaker DF and stronger temperature dependence. Linear DF emission excitation power dependence was measured in all emitters and the slope of (or close to) 1 indicates TADF to be the DF mechanism in all materials at RT (Figure 5.5), Chapter 2.

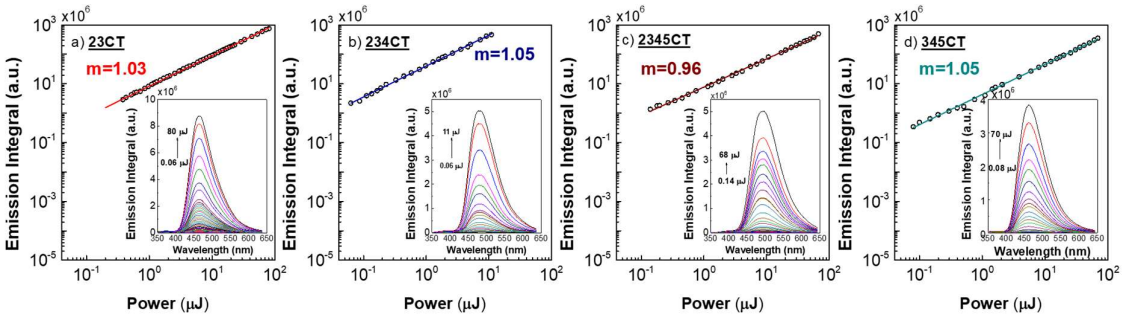

Figure 5.5 – Power dependence of DF for each emitter in zeonex at room temperature and corresponding fit (with slope m). Emission was collected at each delayed fluorescence region: a) 23CT (141 to 9062.9 ns); b) 234CT (300 to 44500 ns); c) 2345CT (200 to 6300 ns); d) 345CT (3.45 μs to 281.82 μs) and power between 60 nJ to 80 μJ.

Recent works by Dias *et al.* and Northey *et al*. have shown that the prompt CT emission of TADF molecules undergoes apparent dynamic redshift over the first few hundred nanoseconds which is explained as arising from heterogeneity of dihedral angles giving rise to a dispersion in CT energy and radiative decay rate.[10,12] The most planar **D-A** have the weakest CT and strongest excited state coupling to the ground state, so emit in the blue with faster radiative rate. The most orthogonal **D-A** have the strongest CT and therefore emit in the red with the slowest radiative rate. To understand this system's ensemble of CT states, a charge-transfer-gaussian density of states (CTGDoS) is defined. To determine the width of the CTGDoS, the earliest prompt CT emission, $^{1}CT_{Early}$, was collected at TD = 1.6 ns and the latest prompt CT emission, $^{1}CT_{Late}$, was collected at $100 \leq TD \leq 300$ ns – Figure 5.6. With increasing number of **D**s, there is also more dihedral inhomogeneity and thus broadening the CTGDoS, from 110 meV bandwidth in **23CT** to 170 meV in **2345CT**.

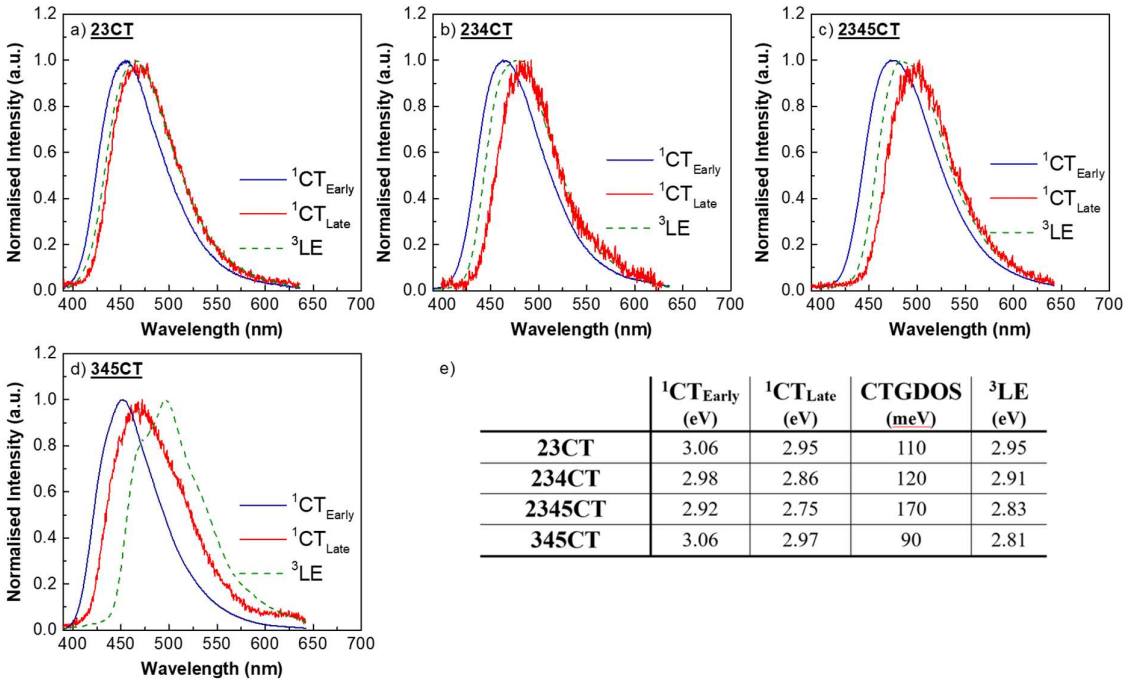

e)

	$^1CT_{Early}$ (eV)	$^1CT_{Late}$ (eV)	CTGDOS (meV)	^3LE (eV)
23CT	3.06	2.95	110	2.95
234CT	2.98	2.86	120	2.91
2345CT	2.92	2.75	170	2.83
345CT	3.06	2.97	90	2.81

Figure 5.6 – Energy levels of the emitters studied in a zeonex matrix at 80 K: a) 23CT, b) 234CT, c) 2345CT and d) 345CT. The spectra were taken at 80K with an excitation of 355 nm with different delay times: $^1CT_{Early}$ – 1.6 ns; $^1CT_{Late}$ – 100 to 300 ns; ^3LE – beyond 25 ms. The onset of each spectrum provides the energy of the correspondent state, with an error of ± 0.02 eV, and the difference between $^1CT_{Early}$ and $^1CT_{Late}$ gives the width of the charge-transfer gaussian density of states (CTGDoS), all summarised in e).

For all emitters at 80K, emission collected at times longer than 25 ms was assigned as phosphorescence (PH) from local carbazole-like triplet states (Chapter 4). PH from the **A** is found at 3.1 ± 0.02 eV for pure TRZ (Figure 5.7) – where without substitution there is no torsion across the molecule. In all -*ortho* emitters, one phenyl ring of the TRZ is twisted by around 40º which will localise the triplet state further, increasing its energy. Hence the **A** ^3LE should play no part in the rISC of these molecules as it is far to couple with the ^3CT. Moreover, the PH is gaussian and lies energetically within the CTGDoS (Figure 5.6). This means that there is a subset of CT and ^3LE states with zero energy gap, yielding very high rISC rates.[6] On the other hand, **345CT** shows a clear and structured PH, lying energetically below the lower edge of the CTGDoS, which explains its poorer TADF performance. This PH has similar shape to the findings on other reports on **D-A** systems based on carbazole and triazine **D** and **A,** (Chapter 4).[13]

By comparing the CTGDoS from the prompt emission to DF (sampling blue to red emissive CT states) the reddest emitters, i.e. with the most orthogonal **D-A**, should give the fastest rISC as these should have smallest ^1CT-^3CT gaps. While the ^1CT-^3LE gap is the most important for rISC,[11,14] the most orthogonal states will have the weakest radiative decay rate as

well. Therefore, it is not simple to correlate TADF efficiency with position within the CTGDoS.

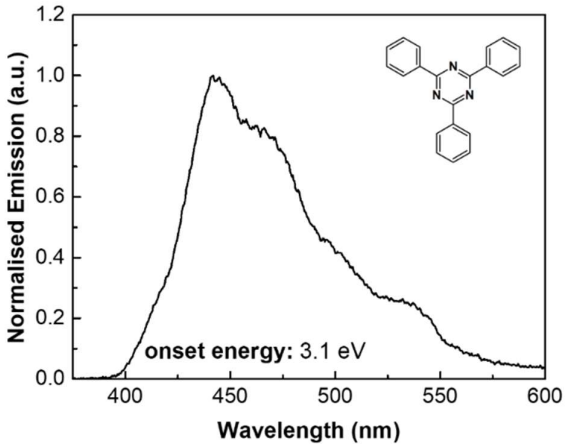

Figure 5.7 – Phosphorescence spectra of 2,4,6-triphenyl-1,3,5-triazine (molecular structure in inset) in a zeonex host collected with a time delay above 25 ms and at 80 K. Onset energy gives a ^{3}LE state of 3.1 eV ± 0.02 eV.

From the PF and DF, the decay rates and rate constants of the intersystem crossing (k_{ISC}) and reverse intersystem crossing (k_{rISC}) processes, Figure 5.8, were calculated following the method presented in Chapter 3 and summarised in Table 5.1.[15] In all emitters containing one carbazole in the *-ortho* position, with increasing number of **D**s, the triplet yield increases, from 80% (**23CT**) to 84% (**234CT**) to 87% (**2345CT**). The fitting of the DF region also becomes more complicated, from a mono-exponential decay in **23CT** to a bi-exponential decay in **234CT** and a triple exponential decay in **2345CT**. From the (multi) exponential fitting, the fastest DF component (with the fastest rISC rate) increases with the number of **D**s (from $5.8x10^5$ to $8.32x10^5$ and $6.78x10^6$ s^{-1} respectively for **23CT**, **234CT** and **2345CT**). However, with additional carbazoles, slower components also start contributing at longer TD. Comparing the pre-exponential fitting factors of these slow components in **234CT** and **2345CT**, they constitute 24% and 79% of the total DF, respectively. **345CT** can be fitted with a bi-exponential decay with a very slow rISC component that has a 55% contribution, in line with the increasing ΔE_{ST} observed.

The fast components must come from the more orthogonal Czs of the emitters, rotated with a β of 70º or higher. In **23CT**, given the evenness of the HOMO/LUMO distributions (Figure 5.2) both **D**s can essentially be thought as identical, and the DF decays mono-exponentially. As more **D**s are added, the dihedral angle of the non-*ortho* **D*s*** go from 70 to around 65º, Figure 5.2, and this difference in angles between -*ortho* and non-*ortho* Czs becomes significant and must be considered as a non-equivalent species. In **234CT**, this adds a second exponential to the DF and in **2345CT**, it becomes even more evident, as the bigger

distribution of HOMO in the *-para* carbazole than in **234CT** results in a third slow component associated with the 45° carbazole. Each of these non-equivalent dihedral angles give rise to an associated distinct ^{3}LE state, having different energies coupling to the CTGDoS with varying rISC rates, dependent on the associated energy gaps. With increasing number of **D**s, this then gives rise to the increasing number of rISC rates and hence more exponential fitting factors are required. These additional slow decay channels act as parasitic traps for the rISC, decreasing the overall up-conversion rate back to the singlet state. The differences in the DF performance are only minimal though as the energy gaps are still small enough to provide efficient TADF and fast enough (overall) rISC rates. However, these slower rISC channels will become more important in device operation.

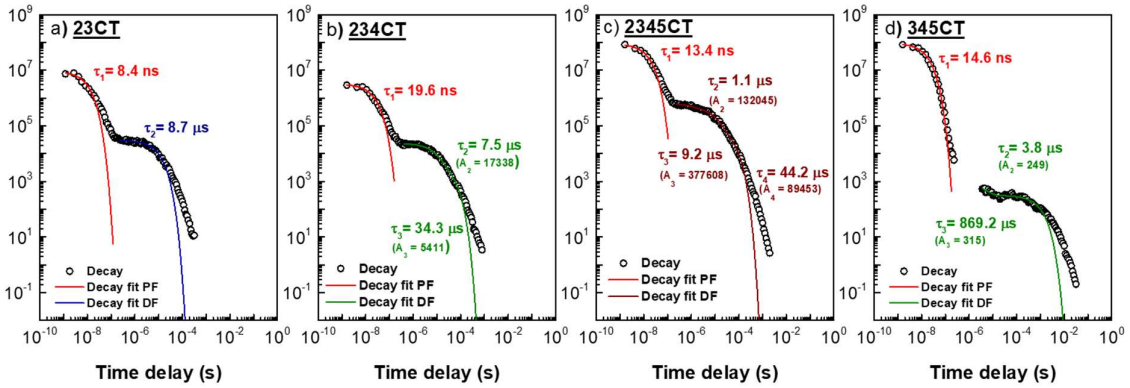

Figure 5.8 – Decay lifetime of the prompt ($\boldsymbol{\tau_1}$) and delayed ($\boldsymbol{\tau_{2,3,4}}$) fluorescence of all emitters in this study: a) 23CT, b) 234CT, c) 2345CT and d) 345CT. All showed a mono-exponential decay for the prompt (red). In the DF region, each material required one fewer exponential than the number of carbazoles: 23CT showed a mono-exponential decay (blue) whereas 234CT and 345CT were fitted with bi-exponential decays (green). 2345CT was fitted with a tri-exponential decays. The fitting used in single, bi and tri-exponential decays followed the expressions in Chapter 3.

Table 5.1 – Time constants and decay rates of 23CT, 234CT, 2345CT and 345CT in the prompt (PF) and delayed (DF) regions. In the latter three emitters either bi or tri-exponential decays were used and correlated with each fitted exponential (1 – 23CT; 2 – 234CT and 345CT; 3 – 2345CT). More details on the calculation of these constants can be found in chapter 3.

	τ_{PF} (ns)	$\tau_{DF}{}^{1}$ (μs)[1]	$\tau_{DF}{}^{2}$ (μs)	$\tau_{DF}{}^{3}$ (μs)	Φ_{DF}/Φ_{PF}	Φ_{ISC} (%)	k_{ISC} (s^{-1})	$k_{rISC}{}^{1}$ (s^{-1})	$k_{rISC}{}^{2}$ (s^{-1})	$k_{rISC}{}^{3}$ (s^{-1})
23CT	8.4 ± 0.8	8.7 ± 0.3	----------	--------	4.0	80	$9.5x10^{7}$	$5.8x10^{5}$	----------	----------
234CT	19.6 ± 1.1	7.5 ± 0.8 (A1 = 17,339)	34.3 ± 11.4 (A2 = 5,411)	--------	5.2	84	$4.3x10^{7}$	$8.3x10^{5}$	$1.8x10^{5}$	----------
2345CT	13.4 ± 0.6	1.1 ± 0.4 (A1 = 132,045)	9.3 ± 2.1 (A2 = 377,608)	44.5 ± 23.5 (A3 = 89,453)	6.5	87	$6.5x10^{7}$	$6.8x10^{6}$	$8.0x10^{5}$	$1.7x10^{5}$
345CT	14.6 ± 0.5	3.8 ± 0.7 (A1 = 249)	869.2 ± 72.3 (A2 = 315)	----------	0.4[a]	26	$1.8x10^{7}$	$3.6x10^{5}$	$1.6x10^{3}$	----------

[a] It is generally accepted that if ΦDF/ΦPF is above 4, the product $\Phi_{ISC}\,\Phi_{rISC}$ will be above 0.8. **345CT** does not fall in this category though the same assumption was applied for comparison purposes.

5.3.3 Photophysics in DPEPO

The photophysical study thus far shows a complex picture with multiple rISC channels and large energy distributions (CTGDoS) of the CT state ensemble. For a good basis of comparison with device data, the complete photophysics of all the emitters in a host appropriate for device studies was also analysed. Bis[2-(diphenylphosphino)phenyl]ether oxide (DPEPO) was the host chosen due to the high triplet energy and polarity for minimising the ΔE_{ST}.[1] Assuming a polarity tuning effect of the host (Chapter 2), with DPEPO being a high polarity host, the CT states should relax to lower energies, by as much as 150 meV.[1] Assuming a stationary triplet, this implies that the emitters that showed a smaller energy gap in zeonex (**23CT** and **234CT**), should have higher energy gaps in DPEPO and therefore decreased device performance. Figure 5.9 shows the $^1CT_{Early}$, $^1CT_{Late}$ and ^3LE emission of all 4 materials in spin-coated samples with DPEPO**.**

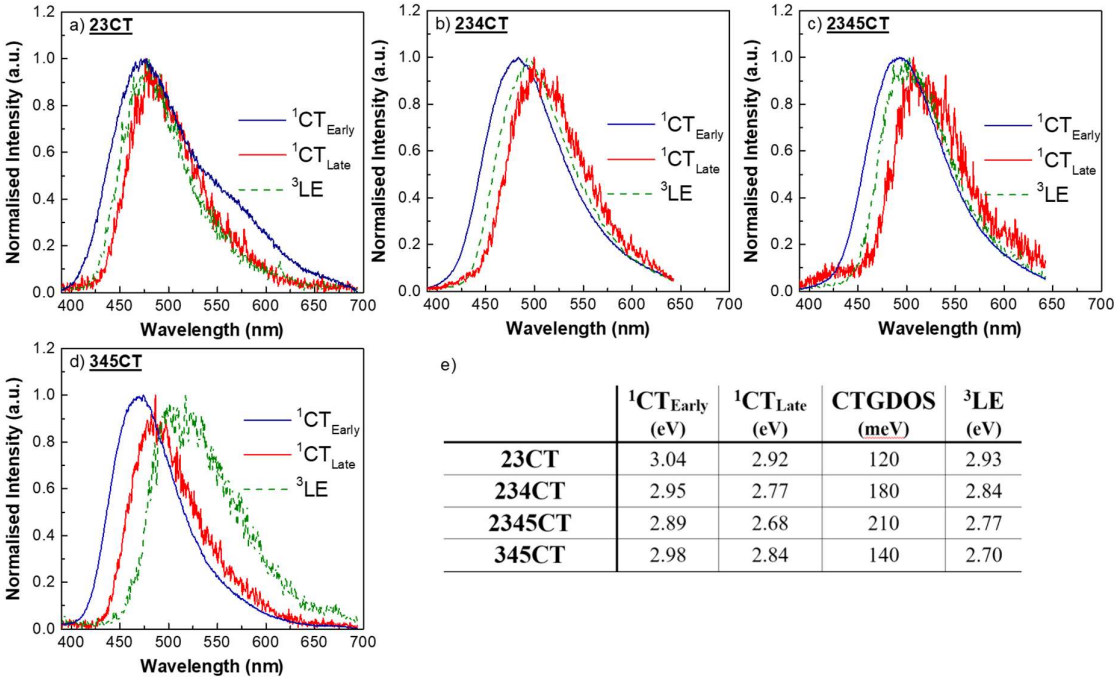

e)

	$^1CT_{Early}$ (eV)	$^1CT_{Late}$ (eV)	CTGDOS (meV)	^3LE (eV)
23CT	3.04	2.92	120	2.93
234CT	2.95	2.77	180	2.84
2345CT	2.89	2.68	210	2.77
345CT	2.98	2.84	140	2.70

Figure 5.9 – Energy levels of the emitters studied in a DPEPO matrix at 80 K: a) 23CT, b) 234CT, c) 2345CT and d) 345CT at 80K and excited at 355 nm with different delay times: $^1CT_{Early}$ – 1.6 ns; $^1CT_{Late}$ – 100 to 300 ns; ^3LE – above 25 ms, with an error of ± 0.02 eV. The charge-transfer gaussian density of states (CTGDoS) is also shown with all onset energies and width of the CTGDoS summarised in e).The Charge-Transfer Gaussian Density of States (CTGDoS) is also shown being generally broader in DPEPO than in zeonex (Figure 5.6).

Whereas the overall behaviour of the emission remains the same as in zeonex, two facts become immediately obvious: i) the CTGDoS broadens in DPEPO, and ii) all PH spectra have redshifted compared to zeonex (Figure 5.10). Therefore, the model where the triplet is assumed to be host independent is not valid for this family of emitters. To rule-out the possibility that the PH shift is polarity dependant, the PH of **345CT** was measured in another polymeric matrix

with a higher polarity than zeonex Poly(methyl)-methacrylate (PMMA), Figure 5.10d), with confirmed that the onset does not change as result of polarity. Therefore, the redshift is thought to be an effect of the rigidity or packing in the host matrix that affects the β angles of the molecules and their conjugation. This changes the energy gaps of the system and especially the energies of the ^{3}LE states. The relaxation of the CT state energies must also be thought as a combination of this packing effect and the polarity of the host. However it should be noted that a relaxation of the excited-state energy through polarity requires that the surrounding polar molecules reorient to stabilise the dipole moment of the CT molecule, and that such 'solid-state' solvatochromism is greatly hindered in a dense host.[10] Thus, for this family of emitters, the major effect for both CT and LE shifts is due to packing-induced changes of the β angles.

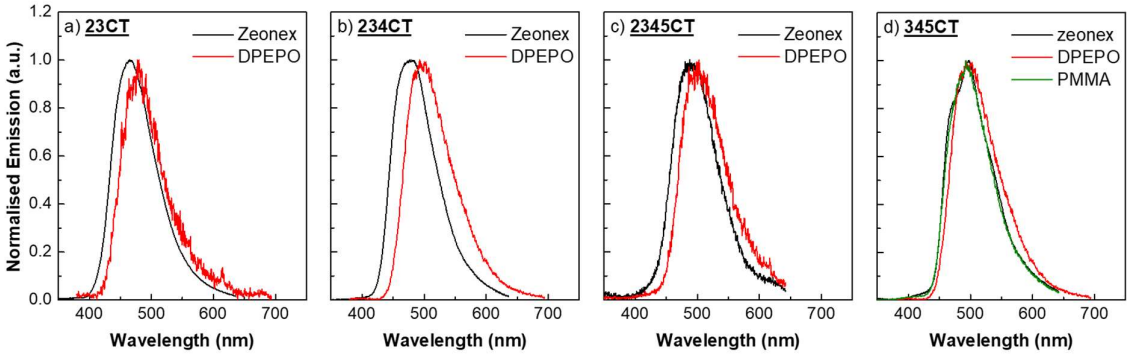

Figure 5.10 – Normalised phosphorescence (PH) spectra of a) 23CT, b) 234CT, c) 2345CT and d) 345CT in zeonex and in DPEPO host. All PH were collected with a time delay above 25 ms and at 80 K to avoid contribution from any delayed singlet emission. Overall, the PH in DPEPO are redshifted compared to zeonex due to changes in the packing of the emitters induced by the host. One that affects the dihedral and torsional angles and in turn affect the conjugation of the molecules. This packing effect is confirmed by looking at the PH of 345CT in another more polymeric matrix (PMMA, d).

The decay curves at RT in DPEPO remain similar for **23CT** and **234CT** (Figure 5.11) and a slight improvement in **345CT** is seen. **2345CT** showed a faster DF in DPEPO when compared to zeonex, however, the best fit still requires three exponentials and indicates that the slow parasitic rISC components are still present. Full fitting data is given in Table 5.1

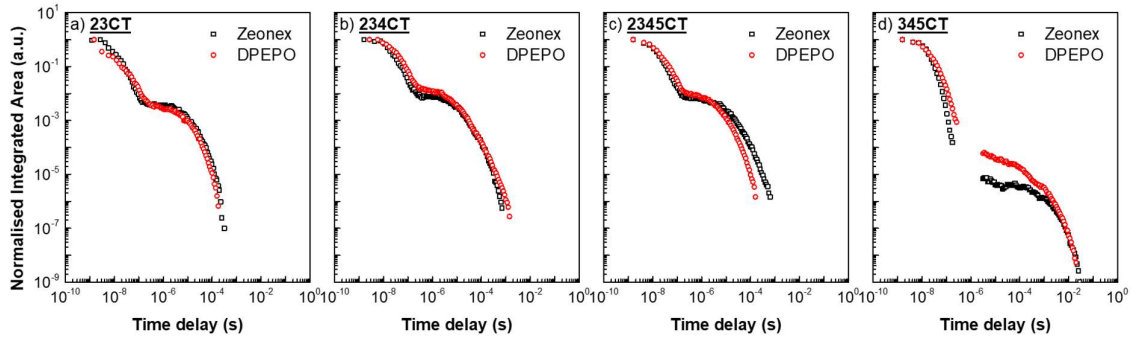

Figure 5.11 – Normalised room temperature decays of a) 23CT, b) 234CT, c) 2345CT and d) 345CT in a zeonex matrix overlapped with their decays in DPEPO.

Table 5.2 – Time constants and decay rates of 23CT, 234CT, 2345CT and 345CT in a DPEPO matrix. More details on the calculation of these constants can be found in Chapter 3.

	τ_{PF} (ns)	$\tau_{DF}{}^{1}$ (μs)[1]	$\tau_{DF}{}^{2}$ (μs)	$\tau_{DF}{}^{3}$ (μs)	Φ_{DF}/Φ_{PF}	Φ_{ISC} (%)	k_{ISC} (s^{-1})	$k_{rISC}{}^{1}$ (s^{-1})	$k_{rISC}{}^{2}$ (s^{-1})	$k_{rISC}{}^{3}$ (s^{-1})
23CT	16.2 ± 1.2	6.8 ± 0.3	----------	----------	3.9	80	$4.9x10^{7}$	$7.3x10^{5}$	----------	----------
234CT	27.2 ± 1.4	3.7 ± 0.4 (A1 = 99,400)	21.4 ± 4.3 (A2 = 43,700)	----------	4.9	83	$3.1x10^{7}$	$1.4x10^{6}$	$2.3x10^{5}$	----------
2345CT	15.7 ± 0.8	0.3 ± 0.2 (A1 = 8,431)	2.8 ± 0.5 (A2 = 67,900)	12.7 ± 3.6 (A3 = 21,000)	2.6[a]	72	$4.6x10^{7}$	$1.7x10^{7}$	$1.8x10^{6}$	$3.9x10^{5}$
345CT	16.2 ± 0.5	3.8 ± 0.7 (A1 = 311)	869.2 ± 72.3 (A2 = 308)	----------	0.7[a]	40	$42.4x10^{7}$	$9.0x10^{5}$	$2.7x10^{4}$	----------

[a] It is generally accepted that if ΦDF/ΦPF is above 4, the product Φ_{ISC} Φ_{rISC} will be above 0.8. **2345CT** and **345CT** do not fall in this category though the same assumption was applied for comparison purposes.

5.3.4 Comparison of the CTGDoS in the different solid-state matrixes

From the photophysics measured in the dense rigid matrix (DPEPO), the dihedral angles of each emitter are directly affected by the host. In effect, the rigidity of the host 'locks-in' the geometric structure of the molecule as it is deposited and there is little chance for dihedral angles to equilibrate before the surrounding host molecules 'freeze-in' the structure. In comparison to "more fluid" zeonex, this increases the width of the CTGDoS of the ensemble of emitters. The CTGDoS broadens further with increasing number of **D**s, as well as a general lowering of local triplet energies, presumably by compressing the dihedral angles increasing planarity.[16] In DPEPO, the simultaneous lowering of the CT energies closely matches the lowering of the local triplet energies. The rISC channels and their rates remain therefore rather unaffected compared to zeonex. **345CT** shows a larger difference in gap although this is proportional to its larger gap size. In this way, all photophysics results can be explained in one model, based on the CTGDoS and non-equivalent local triplets – Figure 5.12.

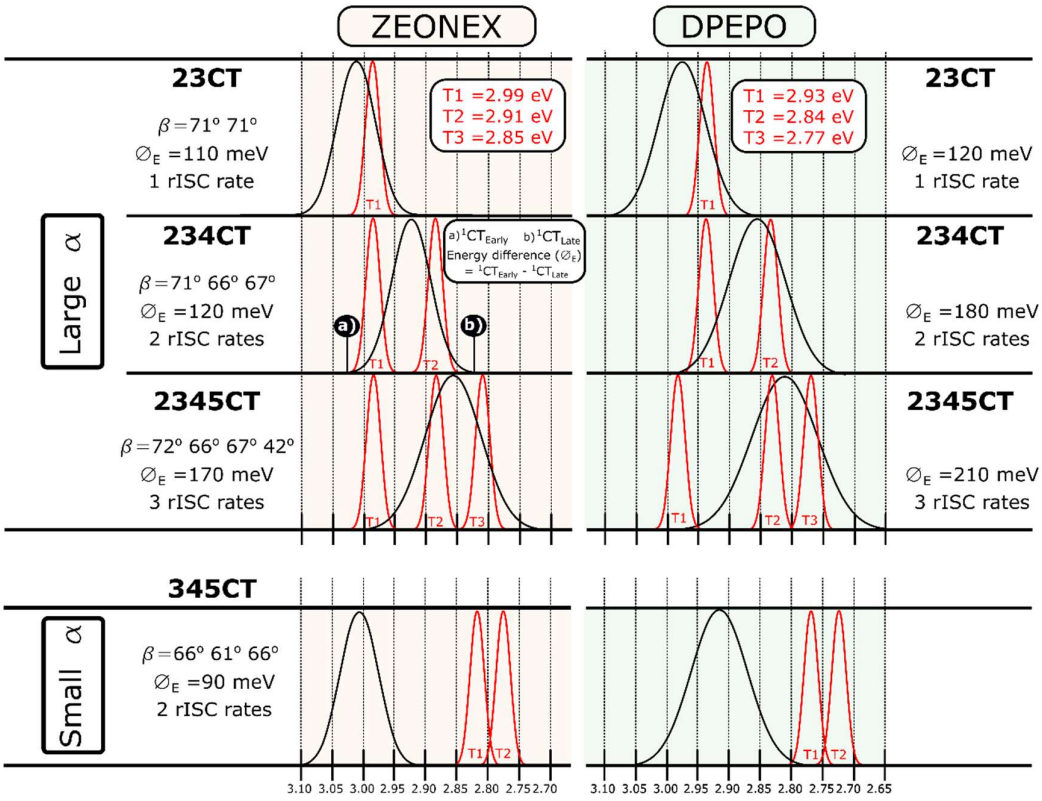

Figure 5.12 – Schematic of the Charge-Transfer Gaussian Density of States (CTGDoS) arising from the inhomogeneity of D-A dihedral angles in solid state, in zeonex (left) and DPEPO (right) of 23CT, 234CT, 2345CT and 345CT, divided into the classes of torsion angles (α) of the TRZ acceptor. The energy difference between $^1CT_{Early}$ and $^1CT_{Late}$ is assumed to be gaussian and labelled $\emptyset_E$. Triplet states arising from non-equivalent Cz donor units are shown approximately in relation to the CTGDoS and can potentially vibronically couple ^3CT and ^3LE states yielding different rISC channels with different rates. The lowest energy ^3LE state (T_1) is taken from the respective phosphorescence (PH) spectra. The higher energy triplets were estimated from molecules with similar dihedral angles with measurable PH.

5.4 Probing OLED roll-off with the CTGDoS

The device performance of **2345CT** in a similar device structure to the one used in **23CT** (Chapter 4), **234CT**[5] and **345CT**[8] in DPEPO host, the performance in terms of external quantum efficiency (η_{ext}) at its maximum, at 100 and 1,000 cd/m^2 is summarised in Table 5.3. The roll-off or the drop in η_{ext} from maximum to 1,000 cd/m^2 and resulting Commission Internationale de l'Eclairage (CIE) colour coordinates are also analysed. All device characterisation is shown in Figure 5.13 with an optimised device structure of ITO (120 nm)/ PEDOT:PSS (60 nm)/ TAPC (20 nm)/ mCP (10 nm)/ DPEPO:TADF dopant (25 nm, 30 wt%)/ TSPO1 (5 nm)/ TPBi (20 nm)/ LiF (1.5 nm)/ Al (200 nm) and energy levels shown in Figure 5.13a). The energy levels of **2345CT** were determined using cyclic voltammetry (CV) with the HOMO found to be -6.15 eV and the LUMO level -3.50 eV as can be estimated from the oxidation and reduction potentials.* All other energy levels were taken from previous reports on these materials.

Firstly, the turn-on voltage of all devices was around 3.8V, similar to the device performance of the emitters in Chapter 4. The current density (J) dependence with voltage shows a decrease in the maximum current in the -*ortho* emitters, Figure 5.13b). Secondly, the external quantum efficiency (η_{ext}) vs luminance (L) of all devices (Figure 5.13c) showed high peak device efficiencies, well above 20 %. However, with increasing number of **D**s, the roll-off exacerbates, dropping η_{ext} by 4.6 % in **23CT**, 9.8 % in **234CT** and 20.8 % in **2345CT**, compared between η_{ext} maximum and that at 1,000 cd/m^2. **2345CT** also has the highest maximum η_{ext}. The emission (Figure 5.13d) also changes from sky-blue to greenish-blue between emitters, a result of the change in CT emission (Figure 5.6). Similarly, **345CT**, shows the largest drop in η_{ext}, (40.6 % relative to maximum) but still high peak η_{ext} and a sky-blue emission. The increase in roll-off directly correlates with the additional slow rISC components of each emitter although that does not impact the low brightness efficiency, which is controlled by the fastest rISC rate component that is similar for each emitter. From these device results, it is therefore clear that the $\eta_{ext, max}$ is controlled by the primary fast rISC channel (Figure 5.12) whilst roll-off correlates strongly with the presence of the secondary, parasitic, slower rISC channels and competition between them controls the overall electrical stability of these TADF emitters. Furthermore, the non-equivalent local triplets all contribute differently to the rISC channels.

* Cyclic voltammetry analysis performed by Chan Seok Oh and Jun Yeob Lee from the Sungkyunkwan University.

Table 5.3 – External quantum efficiency (η_{ext}) of devices based on 23CT, 234CT, 2345CT and 345CT and Commission Internationale de l'éclairage (CIE) at the maximum values, at 100 and 1,000 cd/m^2.†

	$\eta_{ext,max}$ (%)	$\eta_{ext,100\ cd/m^2}$ (%)	$\eta_{ext,1000\ cd/m^2}$ (%)	$\eta_{ext,drop}$ [1] (relative %)	CIE (x,y)
23CT	21.8	21.8	20.8	4.6	(0.17, 0.33)
234CT	20.4	20.3	18.4	9.8	(0.20, 0.44)
2345CT	23.1	22.2	18.3	20.8	(0.22, 0.48)
345CT	22.4	21.2	13.3	40.6	(0.18, 0.37)

[1]between maximum and 1,000 cd/m^2.

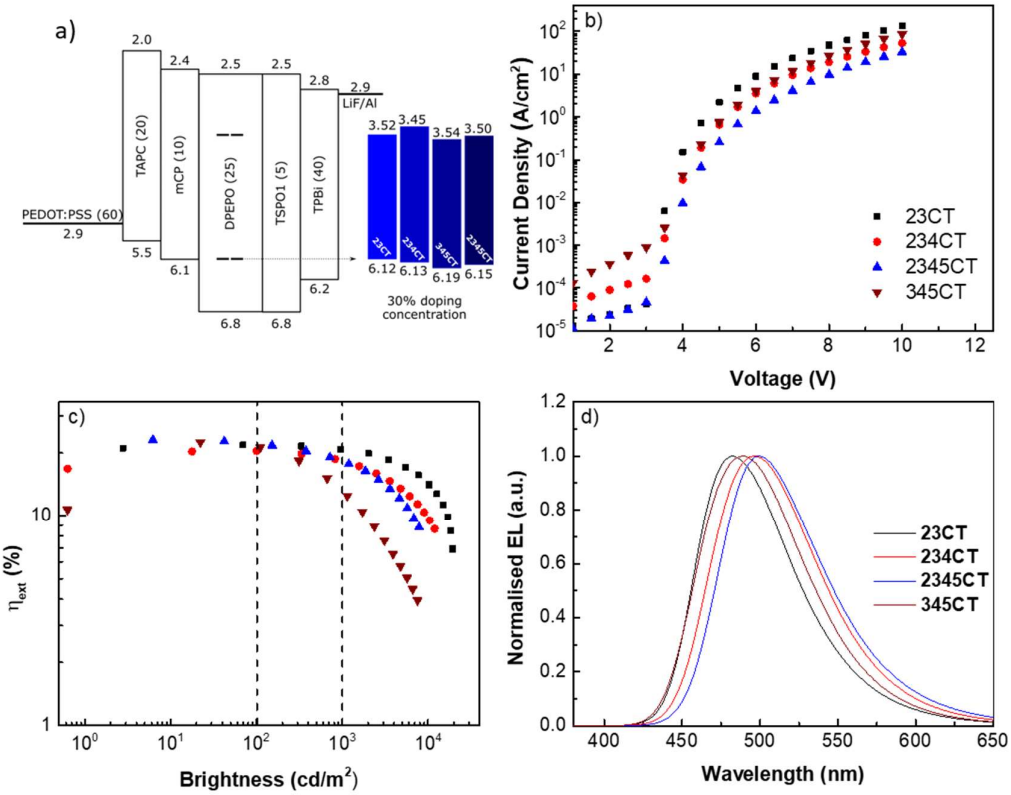

Figure 5.13 – Characterization of devices based on 23CT, 234CT, 2345CT and 345CT. a) Device structure used for each emitter, b) Current density vs Voltage, c) External quantum efficiency vs Brightness and d) Electroluminescence spectra (at 10 V).

Ultimately the large heterogeneity of dihedral angles together with the torsion of the **A** and especially with multiple interacting **D**s broadens the CTGDoS in DPEPO. This allows multiple non-equivalent ^{3}LE states to couple with isoenergetic CT states to yield a large rISC rate. As observed, increasing the number of **D**s increases the number of non-equivalent ^{3}LE

† Devices produced by Ha Lim Lee and Jun Yeob Lee from the Sungkyunkwan University, South Korea. Device interpretation by Daniel de Sa Pereira and Andrew P. Monkman.

states and the number of rISC channels, concomitant with the number of unique **D-A** β angles. The different rates of each of these channels is determined independently through the vibronic coupling model.[4] The fast rISC channel gives rise to the high peak η_{ext} in devices and the rapid DF decay components in the time-resolved photophysics. Therefore, the higher the overlap between the CTGDoS and the highest triplet, the more resistant the device is to roll-off. In contrast, the slow rISC channels lead to poor roll-off behaviour in devices and the long DF tails seen in the photophysics. This model of multiple vibronic coupling modes which gives rise to rISC now allows a fuller appreciation of the complexity of TADF in emitters with multiple **D**s (or **A**s) and explains how one molecule can give high peak η_{ext} with poor roll-off performance while another molecule in the same family provides a similar $\eta_{ext,max}$ with a much higher resistance to efficiency roll-off. Once the ^{3}CT and specific ^{3}LE have become vibronically coupled, they remained locked together until a spin flip occurs and the resultant ^{1}CT state emits, giving rise to fixed branching ratios for the different rISC channels.

5.5 Conclusions

In this chapter, with detailed and comparative photophysical study, the DF performance of a series of multi-donor acceptor TADF systems based on carbazole and triazine gives a full picture of TADF in complex emitters. By increasing the number of closely packed interacting donor carbazoles, placed near the acceptor (the -*ortho* emitters) and away from it as in **345CT**, donors with different sets of β dihedral angles were identified to give rise to local donor triplet states with different energies. The large ensemble of β gives rise to a large dispersion in CT energies, which lead to the introduction of the concept of a Charge-Transfer Gaussian Density of States, CTGDoS. Because the CTGDoS is energetically broad, more than one non-equivalent ^{3}LE state can vibronically couple to the CT states giving rise to multiple rISC channels with different rISC rates. The fastest 'primary' rISC channel causes fast DF decay and high maximum η_{ext} in devices, whereas the slower secondary rISC channels cause long DF decay tails and low resistance to efficiency roll-off. Thus, this can explain how within the same family of TADF emitters can have very high peak η_{ext} and simultaneously different roll-off behaviours. A rigid host matrix also broadens the CTGDoS through packing effects, causing an overall lowering of dihedral angles and reducing the energies of both the CT and local triplet states. These new concepts, along with the vibronic coupling model that explains the spin-flip mechanism and overall rISC rate of each independent channel, it is now possible to fully explain both the photophysical and device behaviour of complex TADF family of emitters.

From this new model, non-equivalent donor units (in terms of position with respect to the acceptor unit) can give rise to parasitic rISC channels that lead to poor roll-off behaviour. Therefore, a better design is to have symmetric multi-donor systems that avoid this inequivalence, such as the TADF emitter recently published by dos Santos *et al.*[3] where very high η_{ext} and excellent roll-off behaviour were found. This work also shows that multiple vibronically coupled processes compete for excited-state energy and the way in which it decays in a molecule. This implies that it may be possible to engineer molecules where undesirable decay pathways are 'out-competed' by desirable channels, through the appropriate structure of the molecule, as an example, non-radiative decay can be effectively switched-off.[3] Bridging the results from chapters 4 and 5 with works by Oh *et al.*[5], one final diagram that correlates molecular structure with device performance in this class of emitters can thus be drawn which may give new perspectives in understanding and designing multifunctional new molecules, Figure 5.14.

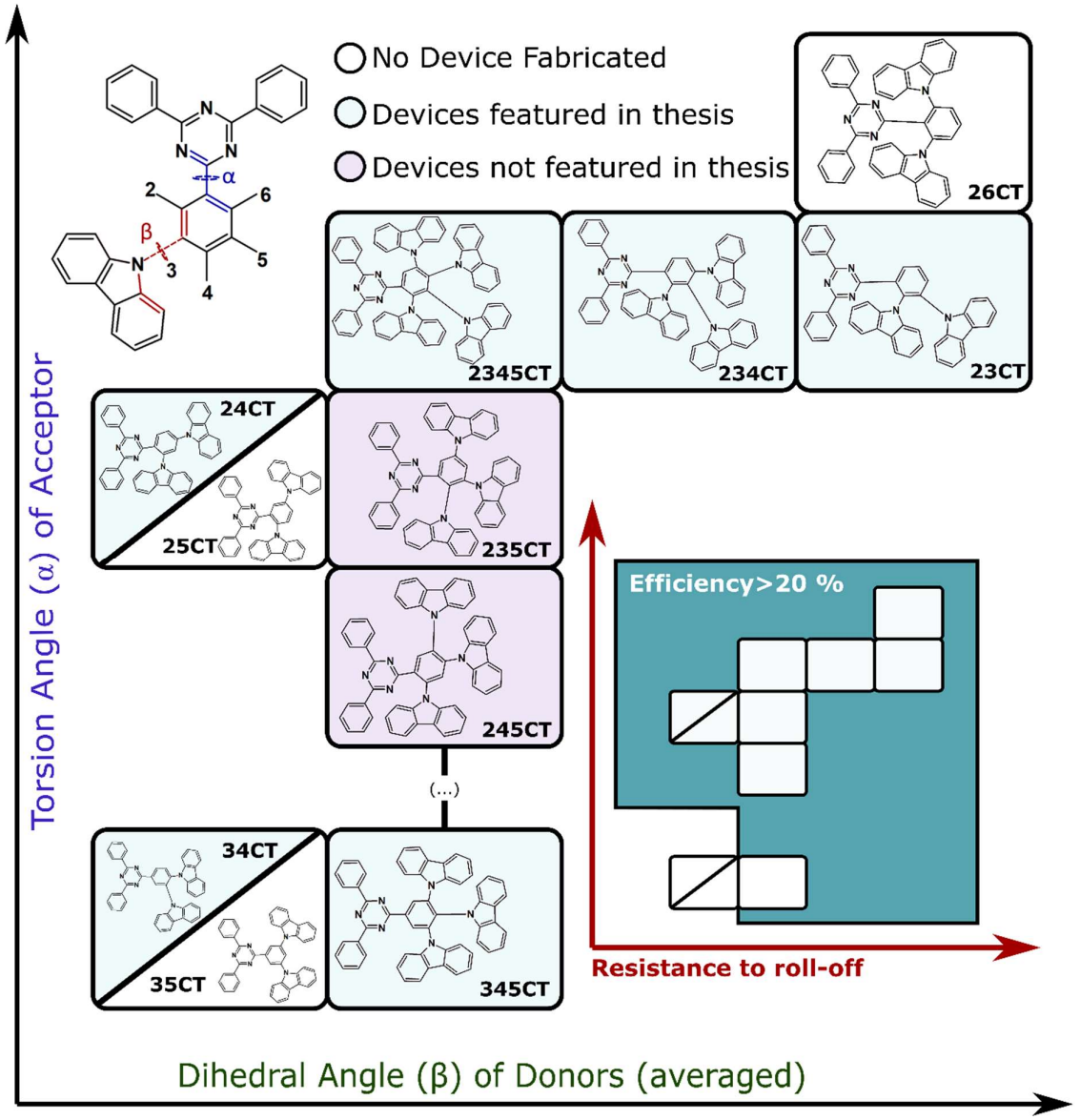

Figure 5.14 – Dihedral (β) and torsional angle (α) control of blue TADF emitters and their impact on energy levels and device performance. All molecules in this family used carbazole and 2,4,6-triphenyl-1,3,5-triazine as donor (D) and acceptor (A), respectively. All devices based on this family of D-A TADF emitters were produced with the same device structure.

5.6 References Chapter 5

1. dos Santos, P. L., Ward, J. S., Bryce, M. R. & Monkman, A. P. Using Guest–Host Interactions To Optimize the Efficiency of TADF OLEDs. *J. Phys. Chem. Lett.* **7,** 3341–3346 (2016).

2. Nobuyasu, R. S. *et al.* Rational Design of TADF Polymers Using a Donor-Acceptor Monomer with Enhanced TADF Efficiency Induced by the Energy Alignment of Charge Transfer and Local Triplet Excited States. *Adv. Opt. Mater.* **4,** 597–607 (2016).

3. dos Santos, P. L. *et al.* Triazatruxene: A Rigid Central Donor Unit for a D-A 3 Thermally

Activated Delayed Fluorescence Material Exhibiting Sub-Microsecond Reverse Intersystem Crossing and Unity Quantum Yield via Multiple Singlet-Triplet State Pairs. *Adv. Sci.* **5,** 1700989 (2018).

4. Goushi, K., Yoshida, K., Sato, K. & Adachi, C. Organic light-emitting diodes employing efficient reverse intersystem crossing for triplet-to-singlet state conversion. *Nat. Photonics* **6,** 253–258 (2012).

5. Oh, C. S., Lee, H. L., Han, S. H. & Lee, J. Y. Rational Molecular Design Overcoming the Long Delayed Fluorescence Lifetime and Serious Efficiency Roll-Off in Blue Thermally Activated Delayed Fluorescent Devices. *Chem. - A Eur. J.* **25,** 642–648 (2019).

6. Santos, P. L. *et al.* Engineering the singlet–triplet energy splitting in a TADF molecule. *J. Mater. Chem. C* **4,** 3815–3824 (2016).

7. Higginbotham, H. F., Yi, C. L., Monkman, A. P. & Wong, K. T. Effects of Ortho-Phenyl Substitution on the rISC Rate of D-A Type TADF Molecules. *J. Phys. Chem. C* **122,** 7627–7634 (2018).

8. Lee, D. R. *et al.* Design strategy for 25% external quantum efficiency in green and blue thermally activated delayed fluorescent devices. *Adv. Mater.* **27,** 5861–7 (2015).

9. Higginbotham, H. F., Etherington, M. K. & Monkman, A. P. Fluorescence and Phosphorescence Anisotropy from Oriented Films of Thermally Activated Delayed Fluorescence Emitters. *J. Phys. Chem. Lett.* **8,** 2930–2935 (2017).

10. Northey, T., Stacey, J. & Penfold, T. J. The role of solid state solvation on the charge transfer state of a thermally activated delayed fluorescence emitter. *J. Mater. Chem. C* **5,** 11001–11009 (2017).

11. Gibson, J. & Penfold, T. J. Nonadiabatic coupling reduces the activation energy in thermally activated delayed fluorescence. *Phys. Chem. Chem. Phys.* **19,** 8428–8434 (2017).

12. Dias, F. B. *et al.* The role of local triplet excited states and D-A relative orientation in thermally activated delayed fluorescence: Photophysics and devices. *Adv. Sci.* **3,** 1600080 (2016).

13. Kukhta, N. A. *et al.* Deep-Blue High-Efficiency TTA OLED Using Para - and Meta -Conjugated Cyanotriphenylbenzene and Carbazole Derivatives as Emitter and Host. *J. Phys. Chem. Lett.* **8,** 6199–6205 (2017).

14. Penfold, T. J., Dias, F. B. & Monkman, A. P. The theory of thermally activated delayed fluorescence for organic light emitting diodes. *Chem. Commun.* **54,** 3926–3935 (2018).

15. Dias, F. B., Penfold, T. J. & Monkman, A. P. Photophysics of thermally activated delayed fluorescence molecules. *Methods Appl. Fluoresc.* **5,** 012001 (2017).

16. Pander, P. *et al.* Thermally Activated Delayed Fluorescence Mediated through the Upper Triplet State Manifold in Non-Charge-Transfer Star-Shaped Triphenylamine–Carbazole Molecules. *J. Phys. Chem. C* **122,** 23934–23942 (2018).

Chapter 6: The Effect of a Heavy Atom on the Radiative Pathways of a TADF Emitter with Dual Conformation

This study investigates the photophysics of a donor-acceptor molecule with a 2,4,6-triphenyl-1,3,5-triazine and phenoselenazine acceptor and donor, respectively. Selenium distinctively folds the phenoselenazine – much like sulphur in the more common phenothiazine analogue – resulting in two conformers that yield room temperature phosphorescence (RTP) and thermally-activated delayed fluorescence (TADF). This combination produces a unique in-depth picture of the mechanisms inherent to dual emission in this family of TADF emitters. The dual emission comes from a shorter lifetime quasi-axial conformer and a longer lifetime quasi-equatorial that gives rise to efficient TADF. The quasi-axial conformer is not TADF active because it has a low energy local triplet that quenches the charge-transfer states, instead resulting in RTP. From sulphur to selenium, the phosphorescence radiative decay is greatly increased with little effect on the reverse intersystem crossing (rISC) process meaning that adding a heavy atom to the donor does not affect the TADF performance. In devices, the interplay between TADF and RTP leads to yellow-green emitting devices with external quantum efficiencies of 17 % by optimisation of the conformer that gives rise to the TADF emission. Therefore, the subtle differences enhanced by the phenoselenazine donor further adds to the knowledge of how structure affects TADF photophysics.

At the time of submission, the work presented in this chapter was under revision: Daniel de Sa Pereira, Dong Ryun Lee, Nadzeya Kukhta, Kyung Hyung Lee, Cho Lung Kim, Andrei Botsanov, Jun Yeob Lee, Andrew P. Monkman, **The Effect of a Heavy Atom on the Radiative Pathways of an Emitter with Dual Conformation, Thermally-Activated Delayed Fluorescence and Room Temperature Phosphorescence,** under revision. Daniel de Sa Pereira, Dong Ryun Lee, Nadzeya Kukhta contributed equally to this work. Dong Ryun Lee designed and synthesised PSeZTRZ while Cho Long Kim synthesised PTZ-TRZ following the synthetic procedure shown in.[1] Dong Ryun Lee and Andrei S. Batsanov analysed the single crystal structure of the materials and Kyung Hyung Lee fabricated the devices. Photophysical characterisation was carried out by Daniel de Sa Pereira and Andrew P. Monkman. NMR spectra and DFT calculations were performed by Nadzeya Kukhta.

6.1 Introduction

Chapters 4 and 5 have focused on the dihedral angle effects on the charge-transfer (CT) character of different donor-acceptor (**D-A**) emitters. As shown, the dihedral angle between the **D** and **A** units is crucial in separating the highest occupied molecular orbital (HOMO) from the lowest unoccupied molecular orbital (LUMO).[2] The torsion of the **A** unit is also important and enhances this MO separation. However, the folding within the donor has not yet been considered, as the overall rigidity of the carbazole unit makes this irrelevant in the materials studied thus far.[3]

In contrast to carbazole **D**s, some thermally-activated delayed fluorescence (TADF) molecules, more particularly those using phenothiazine (PTZ) as a **D**, have shown dual CT emission as a result of two different molecular conformers.[1,4–6] PTZ has two main conformations associated with a folding of the central 6-membered ring bringing the sulphur and nitrogen atoms towards one another: one tetragonally folded and the other planar, also known as "H-intra" and "H-extra", respectively.[7] As extensively studied in PTZ-pyrene dyads,[8–10] when PTZ is bonded to an acceptor, it gives rise to two conformations, quasi-axial (Ax) and quasi-equatorial (Eq), resulting in distinct dihedral angles in both conformers that result in different optical and electronical properties.[9] Thus, the induced CT states will have different strengths, different energies, and undergo different, independent decay mechanisms. In **D-A-D** emitters, both conformers may appear simultaneously and therefore, TADF may be activated or suppressed depending on these states, the energy gaps they give rise to and the presence of different neighbouring triplets.[5,11,12] This chapter aims at getting more depth in emitters that possess this peculiar characteristic (Figure 6.1).

Associated with TADF is the observation of room temperature phosphorescence (RTP). Although not suitable for devices (due to the long lifetime of the triplet excitons in RTP) the rate at which triplets are formed is enhanced through intersystem crossing (ISC) from ^{1}CT to the low-lying local triplet state. In some materials, the rates of TADF and RTP can compete with each other. Therefore, design principles to suppress RTP in favour of TADF must be considered carefully.[13–15] To observe both TADF and RTP in one material is rare and this combination is analysed here in order to gain a better understanding of the rISC process in TADF materials and how it compares to the radiative triplet decay in RTP.

In this chapter, 1,3,5-triphenyl-2,4,6-triazine (TRZ) was again used as an **A** unit with carbazole replaced with a PTZ-like **D** with selenium replacing sulphur. Phenoselenazine

(PSeZ) was connected in the -*para* position of the **A** phenyl ring. By studying the photophysical properties of **PSeZ-TRZ**, four different pathways were revealed: dual CT emission from the two different conformers and similarly, dual phosphorescence. Differences in the **D-A** conjugation of both conformers together with the heavy-atom effect promoted by selenium give rise to both TADF and RTP through the mechanisms interplaying within all four different states. A direct comparison to the complex photophysics of the analogous molecule with a PTZ donor is made to bridge with the heavy atom effect in **PSeZ-Trz**.

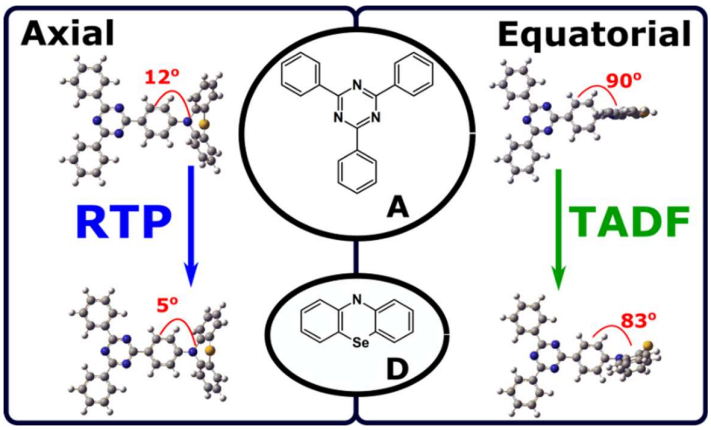

Figure 6.1 – Chapter 6 project diagram. Using selenium in the phenoselenazine donor that has a distinct folding, donor-acceptor (D-A) emitters with dual emission channels from two different conformers – "quasi-axial" and "quasi-equatorial"[9] – where both TADF and RTP are present. These have distinct relaxation pathways: one that leads to room temperature phosphorescence (RTP) and another to thermally-activated delayed fluorescence (TADF). All these pathways result from the more planar and orthogonal nature of the D-A bonding in the different conformers.

6.2 Concept of Study

The molecular structure of **PSeZ-TRZ** investigated in this chapter is presented in Figure 6.1. PSeZ has not been previously considered as an electron-donating moiety for OLED materials. **PSeZ-TRZ** has the same basic design as other well-known TADF analogues with phenothiazine (PTZ) and phenoxazine (POZ) donors, with selenium (Se) replacing sulphur (S) and oxygen (O), respectively. These **D-A** structures, bridged through a N-C bond, ensure near orthogonality and conjugational decoupling of the **D-A** units. Unlike POZ,[16] PTZ has also been known to readily form dual conformations in **D-A** and **D-A-D** combinations.[1,5,6] Employing the PSeZ **D** extends this family of TADF emitters while increasing potential ISC rates by introducing the heavy Se heteroatom and consequently retaining the conformational complexity seen in PTZ.[17] The main question that arises and will be answered in this chapter is: by increasing the size of the heteroatom, will the TADF performance be affected?

Answering this basic question will provide insights on the photophysical mechanisms inherent to molecules that possess emission from dual conformers.

As a starting point, modern understanding of the photophysics of **PTZ-TRZ** should be revisited. Tanaka *et al.* reported dual fluorescence of **PTZ-TRZ** in toluene concluding that the CT band is a combination of the absorption of both conformers. While the axial (Ax) emission occurs when directly excited from the Ax absorption band, emission from the equatorial (Eq) had multiple origins: 1) electron transfer from the local excited state (LE) of the PTZ, 2) energy transfer from Ax to Eq and 3) direct absorption from the Eq band (this one less likely due to almost-zero oscillator strength).[1] Chen *et al.* continued the analysis of the same molecule in cyclohexane to show that, upon excitation, both Ax and Eq relax to a similar configuration, giving rise to the same emission.[6] To gain a fundamental comparative understanding of **PSeZ-TRZ**, time-resolved emission spectroscopy of **PTZ-TRZ** was therefore studied in detail.

6.3 Theoretical Approach

The geometry of **PSeZ-TRZ** as determined using rBMK/6-31G(d) level of theory (Figure 6.2), is considered as the mixture of Ax and Eq conformers. In the ground state (Figure 6.2a), the occurrence of both conformers is almost equally probable, owing to a negligible energy barrier (3.4 meV) between them. However, in comparison to **PTZ-TRZ**,[6] the Ax conformer is slightly more preferable. Both conformers are characterized by the highly twisted PSeZ donor attached to the plane of the TRZ acceptor. The crucial difference between conformers lies in the orientation and degree of bending of the donor unit relative to the plane of acceptor. In the Ax conformer, the PSeZ unit is twisted by 38.71° and is attached to the TRZ with a dihedral angle 11.78°. The Eq conformer features a slightly reduced folding of the donor (34.6°) and nearly orthogonal chromophore orientation (82.3°). This difference in conjugation gives rise to differences in the electron wavefunction distribution. The orthogonal **D** and **A** orientation of the Eq conformer is also responsible for the moderate HOMO/LUMO decoupling, providing CT characteristics, whereas the MOs of the Ax conformer are more overlapped giving more mixed CT-local character. Furthermore, the equatorial conformer possesses a higher HOMO and a smaller $S_1 \rightarrow T_1$ energy gap compared to the Ax conformer.

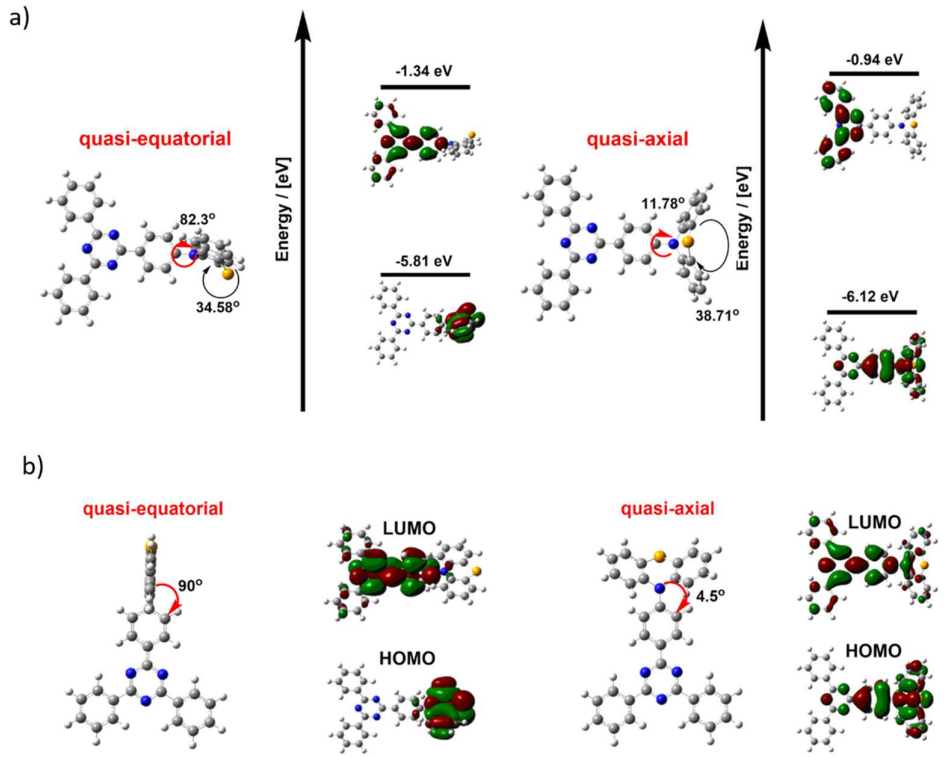

Figure 6.2 – The optimised structures along with profiles, frontier orbitals and corresponding HOMO/LUMO values of the ground state Eq and Ax conformers of PSeZ-TRZ, obtained on the rBMK/6.31G(d) (GS) level of theory; (b) first excited state optimization of Eq and Ax conformers of TRZ-PSeZ (TD rBMK/6.31G(d)).*

Optimization of the first excited state of the conformers provides valuable insights on the relaxation pathways upon excitation. Surprisingly and unlike the case of **PTZ-TRZ**[6] (where computation analysis showed relaxation of both conformers into the same structure in the S_1 state), the conformers of **PSeZ-TRZ** undergo different relaxation routes (Figure 6.2b). While the Eq conformer features planarization of the PSeZ donor in a 90º angle with the acceptor, the Ax retains its original conformational structure, while minimizing the angle between **D** and **A** units (4.5º). Correspondingly, the Eq conformer shows good HOMO/LUMO decoupling in the S_1 state, while the wavefunctions of the Ax are delocalized.

The two conformers also have different theoretical UV/Vis absorption spectra (Figure 6.3). While the absorption of the Eq conformer peaks at 256 nm, the spectrum of the Ax consists of two distinct bands and is significantly redshifted. However, the $S_0 \rightarrow S_1$ excitation of the Eq conformer occurs at much lower energy (3.36 eV) than that of the Ax (3.95 eV), even though the oscillator strength of the former is almost zero, mostly due to the delocalised nature of the axial.

*rBMK/6.31G(d) calculated and analysed by Nadzeya Kukhta and Martin R. Bryce from the chemistry department at Durham University.

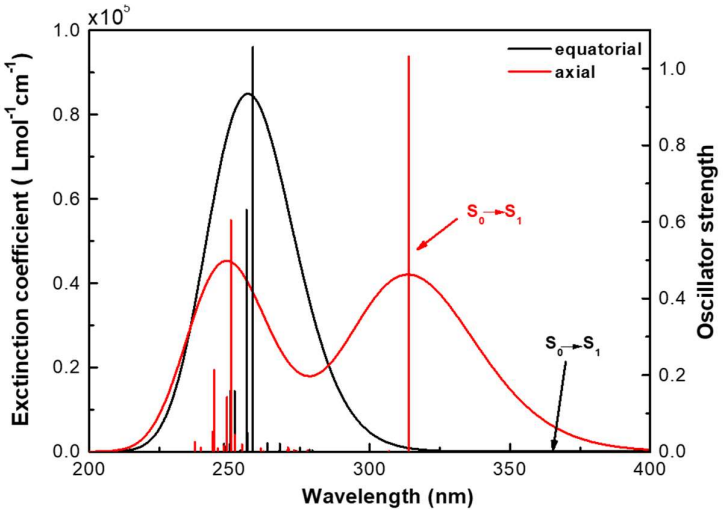

Figure 6.3 – Theoretically calculated UV/Vis spectra along with the oscillator strengths of the electronic transitions of PSeZ-TRZ.[†]

6.4 Photophysical Characterisation

6.4.1 Solution Properties

To evaluate the potential of **PSeZ-TRZ** as a TADF emitter and understand if the Se heavy atom changes the underlying triplet harvesting mechanisms, solution and solid-state photophysics of both materials were studied. Figure 6.4a) shows the absorption of **PSeZ-TRZ** in dichloromethane (DCM) together with the absorption of each individual unit. The absorption of **PSeZ-TRZ** shows two distinct features: the first at around 275 nm is assigned to the overlap of the absorption of both units and the second at around 350 nm, which is a combination of CT absorption and the conjugation-induced redshift of the PSeZ in the Ax conformer, as seen by the theoretical UV-Vis (Figure 6.3). In solvents with increasing polarity, namely methylcyclohexane (MCH), toluene and DCM (Figure 6.5a), respectively, the low energy band redshifts slightly, typical of a transition with mixed nπ* and ππ* characters (Chapter 4).[18,19]

Figure 6.4b) shows the photoluminescence (PL) of **PSeZ-TRZ** in the three different solvents (excitation 355 nm) to understand the induced dipole moment and strength of the CT state it gives rise to. Two distinct sets of peaks appear in each solvent. In the non-polar MCH, there is clear vibronic structure in both bands that is usually assigned to a local excited singlet state (^{1}LE) or mixing of the local and CT states. Upon increasing of polarity – to toluene and DCM – both these bands obtain a gaussian shape and redshift. This solvent-dependent dual

[†] Theoretical UV/Vis spectra calculated and analysed by Nadzeya Kukhta and Martin R. Bryce from the chemistry department at Durham University.

emission confirms the existence of two conformers as found in the molecular structure analysis: a higher energy CT axial (CT_{Ax}) and a lower energy CT equatorial (CT_{Eq}).[4] The high energy possesses a small overlap with the donor (Figure 6.5b) and redshifts less than the low energy one. These data are in line with the simulations (Figure 6.3) where there is strong evidence of charge-transfer with high LE character and therefore decreased strength of CT. Both absorption and emission show similar features to the photophysical characterisation of **PTZ-TRZ** where absorption and emission is identical with that of **PSeZ-TRZ**: two different features in absorption and dual emission confirmed to be from two different conformations.[1]

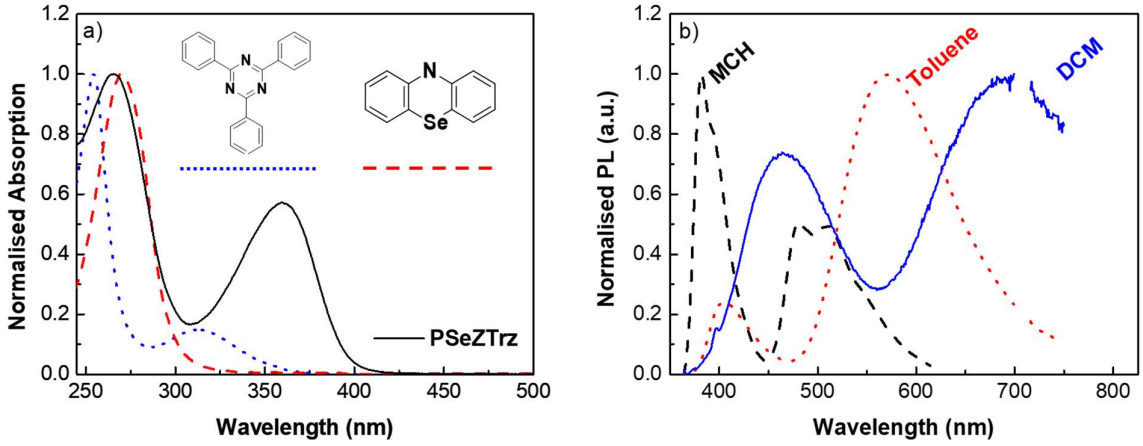

Figure 6.4 – a) Normalised absorption (black straight line) of PSeZ-TRZ overlapped with each individual subunit, 1,3,5-triphenyl-2,4,6-triazine (blue dotted line) and phenoselenazine (red dashed line). b) Normalised photoluminescence (PL) in different solvents: methylcyclohexane (MCH), toluene and dichloromethane (DCM). Excitation at 355 nm.‡

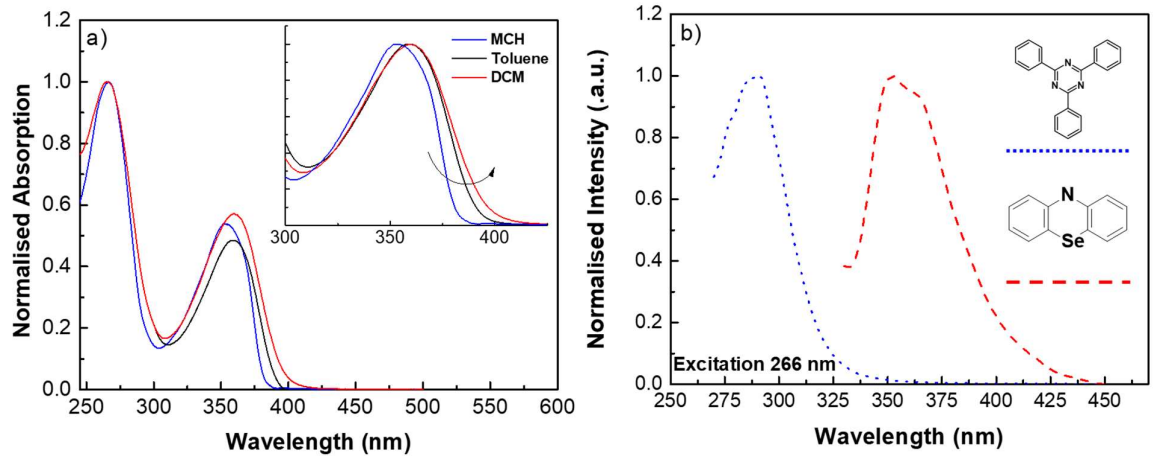

Figure 6.5 – a) Normalised absorption of PSeZ-TRZ in methylcyclohexane (MCH), toluene and dichloromethane (DCM). Inset shows the low energy band (between 300 and 450 nm) showing a positive solvatochromatic effect with polarity. b) Normalised PL intensity of 1,3,5-triphenyl-2,4,6-triazine (blue dotted line) and phenoselenazine (red dashed line) in a DCM solution. Excitation 260 nm.

‡ These spectra are normalised with the purpose of understanding the shift in each band. Therefore, the actual relative intensity may differ from the actual emission spectra.

6.4.2 Solid-state properties

Solid-state analysis was performed on a 1% w:w blend of **PSeZ-TRZ** in a non-polar host environment (zeonex). The time and spectrally resolved emission intensity were recorded at different temperatures between 80 to 320 K – Figure 6.6. This provided the prompt (PF), delayed (DF) fluorescence and phosphorescence (PH) contributions and therefore the energy levels related to the expected emission mechanisms in **PSeZ-TRZ**.

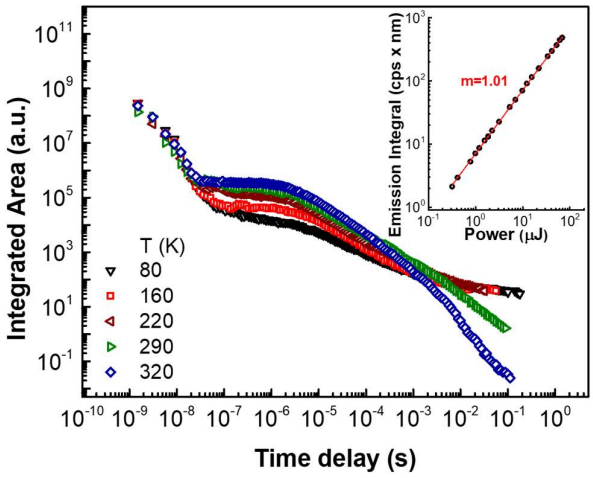

Figure 6.6 – Time-resolved emission decay curves of PSeZ-TRZ in a zeonex matrix excited at 355 nm and at temperatures between 80 and 320 K from 3 ns to 100 ms. Inset shows the emission dependence with laser fluence at room temperature between 35 and 550 ns, assigned as the delayed fluorescence (DF) region.

Figure 6.6 shows two distinct decays, PF and DF, the second being temperature dependent, as seen by the increase in intensity between 80 and 320 K. The emission spectra at 80 and 290 K were studied in more depth and area normalised emission at different time delays (TD) are plotted together with the respective decays (Figure 6.7). At 80K (Figure 6.7a) and very short TD (I - 3 to 100 ns), a fast component with high energy is followed by the appearance of another species at lower energies. This second species increases in intensity at higher TD (II – 100 to 1.000 ns and III – 1.000 to 10.000 ns) showing a small degree of structure. Above a TD of 10 μs (IV – 10 to 100 μs), the emission undergoes a slight shape change that is assigned to the appearance of a fast phosphorescence (PH) component, which then turns into a slower PH (V – above 100 μs) where a clear isoemissive point indicates contribution from two separate states. At 290 K (Figure 6.7b), in region I, the second band rises faster and becomes more intense, showing more clearly a second isoemissive point. It is also clear that from the very earliest time, the emission has a higher local character in the Ax as opposed to the Eq – Figure 6.4b, which decays fast. Regions II, III and IV instead show a single gaussian-shaped emission.

At the latest times (region V), the well-structured RTP grows in again with an associated isoemissive point.

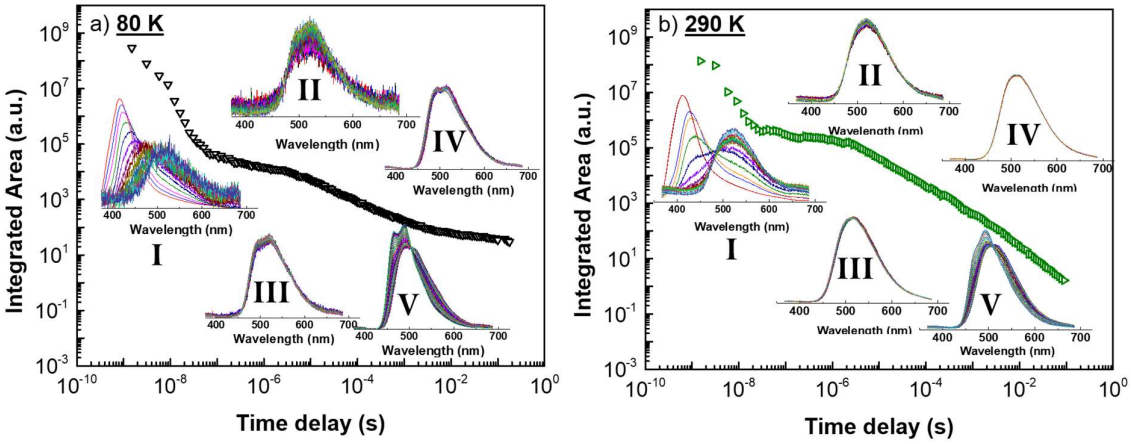

Figure 6.7 – Area normalised emission spectra of PSeZ-TRZ in different stages of its time-resolved decay curves at a) 80 K and b) 290 K. From early ns to late ms, each region is divided by different Time Delays (TD): I. 3 – 100 ns; II. 100 – 1.000 ns; III. 1 – 10 µs; IV. 10 – 100 µs; V. 0.1 – 100 ms.

Looking in more detail at region I (Figure 6.8a), a vestigial Eq emission can be seen at the earliest times of the emission. At 12 ns (Figure 6.8b), two species can clearly be distinguished. Therefore, an isoemissive point forms after a short induction time, corresponding to the stabilisation of the CT states.

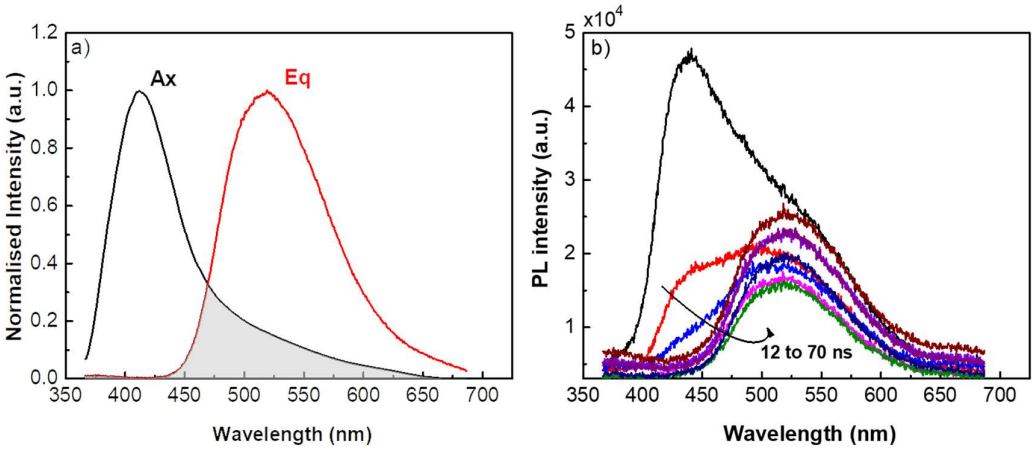

Figure 6.8 – a) Normalised intensity of the axial (Ax) and equatorial (Eq) taken at different time delays. The overlapped grey area indicates that there is still contribution of Eq even at the earliest times of the emission though it is overshadowed by the high intensity Ax emission. b) Photoluminescence (PL) intensity between 12 and 70 ns after excitation. At 12 ns, two different species can be clearly distinguished, proving that the Eq conformer is emitting independently to the Ax.

Comparing these results to the photophysics of **PTZ-TRZ** (Figure 6.9) at room temperature (RT) a similar behaviour to **PSeZ-TRZ** (with some subtle differences) is observed: a much faster decay of the Ax conformer is followed by strong Eq emission (Figure 6.9a) and the appearance of a weaker RTP at very long times (Figure 6.9b). This faster component of

PTZ-TRZ may be a result of a much higher LE character of the Ax conformer (Figure 6.9c), evidenced by the relative redshifted PL emission of the PTZ unit (Figure 6.9d) compared to PSeZ (Figure 6.5b).

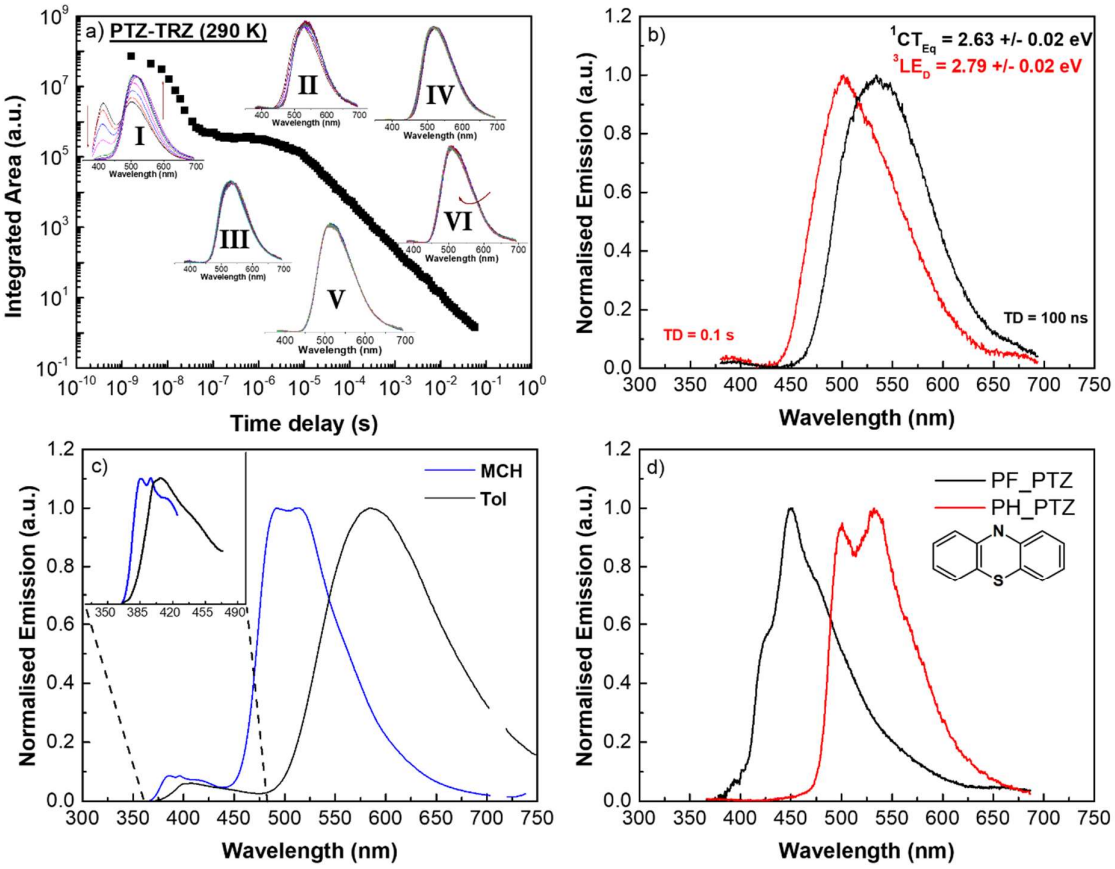

Figure 6.9 – Photophysics of PTZ-TRZ:

a) Decay profile of PTZ-TRZ in a 1% w:w matrix of zeonex at room temperature (RT). From early ns to late ms, each region is divided by I. -2.7 – 12.3 ns; II. 12.3 – 100 ns; III. 0.1 – 10 µs; IV. 10 – 1000 µs; V. 1 – 10 ms; VI. 10 – 100 ms. A TD below 0 ns means we are considering phenomena that is happening before the maximum of the excitation laser (Chapter 2).

b) Normalised emission of PTZ-TRZ at different time delays (TD) at RT. At a TD = 100 ns, a gaussian-like emission assigned to a relaxed charge transfer (^{1}CT) singlet state is identified, with an onset energy of 2.63 ± 0.02 eV. At a TD = 100 ms, a structured emission, a blueshifted from the CT is visible assigned as room temperature phosphorescence (RTP) with an onset energy of 2.79 ± 0.02 eV.

c) Polarity-dependant photoluminescence (PL) spectra of PTZ-TRZ in methylcyclohexane (MCH) and toluene under a 355 nm excitation. Similarly to PSeZ-TRZ, the emission profile shows two bands, a high energy CT_{Ax} that strongly overlaps with the emission band of PTZ and a low energy band CT_{Eq}. While the Ax emission possesses a higher local character, the Eq emission shows strong solvatochromism.

d) Prompt fluorescence (PF) and phosphorescence (PH) spectrum of phenothiazine (PTZ) donor. Excitation at 266 nm.

Considering the PF of both **PSeZ-TRZ** and **PTZ-TRZ**, a question that arises is the origin of these two CT states. Three scenarios are considered: 1) do the states co-exist and emit independently with different lifetimes, a theory experimentally described by dos Santos *et al.*,[4] or 2) in the excited state, does energy transfer feed the CT_{Ax} to CT_{Eq}, stated by Tanaka *et al.*[1]

or 3) according to Chen *et al.*,[6] upon absorption, does the axial conformer undergo molecular relaxation to equatorial? Considering that the concentration of the emitter (either **PSeZ-TRZ** or **PTZ-TRZ**) in zeonex was 1%, the Förster radius is too large to allow any energy transfer, ruling-out scenario number 2). Moreover, the computational analysis showed distinct relaxation behaviours for both conformers. The time-resolved analysis indicates that the appearance of the CT_{Eq} emission becomes faster with the increase of temperature, whereas CT_{Ax} decays more rapidly, suggesting co-existence of the two conformers. With the smaller S heteroatom, the decay of CT_{Ax} becomes even faster (Figure 6.9a), confirming that the Ax conformer possesses a high donor character. The isoemissive point in the area normalised time-resolved emission confirms that the Ax and Eq emission arise from states that are independent of each other. Thus, initial electron transfer from the excited donor unit forms both Ax and Eq states at a fixed branching ratio. Therefore, the Ax conformer decays independently leaving only the emission from the Eq conformer (region I at 80 and 290 K – Figure 6.7), which relaxes more slowly. All DF emission appears to come from the Eq state after this prompt CT_{Eq} emission. Thus scenario 1 appears to fit best the time-resolved emission of both **PSeZ-TRZ** and **PTZ-TRZ**.

Figure 6.10 shows the spectra of **PSeZ-TRZ** relevant to all four different emission pathways. To understand the origin of the PH spectra, the PH of the individual PSeZ donor and the TRZ acceptor, were collected (inset of Figure 6.10b). Increasing the size of the heteroatom enhances the RTP emission (from the ^3LE_D of Figure 6.9b to Figure 6.10b). This confirms that the slow PH comes from the donor and is redshifted from the PH of pure PTZ (onset energy 2.61 ± 0.02 eV) and PSeZ (2.70 ± 0.02 eV) due to conjugation. A conjugated acceptor (wih an onset energy of 3.11 ± 0.02 for pure TRZ to 2.69 ± 0.02 eV) with a fast PH (Figure 6.7) is the species coupling with the ^3CT of both these materials resulting in TADF. Replacing sulphur with selenium therefore enhances the RTP without affecting the TADF efficiency. The two CT emissions have onset energies of 3.40 and 2.74 ± 0.02 eV for the Ax and Eq conformers, respectively while **D** and **A** PH have onset energies of 2.83 and 2.69 ± 0.02 eV respectively. Therefore, the energy gap, $^1CT_{Eq}$-^3LE_A, that mediates rISC is ΔE_{ST} = 0.05 ± 0.04 eV. The excitation power dependence in the DF region (inset of Figure 6.6) gives a slope of 1, obtained between 0.3 and 70 μJ, confirming that the mechanism involved here is indeed thermally-activated (TADF). From this analysis the energy diagram of Figure 6.11 summarises the full **PSeZ-TRZ** and **PTZ-TRZ** behaviours. After excitation of the donor fragment, donor ^1LE emission competes with the electron transfer forming both the CT_{Ax} and CT_{Eq} species. The short-lived and more planar CT_{Ax} conformation undergoes rapid intersystem-crossing (ISC) to

the low lying ^3LE_D state and gives rise to RTP. Concurrently, the orthogonal CT_{Eq} leads to a second short-lived transition, with relaxation to the ground state via radiative (PF) emission and ISC to the ^3LE_A. The small S-T energy-gap of the CT_{Eq} enables efficient rISC, up-converting the exciton back to the CT_{Eq} state where it can decay giving the DF transient.

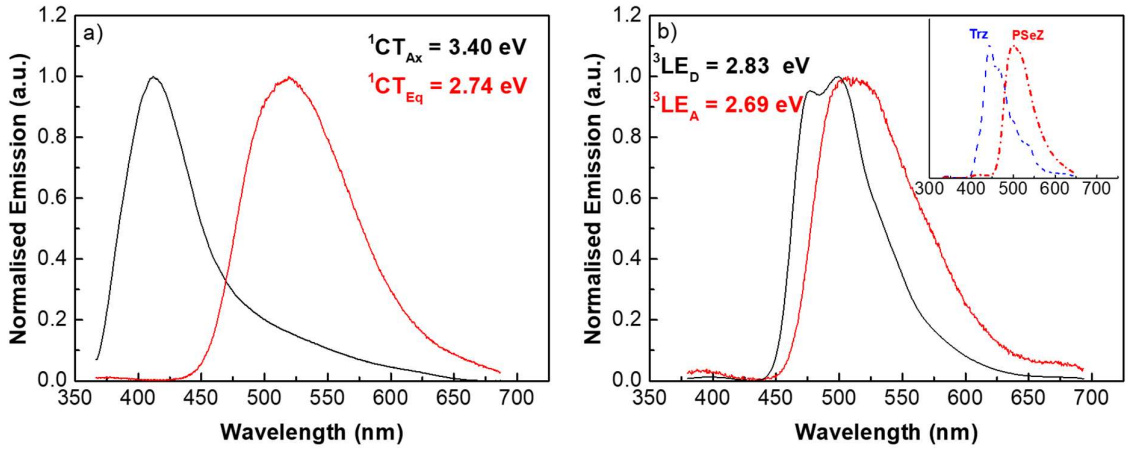

Figure 6.10 - Energy levels (onset) of PSeZ-TRZ taken from the decay profiles. a) Fluorescence spectra of the charge-transfer (CT) conformers at 290 K and b) Phosphorescence (PH) spectra of different PH at 80 K. Onsets with an error of ± 0.02 eV.

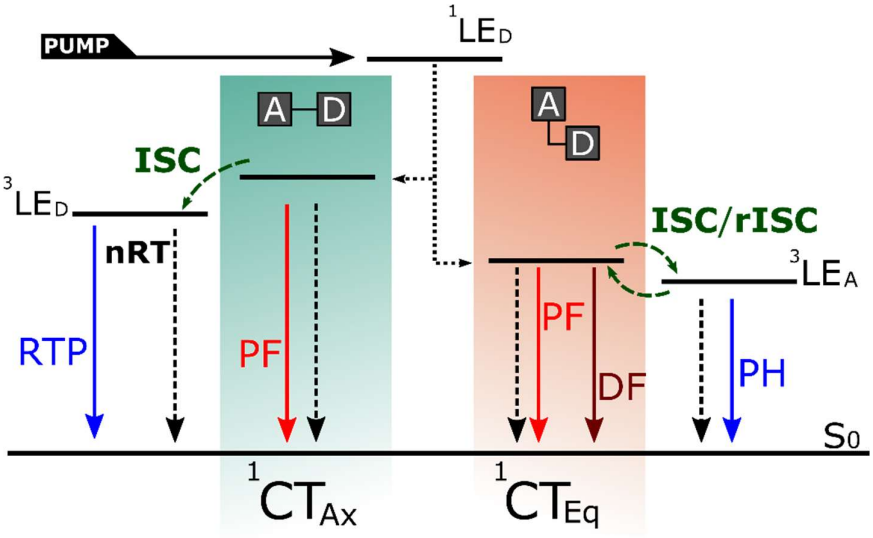

Figure 6.11 – Energy diagram of the mechanisms inherent to PSeZ-TRZ when excited at 355 nm. CT_{ax} – singlet charge transfer axial state; CT_{Eq} – singlet charge transfer equatorial state; ^3LE_A – local excited triplet state of the acceptor; ^3LE_D – local excited triplet state of the donor; S_0 – Ground singlet state; (P)DF – (Prompt) Delayed Fluorescence; nRT – non-radiative transitions; PH – phosphorescence; RTP – room-temperature phosphorescence; (r)ISC – (reverse) intersystem crossing.

6.5 Electroluminescence and OLED Performance

Based on the analysis of the photophysical data, **PSeZ-TRZ** was used as an emitter for organic light-emitting diodes (OLEDs). Cyclic voltammetry of **PSeZ-TRZ** indicates a

HOMO/LUMO levels of -5.43 eV and -2.26 eV, respectively for a band gap of 3.17 eV. Given the relatively small ΔE_{ST} in a low polarity environment (i.e. the CT_{Eq} already being close to the local donor PH), a low polarity host with a triplet higher than **PSeZ-TRZ** energy was used, namely - 3,3-di(9H-carbazol-9-yl)biphenyl (mCBP).[20] Prior to the device production, a series of films of **PSeZ-TRZ** doped in mCBP were prepared with the PL and decays measured to evaluate the extent of any redshift induced by the host and understand if there are different contributions from the scenarios presented in the photophysics section of this work. Results are shown in Figure 6.12 for concentrations of 10, 30 and 50% of emitter in mCBP. The increase of concentration slightly redshifts the CT_{Eq} (Figure 6.12a), suggesting a close packing effect. The relative intensities also change and indicate that the formation CT_{Ax} and CT_{Eq} are also concentration dependent and that the Eq conformation is preferred at higher ratios. Given the relative redshift of the ^3LE_A state in comparison to the CT_{Eq} and this concentration dependence of the CT onset, higher concentrations reduce the resulting energy gap and increase the rISC rate, evidenced in Figure 6.12b. This decrease in energy gap should outcompete any other phenomena and, therefore, scenario 1) still fits best to the performance of **PSeZ-TRZ**.

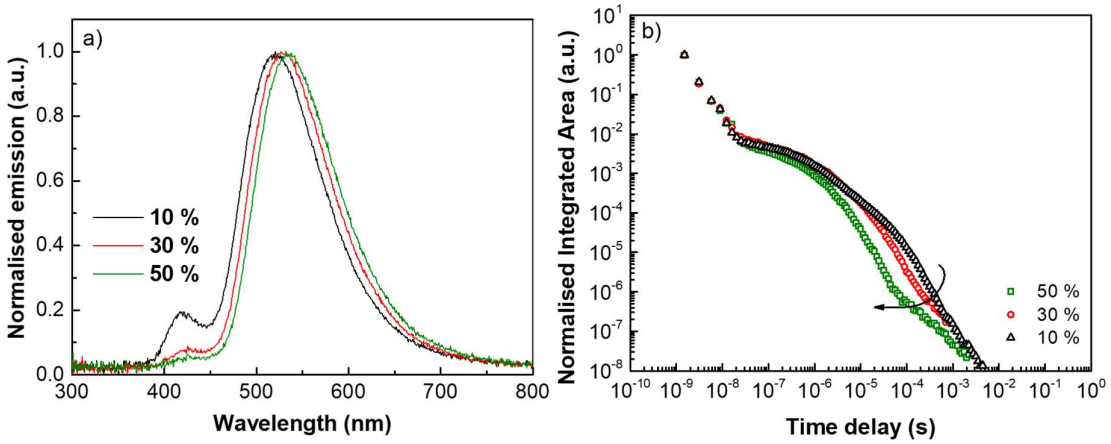

Figure 6.12 – a) Normalised photoluminescence (PL) spectra of PSeZ-TRZ doped films in mCBP at different concentrations: black 10 %, red 30 % and green 50 %. b) Area normalised emission of PSeZTRZ in a mCBP layer at different ratios (10, 30 and 50 %).

Devices were then fabricated and characterised – Figure 6.13 – with an optimised device structure composed of ITO (120 nm)/ PEDOT:PSS (60 nm)/ TAPC (20 nm)/ mCP (10 nm)/ mCBP: **PSeZ-TRZ** (25 nm, x wt%)/ TSPO1 (5 nm)/ TPBi (40 nm)/ LiF (1.5 nm)/ Al (200 nm) (energy diagram in Figure 6.13a) with concentrations (x) of 10, 30 and 50% of **PSeZ-TRZ** in mCBP.

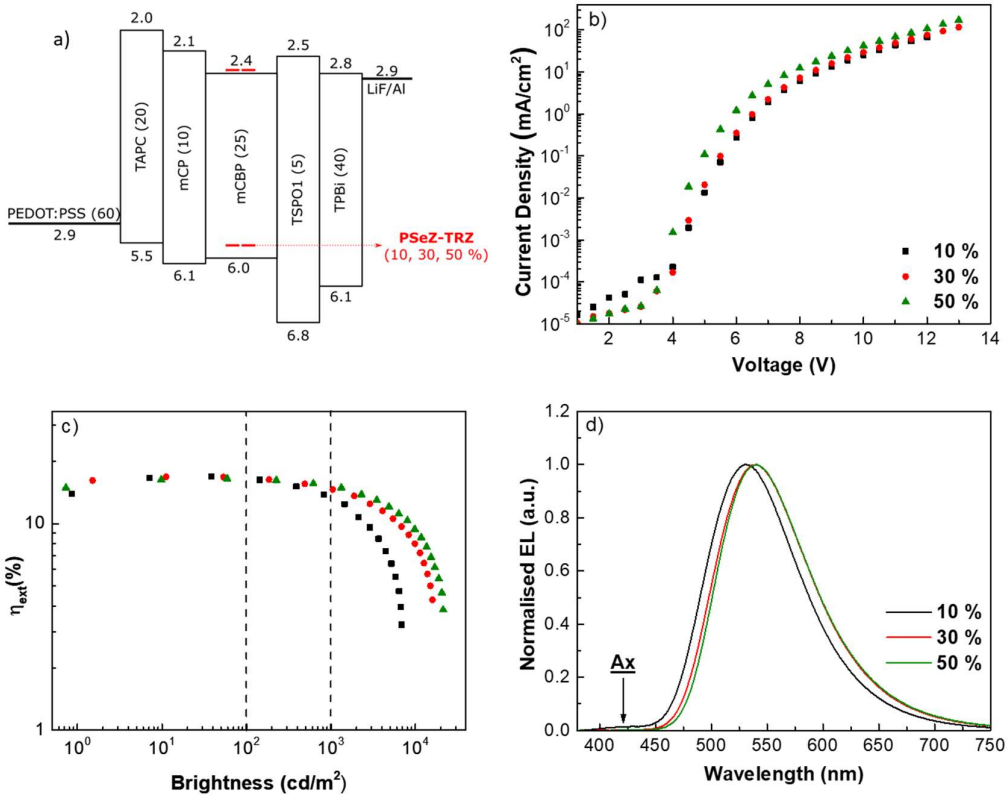

Figure 6.13 – Device performance of PSeZ-TRZ in different concentrations (10, 30 and 50 % wt.). a) Energy diagram of device produced; b) Current density-Voltage; c) External quantum efficiency over brightness; d) Electroluminescence spectra.

From the current density (J)-voltage (V) curves (Figure 6.13b) all three devices have a turn-on voltage between 3 and 4 V. Current-density plots increases with concentration, although with values relatively similar in all three devices. In terms of external quantum efficiency (η_{ext}), Figure 6.13c), the maximum η_{ext} was 16.9 % for 10 % doping, 16.8 % for 30 %, and 16.5 % for 50 %. At 100 cd/m^2 the efficiencies dropped to 16.5 % for all concentrations and at 1,000 cd/m^2 to 13.3 % (10 %), 14.6 (30 %) and 15.3 (50 %). Therefore, although there is no big difference between the different doping concentrations in terms of maximum η_{ext}, here averaging 17 %, the resistance to roll-off increases with increase in concentration. While 10% doping showed a drop of about 21 % from the maximum η_{ext}, 30 % and 50% loading smaller decreased drops in efficiency, 13 % and 7 %, respectively between maximum and 1,000 cd/m^2, a good roll-off. The electroluminescence (EL) spectra of the three devices in Figure 6.13d) shows the main CT_{Eq} yellow-green emission slightly redshifting with the concentration and a vestigial CT_{Ax} appearing only in the device with 10 % loading. The absence of a more pronounced CT_{Ax} emission is explained by the Eq energy gap being smaller than that of the Ax conformer, i.e. it preferentially charge traps whereas no direct Ax population

leads to no charge recombination. This may also influence roll-off, and the decrease in charge population of the Ax leads to increased exciton density in the Eq and that may explain why 50 % loading resulted in the best performing device. These devices are not as efficient as other reports on green or yellow devices,[21,22] as the interplay between all 4 states is expected to induce quenching channels for part of the excitons formed (particularly within the Ax conformer) decreasing the internal quantum efficiency. TADF is the main contributor to the DF mechanism, and the result is η_{ext} above the upper 5 % limit of fluorescent devices.[23]

As a final test to understand the heavy atom effect on the device performance of this **D-A** system, devices based on **PTZ-TRZ** were also evaporated with the same device structure and concentrations to compare with the best performing device of the **PSeZ-TRZ** group in terms of maximum η_{ext} – Figure 6.14. Firstly, the performance dependence with loading of **PTZ-TRZ** devices (Figure 6.14a) sees the best performance at 10 % as the EL spectrum is the most blueshifted (and hence closest to the ^{3}LE). Current-density (Figure 6.14b) and η_{ex} (Figure 6.14c) show similar results for both emitters. The electroluminescence (EL) spectra of both (inset of Figure 6.14b) shows the same CT_{Eq} only slightly redshifted for PTZ-TRZ. Thus, at 17% η_{ext}, heavy atom effect has little quenching effect on the efficiency of both materials, in accord with the finding that selenium (and sulphur) only affects donor phosphorescence and not rISC.

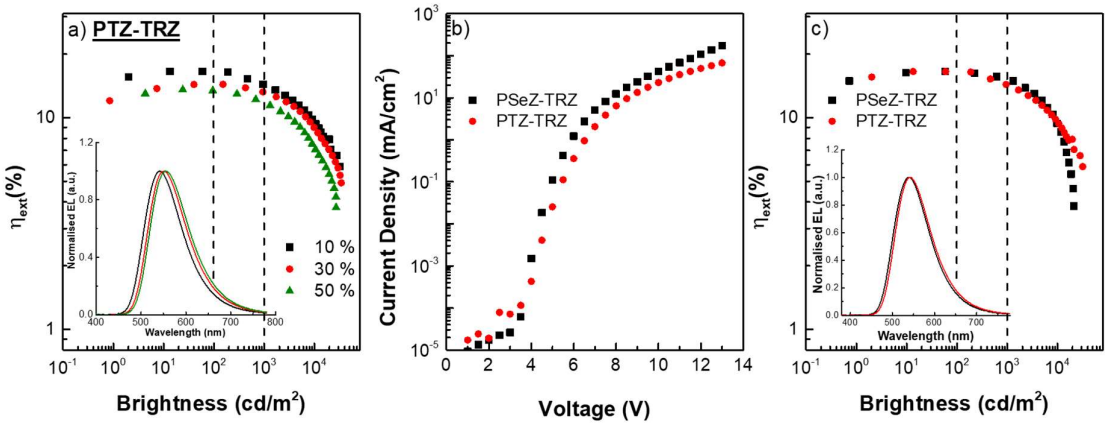

Figure 6.14 – a) Device performance of PTZ-TRZ in different concentrations (10, 30 and 50 % wt.%), b) current density(J)-voltage(V) and b) external quantum efficiency (η_{ext})-brightness of devices based on PSeZ-TRZ (black square dots) and PTZ-TRZ (red circle dots). For each emitter, the optimised host:guest ratio was chosen in terms of maximum η_{ext}: 10 % doping for PTZ-TRZ and 50 % for PSeZ-TRZ. Insets of a) and c) show the normalised electroluminescence (EL) spectra of all devices.

6.6 Conclusion

In conclusion, in this chapter, the main question assumed in this chapter was whether replacing sulphur with a heavier atom such as selenium would influence the TADF performance of this distinctive **D-A** system. The photophysics of **PSeZ-TRZ** in comparison with **PTZ-TRZ** have provided important information on the emission mechanisms involved in molecules that possess CT emission from dual conformers and helped answering this question. The folding of the PSeZ donor is similar to PTZ and therefore **PSeZ-TRZ** shows similar photophysics to **PTZ-TRZ**. However, the replacement of sulphur with a bulkier selenium atom, distinctively differentiates the excited state relaxation of both conformers. **PSeZ-TRZ** shows two different relaxation dynamics with both excited states showing distinct HOMO/LUMO separations: the Ax is more planar and therefore its higher mixed CT/LE character activates RTP from the donor unit. In contrast, the Eq conformer is more orthogonal and consequently has more decoupled HOMO/LUMO orbitals, resulting in a lower energy CT state and a smaller energy gap with the acceptor triplet, which activates TADF. Such duality provides important insights into the molecular design of these **D-A** molecules to obtain efficient TADF. Moreover, **PTZ-TRZ** behaves similarly, and the subtle differences appear to affect the RTP but not the TADF performance, another evidence for the proposed mechanism of emission of **PSeZ-TRZ**. A degree of control over the optical and electrical properties of devices based on **PSeZ-TRZ** is obtainable, however the efficiency is limited by all the inherent mechanisms, with the η_{ext} peaking at 17% and a roll-off of only 7% at a brightness of 1,000 cd/m^2 that is consistent for both **PSeZ-TRZ** and **PTZ-TRZ**, also sustaining the proposed photophysical mechanism. In conclusion, to answer the question proposed for this chapter, in increasing the size of the heteroatom of the donor, the TADF is unaffected.

6.7 References Chapter 6

1. Tanaka, H., Shizu, K., Nakanotani, H. & Adachi, C. Dual intramolecular charge-transfer fluorescence derived from a phenothiazine-triphenyltriazine derivative. *J. Phys. Chem. C* **118,** 15985–15994 (2014).
2. Tsai, W. L. *et al.* A versatile thermally activated delayed fluorescence emitter for both highly efficient doped and non-doped organic light emitting devices. *Chem. Commun.* **51,** 13662–13665 (2015).
3. Shi, H., An, Z., Shi, H. & Huang, W. Twisted Molecular Structure on Tuning Ultralong Organic. (2018). doi:10.1021/acs.jpclett.7b02953
4. dos Santos, P. L., Ward, J. S., Batsanov, A. S., Bryce, M. R. & Monkman, A. P. Optical and

Polarity Control of Donor-Acceptor Conformation and Their Charge-Transfer States in Thermally Activated Delayed-Fluorescence Molecules. *J. Phys. Chem. C* **121,** 16462–16469 (2017).

5. Etherington, M. K. *et al.* Regio- and conformational isomerization critical to design of efficient thermally-activated delayed fluorescence emitters. *Nat. Commun.* **8,** 14987 (2017).

6. Chen, D. G. *et al.* Revisiting Dual Intramolecular Charge-Transfer Fluorescence of Phenothiazine-triphenyltriazine Derivatives. *J. Phys. Chem. C* **122,** 12215–12221 (2018).

7. dos Santos, P. L., Etherington, M. K. & Monkman, A. P. Chemical and conformational control of the energy gaps involved in the thermally activated delayed fluorescence mechanism. *J. Mater. Chem. C* **6,** 4842–4853 (2018).

8. Acar, N. *et al.* Phenothiazine−Pyrene Dyads: Photoinduced Charge Separation and Structural Relaxation in the CT State. *J. Phys. Chem. A* **107,** 9530–9541 (2003).

9. Stockmann, A. *et al.* Conformational Control of Photoinduced Charge Separation within Phenothiazine−Pyrene Dyads. *J. Phys. Chem. A* **106,** 7958–7970 (2002).

10. Daub, J. *et al.* Competition between Conformational Relaxation and Intramolecular Electron Transfer within Phenothiazine−Pyrene Dyads. *J. Phys. Chem. A* **105,** 5655–5665 (2001).

11. Wang, K. *et al.* Control of Dual Conformations: Developing Thermally Activated Delayed Fluorescence Emitters for Highly Efficient Single-Emitter White Organic Light-Emitting Diodes. *ACS Appl. Mater. Interfaces* **10,** 31515–31525 (2018).

12. Etherington, M. K., Gibson, J., Higginbotham, H. F., Penfold, T. J. & Monkman, A. P. Revealing the spin–vibronic coupling mechanism of thermally activated delayed fluorescence. *Nat. Commun.* **7,** 13680 (2016).

13. Huang, R. *et al.* The influence of molecular conformation on the photophysics of organic room temperature phosphorescent luminophores. *J. Mater. Chem. C* **6,** 9238–9247 (2018).

14. Huang, R. *et al.* The contributions of molecular vibrations and higher triplet levels to the intersystem crossing mechanism in metal-free organic emitters. *J. Mater. Chem. C* **5,** 6269–6280 (2017).

15. Ward, J. S. *et al.* The interplay of thermally activated delayed fluorescence (TADF) and room temperature organic phosphorescence in sterically-constrained donor–acceptor charge-transfer molecules. *Chem. Commun.* **52,** 2612–2615 (2016).

16. Tanaka, H., Shizu, K., Miyazaki, H. & Adachi, C. Efficient green thermally activated delayed fluorescence (TADF) from a phenoxazine-triphenyltriazine (PXZ-TRZ) derivative. *Chem. Commun.* **48,** 11392–11394 (2012).

17. Kretzschmar, A., Patze, C., Schwaebel, S. T. & Bunz, U. H. F. Development of Thermally Activated Delayed Fluorescence Materials with Shortened Emissive Lifetimes. *J. Org. Chem.* **80,** 9126–9131 (2015).

18. Higginbotham, H. F., Yi, C. L., Monkman, A. P. & Wong, K. T. Effects of Ortho-Phenyl Substitution on the rISC Rate of D-A Type TADF Molecules. *J. Phys. Chem. C* **122,** 7627–7634 (2018).

19. dos Santos, P. L., Ward, J. S., Bryce, M. R. & Monkman, A. P. Using Guest–Host Interactions To Optimize the Efficiency of TADF OLEDs. *J. Phys. Chem. Lett.* **7,** 3341–3346 (2016).

20. Bagnich, S. A., Rudnick, A., Schroegel, P., Strohriegl, P. & Köhler, A. Triplet energies and excimer formation in meta- and para-linked carbazolebiphenyl matrix materials. *Philos. Trans. R. Soc. A Math. Phys. Eng. Sci.* **373,** (2015).

21. Dias, F. B. *et al.* The role of local triplet excited states and D-A relative orientation in thermally activated delayed fluorescence: Photophysics and devices. *Adv. Sci.* **3,** 1600080 (2016).

22. dos Santos, P. L. *et al.* Triazatruxene: A Rigid Central Donor Unit for a D-A 3 Thermally Activated Delayed Fluorescence Material Exhibiting Sub-Microsecond Reverse Intersystem Crossing and Unity Quantum Yield via Multiple Singlet-Triplet State Pairs. *Adv. Sci.* **5,** 1700989 (2018).

23. de Sa Pereira, D., Data, P. & Monkman, A. P. Methods of Analysis of Organic Light Emitting Diodes. *Disp. Imaging* **2,** 323–337 (2017).

Chapter 7: Electroabsorption Spectroscopy as a Tool to Probe Charge-Transfer and State-mixing in TADF Emitters

Solid-state electroabsorption measurements (Stark spectroscopy) were used to probe the charge-transfer character and state-mixing in the low energy optical transitions of two structurally similar thermally-activated delayed fluorescent (TADF) emitters with divergent photophysical and device performances. Applying the Liptay model to fit the differentials of the low energy absorption bands to the measured electroabsorption spectra, both emitters show very strong charge-transfer characteristics with large associated changes of dipole moments on excitation - even when the associated absorption band appears structured and excitonic-like. The high electric field also resulted in transfer of oscillator strength from the charge-transfer to a neighbouring state in the molecule with efficient TADF properties. With supports through TDDFT-TDA and DFT/MRCI calculations, this state showed $\pi\pi^*$ character as expected of a local acceptor triplet state that strongly mixes with the $\sigma\pi^*$ charge-transfer state. The emitter with poor TADF performance showed no evidence of such mixing. Electroabsorption spectroscopy is thus a powerful tool to gain in-depth understandings into the electronic transitions associated with TADF, enhancing design rules for high efficiency emitters.

The work presented in this chapter was published in The Journal of Physical Chemistry Letters, Daniel de Sa Pereira, Christopher Menelaou, Andrew Danos, Christel Marian and Andrew P. Monkman, **Electroabsorption as a Tool to Probe Charge Transfer and State Mixing in Thermally-Activated Delayed Fluorescence Emitters**, Journal of Physical Chemistry Letters, 2019, 10, 3205−3211. Daniel de Sa Pereira conducted the sample production and characterization using both materials together with Christopher Menelaou who also wrote the software to perform the measurements. Data treatment and analysis was carried out by Daniel de Sa Pereira and Andrew P. Monkman with contributions from Andrew Danos. All TDDFT-TDA and DFT/MRCI calculations were made by Christel Marian.

7.1 Introduction

This thesis has so far focused on the impact of structural features on thermally-activated delayed fluorescence (TADF) emitters in their photophysical and electrical performances. This was done by correlating molecular geometry with delayed fluorescence (DF) and device performances and by identifying small details that greatly affect their TADF mechanism. Continuing this trend, this chapter dives into an advanced physical approach of comparing TADF emitters that examines the mixing of states (optically-allowed or optically-forbidden) that are inherent to these molecules. This is achieved by implementation of Electroabsorption (EA) spectroscopy techniques. Details on the theory and experimental aspects of setting up an EA technique can be found in Chapters 2 and 3, respectively.

EA (also known as absorbance Stark spectroscopy) measures changes in absorption caused by a perturbing external electric field – in particular through peak shifts and line-shape changes – as the field mixes the ground and excited state wavefunctions.[1] Following the fundamental analysis proposed by Liptay,[2] by fitting the zeroth, first, and second differentials of the absorption spectra to the EA spectra, these changes allow determination of parameters such as the change in electric dipole moment ($\Delta\mu$) and polarizability ($\Delta\alpha$) on excitation caused by the perturbing field. EA also reveals the character of the excited states formed on optical transitions, (Figure 7.1a) [3] and therefore becomes particularly interesting for determining the origin of different types of excitons (such as Frenkel or CT), the latter being of interest in TADF.[4,5] As optical absorption is used to measure these perturbation effects, only instantaneous changes are determined. In this sense, the EA measurement is simple and free from complications associated with both internal and host mediated relaxation processes in the excited state.[6]

In this chapter, the solid-state EA spectra of two donor-acceptor-donor (**D-A-D)** materials with a common dibenzo[*a,j*]phenazine (DBPHZ) **A** core and either phenoxazine (POZ) or *tert*-butyl-carbazole (*t*-BuCz) **D** units were analysed (Figure 7.1b). **POZ-DBPHZ** was previously found to give good device performance (maximum η_{ext} of 16% in the orange)[7] as well as complex mechanochromic properties.[8,9] Moreover, the EA spectra are supported by high level time-dependent density functional theory – Tamm-Dancoff approximation (TDDFT-TDA) and density functional theory and multireference configuration interaction (DFT/MRCI) calculations to help bridge with the experimental findings of this work.

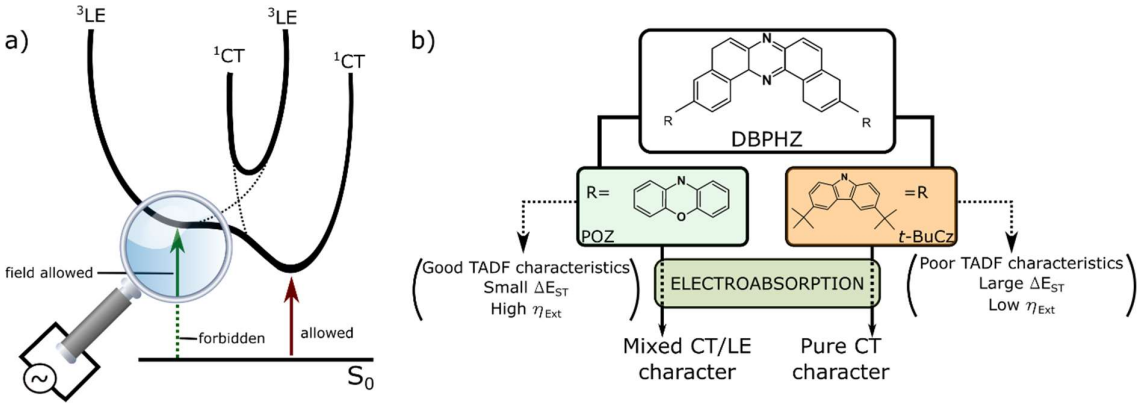

Figure 7.1 – Chapter 7 project diagram. a) Electroabsorption (EA) spectroscopy is particularly interesting to the probe the charge-transfer character and state mixing of materials. This state mixing gives rise to transfer of oscillator strength to a normally-forbidden transition and thus becoming measurable under an applied field. b) Two Donor-Acceptor-Donor (D-A-D) with a common A, dibenzo[*a,j*]phenazine (DBPHZ), and either phenoxazine (POZ) or *tert*-butyl-carbazole (*t*-BuCz) as donor units showing opposite TADF performances, were analysed through EA and bridged with their performance.

7.2 Results and Discussion

7.2.1 Solid-state Absorption

POZ-DBPHZ and ***t*-BuCz-DBPHZ**, were chosen for this study due to their similar structures (sharing the same acceptor core) yet distinct TADF properties; while the former gives efficient TADF and OLEDs, with an external quantum efficiency of 16%, ***t*-BuCz-DBPHZ** has much weaker TADF and OLED performance *ca.* 8%.[7] This is in part due to the difference in ΔE_{ST} gap of 0.03 eV of **POZ-DBPHZ** compared to the 0.33 eV of ***t*-BuCz-DBPHZ**. Here, EA spectroscopy is used to bridge further how the differences in structure and energy levels lead to changes in TADF and device performance.

Figure 7.2 shows the absorption spectra of both **POZ-DBPHZ** and ***t*-BuCz-DBPHZ**. As seen elsewhere throughout this thesis, it is very common for these intramolecular CT molecules to have absorption simply as a superposition of **D** and **A** unit absorption – an indication of the effective electronic decoupling required for charge-transfer.[10] Therefore in **POZ-DBPHZ** (Figure 7.2a) the peaks above 4 eV and between 2.9-3.5 eV correlate to the ππ* absorptions also observed in the pure DBPHZ **A**, along with a slight contribution from the ππ* absorption of the POZ **D** between 3.5 and 4 eV. At lower energies an extra low intensity band with a gaussian line shape appears, assigned to a direct CT absorption, typical of **D-A-D** systems (Chapters 4-6).[6,11,12] In ***t*-BuCz-DBPHZ** (Figure 7.2b), the absorption is composed of three bands, however none overlap with either the **D** nor the **A**, hinting at a higher conjugation.

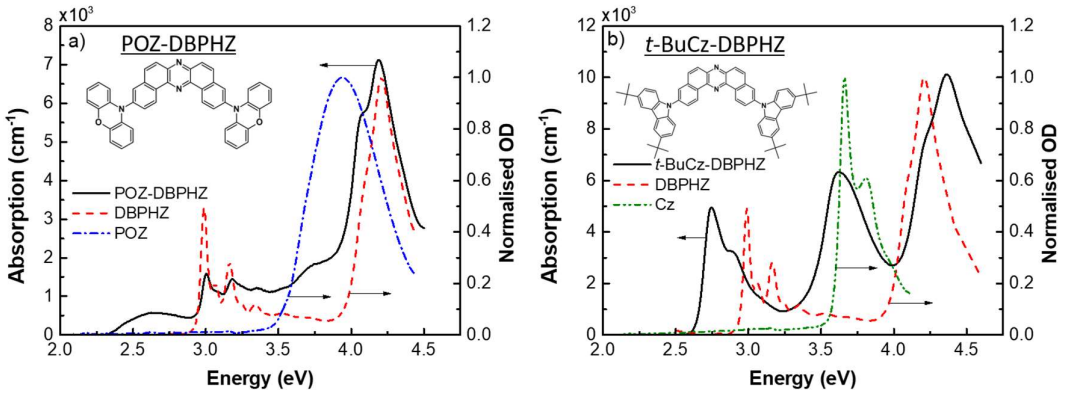

Figure 7.2 – Absorption spectra of a) POZ-DBPHZ and b) *t*-BuCZ-DBPHZ in a zeonex matrix and respective molecular structures (inset). The normalised absorption of DBPHZ (red dashed lines), POZ (blue dot-dashed line) and CZ (green dot-dot-dashed line) are also shown. The absorption was collected on samples similar to the ones used in Electroabsorption measurements. Details on the calculation of the absorption coefficient can be found in Chapter 3.

In Chapters 4 and 5, the effects of lower **D-A** dihedral angles (β) on the performance of TADF-based emitters were shown. In **POZ-DBPHZ**, the x-ray analysis shows the **D-A** β to be close to 90º in the ground state,[7] whereas in ***t*-BuCz-DBPHZ**, this angle is around 60º, meaning that differences in emitters' TADF performance are expected (Figure 7.1). Thus, any CT excited state in ***t*-BuCz-DBPHZ** should have far more local exciton character,[13] with π delocalisation across the **D-A** bond and hence a greater oscillator strength than **POZ-DBPHZ**.[14] This **D-A** conjugation should redshift the DBPHZ absorption and introduce weak CT character to the transition instead of creating a wholly new, direct CT absorption feature. With carbazole, the non-bonding *n* electrons delocalise into the carbazole ring, potentially limiting the formation of a direct CT transition below the DBPHZ absorption.

7.2.2 Solid-state Electroabsorption

Figure 7.3 shows the EA spectra of both a) **POZ-DBPHZ**, and b) ***t*-BuCz-DBPHZ**. The spectra are characterised by high intensity and low energy EA bands and high energy bands that possibly resemble those coming from the **D** and **A.** Without measuring the EA on both units it is not possible to confirm this statement, however due to difficulties in sample production such EA spectra were not possible to collect. Moreover, at high energies, the spectra are complex and cannot be described well using Liptay analysis. This model considers transitions to a series of non-interacting excited states and their associated transitions which cannot take into account optically-forbidden states that are not featured in the absorption spectrum.[2] As a result, a simple Liptay model assuming separately **D** and **A** responses is not enough to fit the entire spectrum. As can be seen from Figure 7.3, the full EA spectrum of

POZ-DBPHZ is also far more complex than ***t*-BuCz-DBPHZ**, suggesting complex phenomena within the CT absorption band, such as strong state-mixing and transfer of oscillator strength across the whole ππ* spectral region. A more comprehensive sum-over-states model was considered,[15] but fitting such complex spectra was deemed beyond the scope of this initial study.

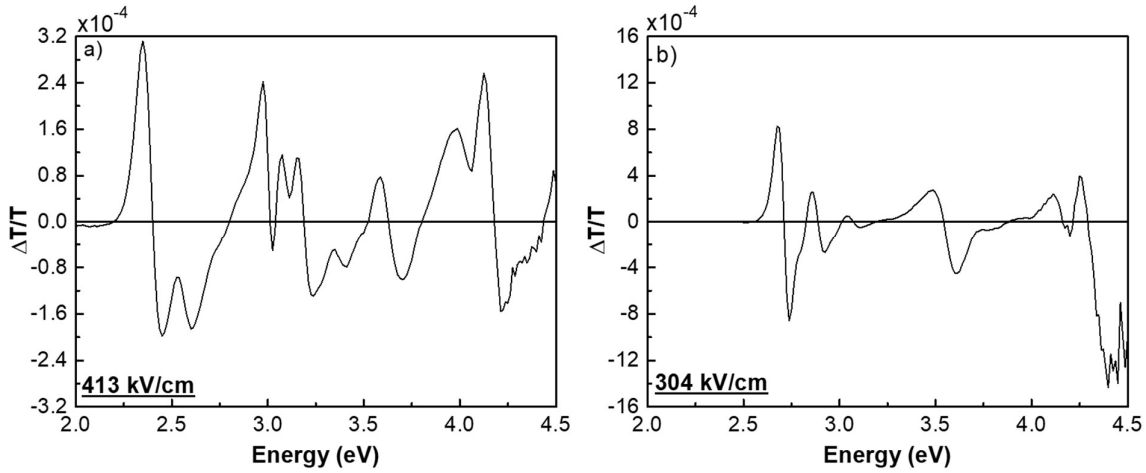

Figure 7.3 – Full Electroabsorption spectra of a) POZ-DBPHZ at 95 V and b) *t*-BuCz-DBPHZ at 70 V. Sample thickness was about 2.3 µm, Chapter 3.

Instead, by focusing this analysis on the low energy absorption bands the Liptay model may be applicable given the lower number of states involved. For this, the absorption bands of both molecules below 3.2 eV were reconstructed with a set of gaussian components, Figure 7.4 as described in the experimental section (Chapter 3).

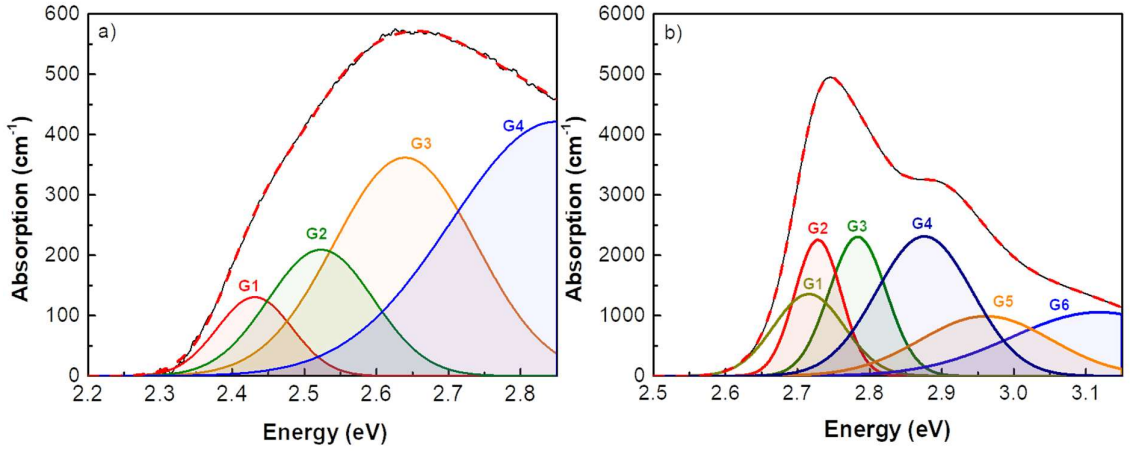

Figure 7.4 – Gaussian deconstruction of the CT absorption band of a) POZ-DBPHZ and b) *t*-BuCz-DBPHZ. Each gaussian distribution and their relative weight is fit such that the sum (dashed red line) faithfully reproduces the experimental absorption line (full black line). More details on this deconstruction can be found in Chapter 3.

Using the analytic derivatives of the fitted gaussians, the first and second differentials of the low energy absorption spectra were calculated (insets of Figure 7.5). Least squares fitting allowed a sum of zeroth, first and second differentials to reconstruct the experimental EA spectra (Chapter 3) and the results are shown in Figure 7.5.

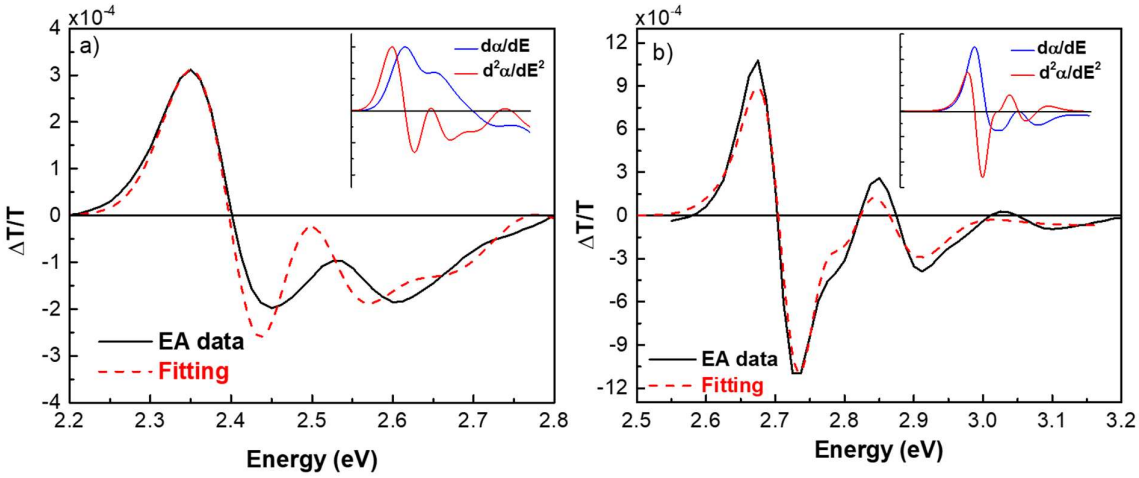

Figure 7.5 – Low energy band Electroabsorption (full black line) spectra of a) POZ-DBPHZ and b) t-BuCz-DBPHZ overlapped with the fitting (dashed red line) using the model described in the Stark Spectra analysis section (Chapter 3). For comparison purposes, the inset of both figures shows the first and second derivatives of the lowest energy absorption bands calculated from the gaussian deconstruction (Figure 7.4).

At first glance the EA spectra of both a) **POZ-DBPHZ**, and b) ***t*-BuCz-DBPHZ** predominantly follow the second derivative of the absorption spectra, showing both materials have strong CT character associated with the lowest energy absorption bands. **POZ-DBPHZ** (Figure 7.5a) does not fit entirely well (particularly in the region above 2.45 eV) suggesting the existence of contributions from optically-forbidden states that overlap with the main CT electroabsorption band. The ***t*-BuCz-DBPHZ** EA spectrum in comparison is reproduced very well and is almost a pure 2nd order response (i.e. CT character, Figure 7.5b).

For **POZ-DBPHZ**, by calculating the residuals between the best fit and the experimental EA a non-Liptay feature is revealed at around 2.45 eV. This indicates transfer of oscillator strength caused by the perturbing electric field coupling a dark state to an allowed transition,[16] Figure 7.6a). A 1st derivative-like feature is observed, between 2.35 and 2.6 eV, centred at around 2.49 eV. Thus, the onset of the corresponding optical transition is estimated to be at 2.35 eV. This transfer of oscillator strength arises from the main CT transition, coupling to an otherwise optically forbidden transition due to the perturbation of the electric field. From the absorption spectrum of **POZ-DBPHZ** (Figure 7.2a) since the lowest energy allowed local transition lies at 3 eV, this new lower energy local transition found in EA has to be optically

forbidden. Further, looking at the phosphorescence spectrum of DBPHZ gives an onset energy of 2.40 eV ± 0.02 eV, strongly fitting with the EA data (Figure 7.6b).

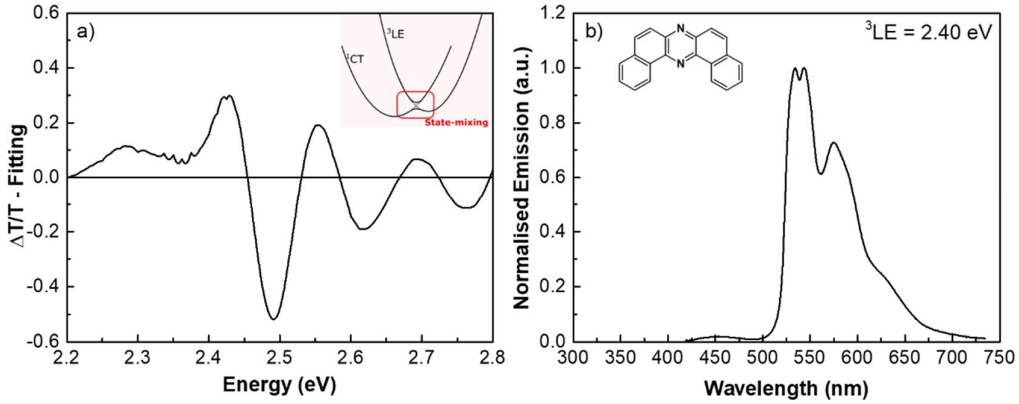

Figure 7.6 – a) Difference between the experimental and fitted EA spectra of POZ-DBPHZ. A new state becomes evident through the transfer of oscillator strength from the charge-transfer state that mixes with a nearby optically-inaccessible state (inset). b) Phosphorescence spectrum of DBPHZ collected in a 1% w:w emitter-in-zeonex matrix at 80 K and a time delay of 65 ms. Onset energy with an error of ± 0.02 eV and inset with the molecular structure of DBPHZ.

7.2.3 Data Analysis

In order to confirm that this newly revealed state is local and optically forbidden (becoming observable from the transfer of oscillator strength of the neighbouring CT state), combined density functional theory and multireference configuration interaction (DFT/MRCI) of **POZ-DBPHZ** was performed. The lowest energy optical transitions (1^1B_1 and 1^1A_2) both have pure CT character with calculated adiabatic transition energies of 2.29 eV in agreement with the measured onset of optical absorption, Figure 7.2. The lowest singlet local transitions (of the acceptor) are calculated at 2.95 eV and 3.22 eV, strongly separated from the CT transitions. Moreover, DFT/MRCI does find a local 1^3A_1 triplet state (of the acceptor) of ππ* character at 2.32 eV, again in excellent agreement with the EA residual feature and time-resolved measurements (Table 7.1).

Given the first order line shape of the EA associated with this underlying transition, centred at 2.51 eV mostly a dipolar response and therefore, it must be a Frenkel exciton local state that strongly overlaps with the CT feature in the EA spectrum. Previous solvatochromism measurements have shown that the CT transition has strong mixed nπ*/ππ* character.[7] From TD(DFT) calculations and phosphorescence measurements, this local transition is identified as the lowest lying ππ* local triplet state of the acceptor, and is the only local state close in energy to the lowest lying CT states in POZ-DBPHZ.[9] While direct optical excitation to this state is forbidden, transition becomes visible in the EA spectrum through transfer of oscillator strength.

This is also in agreement with El-Sayed's rule, which states that a S(ππ*) state is expected to couple strongly if the p-orbital at an atomic centre changes its orientation upon excitation (Chapter 2). The difference densities of the CT states (Figure 7.7) reveal small local σπ* type contributions to the CT excitations which may couple to the ππ* type excitations of the T_3(ππ*) state on the same centre. The computed spin-orbit coupling matrix element between the energetically close-lying S_1(CT) and T_3(ππ*) states (0.279 cm^{-1}) is about 50 times stronger than the direct and symmetry-allowed coupling between S_1(CT) and T_2(CT). The effects of such state-mixing have been discussed in detail by C. Marian *et al.* and strongly influences the TADF mechanism[17] but on their own are still orders of magnitude too small to account for the experimental rISC rates observed which require the vibronic coupling mechanism to achieve rISC rates approaching 10^7 s^{-1}.[18] Thus, EA spectroscopy gives experimental verification that the lowest lying optical transition in **POZ-DBPHZ** is a pure CT transition, but couples (mixes) with the lowest energy local triplet state (inset of Figure 7.6a). Given this triplet state is ππ* in character, the CT transition has to be, σπ* as predicted and mixing of the two states yields enhanced transition oscillator strength, even though one state has triplet multiplicity.

Table 7.1 – DFT/MRCI excitation energies ΔE (eV), oscillator strengths f (r), and dipole moments μ (D) of low-lying singlet and triplet states of POZ-DBPHZ.*

State	ΔE_{vert}	f (r)	μ	ΔE_{adia}	Character
1^1A_1			1.82		ground state
1^1B_1	2.45	0.00003	11.06	2.29	CT (POZ→DBPHZ)
1^1A_2	2.45	0.00000	11.07	2.29	CT (POZ→DBPHZ)
2^1A_2	3.04	0.00000	9.20		CT (POZ→DBPHZ)
2^1B_1	3.04	0.00093	9.22		CT (POZ→DBPHZ)
1^1B_2	3.07	0.35011	0.82	2.95	LE ππ* (DBPHZ)
2^1A_1	3.40	0.04663	1.82	3.22	LE ππ* (DBPHZ)
3^1B_1	3.41	0.00519	2.84		LE nπ* (DBPHZ)
1^3B_1	2.37		11.12	2.20	CT (POZ→DBPHZ)
1^3A_2	2.37		11.15	2.20	CT (POZ→DBPHZ)
1^3A_1	2.53		1.90	2.32	LE ππ* (DBPHZ)
1^3B_2	2.71		0.76	2.61	LE ππ* (DBPHZ)
2^3A_2	2.81		0.60		LE ππ* (POZ)
2^3B_1	2.81		0.59		LE ππ* (POZ)
3^3A_2	3.01		6.41		mixed CT (POZ→DBPHZ) / LE ππ* (POZ)
3^3B_1	3.01		6.42		mixed CT (POZ→DBPHZ) / LE ππ* (POZ)

In comparison, DFT/MRCI calculations show that ***t*-BuCz-DBPHZ** which also has pure CT character, has no such triplet state coupling to the lowest energy optical transition, Table 7.2. The lowest energy triplet state from phosphorescence onset[7] and DFT/MRCI has

*Combined density functional theory and multireference configuration interaction (DFT/MRCI) calculations performed by Prof Christel Marian from the University of Düsseldorf.

energy of 2.34 eV (well below its higher energy CT states) and so no major deviation from the pure second-order line shape is seen in the EA spectrum. Though this transition in ***t*-BuCz-DBPHZ** seems at first glance excitonic, being sharp and well featured, EA clearly shows that this transition is pure CT in character, which hints at a peculiar behaviour of the carbazole donor and the fact that the non-bonding electrons are delocalised into the carbazole ring.

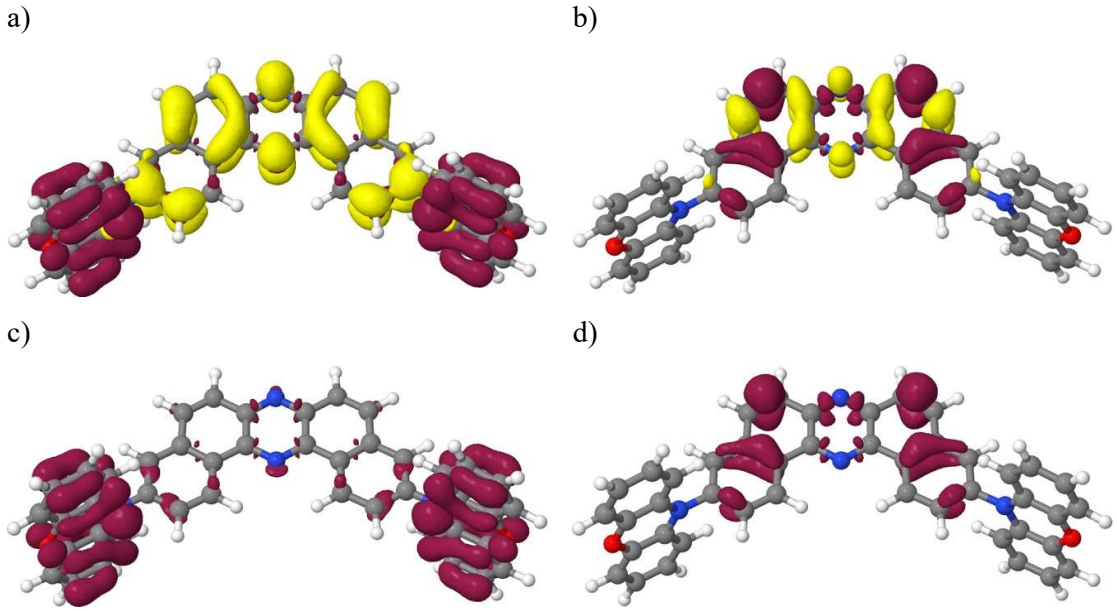

Figure 7.7 – Difference densities (|isovalue| = 0.001) of (a) the S_1(CT) and (b) the T_3(ππ*) state of POZ-DBPHZ. A loss of electron density with respect to the ground state is indicated in dark red, a gain in yellow. For clarity, the negative parts of the corresponding difference densities are shown in (c) and (d), respectively.[†]

Table 7.2 – DFT/MRCI excitation energies ΔE (eV), oscillator strengths f (r), and dipole moments μ (D) of low-lying singlet and triplet states of t-BuCz-DBPHZ. The density distribution of states can be found in [19].
[a]Estimated by adding vertical energy shifts, determined at the ground-state geometry, to adiabatic energies of corresponding states in CZ-DBPHZ.

State	ΔE_{vert}	f (r)	μ	ΔE_{adia}[a]	Character
1^1A_1			1.07		ground state
1^1B_1	3.00	0.00010	12.71	2.86	CT (Cz→DBPHZ)
1^1A_2	3.01	0.00000	12.82	2.87	CT (Cz→DBPHZ)
1^1B_2	3.11	0.38438	0.03	2.98	LE ππ* (DBPHZ)
2^1B_1	3.40	0.00492	2.03		LE nπ* (DBPHZ)
2^1A_1	3.42	0.04340	1.01	3.25	LE ππ* (DBPHZ)
1^3A_1	2.54		1.02	2.33	LE ππ* (DBPHZ)
1^3B_2	2.72		0.29	2.61	LE ππ* (DBPHZ)
1^3B_1	2.93		13.41	2.79	CT (Cz→DBPHZ)
1^3A_2	2.94		13.53	2.80	CT (Cz→DBPHZ)
2^3B_1	3.08		0.67		LE nπ* (DBPHZ)
3^3B_1	3.21		1.95		LE ππ* (Cz)
2^3A_2	3.21		1.94		LE ππ* (Cz)
2^3A_1	3.23		1.03		LE ππ* (Cz)
2^3B_2	3.23		1.03		LE ππ* (Cz)

[†]Differences in the density of CT states calculations performed by Prof Christel Marian from the University of Düsseldorf.

In Table 7.3 the local-field corrected and uncorrected changes in polarizability and dipole moment of these two materials are summarised, using the Liptay analysis presented in Chapter 3. **POZ-DBPHZ**, having both the smallest ΔE_{ST} and highest photoluminescence quantum yield (PLQY), also shows a large change in dipole moment ($\Delta\mu^*$) of 17.46 D. This change is indicative of a complete one-electron transfer over a distance of 5-7 Å, thoroughly consistent with one electron moving from the donor unit into the middle of the acceptor unit. A change in first order polarizability is also seen, indicating the transfer of oscillator strength to the local acceptor S_0-T_1 transition. In the case of ***t*-BuCz-DBPHZ** the change in dipole moment is smaller, calculated at 6.25 D. The smaller $\Delta\mu$ is attributed to the smaller dihedral angle in ***t*-BuCz-DBPHZ** and to some degree of conjugation across donor and acceptor units. Conjugation and associated ground state delocalisation across the **D** and **A** units reduces the distance the electron must travel in forming the CT state, resulting in a smaller change in dipole moment on excitation. Even with the weaker CT character and increased **D-A** conjugation, ***t*-BuCz-DBPHZ** has a smaller PLQY. This and the large ΔE_{ST} (of 0.33 eV) result in poor TADF performance and give efficiency devices. These features could be a direct result of the fact that there is no mixing of CT and LE states in this molecule as confirmed by its purely Liptay EA behaviour.

Given the non-polar host environment (zeonex polymer) correcting the applied field for such a non-polar host reduces the calculated change in dipole moment. This reduction on the low values seems rather un-physical for such strongly charge-transfer molecules that show very large solvatochromic shifts.[19] It is possible that 5% w:w loading of the polar TADF molecules in zeonex establishes a polar environment due to the dopant, and that a different local field correction factor needs to be used. However, all such corrections greatly increase the calculated change in dipole moment, again to non-physical values. Further studies to fully understand the interaction of the TADF guest in a host medium need to be performed to resolve this. Nonetheless, this initial study already demonstrates that EA spectroscopy is a powerful tool for predicting efficient TADF in materials for OLEDs, as it quickly reveals the presence or absence of this important CT-LE mixing.

Table 7.3 – Contributions of first and second derivatives to the fitting of the EA spectra of both POZ-DBPHZ and *t*-BuCz-DBPHZ. Following the fundamental analysis of chapter 3, the field-induced change in polarizability and dipole moment were calculated.

	1st Derivative contribution (x10^{-5})	**Δp x10^{-38} (Dm/V)**	**Δp x10^{-38} (Dm/V)***	**2nd Derivative contribution (x10^{-5})**	**$\Delta\mu$ (D)**	**$\Delta\mu$ (D)***
POZ-DBPHZ	5.3	1.05	0.29	3.8	17.46	9.35
***t*-BuCz-DBPHZ**	-2.7	-0.94	-0.27	0.3	6.25	3.35

*corrected for a non-polar environment using a local field correction factor of $F = (2\varepsilon+1)F_{app}/3$.

7.3 Conclusion

In summary, this work establishes Electroabsorption spectroscopy as a powerful tool in understanding the character and state-mixing of the molecular excited states of TADF emitters. Both studied emitters have the low energy absorption bands with strong CT character, which is not obvious in ***t*-BuCz-DBPHZ** from the absorption band line shape alone. More importantly, in **POZ-DBPHZ** transfer of oscillator strength reveals the presence of a second optically inaccessible state that is overlapping with the CT band and is not found in ***t*-BuCz-DBPHZ** (which has pure CT character). This new state in **POZ-DBPHZ** is identified as the lowest energy ππ* local triplet of the acceptor, and mixing with the ^{1}CT gives a direct CT transition having enhanced oscillator strength. In ***t*-BuCz-DBPHZ**, the lowest triplet state is much lower in energy than the CT transition and does not mix, which in part leads to much poorer TADF efficiency. No higher lying local triplet states are in resonance either although this may be a peculiarity of the carbazole donors in ***t*-BuCz-DBPHZ**. Further studies of ^{1}CT-^{3}LE coupling with a combined EA and quantum chemistry approaches, may well yield a deeper understanding of the molecular characteristics and design rules of efficient TADF molecules.

7.4 References Chapter 7

1. Oh, D. H., Sano, M. & Boxer, S. G. Electroabsorption (Stark effect) spectroscopy of mono- and biruthenium charge-transfer complexes: measurements of changes in dipole moments and other electrooptic properties. *J. Am. Chem. Soc.* **113,** 6880–6890 (1991).
2. Liptay, W. in *Excited States* **1,** 129–229 (Elsevier, 1974).
3. Sebastian, L., Weiser, G. & Bässler, H. Charge transfer transitions in solid tetracene and pentacene studied by electroabsorption. *Chem. Phys.* **61,** 125–135 (1981).
4. Legaspi, C. M. *et al.* Rigidity and Polarity Effects on the Electronic Properties of Two Deep Blue Delayed Fluorescence Emitters. *J. Phys. Chem. C* **122,** 11961–11972 (2018).
5. Feller, F. & Monkman, A. Optical spectroscopy of oriented films of poly(2,5-pyridinediyl). *Phys. Rev. B* **61,** 13560–13564 (2000).
6. dos Santos, P. L., Ward, J. S., Bryce, M. R. & Monkman, A. P. Using Guest–Host Interactions To Optimize the Efficiency of TADF OLEDs. *J. Phys. Chem. Lett.* **7,** 3341–3346 (2016).
7. Data, P. *et al.* Dibenzo[a,j]phenazine-Cored Donor-Acceptor-Donor Compounds as Green-to-Red/NIR Thermally Activated Delayed Fluorescence Organic Light Emitters. *Angew. Chem., Int. Ed.* **55,** 5739–5744 (2016).
8. Pereira, D. de S. *et al.* An optical and electrical study of full thermally activated delayed fluorescent white organic light-emitting diodes. *Sci. Rep.* **7,** (2017).
9. Okazaki, M. *et al.* Thermally activated delayed fluorescent phenothiazine–dibenzo[a,j]phenazine–phenothiazine triads exhibiting tricolor-changing mechanochromic

luminescence. *Chem. Sci.* **8,** 2677–2686 (2017).

10. Dias, F. B. *et al.* The role of local triplet excited states and D-A relative orientation in thermally activated delayed fluorescence: Photophysics and devices. *Adv. Sci.* **3,** 1600080 (2016).

11. Santos, P. L. *et al.* Engineering the singlet–triplet energy splitting in a TADF molecule. *J. Mater. Chem. C* **4,** 3815–3824 (2016).

12. Dias, F. B. *et al.* Triplet Harvesting with 100% Efficiency by way of Thermally Activated Delayed Fluorescence in Charge Transfer OLED Emitters. *Adv. Mater.* **25,** 3707–3714 (2013).

13. Al-Attar, H. A. *et al.* Highly efficient, solution-processed, single-layer, electrophosphorescent diodes and the effect of molecular dipole moment. *Adv. Funct. Mater.* **21,** 2376–2382 (2011).

14. Bui, T.-T., Goubard, F., Ibrahim-Ouali, M., Gigmes, D. & Dumur, F. Thermally Activated Delayed Fluorescence Emitters for Deep Blue Organic Light Emitting Diodes: A Review of Recent Advances. *Appl. Sci.* **8,** 494 (2018).

15. Saito, K., Yanagi, K., Cogdell, R. J. & Hashimoto, H. A comparison of the Liptay theory of electroabsorption spectroscopy with the sum-over-state model and its modification for the degenerate case. *J. Chem. Phys.* **134,** 044138 (2011).

16. Liess, M. *et al.* Electroabsorption spectroscopy of luminescent and nonluminescent π-conjugated polymers. *Phys. Rev. B* **56,** 15712–15724 (1997).

17. Lyskov, I. & Marian, C. M. Climbing up the ladder: Intermediate triplet states promote the reverse intersystem crossing in the efficient TADF emitter ACRSA. *J. Phys. Chem. C* **121,** 21145–21153 (2017).

18. dos Santos, P. L. *et al.* Triazatruxene: A Rigid Central Donor Unit for a D-A 3 Thermally Activated Delayed Fluorescence Material Exhibiting Sub-Microsecond Reverse Intersystem Crossing and Unity Quantum Yield via Multiple Singlet-Triplet State Pairs. *Adv. Sci.* **5,** 1700989 (2018).

19. de Sa Pereira, D., Menelaou, C., Danos, A., Marian, C. & Monkman, A. P. Electroabsorption Spectroscopy as a Tool for Probing Charge Transfer and State Mixing in Thermally Activated Delayed Fluorescence Emitters. *J. Phys. Chem. Lett.* **10,** 3205–3211 (2019).

Chapter 8: An Optical and Electrical Study of Full TADF White OLEDs

This chapter reports the engineering of thermally-activated delayed fluorescence – based white organic light-emitting diodes (W-OLEDs) composed of three emitters, 2,7-bis(9,9-dimethyl-acridin-10-yl)-9,9-dimethylthioxanthene-S,S-dioxide (DDMA-TXO2), 2,7-bis(phenoxazin-10-yl)-9,9-dimethylthioxanthene-S,S-dioxide (DPO-TXO2) and 3,11-di(10H-phenoxazin-10-yl)dibenzo[a,j]phenazine (POZ-DBPHZ), respectively in two different hosts. By controlling the device design and optimising through different combinatorial studies, the emission of DDMA-TXO2 and DPO-TXO2, the behaviour of POZ-DBPHZ in a device with more than one emitter and the combination of the three materials were studied. Results show external quantum efficiencies as high as 16 % for a structure with a correlated colour temperature close to warm white, and colour rendering index close to 80. However, it is in their performance stability that provides the true breakthrough: at 1,000 cd/m^2 the efficiencies were still above 10 %, which constituted a promising result for this type of devices.

The work presented in this chapter was published in Scientific Reports, Daniel de Sa Pereira, Paloma L. dos Santos, Jonathan S. Ward, Przemyslaw Data, Masato Okazaki, Youhei Takeda, Satoshi Minakata, Martin R. Bryce and Andrew P. Monkman, **An Optical and Electrical study of full TADF White OLEDs,** Sci. Rep. 2017, 7, 6234. Daniel de Sa Pereira carried out the device production, optimization studies and data interpretation together with Paloma L. dos Santos, Przemyslaw Data and Andrew P. Monkman. Jonathan S. Ward and Martin R. Bryce designed and synthesized both DDMA-TXO2 and DPO-TXO2 while Masato Okazadi, Youhei Takeda and Satoshi Minakata designed and synthesized POZ-DBPHZ.

8.1 Introduction

Thermally-activated delayed fluorescence (TADF) is the leading concept enabling high efficiency devices and understanding the extended photophysical mechanisms inherent to the molecular design of TADF emitters has been the focus of this thesis has focused so far. These mechanisms have also been bridged with their electroluminescence behaviours, i.e. their performance in devices, but only as a complement rather than an in-depth analysis. Therefore, to come full-picture, as a more application-driven work, this chapter looks into the use of an orange-green-blue TADF-based emitting structure applied in a white organic light-emitting (W-OLED) device.

An optimised three-component, full TADF W-OLED structure is investigated both in terms of Commission Internationale de l'Eclairage (CIE 1931), correlated colour temperature (CCT) and colour rendering index (CRI) (Chapter 3) and electrical properties. Three TADF emitters were chosen due to their previously demonstrated exceptional performance, both in photophysics and in devices: 2,7-bis(9,9-dimethyl-acridin-10-yl)-9,9-dimethylthioxanthene-S,S-dioxide (**DDMA-TXO2**)[1], 2,7-bis(phenoxazin-10-yl)-9,9-dimethylthioxanthene-S,S-dioxide (**DPO-TXO2**)[2] and 3,11-di(10H-phenoxazin-10-yl)dibenzo[a,j]phenazine (**POZ-DBPHZ**)[3] as blue, green and orange emitters, respectively. After optimisation, efficiencies as high as 16 %, 32.2 cd/A and 22.8 lm/W together with CRI of 77.6 and CCT of around 6,200 K were obtained. At 1,000 cd/m^2, the efficiency remained above 10 %, a promising low roll-off. This study demonstrates proof of concept that TADF emitters are suitable as candidates for solid-state lighting (SSL) structures strongly suggesting that by using standard transport materials and hosts, one can easily obtain high efficiency and stable W-OLEDs.

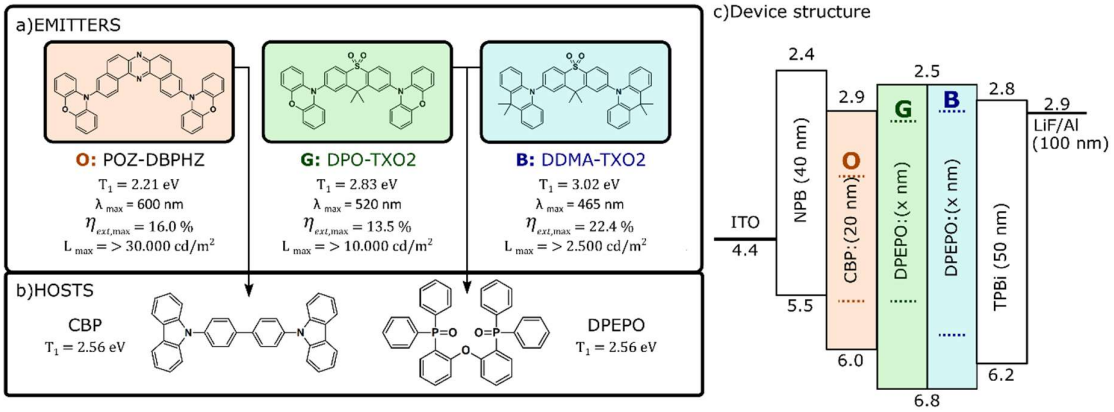

Figure 8.1 – Chapter 8 project diagram. a) Emitters used to obtain white light emission and their respective triplet levels, peak emission, single-emitting device maximum efficiency and maximum brightness. b) Co-evaporated hosts. c) Energy diagram of the final device produced on this study.

8.2 Results and Discussion

To understand the dynamics and control the colour balance inside this TADF W-OLED with stacked single-emitting layers, three sets of studies were conducted, culminating in an optimised white light-emitting structure. The molecular structure of each TADF emitter and corresponding host is shown in Figure 8.1a) and b), respectively. For the device optimisation, triplet levels (T_1), peak emission (λ_{max}), maximum efficiency in single-emitting structures ($\eta_{ext,max}$) and maximum brightness (L_{max}) of each emitter were considered. Both optical and electrical properties were analysed for this optimisation study, the final device structure shown Figure 8.1c). For simplicity reasons, combinations of **POZ-DBPHZ**, **DPO-TXO2** and **DDMA-TXO2** will be revealed as Orange (O), Green (G), and Blue (B), respectively.

8.2.1 Green-Blue Structure

The first part of this work focuses on the positioning and thickness of the DPEPO layers of a Blue(B)-Green(G) emitting structure. Two devices with BG and GB orientations were deposited at fixed thicknesses of 15 nm for each host:guest blend and 10% guest concentration. The results are shown in Figure 8.2.

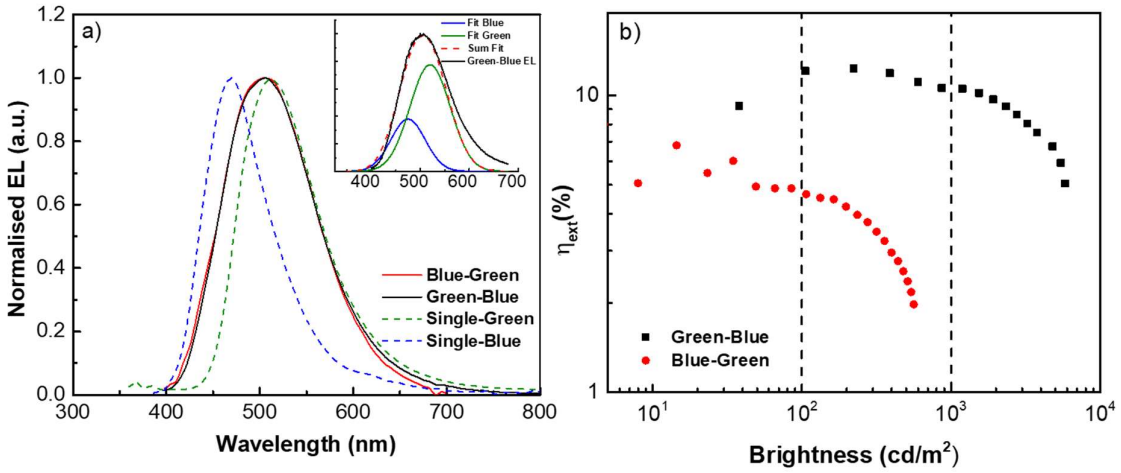

Figure 8.2 - Study of the orientation of the layers in a Green(G)-Blue(B) structure. a) Electroluminescence (EL) spectra of both devices at 10 V overlapped with the EL of each material independently.[1,2] The inset shows the deconvolution of the EL spectrum of the GB structure. b) External quantum efficiency dependence with brightness of the devices used for both studies.

From the electroluminescence (EL) spectra of Figure 8.2a) alternating BG and GB orientations has no effect on device emission, since both electroluminescence (EL) spectra almost entirely overlap. Rather than having individualized peaks, both structures showed an emission that is the sum of the independent emitters, evidenced by the overlap of the EL spectra

with both green and blue individual devices. The inset of Figure 8.2a) shows the fitted EL deconvolution into contribution from the two emitters to understand the weight of each part. This hints at a recombination zone that is spread across both DPEPO layers (Figure 8.1). Evidently, given the overall green emission, the biggest contributor to the device performance is **DPO-TXO2** representing around 70% of the total contribution. The remaining 30% comes from **DDMA-TXO2.** This hints at a potential SSL device with low emission from the blue counterpart (Chapter 2), although still enough contribution to obtain white OLEDs with further tuning.

In terms of electrical properties (Figure 8.2b), there are substantial differences performance-wise with the GB structure showing significantly improved performance with higher $\eta_{ext,max}$ and L. Moreover, the resistance to roll-off of green-blue was substantially higher, maintaining an efficiency above 10 % even at 1,000 cd/m^2, indicating a relatively stable device.

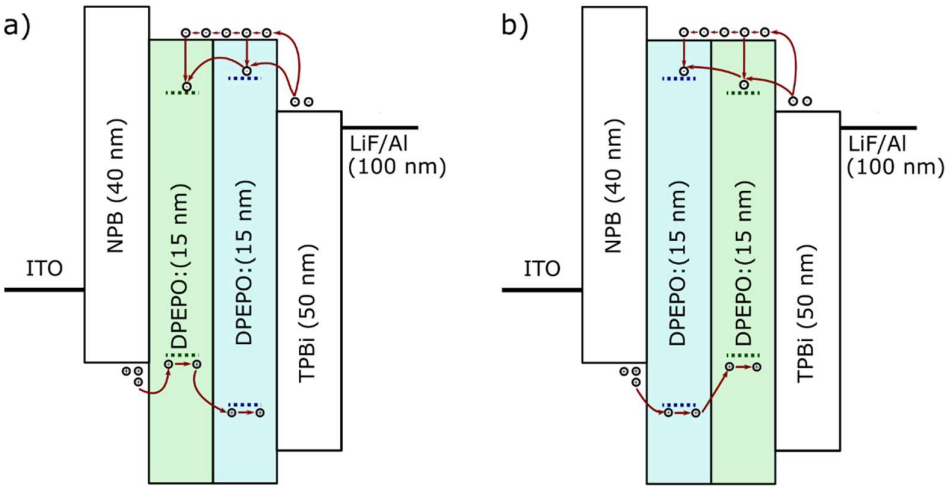

Figure 8.3 - Direct carrier injection mechanism in a) Green-Blue and b) blue-green structures. Given that DPEPO is a good electron conducting material but poor hole conducting, direct injection from NPB to DPO-TXO2 is vastly enhanced by optimise transport properties in the Green-Blue structure.

An explanation for this difference in electrical performance lies in the carrier balance inside both emitting layers (Figure 8.3). DPEPO is a known electron transport/host material[4] for TADF materials.[1,5] This comes from its high HOMO/LUMO gap and a high triplet level (Figure 8.1b), limiting carrier quenching in a device. The high polarity of DPEPO is also important for host tuning of TADF emitters (Chapters 4 and 5) however, a limiting factor is the relatively low hole mobility. Given that both structures have similar emissions, the better electrical performance is likely a result of a better electron-hole distribution across the GB emitting layers (Figure 8.3a). **DDMA-TXO2** has lower HOMO than **DPO-TXO2**, therefore direct injection in GB is much more favourable than in the BG (Figure 8.3b) and the result is a

better carrier density with minimal effect on the emission. Figure 8.4a) shows the current efficiency and luminous efficacy of both these devices to confirm that indeed the carrier balance plays a pivotal role and can explain the difference in performance for the GB and BG.

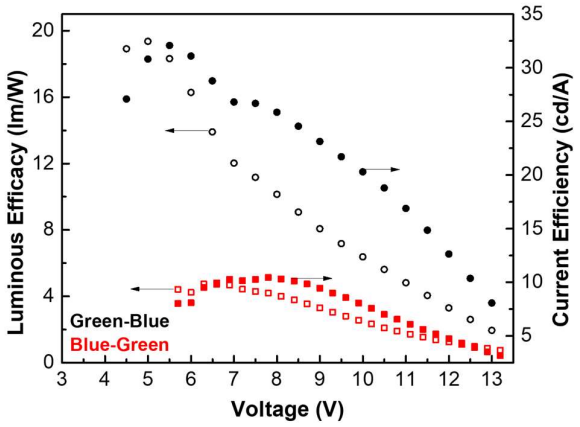

Figure 8.4 – The luminous efficacy (open dots) and the current efficiency (solid dots) of devices Green-Blue and Blue(B)-Green(G). BG has much smaller efficiency values as the carrier balance in the structure pays hinders the overall operating mechanism.

It is worth noting the η_{ext} above 10 % at brightness levels above 1,000 cd/m^2 in the GB device. This result prompted for an increase in the green layer's DPEPO thickness to 20 nm to improve the carrier balance. From Figure 8.5, making this change resulted in the maximum η_{ext} increased from approximately 12 to around 16 %, maintaining the low roll-off and increasing the maximum luminance to around 8,000 cd/m^2 from the previous 6,000 cd/m^2. At around 8 V (corresponding to 1,000 cd/m^2), there is a bump in the electrical performance (Figure 8.5a) which can be assigned to an increased injection of carriers to the DPEPO layers. Nonetheless, the EL remained the same, as seen from the inset of Figure 8.5a. Overall, the use of thinner blue-emitting electron transport layers together with the device optimised sum of individual EL of green and blue counterparts constitute the main results of this part of the study.

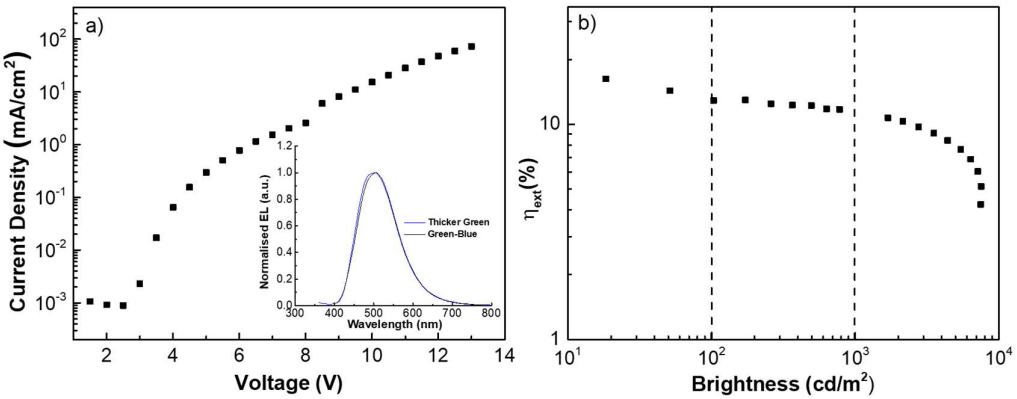

Figure 8.5 - Electrical performance of the Green-Blue device with a thicker layer of DPEPO:DPO-TXO2. a) Current density-voltage and b) external quantum efficiency dependence with brightness. The inset of a) shows the normalized EL spectrum at 10 V overlapped with the device with equal layers of DPEPO in both green and blue layers.

8.2.2 Orange-Blue Structure

The next part of constructing the W-OLED was to examine the balance between blue (B) and orange (O) emitters. Fixing the thickness of both hosts (from their single emitter structures) and the concentration of **DDMA-TXO2**, the concentration of **POZ-DBPHZ** was varied between 5 % (OB5), 8 % (OB8) and 11 % (OB11) with optical and electrical performances characterized or each – Figure 8.6.

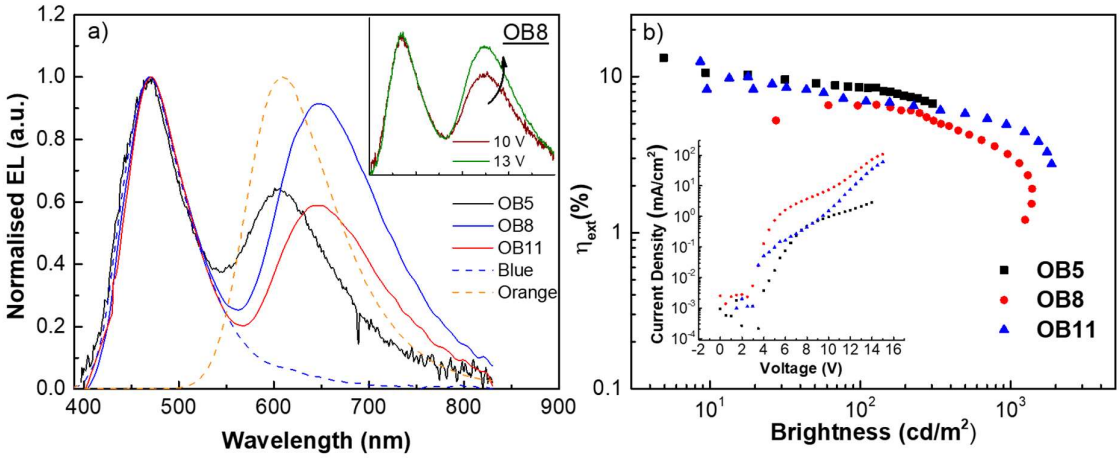

Figure 8.6 - Study of POZ-DBPHZ in an orange-blue device structure with orange concentrations of 5 (OB5), 8 (OB8) and 11 % (OB11). a) Electroluminescence (EL) spectra at 13 V overlapped with the EL of each individual material.[6,7] Inset shows the EL spectra of OB8 at 10 and 13 V. b) External quantum efficiency dependence with brightness with the current density dependence with voltage as an inset.

Figure 8.6a) shows the EL spectra of OB5, OB8 and OB11, overlapped with the EL of the single-emitting devices. In Figure 8.6b) the effect on the η_{ext} is also presented. For consistency, the EL was collected at 13 V as the change in current regime (insets of Figure 8.6) affects the EL. Overall, two distinct features can be seen: one at 450 nm that overlaps with the emission of **DDMA-TXO2** on its own and a second at around 600 nm (OB5) that overlaps with **POZ-DBPHZ**. However, when increasing the concentration to 8 and 11 %, this peak redshifts to 650 nm, which is interpreted as the appearance of an excimer. In EL, this reveals the low energy excimer states formed by charge recombination similarly, to keto defects in polyfluorene giving rise to different EL spectra to the PL.[8] The change in intensity, from OB8 to OB11 may be related with different carrier densities between orange and blue host:guest layers. In terms of electrical performances, all three performed similarly in terms of η_{ext} at low brightness levels. Increased concentrations of **POZ-DBPHZ** also increased the maximum brightness and the electrical stability. Although the concentration redshift needs to be studied in more detail, for the purpose of this study the main conclusions taken was that lower

concentrations of **POZ-DBPHZ** are preferred for the EL, but higher concentrations seem to allow for better device electrical performance.

Given that the EL spectra of the 2-component devices cover the entire visible spectrum, i.e. within white emission, the optical properties were studied in depth and the figures of merit in a standard white device analysed – Figure 8.7. All devices show CIE coordinates around the white region, however the lack of green coverage in OB8 and OB11 results in poor colour rendering. The pure **POZ-DBPHZ** emission of OB5, i.e. the blueshift of the second peak when comparing to OB8 and OB11, resulted in a substantial increase in CRI, from around 40 to 73.3 and much warmer colour temperatures. The CCT of the devices at 13 V have similar values in OB5 and OB8, OB11 shows a much cooler white emission, in line with each colour coordinates and the higher emission of **DDMA-TXO2.** Using the optimised GB structure of the previous section (8.2.1) and combining with the optimised ratios studied here, an orange-green-blue device structure was expected to give good colour rendering and electrical properties.

Device	CIEx	CIEy	CRI	CCT (K)
OB5	0.31	0.28	73.3	7024
OB8	0.32	0.29	38.7	6109.3
OB11	0.28	0.26	40.0	11878.9

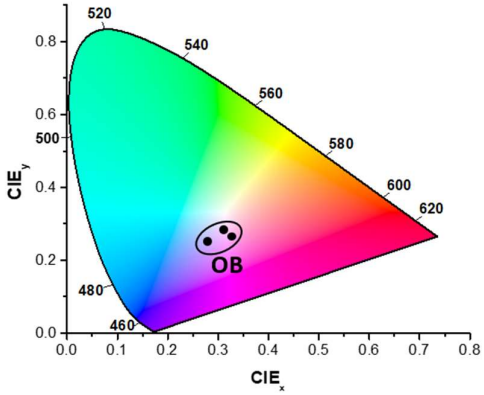

Figure 8.7 – Colour figures of merit of the devices based on orange-blue emitting structures. On the right is the colour coordinates (CIE) diagram with all three devices identified.

8.2.3 Orange-Green-Blue Structure

The information acquired from the bi-colour devices was used to fabricate a device structure with the three emitters in the three different host:guest layers (Figure 8.1c). **DPO-TXO2** was added to the previous OB to improve the rendering at visible wavelengths and possibly enhance the η_{ext} by direct injection but also decrease the relative contribution of **DDMA-TXO2** as a blue emitter. The three device stack considerations from the previous sections were taken in consideration to help optimise the interfaces: i. Minimising energy barriers between consecutive emitters; ii. Thicker hole transport layers to improve carrier balance; iii. Lower concentrations of **POZ-DBPHZ** to avoid excimer formation. Subsequently, one final set of devices were produced using an orange-green-blue (OGB) structure, where

each DPEPO layer thickness was changed between 15 nm (OGB15 – Figure 8.8) and 7 nm (OGB 7 – Figure 8.9) to elucidate on the effect on the electron injection to the CBP side.

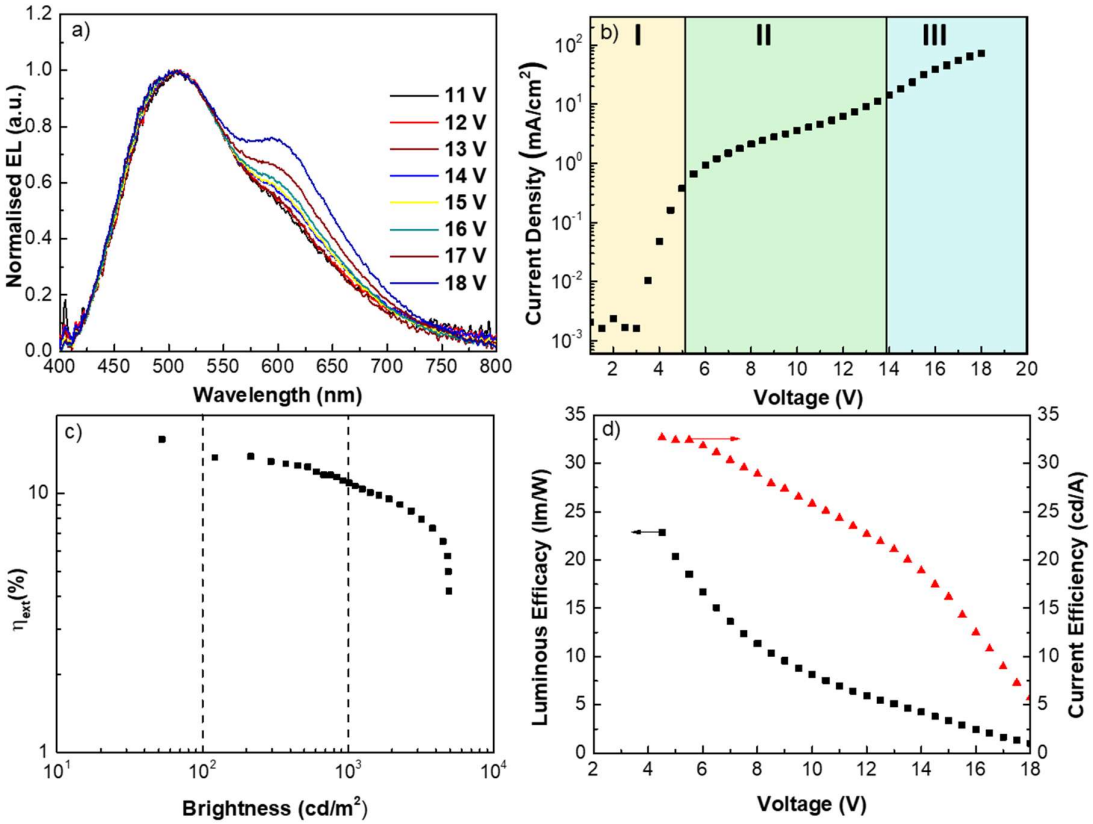

Figure 8.8 – Performance of devices containing the optimised W-OLED with two 15-nm DPEPO layers (OGB15). a) EL spectra at different voltages. b) Current density-voltage (JV) with three different regimes: I the space charge limited current (SCLC); II and III the different carrier balance regimes. c) η_{ext} and luminance dependences with brightness and d) Luminous and current efficiencies of the device.

Figure 8.8a) and 8.9a) show the emission of the W-OLEDs at different voltages. As expected, the EL shows two peaks that are coming from the GB combination (8.2.1) and the low concentration of **POZ-DBPHZ** chosen to decrease the formation of excimers (8.2.2). Moreover, a thinner device showed an increased emission from **POZ-DBPHZ** (Figure 8.9a), which is an evidence of a higher exciton formation in the CBP layer. Both devices are also optically stable up to a certain voltage where the emission of **POZ-DBPHZ** starts increasing. In OGB15, this limit occurs at 14 V and in OGB7 at 12 V, in line with what would be expected by the change in thickness.

In terms of electrical performance, OGB15 presented slightly better performance than OGB7 in terms of maximum efficiency and roll-off. Both structures showed similar current density-voltage curves (Figure 8.8b) and 8.9b), with a turn-on voltage between 2 and 3 V. At higher voltages, there is a change in carrier balance regime, as the carrier density in the CBP

layer increases the orange emission. This can be seen in both figures where the space charge limited current (SCLC, the current is dominated by charge carriers injected from the contacts and so $I \sim V^2$), region I is followed by two distinct current behaviours, region II and III assigned as optically stable and unstable regimes, respectively. In terms of maximum brightness, both devices achieved values between 4,000 and 5,000 cd/m^2, a practical value for lighting applications.[9] More impressive is that OGB15 achieved η_{ext} as high as 16 % and stabilized at around 13 % (Figure 8.8c). At 1,000 cd/m^2 the η_{ext} is still around 10 % from which it starts to decrease as expected given the potential stress applied in the device. In terms of other efficiencies (Figure 8.8d), the maximum current efficiency and power efficiency were 31.2 cd/A and 23.6 lm/W, comparable with the individual emitter devices.[1–3] At 1,000 cd/m^2 the values are as high as 22.8 cd/A and 7.8 lm/W, which together with the $\eta_{ext,}$ indicate a good resistance to roll-off. The thinner device showed lower slightly lower η_{ext} though still comparable to the thicker one. Table 8.1 highlights all the electrical properties of both devices and the values of each efficiency measured at 100 and 1,000 cd/m^2.

Table 8.1 - Electrical properties of the orange-green-blue devices with both layers of DPEPO with 15 nm (OGB15) and 7 nm (OGB7) including luminance and efficiencies.

Dev	V_{ON} (V)	L_{MAX} (cd/m^2)	η_{ext}[1] %	η_L[1] lm/W	η_P[1] cd/A	η_{ext}[2] %	η_L[2] lm/W	η_P[2] cd/A	η_{ext}[3] %	η_L[3] lm/W	η_P[3] cd/A
OGB15	3	4924	16.1	32.7	22.4	13.7	32.4	20.4	11.0	25.1	7.5
OGB7	2	4372	13.0	31.2	23.6	12.4	31.0	20.5	9.8	22.2	7.4

[1]Measured maximum values. [2]Measured values at a luminance of 100 cd/m^2. [3]Measured values at a luminance of 1,000 cd/m^2.

In terms of colour properties, Performance of devices containing the optimised W-OLED with two 7-nm DPEPO layers (OGB7). a) EL spectra at different voltages. b) Current density-voltage (JV) with three different regimes: I the space charge limited current (SCLC); II and III the different carrier balance regimes. c) ηext and luminance dependences with brightness and d) Luminous and current efficiencies of the device.

Table 8.2 shows the change in figures of merit of the OGB devices at different voltages. For OGB15, as described before, below 14 V the values remain constant (Figure 8.8a). By comparing with the OB study, the introduction of **DPO-TXO2** (G) broadened the first peak and stabilized the colour coordinates and colour temperatures while increasing the CRI (from 73 to 77). With the increased emission of **POZ-DBPHZ** (O), the better CRI indicates a better rendering of reddish colours. A similar effect can be seen in OGB7 where the improved carrier density of **POZ-DBPHZ** (O) red-shifted the CIE and the CCT while increasing the CRI of the devices, even though their electrical performance decreased. Figure 8.10 plots the CIE

coordinates in the colour coordinates diagram to show that both studies result in devices in the white region. Therefore, the optical and electrical properties of a W-OLED purely built with TADF emitters was tailored to obtain more colour-efficient or more electric-efficient structures with colour performance from simple device modifications making these values comparable to other light sources (Chapter 2).

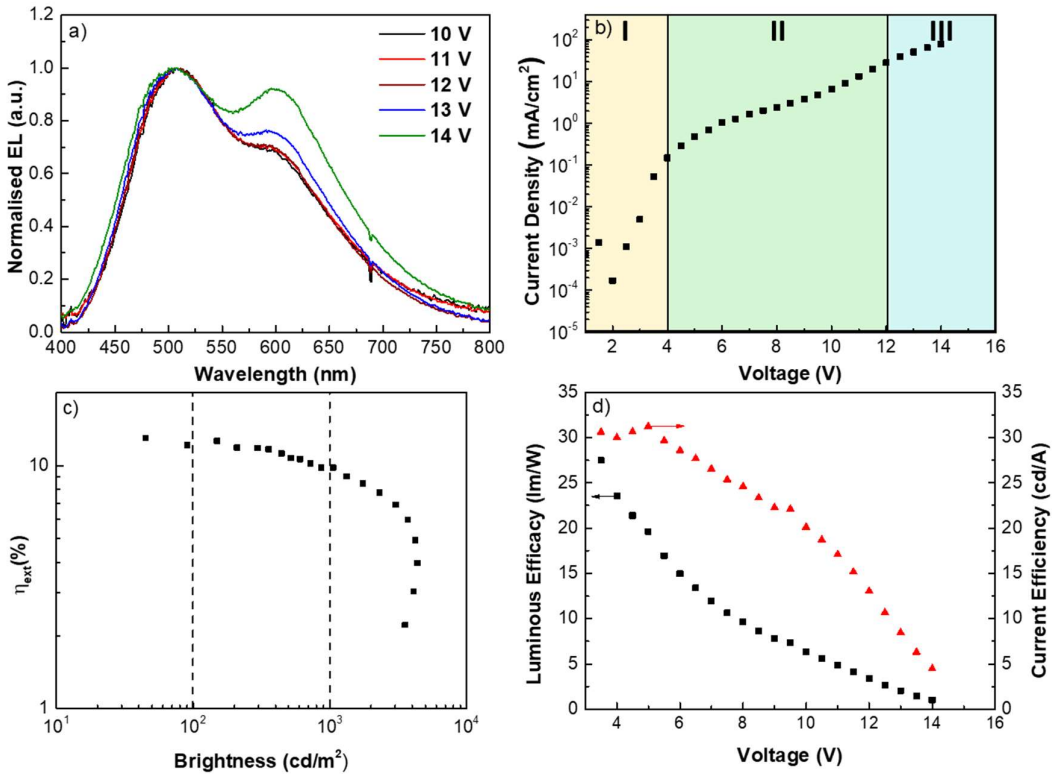

Figure 8.9 - Performance of devices containing the optimised W-OLED with two 7-nm DPEPO layers (OGB7). a) EL spectra at different voltages. b) Current density-voltage (JV) with three different regimes: I the space charge limited current (SCLC); II and III the different carrier balance regimes. c) η_{ext} and luminance dependences with brightness and d) Luminous and current efficiencies of the device.

Table 8.2 - Colour figures of merit of the orange-green-blue device at voltages before and after the change in electrical stability.

Dev	Voltage (V)	CIEx	CIEy	CCT (K)	CRI
OGB15	14	0.30	0.40	6313	77.6
	18	0.33	0.39	5505	86.7
OGB7	12	0.33	0.42	5451	80.3
	14	0.36	0.40	4816	87.5

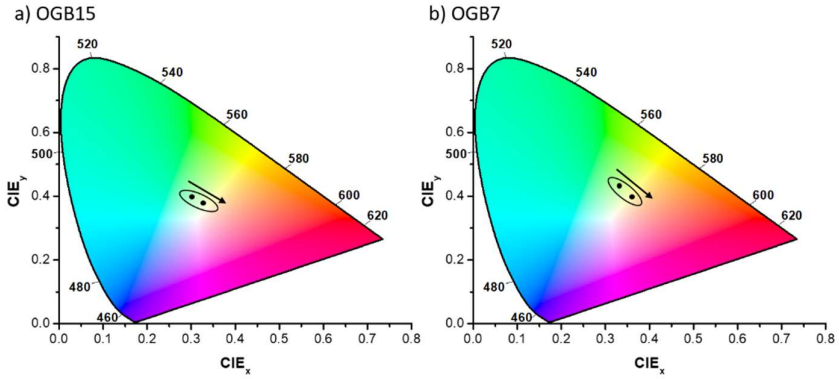

Figure 8.10 – Change of colour coordinates (CIE) diagram of a) OGB15 and b) OGB7 before and after the change in electrical stability.

8.3 Conclusion

In summary, three different TADF emitters were combined into a W-OLED structure, and the device's optical and electrical characteristics studied in detail. The white emission in the final device came from: 1 – the superposition of the blue and green emitters that with a lower contribution from the blue emitter, (important given the current lighting paradigm of the phototoxicity from blue emitters),[10] and 2 – the use of low concentrations of the orange emitter to avoid the formation of excimers. Given the device structure, it was shown that in order to obtain a higher carrier density control, the low energy gap materials should be closer to the hole injection layers and their ratios should be fine-tuned to secure good colour rendering properties. With simple device modifications, two structures were obtained for either colour-efficient or electrical-efficient devices. From this optimisation, efficiencies as high as 16 % and CRI close to 80 were obtained. Also, the η_{ext} of 11 %, even at a luminance above 1,000 cd/m^2 constitutes an important achievement for full TADF W-OLEDs.[11–15]

Based on the colour properties of such devices, their efficiencies and stabilities, a structure which is interesting for lighting applications using purely TADF emitters, known transport materials and hosts is therefore demonstrated, a key aspect when considering cost effective structures. With use of a higher η_{ext} green emitter and a more in-depth analysis into the origin of the **POZ-DBPHZ** excimer, better control of both electrical and optical performances may be achieved in future studies.

8.4 References Chapter 8

1. dos Santos, P. L., Ward, J. S., Bryce, M. R. & Monkman, A. P. Using Guest–Host Interactions To Optimize the Efficiency of TADF OLEDs. *J. Phys. Chem. Lett.* **7,** 3341–3346 (2016).

2. Santos, P. L. *et al.* Engineering the singlet–triplet energy splitting in a TADF molecule. *J. Mater. Chem. C* **4,** 3815–3824 (2016).

3. Data, P. *et al.* Dibenzo[a,j]phenazine-Cored Donor-Acceptor-Donor Compounds as Green-to-Red/NIR Thermally Activated Delayed Fluorescence Organic Light Emitters. *Angew. Chem., Int. Ed.* **55,** 5739–5744 (2016).

4. Xu, H. *et al.* Application of chelate phosphine oxide ligand in EuIII complex with mezzo triplet energy level, highly efficient photoluminescent, and electroluminescent performances. *J. Phys. Chem. B* **110,** 3023–3029 (2006).

5. Santos, P. L. *et al.* Engineering the singlet–triplet energy splitting in a TADF molecule. *J. Mater. Chem. C* **4,** 3815–3824 (2016).

6. Dos Santos, P. L., Dias, F. B. & Monkman, A. P. An Investigation of the Mechanisms Giving Rise to TADF in Exciplex States. *J. Phys. Chem. C* **120,** 18259–18267 (2016).

7. Data, P. *et al.* Exciplex Enhancement as a Tool to Increase OLED Device Efficiency. *J. Phys. Chem. C* **120,** 2070–2078 (2016).

8. List, E. J. W., Guentner, R., Scanducci de Freitas, P. & Scherf, U. The Effect of Keto Defect Sites on the Emission Properties of Polyfluorene-Type Materials. *Adv. Mater.* **14,** 374–378 (2002).

9. Gather, M. C., Köhnen, A. & Meerholz, K. White organic light-emitting diodes. *Adv. Mater.* **23,** 233–248 (2011).

10. Zhang, X. *et al.* Host-free Yellow-Green Organic Light-Emitting Diodes with External Quantum Efficiency over 20% based on a Compound Exhibiting Thermally Activated Delayed Fluorescence. *ACS Appl. Mater. Interfaces* acsami.8b18798 (2019). doi:10.1021/acsami.8b18798

11. Nishide, J., Nakanotani, H., Hiraga, Y. & Adachi, C. High-efficiency white organic light-emitting diodes using thermally activated delayed fluorescence. *Appl. Phys. Lett.* **104,** 233304 (2014).

12. Duan, C. *et al.* Multi-dipolar Chromophores Featuring Phosphine Oxide as Joint Acceptor: A New Strategy toward High-Efficiency Blue Thermally Activated Delayed Fluorescence Dyes. *Chem. Mater.* **28,** 5667–5679 (2016).

13. Liu, Z. *et al.* Simple-structure organic light emitting diodes: Exploring the use of thermally activated delayed fluorescence host and guest materials. *Org. Electron.* **41,** 237–244 (2017).

14. Yu, Y. *et al.* Fluorinated 9,9[prime or minute]-bianthracene derivatives with twisted intramolecular charge-transfer excited states as blue host materials for high-performance fluorescent electroluminescence. *J. Mater. Chem. C* **2,** 9375–9384 (2014).

15. Liu, W. *et al.* High Performance All Fluorescence White Organic Light Emitting Devices with A Highly Simplified Structure Based On Thermally Activated Delayed Fluorescence Dopants and Host. *ACS Appl. Mater. Interfaces* **8,** 32984–32991 (2016).

Chapter 9: Concluding Remarks

With thermally-activated delayed fluorescence (TADF) being its own multidisciplinary field, this thesis discussed three main subjects: design principles, physics and device engineering. The aim was to elucidate on more efficient systems, and in those systems, the inherent TADF mechanism, the TADF in a host, the optimised host:guest interaction in an organic light-emitting diode (OLED) and finally the strategies to improve the device performance beyond the emitting layer were all considered. Combining these three interconnecting subtopics, the main contributions came from comparing different systems, where details in the mechanism that are not entirely evident when looking only at one-molecule systems were obtained, making the picture of TADF more complicated than first assumed. And in that sense, it brought TADF into the next level of research.

The scientific community is starting to shift their focus into obtaining better TADF performance at high brightness levels, more than just maximum efficiency itself, as roll-off is one of the hurdles that is keeping it from its industrial goal. The mechanisms giving rise to efficiency roll-off vary[1] but, particularly in TADF, one thing that is certain is that both the molecular and device performances should be tackled moving forward. As shown in the early chapters of this thesis, it is not guaranteed that producing molecules with smaller energy gaps (ΔE_{ST}) will necessarily translate into a better roll-off. Designing multi-unit emitters helps in the steric crowding of the donor-acceptor (D-A) manifold, effectively decreasing the ΔE_{ST}, but the dispersion of D-A angles may induce different charge-transfer (CT) states and multiple TADF channels happening in one system. With smart design strategies, these multiple conformations may be beneficial to obtain the seemingly contradictory combination of rISC rates $> 10^7\ s^{-1}$ and high photoluminescence quantum yield (PLQY) reaching unity,[2] however they may also act as parasitic traps to the DF. And while the device efficiency of those emitters is high, these traps affect negatively the device performance at high brightness. So, in designing these multi-donor structures, the trade-off between the number and relative position of donors to the DF mechanism and device performance needs to be met.

Another important aspect that is worth mentioning is the real host effect on the TADF mechanism. The effects of the rigidity of the host on the emitter have been widely overlooked

in TADF science and, in that sense, both rigidity effects on the angles of the molecule and polarity should be equally considered. Given the limited number of available hosts, particularly for blue emitters,[3] it has become imperative (more than even emitters itself) to synthesise different high band gap hosts with the right polarity and the right rigidity, to properly "lock" the CT states and improve the inherent TADF. In devices, those hosts should also possess good and balanced hole and electron mobilities. This is something that is still missing in TADF research.

With all said and done, we should not forget that, while new and advanced strategies are necessary for better molecules, the ones that we know and use should still be used. The comparative work on PSeZ-Trz and PTZ-Trz, the latter already involved in multiple iterations,[4,5] connected topics like room-temperature phosphorescence (RTP), TADF and dual conformation pointing to a more effective way of designing these systems while using known strategies like the use of heavy-atoms[6] or the suppression of one of the main conformers. The same can be said for combining three different TADF emitters to form white OLEDs (W-OLEDs) where the same strategies used for non-TADF W-OLEDs stacks[7] were successfully applied.

Lastly, going in detail into the physical mechanism of TADF, it is also important to probe the character of the states that participate in the DF of each molecule. Though this requires more complex spectroscopic techniques, like the one shown in this thesis, by looking at different TADF materials, the current model was put to test. Here, by focusing on absorption rather than emission, the electroabsorption (EA) experimentally showed the LE-CT state mixing without the extra layer of complexity due to polarity, something that is not easy in the typical spectroscopy techniques and is of extreme relevance to the efficiency of these molecules. One can now start wondering what the Stark fluorescence will look like as well and if it will be possible to tune-in the character of the CT state with both polarity and temperature. Connecting these techniques with advanced computational studies and models, a better filtering through the best design principles can be obtained.

In that sense, the take-home message is that in thoroughly comparing different performing TADF emitters (which do not necessarily offer high efficiencies) and connecting it to their device properties, one can pick-out the small details that are not evident if looking at these molecules individually. If the main aspect of this thesis was in its multidisciplinary, in TADF science, more than ever those joint efforts should be pursued.

9.1 References Chapter 9

1. Murawski, C., Leo, K. & Gather, M. C. Efficiency Roll-Off in Organic Light-Emitting Diodes. *Adv. Mater.* **25,** 6801–6827 (2013).

2. dos Santos, P. L. *et al.* Triazatruxene: A Rigid Central Donor Unit for a D-A 3 Thermally Activated Delayed Fluorescence Material Exhibiting Sub-Microsecond Reverse Intersystem Crossing and Unity Quantum Yield via Multiple Singlet-Triplet State Pairs. *Adv. Sci.* **5,** 1700989 (2018).

3. Bui, T.-T., Goubard, F., Ibrahim-Ouali, M., Gigmes, D. & Dumur, F. Recent advances on organic blue thermally activated delayed fluorescence (TADF) emitters for organic light-emitting diodes (OLEDs). *Beilstein J. Org. Chem.* **14,** 282–308 (2018).

4. Tanaka, H., Shizu, K., Nakanotani, H. & Adachi, C. Dual intramolecular charge-transfer fluorescence derived from a phenothiazine-triphenyltriazine derivative. *J. Phys. Chem. C* **118,** 15985–15994 (2014).

5. Chen, D. G. *et al.* Revisiting Dual Intramolecular Charge-Transfer Fluorescence of Phenothiazine-triphenyltriazine Derivatives. *J. Phys. Chem. C* **122,** 12215–12221 (2018).

6. Huang, R. *et al.* The influence of molecular conformation on the photophysics of organic room temperature phosphorescent luminophores. *J. Mater. Chem. C* **6,** 9238–9247 (2018).

7. Reineke, S., Thomschke, M., Lüssem, B. & Leo, K. White organic light-emitting diodes: Status and perspective. *Rev. Mod. Phys.* **85,** 1245–1293 (2013).